Hyperpolarized Nanodiamonds for Magnetic Resonance Imaging

Ewa Rej

School of Physics

University of Sydney

A thesis submitted in fulfillment of the requirements for the degree of

Doctor of Philosophy

2016

Abstract

This thesis describes a new MRI contrast agent based on hyperpolarized ^{13}C in nanodiamond. Nanodiamonds are readily available, non-toxic, can be surface functionalized, and have long T_1 relaxation times. Electronic defects in the nanodiamonds are used to hyperpolarize the ^{13}C nuclear spins through dynamic nuclear polarization, building up large nuclear magnetic resonance signals that persist for a long time. Enhancements are comparable to those used in liquid state hyperpolarization experiments, and can be detected in an MRI scan with low background signal. This imaging modality encompasses no ionizing radiation, and long imaging windows stemming from the long T_1 relaxation times of solids.

Firstly a major component of this thesis involved the construction of a polarizer at X-band frequencies for DNP of ^{1}H and ^{13}C at room temperature, based on a horn-mirror cavity and SpinCore NMR console. This thesis also details a W-band hyperpolarizer (based on a cryostat, probe, and microwave source on loan from M. Cassidy and C. Marcus) for ^{13}C DNP in ND with a Redstone NMR console and a $B \sim 3$ T magnet. A setup for brute force cryogenic hyperpolarization at millikelvin temperatures using a dilution refrigerator and hot swap probe is also described.

Data was collected exploring many aspects of the electron and nuclear spin dynamics across a range of nanodiamonds (NDs) between 18 nm and 2 μm. Nuclear T_1 relaxation is dominated by paramagnetic impurities, and long relaxation times up to 1 hr are measured for 2 μm ND. The T_1 relaxation time was found to increase with ND particle size. The main defects in ND are found to be P1 centres, spin-1/2 defects from the ND core, and spin-1/2 defects from the ND surface. Surface modification of

the NDs through air oxidation etches away the ND surface, removing sp^2 hybridized carbon and surface spin-1/2 electronic defects.

This thesis reports measurements of nanodiamond particles that are hyperpolarized via the solid effect mechanism at $T = 4\,\mathrm{K}$ and $B = 3$ T, with moderate polarizations also achieved at $T = 77$ K and room temperature. An increase in enhancement, and polarization decay time is observed with increasing ND particle size. Room temperature hyperpolarization of ND in the presence of water is also demonstrated, opening the possibility of an in vivo hyperpolarization modality. Different ND polarization and decay behavior is observed when hyperpolarizing using different electronic defects, with longer T_1 relaxation times measured when polarizing via spin-1/2 defects.

Spin-spin interactions in ND are also examined and long stimulated echo tails are observed when measuring under CPMG conditions, increasing T_2 by two orders of magnitude. An increase in T_2 with polarization time is also observed.

The surface defects in ND are used to polarize adsorbed liquids on the ND surface at X-band frequencies. Solid effect hyperpolarization of ^{1}H nuclear spin in a variety of liquids is demonstrated, and T_1 relaxation and hyperpolarization dynamics are examined. Results enable adsorbed and non-adsorbed liquids to be distinguised based on enhancement and relaxation time. NDs are also used as a conventional contrast agent, modifying the T_1 relaxation time of water based upon ND concentration.

Finally hyperpolarized ^{13}C ND MRI in a phantom is demonstrated.

Acknowledgements

Firstly, I am very grateful to my supervisor David Reilly. Thank you for all the support and guidance throughout the PhD, especially in the early years when we were both starting in this new field, and working everything out. David's enthusiasm and ability to inspire has led to the development of a remarkable lab with amazing people. I'm glad I was around to see the transformation of an empty room in the flooded basement to the nanoscience lab that we now work in.

I am also very grateful to Torsten Gaebel. I have learned a great deal from working alongside Torsten, especially about experimental techniques, and spin physics. Working together as a team has been very rewarding. Thank you for always answering my questions (especially all those on NV centres), correcting my German, and in general being a great person to work with.

Thanks also go to the other members of team NMR, Thomas Boele, and David Waddington. Working with Tom has been a pleasure, due to his kindness, sense of humor and need to put everything back in its proper place at the end of the day. The lab is a much cleaner and nicer environment thanks to his tireless efforts. David Waddington's attention to detail and need to understand each problem from the start ensured that all experiments were well thought out and on track. Thanks also to other students who worked in team NMR along the way: Hannah, Daphne, Tash and Maaika.

I am particularly grateful to Maja Cassidy, Charlie Marcus and Matt Rosen, for the generous loan of the probe and cryostat making up the W-band hyperpolarizer, and the microwave source and amplifier. Special

thanks to Maja for designing the hyperpolarizer and explaining its operation, as well as for the many conversations about hyperpolarized nanoparticles.

I would like to acknowledge the facilities and technical assistance of the staff at the Australian Centre for Microscopy & Microanalysis at the University of Sydney for help with the SEM measurements, the facilities and the technical assistance of staff at the Vibrational spectroscopy Core facility at the University of Sydney for Raman measurements, and the staff and facilities at the Nuclear Magnetic Resonance Facility at the Mark Wainwright Analytic Centre at the University of New South Wales for MAS NMR measurements and assistance with ESR measurements.

Experimental physics is a team effort, and I would like to thank the others in the lab. John started in the lab at the same time as me, and has been a constant companion over the past years. Thanks for the boardgames parties and marrying a part-time wedding cake maker. James has also been there from the beginning, introducing me to my dislike of techno music. Working with James and John taught me about perseverance and dedication. Thanks Xanthe for all the optimism, and slightly too long hikes, and Alice for imparting popular culture knowledge. Thanks also to the other PhD students, Masters students, and post-docs I've overlapped with: Steven, M.C., Seb, Ian, Kushal, Sylvain, Romain, Yuan Yuan, Charles, Matt, Graham, Christine, Joanna, and Harry. Thanks to Dane McCamey, Pratip Bhattacharya, Sekhar Ramanathan, Matt Rosen, Andrew Doherty, and Charlie Marcus for useful discussions. I would like to thank the workshop staff, the staff in the school of physics, and the lab administrators, Leanne, Jeremy and Wicky, for making paperwork easy. Finally I would like to thank my family for their support.

Contents

List of Figures

LIST OF FIGURES

List of Tables

Included Publications

Listed below are details of the papers that have been included in chapters in this thesis.

The work in Chapter 5 includes supplementary material from the paper:

E. Rej, T. Gaebel, T. Boele, D. E. J. Waddington, and D. J. Reilly.
Hyperpolarized nanodiamond with long spin-relaxation times.
Nature Communications **6**, 8459 (2015)

The work in Chapter 6 is based on the paper:

E. Rej, T. Gaebel, T. Boele, D. E. J. Waddington, and D. J. Reilly.
Hyperpolarized nanodiamond with long spin-relaxation times.
Nature Communications **6**, 8459 (2015)

The work in Chapter 7 is based on the paper:

E. Rej, T. Gaebel, D. E. J. Waddington, and D. J. Reilly.
Hyperpolarized nanodiamond surfaces.
Submitted to JACS.

The work in Section 6.10.5 is based on the paper:

T. Gaebel, **E. Rej**, T. Boele, D. E. J. Waddington, and D. J. Reilly.
^{13}C *spin dephasing in hyperpolarized nanodiamond.*
Manuscript in preparation.

Declaration

I herewith declare that I have produced this work without the prohibited assistance of third parties and without making use of aids other than those specified; notions taken over directly or indirectly from other sources have been identified as such. This paper has not previously been presented in identical or similar form to any other Australian or foreign examination board. The thesis work was conducted from 31/03/2010 to 29/02/2016 under the supervision of Professor David Reilly at the University of Sydney.

Student Signature:

Declaration

1

Introduction

Nanoparticles are becoming more common in everyday medicine, being used in the treatment of cancers [1, 2], the study of autoimmune diseases [3] and cardiovascular affections [4]. Of particular interest are nanoparticle theranostic agents in personalized medicine, combining both diagnostic and therapeutic characteristics. The ultimate goal for these nanoparticle bioagents is to create a platform which integrates imaging, tracking, and monitoring capabilities with targeted delivery of compounds to tumors, specific organs or cellular processes [5].

The use of nanoparticles has stemmed from an advance in nanotechnology, which has allowed for the growth of materials with micro and nano scale tailored properties for specific applications. In particular, in the emerging field of nanomedicine, the use of materials such as nanotubes [6, 7], silica [8], polymer nanoparticles [9, 10], and porous silicon [11, 12] is becoming widespread. Micro and nanoparticles are uniquely suited to act as a targeting bioprobe. Not only does the high surface to volume ratio enable a high concentration of biofunctionalization, but in addition, the enhanced permeability and retention effect, due to the high vascular nature of tumors leads to passive nanoparticle accumulation [13, 14].

Of all the available nanoparticle compounds, nanodiamonds (NDs) are emerging as a leading theranostic platform in nanomedicine. They are non-toxic and have been found to be compatible with biological environments [15–18]. Their easily adaptable carbon surface is readily functionalized [19] and allows for precise control over the surface chemistry [20]. As a result NDs have been conjugated to specific molecules [21], such as DNA, demonstrating potential for gene therapy treatments for inherited

disorders [22], chemotherapeutics, allowing for pharmaceutical delivery [18] of water-insoluble drugs [23] and enhancing the efficiency of chemotherapy by reducing drug efflux from tumor sites [24], and antigens, to evoke an immune response [25].

Advances in fabrication techniques have allowed affordable production of synthetic diamond with precise control of bulk characteristics. However, as the designs of the nanoparticle bioprobes become more complex, and the particle shape and surface chemistry change, the in-vivo behaviour (such as targeting, circulation time, and biocompatibility) can alter. Non-invasive detection of the nanoparticles is key to providing information about their location in a fast and cost effective manner.

Towards this goal the unique optical properties of the NV centre in diamond have allowed for optical tracking of single nanodiamonds in inter-cellular environments [26]. These properties also provide a means of detecting magnetic fields on the nanoscale using methods pioneered in controlling quantum devices [27–33]. However, beyond luminescence-based techniques, approaches to non-invasively detect and image diamond nanoparticles in-vivo have, to date, been lacking.

In general, fluorescent markers and optical imaging have not found wide use in in-vivo environments due to photo-bleaching and stability concerns. Other non-invasive imaging techniques such as computer assisted tomography (CT), and positron emission tomography (PET) have been used for nanoparticle imaging [34, 35], however, these methods involve ionizing radiation and there are toxicity concerns about long term use of these techniques.

Magnetic resonance imaging (MRI) is not well suited to detecting nuclei other than hydrogen due to its low sensitivity. Although in principle any nucleus with an unpaired spin can be detected in an MRI scan, the low concentrations, low gyromagnetic ratios and often low natural abundance of a spinful isotope, mean that the signal is not sufficient to be seen in an MRI scan. This thesis presents work showing how this limitation can be overcome by using hyperpolarization techniques, which can boost signals by 10,000 times [36]. With this increased signal, nanoparticles can be detected in an MRI scan [37, 38].

This new imaging modality is now coming into practice with commercial sterile hyperpolarizers being developed for in-vivo hyperpolarized MRI studies. Molecules are polarized in a polarizer (the nuclear magnetic resonance (NMR) signal is boosted through a number of hyperpolarization techniques such as dynamic nuclear polarization

(DNP), parahydrogen induced polarization (PHIP) or optical pumping), transferred out of the polarizer, injected into the patient or animal, allowed to circulate and accumulate at the targeted areas and then imaged with an MRI scan. Clinical applications for hyperpolarized MRI have developed, including hyperpolarized noble gases for MRI lung imaging [39], and hyperpolarized metabolites (such as [1-^{13}C]pyruvate) for disease diagnosis [40], or assessment of cell function [41] and tumor treatments [37, 42]. The success of these techniques have led to the first human trials [43].

Both these examples involve imaging processes invisible to conventional MRI, and while they highlight the improvements that hyperpolarized molecules can make, there is a limitation. The hyperpolarized nuclear state does not exist indefinitely. It only exists for the spin lattice T_1 relaxation time of the material, which, for the liquid metabolites mentioned, is typically $T_1 < 60$ s [44]. This limits hyperpolarized liquids to imaging processes that occur on short time scales.

Solid materials have much longer T_1 times, and nanoparticles with bulk characteristics can have long relaxation times, while being small enough to be introduced into the human body. This idea has been demonstrated using hyperpolarized silicon nanoparticles to produce real-time MRI images of mice with imaging time frames of half an hour [38, 45]

This thesis presents work towards extending the capabilities of ND as a theranostic platform with imaging through hyperpolarized MRI. Bulk, high-purity diamond can exhibit ^{13}C T_1 times of many hours [46] and the challenge therefore is to maintain these long spin lifetimes even when diamond is produced in nanoparticle form and in sufficient quantities to be of clinical relevance. The natural defects in diamond provide free electrons which can be used for hyperpolarization [47–52]. Of particular interest in the context of this thesis are the applications of DNP hyperpolarization techniques to nanodiamonds.

1.1 Outline of this thesis

This thesis details a new type of MRI contrast agent based on ^{13}C in nanodiamond. The imaging modality encompasses no ionizing radiation, with long imaging windows from long T_1 relaxation times of solids.

Nanodiamonds have been chosen for this work as they are non-toxic and can be

biofunctionalized. Nanodiamonds are readily available and easy to produce. They have promising bulk nuclear spin properties leading to long T_1 relaxation times, as well as a large concentration of electronic defects which can be used for hyperpolarization. Their configurable material properties allow for both tailoring of electron and ^{13}C nuclear spins through the material growth process.

Tailoring NDs as a new hyperpolarized bioprobe requires a detailed understanding of particle size effects, the structure of internal crystal defects, contaminants and spin-relaxation channels that arise from the nanoparticle surface. Spin dynamics in the core and the surface of the NDs are examined using hyperpolarized states to resolve new phenomena associated with defects in this versatile material system.

- **Chapter 2** outlines basic NMR theory, describing precessing spins in a magnetic field, how these translate to a macroscopic magnetization, and relaxation pathways. Experimental NMR techniques and pulse sequences which are implemented in this thesis are described.

- **Chapter 3** explains hyperpolarization techniques with specific focus on methods that are used for hyperpolarizing diamonds. Dynamic nuclear polarization is explained in more detail, with information given on electron-nuclear interactions, the Overhauser effect, the solid effect, thermal mixing and the cross effect.

- **Chapter 4** details the experimental setups used for W-band hyperpolarization at $f \sim 80$ GHz, for X-band hyperpolarization at $f \sim 9$ GHz, for polarization transfer experiments, and brute force hyperpolarization in a dilution refrigerator.

- **Chapter 5** gives a brief introduction to the physical characteristics of diamonds, with focus on electronic defects and impurities. Methods for producing synthetic diamonds are described. Characterization of various nanodiamonds are detailed, including SEM images and size distributions, room temperature ^{13}C spin-lattice relaxation measurements, MAS NMR studies, ESR spectra and Raman studies. Comparisons are made between different diamond types.

- **Chapter 6** details the hyperpolarization experiments performed on ^{13}C in ND at W-band frequencies at $T = 4$ K, 77 K and 300 K. Polarization build up times, polarization decay times, enhancements and spin-spin interactions of hyperpolarized nanodiamonds for applications as a magnetic resonance contrast agent

are examined. ND hyperpolarization in the presence of water simulating in-vivo environments is also explored.

- **Chapter 7** describes experiments performed at X-band frequencies to hyperpolarize nanodiamond surfaces. We use intrinsic free electrons on the ND surface to hyperpolarize molecules adsorbed onto ND, detailing ^{1}H polarization build up, enhancement, and T_1 spin-lattice relaxation. In addition ND is used as a contrast agent to modify the T_1 relaxation time of water based on ND concentration.

- **Chapter 8** provides concluding remarks, and the first demonstration of hyperpolarized ^{13}C ND MRI in a phantom.

2

Background NMR theory and NMR experimental methods

Nuclear magnetic resonance (NMR) utilizes the phenomenon of the response of atomic nuclei to the application of an external magnetic field. NMR was first described by Rabi in 1938 [53] and extended and refined by Bloch, Bloembergen, Pound and Purcell [54–57]. NMR was further developed using magnetic field gradients to provide spatial resolution and 2D images, leading to MRI [58–62].

NMR has now become an important tool in chemistry, biochemistry, medicine and physics, utilized for example in material characterization, spectroscopy, chemical structure determination, and disease diagnosis. In this thesis NMR techniques are used to probe the spin interactions between electron and nuclear spins and to measure the nuclear magnetization.

This chapter gives a brief description of NMR theory, giving a general treatment of spins in a magnetic field and details of relaxation mechanisms for nuclei in magnetic environments. The sections follow the theory provided by Slichter [63], Abragam [64], Keeler [65], and Corvaja [66]. Experimental measurements of NMR signals are described, including pulse sequences for T_1 and T_2 measurements.

2.1 Quantum mechanical treatment of a single spin in a magnetic field

Atomic nucleons and electrons have a fundamental property called spin, described by the spin quantum number S. Electrons are spin-1/2 particles ($S = 1/2$) while nuclei can either have integer or half-integer values of spin. A nucleus has a spin angular momentum of $S > 0$ when the number of protons, neutrons, or both is odd. The associated quantum number, m, can take values between $-S$ and $+S$ in integer steps, resulting in $2S + 1$ allowed values. In a magnetic field B along the z-direction, taken to be B_0, the spin angular momentum gives rise to a magnetic moment, μ_z, given by:

$$\mu_z = \gamma S_z = \gamma m \hbar \tag{2.1}$$

where γ is a constant of proportionality, known as the gyromagnetic ratio and $\hbar$ is Planck's constant divided by 2π. The gyromagnetic ratios of some commonly used nuclei in NMR, along with their abundance, are summarized in Table 2.1.

Nucleus	Gyromagnetic ratio [MHz/T]	Abundance [%]	Spin
^{1}H	42.576	99.9885	1/2
^{13}C	10.705	1.07	1/2
^{129}Xe	11.777	26.44	1/2
^{3}He	32.434	0.000137	1/2
^{15}N	-4.316	0.367	1/2
^{17}O	5.772	0.038	5/2
^{19}F	40.052	100	1/2
^{29}Si	-8.465	4.6832	1/2
^{31}P	17.235	100	1/2
e	28024.95	100	1/2

Table 2.1: Gyromagnetic ratios. Gyromagnetic ratios of nuclei typically used in NMR experiments.

A magnetic moment in a magnetic field produces an interaction energy, described by the Hamiltonian

$$\widehat{H} = -\vec{\mu} \bullet \vec{B} = -\gamma B_0 S_z \tag{2.2}$$

with eigenvalues

$$E_m = -\gamma \hbar B_0 m \tag{2.3}$$

This splitting in energy levels is known as Zeeman splitting and is shown in Fig. 2.1 for a spin-1/2 system. The spacing between consecutive energy levels is given by

$$\Delta E = \hbar\omega = \gamma \hbar B_0 \tag{2.4}$$

leading to the condition required for resonance:

$$\omega = \gamma B_0 \tag{2.5}$$

where ω is known as the resonance frequency, or the Larmor frequency.

Similarly, for electrons in a magnetic field, the magnetic moment is given by:

$$\mu_z = \frac{g_e \mu_B}{\hbar} S_z \tag{2.6}$$

where g_e is the g-factor and μ_B is the Bohr magnetron. For a free electron

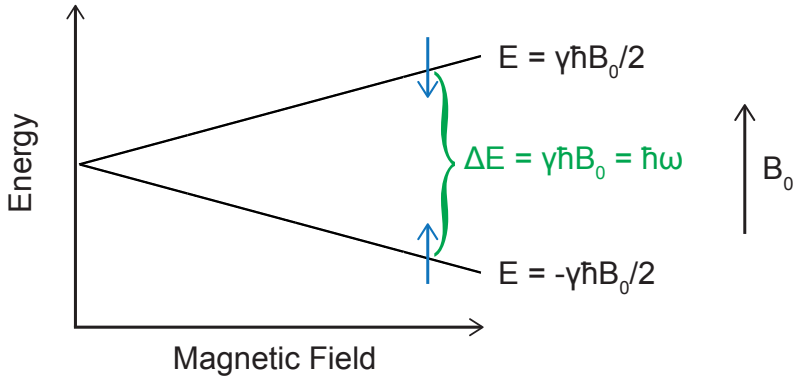

Figure 2.1: Energy level schematic for a spin-1/2 particle in a magnetic field. The lower energy state has an energy of $E = -\gamma\hbar B_0/2$ and the higher energy state has an energy of $E = \gamma\hbar B_0/2$. The energy level splitting is given by $\Delta E = \hbar\omega = \gamma\hbar B_0$. This frequency, ω, is known as the resonance frequency and radiation at this frequency can be used to drive transitions between energy levels.

$g_e = 2.0023$, however this changes depending on the chemical environment.

In much the same way as for nuclear spins, electron spins are polarized by a static magnetic field leading to a Zeeman splitting, with energy separation

$$\Delta E = g\mu_B B_0 \tag{2.7}$$

2.2 Boltzmann polarization

NMR experiments are performed on bulk samples and a macroscopic number of spins are measured. Each nuclear spin interacts with the magnetic field and exists in a Zeeman energy state. A macroscopic magnetization (M) for a spin-1/2 system, is created by the difference in the number of spins in the spin up and spin down states. The net magnetization is given by

$$\vec{M} = \sum \vec{\mu}_{up} + \sum \vec{\mu}_{down} \tag{2.8}$$

where μ_{up} and μ_{down} are the magnetic moments parallel and anti-parallel to the external magnetic field respectively. At thermal equilibrium, the populations of these energy levels obey Boltzmann statistics, and the population in each state is given by

$$N_i = \frac{N}{Z} g_i e^{-E_i/k_B T} \tag{2.9}$$

where N_i is the number of particles in the state with energy E_i, g_i is the degeneracy of the energy level, k_{B} is Boltzmann's constant, T is the temperature, N is the total number of particles $N = \sum_i N_i$, and Z is the partition function $Z = \sum_i g_i e^{-E_i/k_B T}$.

The polarization, P, of the system is proportional to the magnetization and is defined as the population difference between the upper (N_+) and lower (N_-) energy levels. The polarization is given by

$$P = \frac{N_- - N_+}{N_+ + N_-} \tag{2.10}$$

A spin-1/2 system, with no degeneracy has a polarization given by

$$P = \tanh\left(\frac{\gamma \hbar B_0}{2 k_B T}\right) \tag{2.11}$$

The polarization is plotted for varying magnetic fields and temperatures for an electron, a ^{13}C nucleus and ^{1}H nucleus, see Fig. 2.2. We note polarization increases with increasing magnetic field (as the Zeeman splitting increases, additional thermal energy is required to populate the higher energy levels) and polarization increases with decreasing temperature (there is less thermal energy to excite the particles to the higher energy levels). The electron spin polarization is much larger than the nuclear spin polarization, due to the difference in gyromagnetic ratios.

A system that is driven out of thermal equilibrium is typically called hyperpolarized, and can have polarizations greater or less than the polarization at thermal equilibrium.

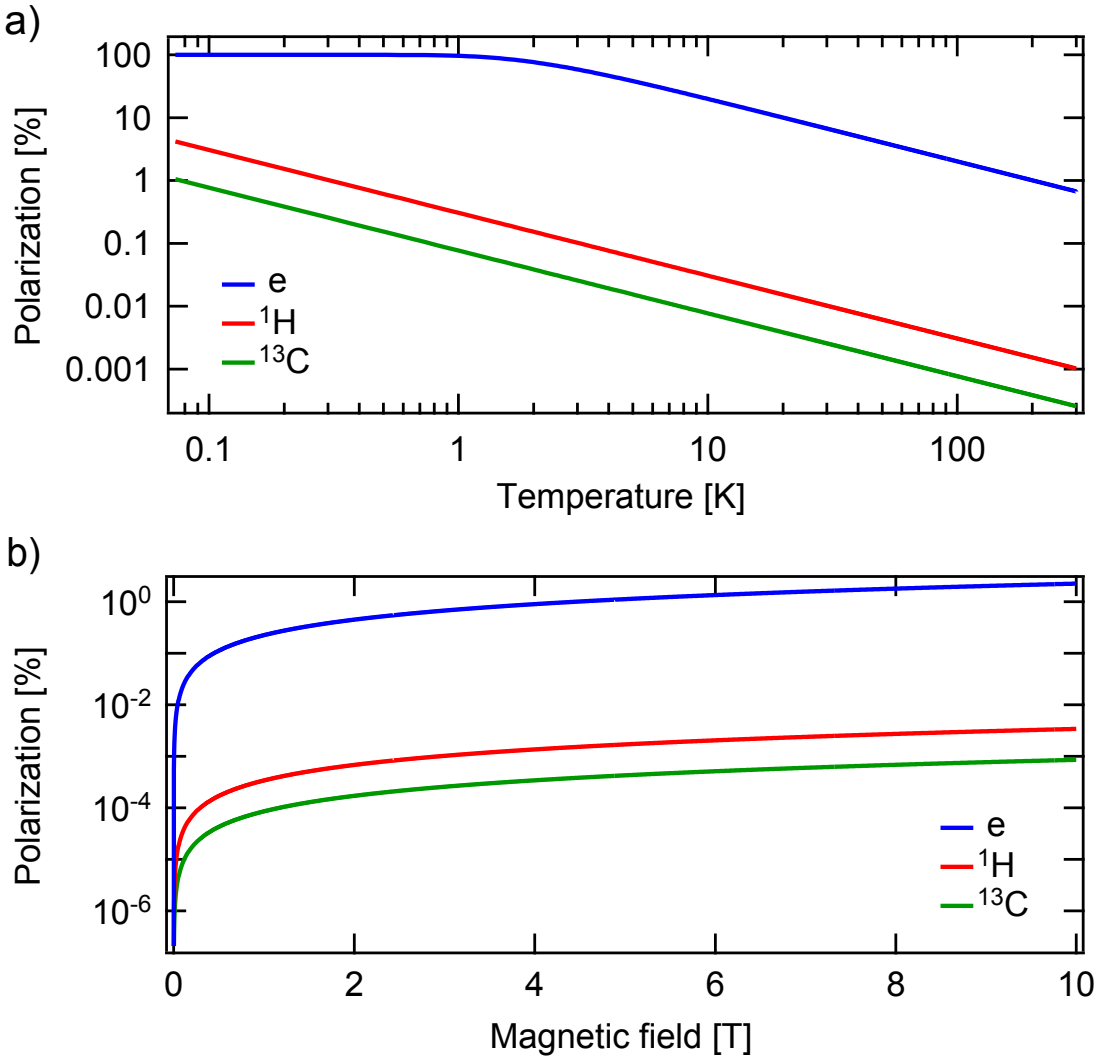

Figure 2.2: Boltzmann polarization as a function of magnetic field and temperature. Boltzmann polarization as a function of **a)** temperature (at $B = 3$ T) and **b)** magnetic field (at $T = 300$ K) for an electron (blue), a ^{13}C nucleus (green) and a ^{1}H nucleus (red). The polarization increases with decreasing temperature and increasing magnetic field. The electron has a much larger polarization than the nuclear spins due to its larger gyromagnetic ratio.

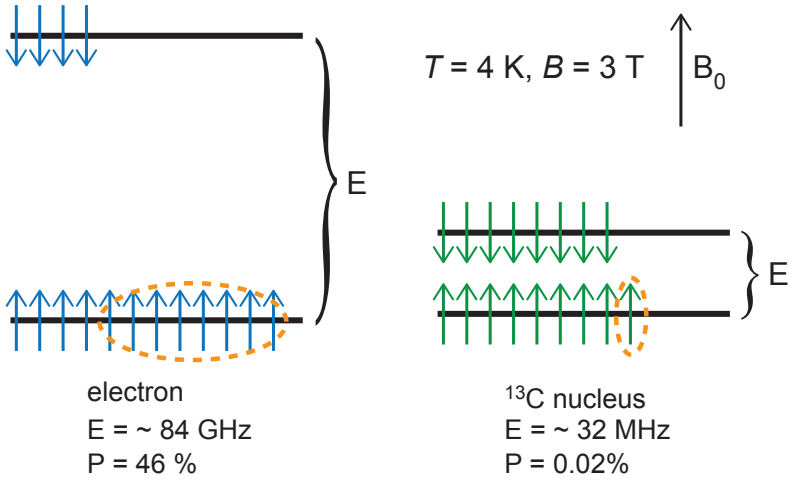

Figure 2.3: Schematic of a two level energy diagram for an electron spin and a ^{13}C nuclear spin. The electron spin system is highly polarized while the nuclear system remains relatively unpolarized at $B = 3$ T and $T = 4$ K, conditions typically used for hyperpolarization. The spin excess, which is proportional to the magnetization, is highlighted in yellow. The Zeeman energy splitting (E) and polarization (P) are shown.

A schematic of energy level diagrams for an electron and a ^{13}C nuclear spin at $B = 3$ T and $T = 4$ K (typical conditions under which many hyperpolarization experiments are performed), with exaggerated populations is shown in Fig. 2.3. The spin excess which leads to the magnetization is highlighted. The precession of the net magnetization is the quantity which is detected in an NMR experiment using pulse sequences and induction coils.

2.3 Rotating frame treatment of spin in a time dependent magnetic field

The motion of a spin in a magnetic field can also be described in a semi-classical framework. An external magnetic field B produces a torque on the magnetic moment μ, given by $\mu \times B$. The torque is equated with the change in angular momentum:

$$\frac{d\mu}{dt} = \mu \times (\gamma B) \tag{2.12}$$

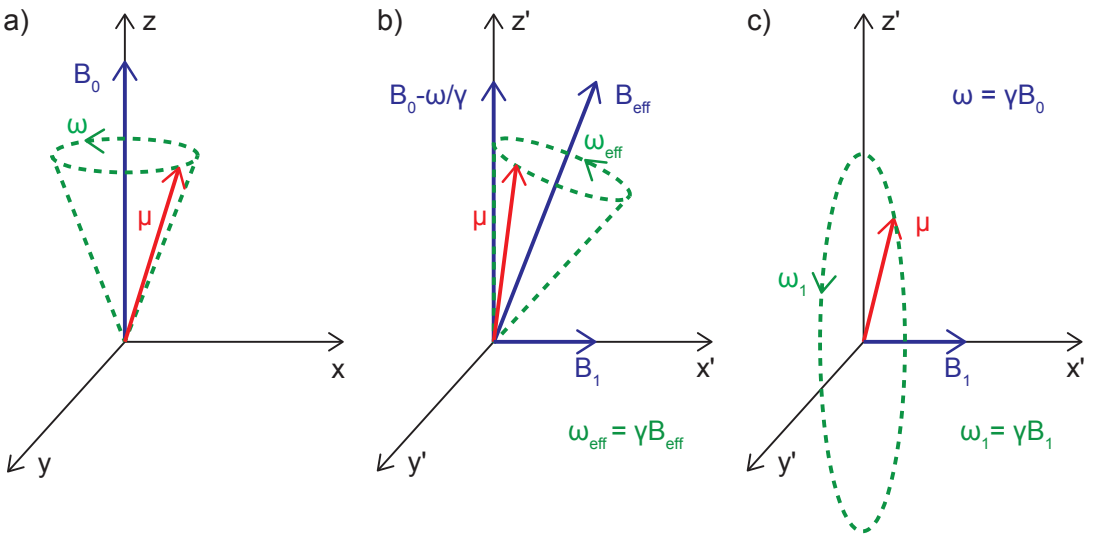

Figure 2.4: Precession of a magnetic moment in a magnetic field. a) Precession of a magnetic moment (μ) about a magnetic field (B_0) applied in the z-direction. The precession occurs at the resonance frequency ω, governed by the gyromagnetic ratio and applied field, $\omega = \gamma B_0$. **b)** Precession in the rotating frame about an effective magnetic field $B_{eff} = (\hat{z}(B_0 - \omega/\gamma) + \hat{x}B_1)$. The precession occurs at a frequency of $\omega_{eff} = \gamma B_{eff}$ in a fixed cone about B_{eff}. **c)** When the resonance condition is met and $\omega = \gamma B_0$, precession occurs in the y′-z′ plane about B_1 at a frequency $\omega_1 = \gamma B_1$.

This equation holds for both time dependent and static magnetic fields. In the case of a static magnetic field, B_0, the magnetic moment precesses at a fixed angle about B_0, see Fig. 2.4a.

A useful approach to studying time dependent applied magnetic fields is to consider the spin system in a frame rotating about the z-axis at an angular velocity Ω. The torque is then given by

$$\frac{d\mu}{dt} = \mu \times (\gamma B + \Omega) \tag{2.13}$$

If this frame in chosen to rotate at the Larmor frequency (Ω = -γB_0) then $d\mu/dt$ = 0, and the angular momentum appears static in this frame.

An alternating magnetic field (B_1) perpendicular to the static field (considering

only components rotating in the direction of the magnetic moments) can be described as

$$\vec{B_1} = B_1(\hat{x}\cos\omega_z t + \hat{y}\sin\omega_z t) \tag{2.14}$$

Applying this field (B_1) in conjunction with the static field (B_0), gives an equation of motion for the magnetic moment

$$\frac{d\mu}{dt} = \mu \times \gamma(B_0 + B_1(t)) \tag{2.15}$$

In a frame rotating at $\Omega = \omega_z$ about the z-direction (denoted by x′,y′,z′), B_1(t) is static. Additional, near resonance $\omega_z + \gamma B_0 \cong 0$. Applying these two conditions, we obtain

$$\frac{d\mu}{dt} = \mu \times (\widehat{z}(\omega_z + \gamma B_0) + \widehat{x}\gamma B_1) = \mu \times \gamma B_{eff} \tag{2.16}$$

$$\text{where} \qquad B_{eff} = (\widehat{z}(B_0 - \omega/\gamma) + \widehat{x}B_1) \tag{2.17}$$

The magnetic moment precesses in a cone of fixed angle about B_{eff} (which appears as a static applied field in the rotating frame) at a frequency $\omega_{eff} = \gamma B_{eff}$, see Fig 2.4b.

If the resonance condition is met and $\omega = \gamma B_0$, then $B_{eff} = \widehat{x}B_1$ resulting in precession in the y′-z′ plane about B_1 at a frequency $\omega_1 = \gamma B_1$, see Fig. 2.4c.

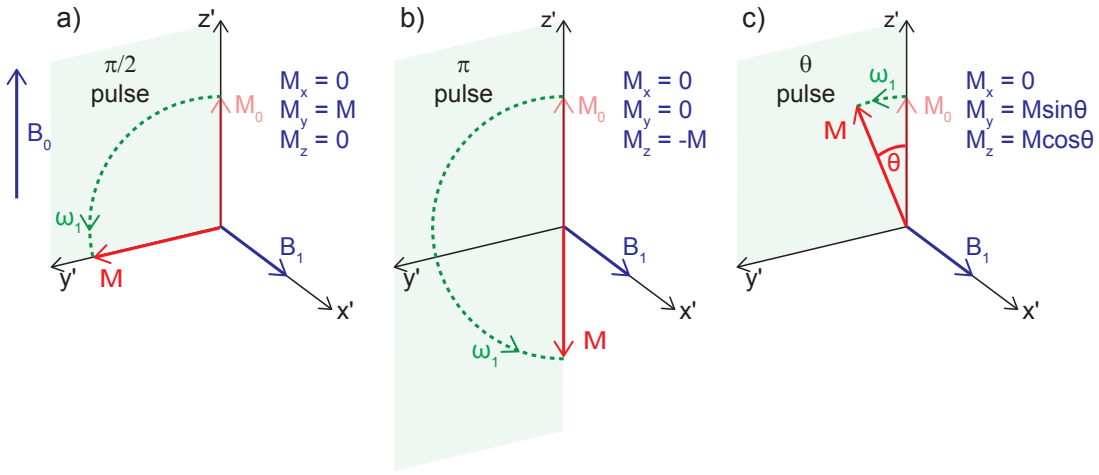

Figure 2.5: Schematic of NMR tip angles. **a)** When a $\pi/2$ pulse is applied the magnetization (M) is rotated by 90° from the z-direction to the y-direction. **b)** When a π pulse is applied the magnetization is flipped (rotated from the z direction to the -z direction). c) Arbitrary pulse lengths result in a tip angle of θ, with magnetization left in both the y and z directions.

2.4 NMR pulses and signal detection

If the magnetic field B_1 is applied on resonance for a time t_w (in the form of a microwave pulse), the precession of the magnetization in the y′-z′ plane results in a tip by an angle θ given by

$$\theta = \gamma B_1 t_w \tag{2.18}$$

When the microwaves are applied for a time and amplitude such that $\theta = \pi/2$, the pulse is known as a 90° pulse or a $\pi/2$ pulse, and the magnetic moment is transferred from the z-direction to the y-direction, see Fig. 2.5a. When the microwaves are applied for a time and amplitude such that $\theta = \pi$ the microwave pulse is known as a 180° pulse or a π pulse and the magnetic moment is flipped (transferred from the z direction to the -z direction), see Fig. 2.5b. Arbitrary pulse lengths result in a tip angle of θ, leaving some magnetization in both the y and z directions, see Fig. 2.5c.

At the end of the pulse, when B_1 is turned off, the magnetic moment precesses

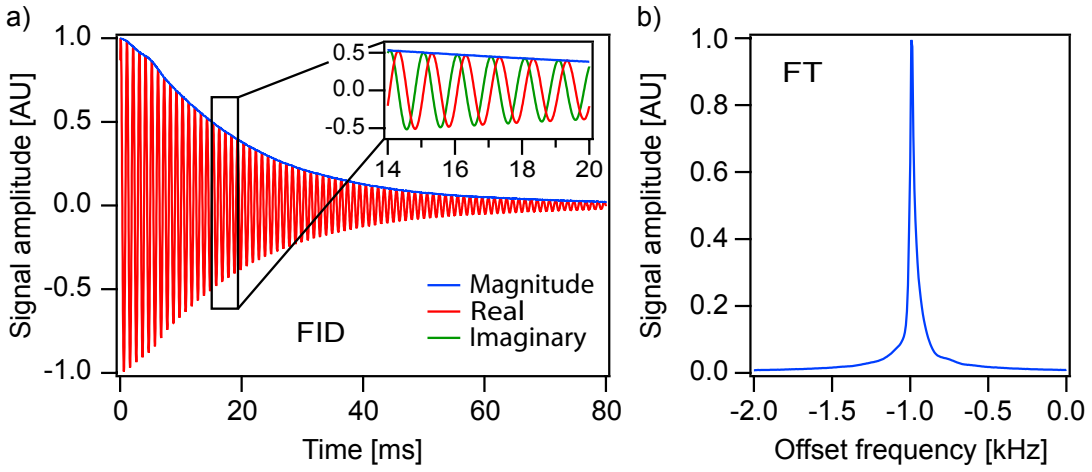

Figure 2.6: Free induction decay and Fourier transform of an NMR signal. **a)** The free induction decay (FID) of ^{1}H spins in an 50:50 H_2O:D_2O sample at $B = 7\,\mathrm{T}$. The detected NMR signal is mixed with a carrier wave at the same frequency as the applied microwave B_1 resulting in real (red) and imaginary (green) (carrier offset by $90°$) signals. **b)** The Fourier transform of the FID shows an NMR peak at the offset frequency from resonance.

about B_0 in the lab frame at a frequency $\omega = \gamma B_0$. This precession results in a flux through a coil (placed around the spins in the x-y plane), and the resulting electromotive force (EMF) can be detected. This EMF is called the free induction decay (FID), see Fig. 2.6a.

The detected NMR signal is mixed with a carrier wave at the same frequency as the applied microwave B_1 resulting in real and imaginary (carrier offset by $90°$) signals. A Fourier transform (FT) is performed resulting in peaks at the offset frequency from resonance, see Fig. 2.6b.

The amplitude of the NMR signal depends upon the angle through which the magnetization has been tipped. A maximum signal is detected after a $\pi/2$ pulse, when the magnetization is in the x-y plane, and a minimum signal is detected after a π pulse. The detected magnetization, M_y for example, follows a sinusoidal shape with pulse time, see Fig 2.7. These oscillations, known as Rabi oscillations, occur at a frequency:

$$\Omega_r = \sqrt{\omega_1^2 + \Delta^2} \tag{2.19}$$

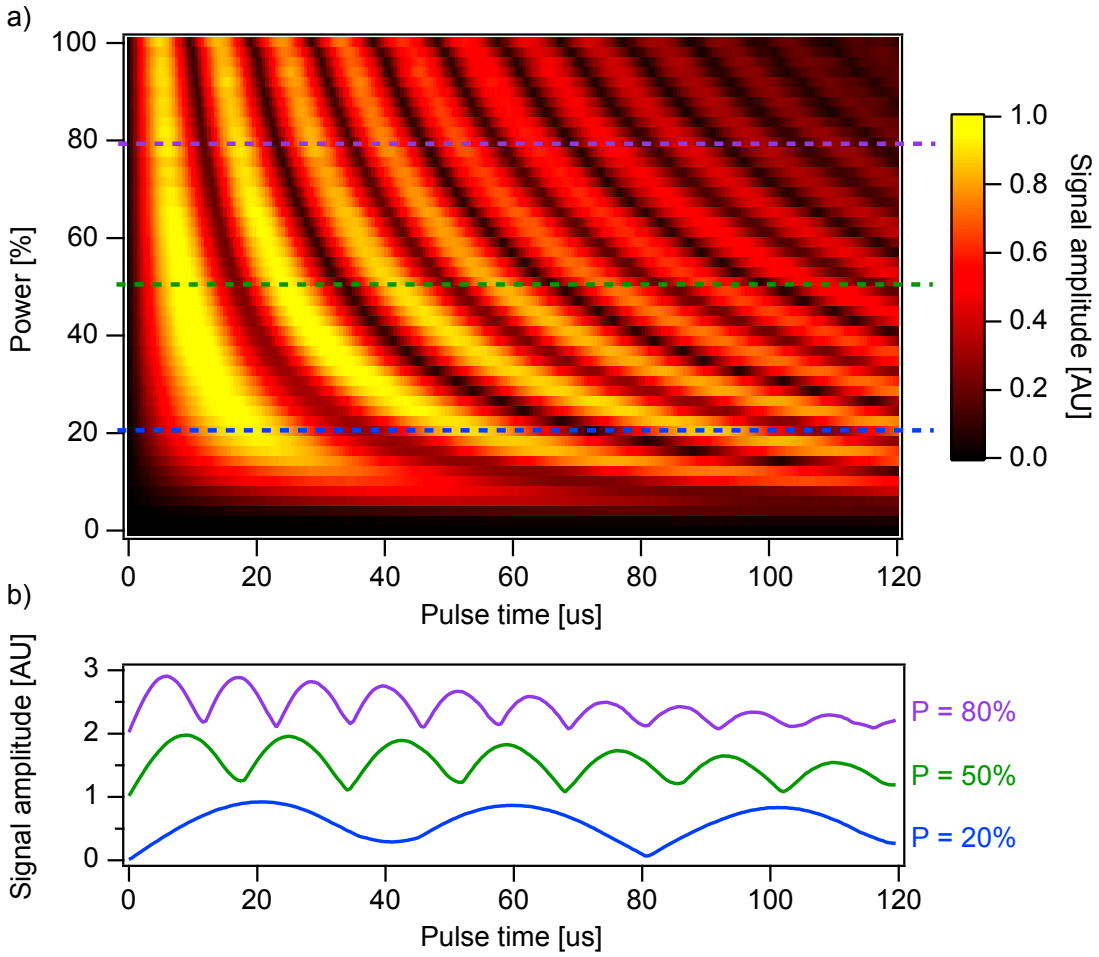

Figure 2.7: NMR Rabi oscillations. a) Rabi oscillations measured on ^{1}H spins in olive oil at $B = 450$ mT. The absolute value of the FT NMR signal amplitude (colour scale) is shown as a function of pulse time and amplitude as a percentage. A maximum signal is detected after a $\pi/2$ pulse when the magnetization is in the x-y plane, and a minimum signal is detected after a π pulse. **b)** Cross sections of the colour plot, showing the decrease in Rabi frequency with decreasing power.

where Δ is the detuning (the offset from resonance frequency), and ω_1 is the Rabi frequency at resonance. The Rabi oscillation frequency increases with pulse amplitude and detuning.

The induced EMF does not exist indefinitely. The signal decays through two processes, spin-lattice relaxation (T_1 decay) caused by spins returning to thermal equilibrium after an applied pulse, and spin-spin relaxation (T_2 decay) caused by dephasing.

2.5 Spin-lattice relaxation

The spin-lattice relaxation time (T_1) is the time constant for the nuclear spin system to return to thermal equilibrium following a perturbation. The T_1 relaxation time can range between $T_1 \sim$ ms for some liquids, such as oil, to $T_1 \sim$ days for some bulk solids, such as diamond. In general the magnetization returns to thermal equilibrium following an exponential curve with time constant T_1.

The application of an alternating electromagnetic field at the resonance frequency will cause the number of particles in each energy level to change. However, only considering the applied microwave field and the spins in a static field is not enough to completely describe the system. The nuclei transfer energy and undergo spin flips with an additional reservoir coupled to the nuclei. In this case, it is the lattice and it is able to provide and absorb energy in the form of phonons.

Assuming that the lattice is a two level system with the same energy levels as the nucleus, a conservation of energy argument can be used to explain the allowed transitions. A transition from the lower to the higher energy level of the nucleus, with the spin absorbing energy E, occurs with a transition of the lattice from the higher to the lower energy state via a phonon of energy E and vice versa. Transitions where both the nucleus and the lattice move from the lower to the higher energy state and vice versa are forbidden. A schematic of the allowed and forbidden transitions are shown in Fig. 2.8.

A rate equation for the population difference after a perturbation for a coupled lattice and nuclear systems is given by:

$$\frac{dn}{dt} = N(W_\downarrow - W_\uparrow) - n(W_\downarrow + W_\uparrow) = \frac{n_0 - n}{T_1} \tag{2.20}$$

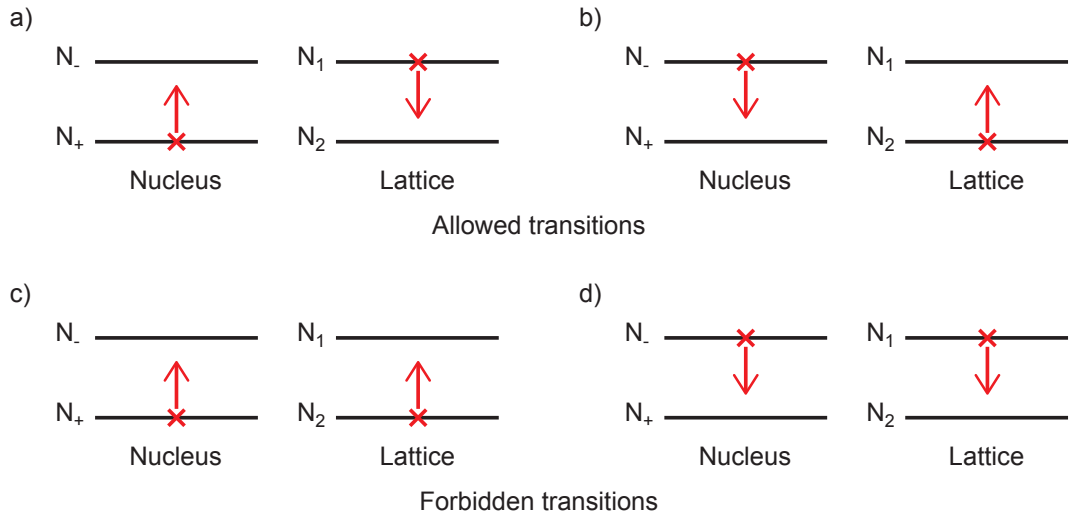

Figure 2.8: Allowed and forbidden transitions for a nucleus coupled with a lattice. The nucleus moves between spin up and spin down states emitting or absorbing energy, which is absorbed or supplied by the lattice as a phonon. **a, b)** Allowed transitions, and **c, d)** forbidden transitions.

$$\text{with} \qquad n_0 = N\frac{W_\downarrow - W_\uparrow}{W_\downarrow + W_\uparrow} \qquad \text{and} \qquad \frac{1}{T_1} = W_\downarrow + W_\uparrow \tag{2.21}$$

where n is the population difference between the two energy states, N is the total number of spins, $W_\downarrow$ is the probability that a transition from N_- to N_+ is induced and $W_\uparrow$ is the probability that a transition from N_+ to N_- is induced.

The magnetization is proportional to n, as $M_z = \gamma\hbar n/2$, which gives us

$$\frac{dM_z}{dt} = \frac{M_0 - M_z}{T_1} \tag{2.22}$$

with a solution given by

$$M_z = M_0 + Ae^{-t/T_1} \tag{2.23}$$

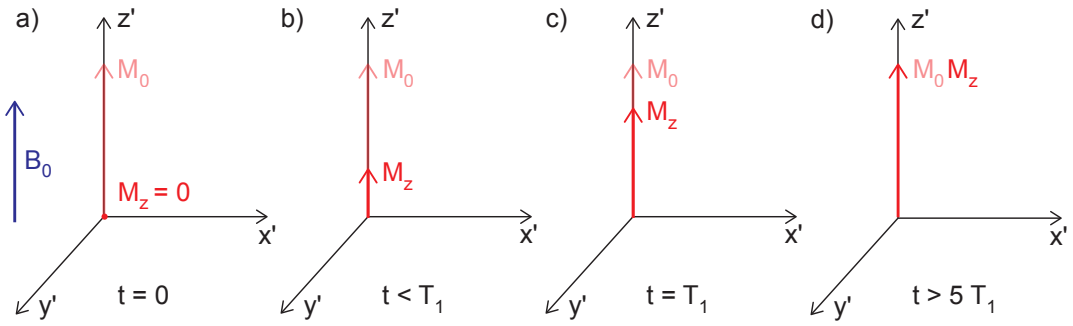

Figure 2.9: Spin-lattice T_1 build up for a sample placed in a magnetic field. **a)** Initially there is no net magnetization. **b)** After a certain time the magnetization along the z-axis begins to build up. **c)** When $t = T_1$, 2/3 of the equilibrium magnetization has built up. **d)** When $t > 5T_1$ all the magnetization has aligned along the z-axis and the magnetization has saturated.

where M_0 is the thermal equilibrium magnetization, A is a constant and T_1 is the characteristic time associated with the approach to thermal equilibrium. A schematic of the T_1 build up for a macroscopic sample that is placed in an external magnetic field is shown in Fig. 2.9.

The main source of relaxation for liquids and gasses comes from the tumbling of molecules and bond rotations, which typically have an energy similar to the Larmor frequency. Fluctuations of fixed paramagnetic impurities within a solid lattice are the main source of decay for solids such as ND.

For a system of spins with a homogenous environment a single characteristic time scale (T_1) exists for the system. In a system with spins in inhomogeneous environments, the T_1 of the bulk sample is an average over all the T_1 relaxation times in the system. If there are multiple distinct baths, the return to thermal equilibrium can be described as a sum of the individual exponential characteristic times for each spin bath, for example we would expect bi-exponential behavior for a nanoparticle with a surface and a core structure.

2.6 Measuring T_1

Several techniques exist to measure the T_1 relaxation time of a material. The two most common are to invert the magnetization and observe how it returns to thermal

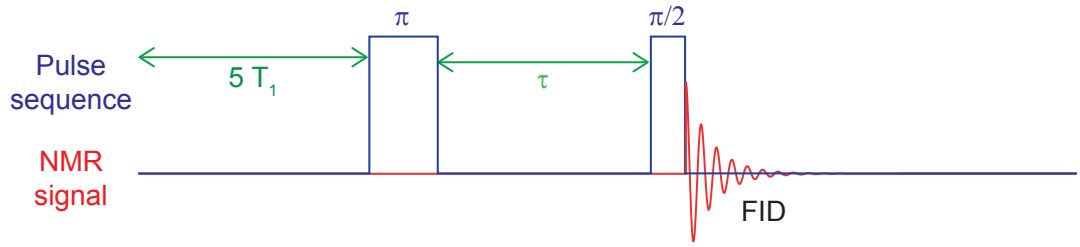

Figure 2.10: An inversion recovery pulse sequence to measure T_1. An NMR sample is placed in a magnetic field and the spins are allowed to reach thermal equilibrium ($\sim 5T_1$). A π pulse is applied to invert the magnetization. After a time τ, a $\pi/2$ pulse is applied to tip the magnetization into the x-y plane for detection. The magnetization follows a build up curve given by Equation 2.24.

equilibrium using an inversion recovery sequence, or to destroy all magnetization and observe it rise to thermal equilibrium using a saturation recovery pulse sequence.

For inversion recovery the saturated magnetization is flipped with a π pulse and the return to thermal equilibrium is monitored using a $\pi/2$ pulse, after a time τ, to tip the built up magnetization into the x-y plane for detection, see Fig. 2.10. The built up magnetization returns from $-M_0$ to $+M_0$ following the equation:

$$M = M_0(1 - 2e^{-\tau/T_1}) \tag{2.24}$$

This pulse sequence becomes impractical when measuring samples with long T_1 relaxation times as $t \sim 5$ T_1 must elapse for the system to return to thermal equilibrium before the magnetization can be flipped again.

For saturation recovery, initial magnetization is destroyed with n x $\pi/2$ pulses (where n is the number of pulses) and the return to thermal equilibrium is monitored using a $\pi/2$ pulse (after a time τ to tip the magnetization into the x-y plane for detection), see Fig. 2.11. The $\pi/2$ saturation pulses are applied at a rate longer than T_2^* (the time constant of the FID), such that complete dephasing of the spins has occurred, and much less than T_1, such that no polarization build up occurs. The build up magnetization returns from 0 to M_0 following the equation:

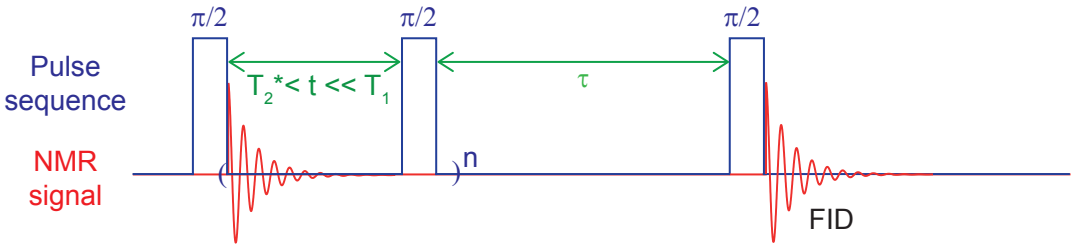

Figure 2.11: A saturation recovery pulse sequence used to measure T_1. All magnetization is destroyed by applying n x $\pi/2$. After a time τ, a $\pi/2$ pulse is applied to tip the built up magnetization into the x-y plane for detection. The magnetization follows a build up curve given by Equation 2.25.

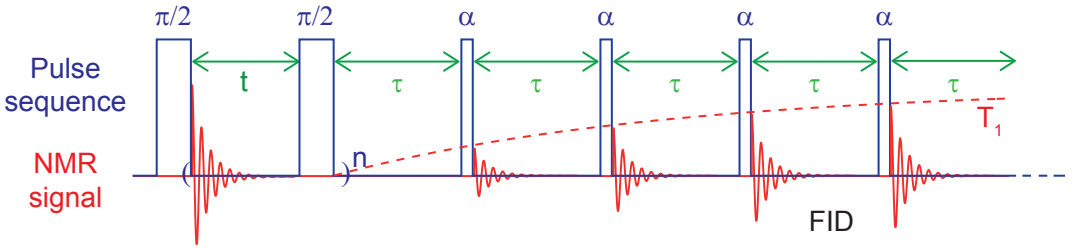

Figure 2.12: A small tip angle pulse sequence used to measure T_1. All magnetization is destroyed with n x $\pi/2$ pulses. After a time τ, a small tip angle (α) pulse is applied to tip some of the built up magnetization ($M_0 \cos\alpha$) into the x-y plane for detection. The rest ($M_0 \sin\alpha$) of the magnetization and any more that is built up due to T_1 can be detected in successive pulses. The magnetization follows a build up curve given by Equation 2.26.

$$M = M_0(1 - e^{-\tau/T_1}) \tag{2.25}$$

In this measurement scheme successive data points or averages can be taken without waiting for the system to reach thermal equilibrium ~ 5 T_1.

By replacing the readout $\pi/2$ pulse with a smaller tip angle (α) pulse, only a small amount of magnetization tips into the x-y plane ($M_0 \cos\alpha$) and the rest ($M_0 \sin\alpha$) can still be detected with successive pulses, see Fig. 2.12. After the initial saturation m x α pulses are applied to tip a small amount of the magnetization into the x-y plane for detection. The magnetization returns to thermal equilibrium following the equation:

$$M = M_0(1 - \cos(\alpha)^{m-1} e^{-t/T_1}) \tag{2.26}$$

where m is the pulse number and $t = \tau m$. In this sequence the pulse length must be small and the time between pulses must be sufficiently long such that only a small amount of polarization is lost due to the measurement.

2.7 Spin-spin relaxation

The spin-spin relaxation time (T_2) is the characteristic time for the transverse component of the magnetization to dephase and can be thought of as the coherence time of the spins. This decay is caused by inhomogeneities in the magnetic field, both time dependent and time independent.

Each nuclear spin experiences a local field which is a combination of the applied fields and the dipole-dipole fields caused by surrounding spins. Although these fields average to zero over the bulk sample, variations in the local field lead to differences in the precession frequency of the nuclei. The result is a fanning out, or dephasing, of the moments in the x-y plane (assuming applied fields are along the z-axis) and a reduction of the transverse magnetization vector, see Fig. 2.13. The decay of the transverse magnetization, given by $\vec{M}_\perp = M_x\hat{x} + M_y\hat{y}$, generally follows an exponential curve with time constant T_2. In the rotating frame:

$$\frac{d}{dt}\vec{M}_\perp = -\frac{1}{T_2}\vec{M}_\perp \tag{2.27}$$

with solution

$$M_\perp(t) = M_\perp(0)e^{-t/T_2} \tag{2.28}$$

where $M_\perp(0)$ is the initial magnetization.

Theoretically $T_2 \leq 2\ T_1$, however in general spin-spin relaxation is faster than

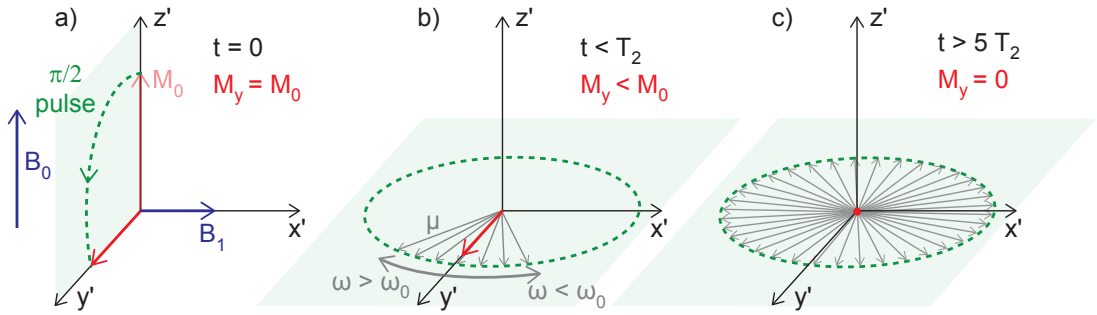

Figure 2.13: T_2 dephasing for an ensemble of spins. a) After a $\pi/2$ pulse to tip the magnetization, the spins precess in the x-y plane. **b)** Variation in local magnetic field experienced by individual spins lead to differences in the precession frequency. This results in the magnetic moments fanning out in the x-y plane, reducing the transverse magnetization vector. **c)** The dephasing continues until there is no magnetization left in the x-y plane.

spin-lattice relaxation. Typically liquids have the longest T_2 relaxation times, ranging between milliseconds and seconds due to motional narrowing. Amorphous and crystalline solids generally have T_2 relaxation times in the range of a few milliseconds.

Experimentally, the largest contribution to dephasing is from static magnetic field inhomogeneities in B_0 resulting in an FID with an envelope given by a time constant T_2^*. Typically $T_2^* << T_2$.

The loss of transverse magnetization due to static field inhomogeneities can be recovered using spin echo pulse sequences, see Fig. 2.14. After the magnetic moments have dephased, a π_x pulse (a π pulse about the x-axis) is applied at time τ, flipping the spins in the x-y plane. The spins which precessed faster (and were in front of the net magnetization vector) are now behind the net magnetization vector and vice versa. These magnetic moments refocus after time τ after the π pulse (known as the echo time). Pulse echos can only be used to refocus dephasing processes that occur on a time scale longer than the echo time. Intrinsic dephasing due to surrounding spins typically occurs on a faster time scale than the echo time and can not be refocused. The refocusing sequence is known as a Hahn echo [67]. Additional π pulses can also be used to refocus the magnetization after it has dephased again until the intrinsic dephasing time of the material (T_2) is obtained. These trains of π pulses will additionally eliminate any time-dependent dephasing effects occurring on a time scale slower than $1/\tau$. This sequence

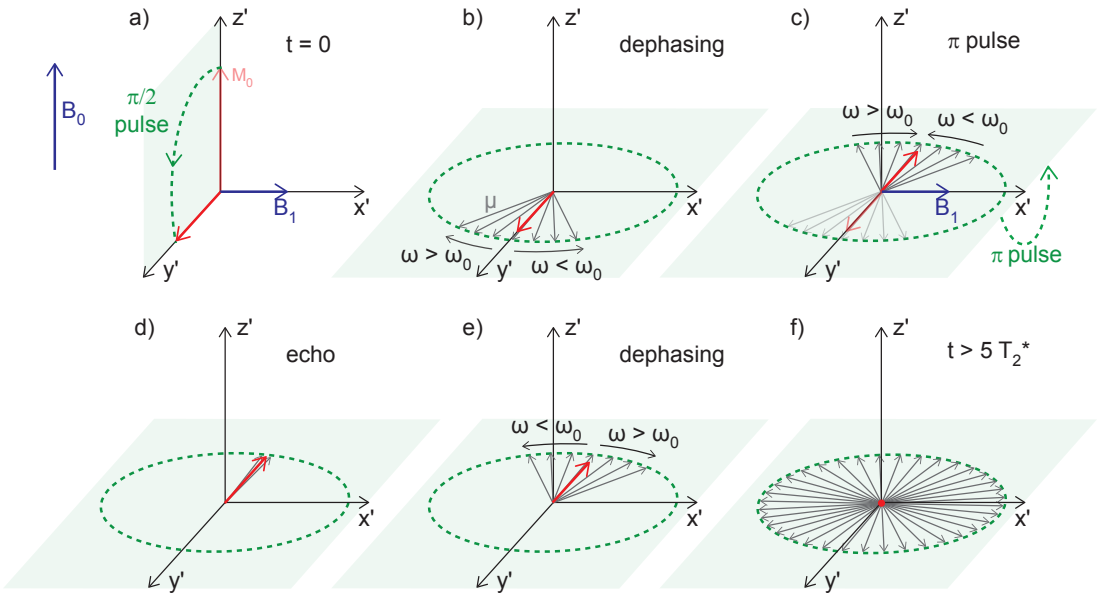

Figure 2.14: Spin-spin T_2 dephasing for an ensemble of spins using a Hahn echo. a) A $\pi/2$ pulse tips the magnetization (red arrow), and the spins precess in the x-y plane. **b)** Dephasing of the magnetization occurs due to local magnetic field variations, leading to differences in the precession frequency of individual spins (grey arrows). **c)** The dephasing due to time static field variation can be refocused. A π pulse flips the spins in the x-y plane, and spins which were precessing faster are now behind spins that were precessing slower and vice versa. **d)** A refocusing of the magnetic moment after a time τ (the time between the $\pi/2$ and the π pulse) occurs. **e)** The magnetic moments continue to fan out in the x-y plane, leading to a loss of magnetization. Additional π pulses can be used to continue refocusing the dephased magnetization, extending the coherence time from T_2^* to T_2. Loss of magnetization due to time dependent fluctuations in the magnetic field, such as from intrinsic spins in the sample, can not be refocused. **f)** The dephasing continues until there is no magnetization left in the x-y plane.

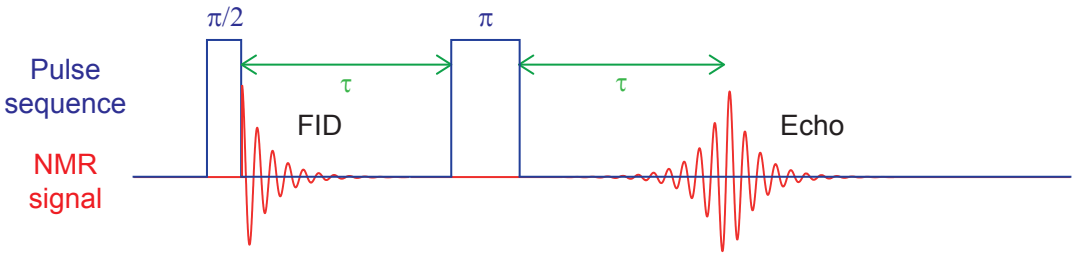

Figure 2.15: A Hahn echo pulse sequence used to measure T_2. After the system has reached thermal equilibrium a $\pi/2$ pulse tips the magnetization into the x-y plane. The dephasing of the spins can be refocused using a π pulse applied after a time period τ, which results in an echo at a time τ after the π pulse. The decay of transverse magnetization follows a curve given by Equation 2.29.

is known as a Carr-Purcell sequence [68] and adding an additional phase to counter pulse length errors results in a Carr-Purcell-Mieboom-Gill (CPMG) sequence [69].

2.8 Measuring T_2

For a Hahn echo sequence, an NMR sample is placed in a strong magnetic field and a $\pi/2$ pulse tips the magnetization into the x-y plane. After waiting a time τ, a π pulse is applied to reverse the magnetization in the x-y plane, which leads to a refocused signal at a time τ after the π pulse. By varying τ, the decay of the echo peak can be measured, see Fig. 2.15. The transverse magnetization decays from M_0 to 0 following:

$$M = M_0 e^{-\tau/T_2} \tag{2.29}$$

For a CPMG sequence, additional π pulses are applied at intervals of 2τ to refocus the magnetization, canceling time independent dephasing, see Fig.2.16. The transverse magnetization decays from M_0 to 0 following Equation 2.29.

A CPMG experiment can result in a shorter experimental time than Hahn echo, as all the echos can be measured in one experiment, however care must be taken to ensure no accumulation of pulse time errors.

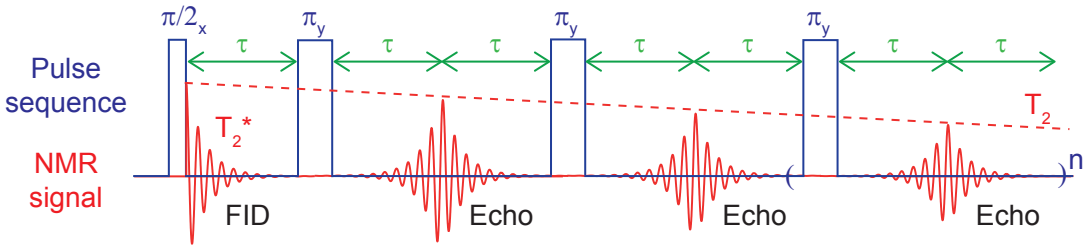

Figure 2.16: A CPMG sequence used to measure T_2. After the magnetization has been tipped into the x-y plane using a $\pi/2$ pulse, a π pulse (at time τ) can be used to refocus the dephasing due to static field inhomogeneities (at a time τ after the π pulse). Additional π pulses can be used to refocus the magnetization after it dephases again. Applying the π pulses along the y axis stops the accumulation in pulse time errors. The decay of the transverse magnetization follows a curve given by Equation 2.29.

2.9 Summary

In this thesis the NMR techniques outlined in this chapter are used to detect the NMR signals (and hence polarizations) from ^{13}C and ^{1}H nuclear spins. The spin dynamics of the systems are probed by measuring T_1 and T_2 relaxation times. Hyperpolarization techniques boost the nuclear polarization and result in larger NMR signals.

3

Hyperpolarization theory

Hyperpolarization is a term encompassing techniques that move a spin system out of Boltzmann thermal equilibrium. Experimentally, in NMR, hyperpolarization is used to increase the polarization of nuclear spins, increasing the spin excess and hence the signal to noise ratio. This allows for measurement of previously undetectable NMR signals, shorter experimental times, and structural determination of molecules. Outside NMR hyperpolarization has been used for quantum computation applications, such as state preparation and extension of coherence times in highly polarized states, and in high energy physics for preparation of targets, to name two examples.

This chapter gives a brief description of hyperpolarization techniques, with a focus on methods for polarizing diamonds. More details are given on DNP as the chosen method of hyperpolarization in this thesis, with brief descriptions of the Overhauser effect, solid effect, cross effect, and thermal mixing. This chapter follows theory presented by Wenckebach [70], Abragam [71], Goldman [72, 73] and Maly [74].

3.1 Hyperpolarization techniques

Several methods exist to create a hyperpolarized state. The most common are:

- CIDNP: In CIDNP (chemically induced dynamic nuclear polarization), polarization transfer is mediated by a chemical reaction. The most well known method is PHIP (parahydrogen induced polarization) where spin order in parahydrogen is transferred to other nuclear species (for example ^{13}C) after a chemical reaction with the hydrogen gas [75]. Another example is photo-CIDNP (photochemical induced dynamic nuclear polarization), such as in chloroplasts [76].

- Brute force polarization: High magnetic fields and low temperatures are used to achieve a high Boltzmann polarization in the nuclear spin system. Removal of the sample to lower fields and higher temperatures results in a boosted NMR signal, compared to the new thermal equilibrium. The system is considered hyperpolarized until it re-equilibrates.

- Optical pumping: Laser light is used to move electrons from one energy state in an atom or molecule to another, creating a system out of thermal equilibrium. Optical pumping has found use in quantum science, where electrons have been moved to a well defined quantum state, such as a single hyperfine sublevel. An example is in NV centres, where close to 100% electron polarization can be obtained [77,78]. Another common method is SEOP (spin exchange optical pumping) where circularly polarized light excites atoms in an alkali metal (such as rubidium) and the angular momentum can be transferred to nuclear spins in noble gasses such as ^{3}He and ^{129}Xe through collisions [79]. Hyperpolarized noble gases have found use in hyperpolarized MRI lung imaging [39].

- DNP: In DNP (dynamic nuclear polarization) the much larger electron spin polarization is transferred to the nuclear spins through hyperfine interactions using microwave radiation. DNP can occur through the solid effect, the cross effect, thermal mixing and the Overhauser effect. Further explanation of these mechanisms follows.

- Hartmann-Hahn polarization: Spin polarization is transferred from one spin species to another through a spin locking process. Effective polarization occurs

when the Hartmann-Hahn condition is met and the two spin species are driven to precess at the same frequency $\gamma_1 B_1 = \gamma_2 B_2$, where B is the driving microwave field, and γ is the gyromagnetic ratio of the spin species. Polarization can be transferred between nuclear species (known as cross polarization), for example between ^{1}H and ^{13}C, giving an enhancement of $\gamma_H/\gamma_C \sim 4$ [80–82]. Polarization can also be transferred between electron and nuclear spins, however the Hartmann-Hahn condition is more difficult to satisfy in an electron-nuclear system [83]. Another example is NOVEL (nuclear spin orientation via electron-spin locking) where electron magnetization can be transferred to the nuclear system through dipolar interactions if the condition $\gamma_e B_1 = \gamma B_0$ is met, where B_0 is the external magnetic field, B_1 is the spin locking pulse, and γ_e and γ are the electron and nuclear gyromagnetic ratios respectively [84].

- Quantum dots: The architecture used to define a quantum dot can be used to boost spin polarizations, for example gate voltages are able to tune the nuclear spin polarization [85], or spin blockade and RF radiation can be used to polarize the nuclear spins surrounding the quantum dots [86, 87].

Signal enhancements can also be obtained by using a combination of hyperpolarization techniques, which can save experimental time, boost signal enhancements further and polarize systems that would otherwise be impossible to polarize using only one technique. For example instead of directly polarizing ^{13}C using DNP (which can take a long time due to long ^{13}C T_1 relaxation times), ^{1}H in the same molecule can be polarized, and cross polarization can be used to transfer the ^{1}H polarization to the ^{13}C, saving on experimental time [88]. Another example involves polarizing liquids indirectly using a combination of optical pumping to polarize a gas, and Overhauser cross relaxation to transfer this polarization to the liquid [89].

3.2 Hyperpolarization in diamond

The unique spin properties of diamond, stemming from the many different paramagnetic impurities within the diamond crystalline lattice, see Section 5.1.2, have led to the development of many methods to hyperpolarize diamond.

A number of hyperpolarization techniques rely on the NV centre as a free radical

for hyperpolarization. A laser preferentially pumps the electron spin to one sublevel of the spin triplet ground state, leaving a highly polarized electron system. Several techniques exist to then transfer this NV polarization to the surrounding nuclear spins. The fluctuations of the polarized NV centre can induce nuclear transitions in a process where the nuclear spin bath equilibrates with the cooled dipolar NV centre spin bath [47]. The polarized NV centre can be driven optically at the nuclear Larmor frequency, leading to Hartmann-Hahn polarization transfer between the NV and nuclear spins around the NV centre [83]. At the NV centre level anti-crossings (LACs) polarization can be transferred through the hyperfine interactions. At the LACs the electron resonance frequency approaches the nuclear resonance frequency, allowing for polarization transfer. Nuclear hyperpolarization has been demonstrated at both the ground state level anti-crossing (GSLAC at $B = 100$ mT) [90], and in the excited state level anti-crossing (ESLAC at $B = 50$ mT) [48, 91]. At other magnetic fields, the NV spin polarization can be transferred to nuclear spins using microwave radiation driving flip-flop transitions in a DNP process [50].

Although these techniques, using NV centre polarization, work well for bulk diamond where the NV centre has a well defined orientation with respect to the static and driving fields, they do not work when polarizing nanodiamonds due to the random NV orientations. In particular the random orientations lead to large energy variations in the electron spin levels that make coherent control of the interactions between NV centres and surrounding spins very inefficient.

Methods resistant to orientation effects have been proposed for hyperpolarization using NV centres, and could be applied to NDs. A method involving off resonant MW double resonance schemes, with the integrated solid effect, and adiabatic variations of the MW frequency has been proposed and should be resistant to NV orientations [92, 93]. Another method involves small magnetic fields, with incoherent laser-induced transitions and coherent microwave transitions to drive electron-nuclear states [49].

Other than NV centre hyperpolarization, methods exist which use spin-1/2 defects to polarize diamonds. Bulk diamonds have been hyperpolarized using spin locking NOVEL techniques driving the P1 centre electronic defects with MW radiation and transferring polarization from the electron to the nuclear spin [94]. DNP using microwave radiation to drive forbidden transitions between intrinsic spin-1/2 impurities and nuclear spins have been used to polarize diamond. The mechanism governing DNP

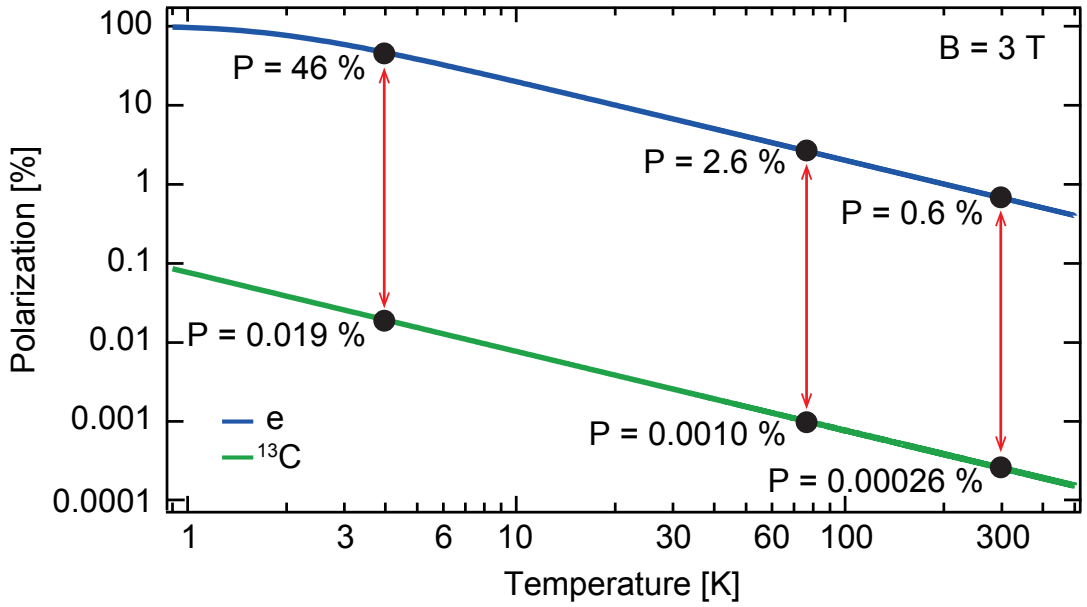

Figure 3.1: Schematic of nuclear enhancement using DNP. Electron polarization is transferred to the nuclear spins leading to a nuclear enhancement (red arrows). Polarizations (P) are shown at T = 4 K, 77 K and 300 K.

was either the solid effect or thermal mixing, depending on the concentration of free electrons [95–97]. These techniques have been used for applications such as diamond characterization using NMR spectroscopy [98, 99], and studying methods for diamond production, eg. diamond films [100]. These techniques have now been extended to hyperpolarizing detonation ND [52] and HPHT ND [51].

In this thesis we use DNP and brute force for hyperpolarizing nanodiamond. DNP was chosen because although it is a well understood method of hyperpolarization, it had yet to be applied in nanoparticle hyperpolarization for medical applications. A further description of electron nuclear interactions and the DNP mechanisms which govern polarization transfer is given.

3.3 Electron-nuclear interactions

DNP makes use of high electron spin polarization and hyperfine interactions to transfer polarization from electron to nuclear spins. Theoretically a maximum enhancement of $\epsilon = \gamma_e/\gamma_n$ can be achieved, (ϵ = 2600 for ^{13}C and ϵ = 660 for ^{1}H), see Fig. 3.1.

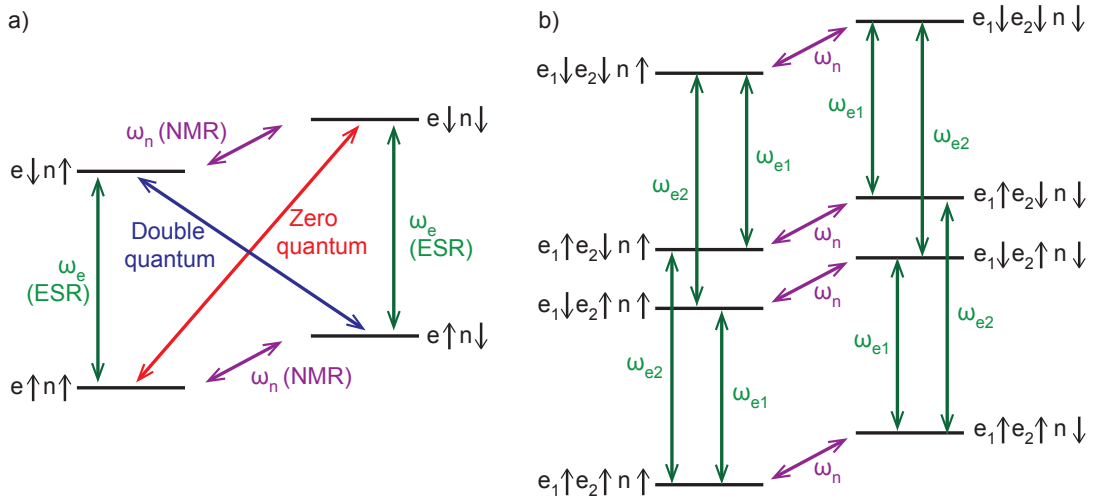

Figure 3.2: Energy level diagram for coupled electron and nuclear spin systems. **a)** Energy level diagram for a 2 spin system - one electron and one nuclear spin, relevant for solid effect and Overhauser effect hyperpolarization. **b)** Energy level diagram for a 3 spin system - two electron and one nuclear spin, relevant for cross effect hyperpolarization. Electronic transitions (ESR) are shown in green, nuclear transitions (NMR) are shown in purple and the zero and double quantum transitions are shown in red and blue.

The Hamiltonian governing an interacting electron-nuclear spin system in an external magnetic field along the z-direction is given by:

$$\begin{aligned} H &= H_e + H_n + H_{ee} + H_{nn} + H_{en} \\ &= -\omega_e S_z + \omega_n I_z + H_{ee} + H_{nn} + H_{en} \end{aligned} \tag{3.1}$$

The H_e and H_n terms in the Hamiltonian represent the Zeeman interactions of the electrons and nuclei respectively, the H_{ee} and H_{nn} terms govern spin-spin interactions between the electrons and nuclei respectively (leading to spin diffusion), and the H_{en} term represents electron and nuclear hyperfine interactions which govern DNP, see Fig. 3.2.

The hyperfine interaction consists of an isotropic Fermi contact interaction ($\mathrm{H}_{en}^{\mathrm{iso}}$)

and an anisotropic dipolar coupling (H_{en}^{dip}):

$$H_{en} = H_{en}^{\text{iso}} + H_{en}^{\text{dip}} \tag{3.2}$$

The contact hyperfine interaction is a scalar coupling between an electron and a nucleus. The strength of the coupling, A, is determined by the overlap between the electron and nuclear wave functions. The Hamiltonian governing this interaction is:

$$\begin{aligned} H_{en}^{\text{iso}} &= A(\vec{S} \bullet \vec{I}) \\ &= A(S_x I_x + S_y I_y + S_z I_z) \\ &= A(\frac{1}{2}(S_+ I_- + S_- I_+) + S_z I_z) \end{aligned} \tag{3.3}$$

where S and I are the electron and nuclear spin operators respectively, and S_+ and S_- are the electron raising and lowering operators respectively: $S_+ = S_x + iS_y$ and $S_- = S_x - iS_y$ (I_+ and I_- are the equivalent nuclear operators).

The hyperfine interaction can lead to flip-flop interactions $|\uparrow_e\downarrow_n\rangle \longleftrightarrow |\downarrow_e\uparrow_n\rangle$, where electron and nuclear spins are flipped in opposite directions (indicated by the raising and lowering terms in the Hamiltonian).

Dipolar coupling arises from an interaction between two spins due to their intrinsic magnetic dipoles, where the magnetic moment of one spin generates a magnetic field at the other. The dipolar Hamiltonian for an electron and nucleus is given by:

$$H_{en}^{\text{dip}} = \frac{-\mu_0}{4\pi}\frac{\gamma_e\gamma_n\hbar}{r^3}(I \bullet S - 3\frac{(I \bullet r)(S \bullet r)}{r^2}) \tag{3.4}$$

where r is the distance between the electron and nucleus, μ_0 is the vacuum permeability and I and S are the nuclear and electron spin operators respectively.

Dipolar interactions allow for flip-flip transitions $|\uparrow_e\uparrow_n\rangle \longleftrightarrow |\downarrow_e\downarrow_n\rangle$, flipping both electron and nuclear spins at the same time, and flip-flop transitions, $|\uparrow_e\downarrow_n\rangle \longleftrightarrow |\downarrow_e\uparrow_n\rangle$, flipping electron and nuclear spins in opposite directions.

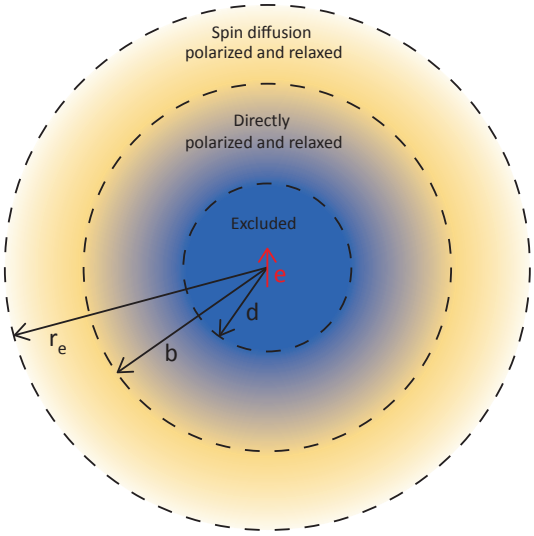

Figure 3.3: Schematic of direct and spin diffusion mediated hyperpolarization. Schematic of the hyperpolarization and relaxation mechanisms that dominate in a bulk sample with a dilute paramagnetic spin system. The electron spin is shown in red. Nuclear spins within a region d have shifted Zeeman energies and do not contribute of an NMR line. Spins in the region between d and b are directly polarized and relaxed by the paramagnetic impurities. Spins further away from the impurity are polarized through spin diffusion.

The hyperfine interaction leads to polarization of nuclear spins close to the paramagnetic impurity. Bulk nuclear polarization is achieved through spin diffusion, which transfers this polarization to spins further away. Spin diffusion is mediated through dipolar spin flip-flops of the nuclear spins in energy conserving transitions [101]. Additionally when nuclear T_1 relaxation is dominated by paramagnetic impurities, spin diffusion plays a role in the relaxation of nuclear spins far from the impurity, see Fig. 3.3.

In a diamond lattice, spin diffusion is given by [102]:

$$\begin{aligned} \frac{\partial P}{\partial t} &= D\nabla^2 P \\ D &= \frac{(r_{c-c})^2}{50 T_{2n}} \end{aligned} \tag{3.5}$$

where P is the polarization, D is the diffusion constant, r_{c-c} is the nearest neigh-

bor distance and T_{2n} is the nuclear decoherence time. For diamond particles the distance between ^{13}C atoms is $r_{c-c} = 0.58$ nm [46].

The magnetic field from a paramagnetic impurity shifts the Zeeman energies of nearby nuclear spins. These spins will not contribute to an NMR line, and spin diffusion is suppressed. This spin diffusion barrier occurs at the distance at which the field from the electron is approximately the same as the width of the NMR line [102]

$$d = (\frac{\gamma_e}{\gamma_c}\frac{\hbar\gamma_e B_0}{2kT})^a r_{c-c}, \qquad a \sim 1/3 - 1/4 \tag{3.6}$$

In diamond, at $B = 2.89$ T and $T = 300$ K, this distance is $d \sim 1.3$ nm.

Direct hyperpolarization between the electron and nuclear spins is affective up to a distance b from the paramagnetic impurity, which depends upon the transition probabilities of the hyperpolarization mechanisms, and Zeeman relaxation [102]. Further away from the impurity, spin diffusion dominates over paramagnetic impurity mediated interactions. Typically this distance is a few nm [95].

3.4 DNP mechanisms

DNP encompasses four hyperpolarization mechanisms: the Overhauser effect, the solid effect, the cross effect and thermal mixing. In each of these, the larger electron polarization is transferred to nuclear polarization using driving microwave radiation.

All four of these DNP mechanisms can play a role when polarizing a solid. The dominant mechanism governing DNP depends upon both the electron concentration and the coupling between the electrons. The efficiency of the DNP process depends on the hyperpolarization mechanism, the gyromagnetic ratios of the electron and nuclear spins γ_e and γ_n respectively, the magnetic field B_0, the driving RF field B_1, the spin lattice relaxation times T_{1e} and T_{1n}, spin diffusion, and the number of nuclear spins N_n.

The Overhauser effect was first proposed in 1953 suggesting a mechanism where the electron spin system is saturated, and electron polarization is transferred to nuclear polarization through relaxation via hyperfine interactions [103–105]. This mechanism is used for hyperpolarizing metals and liquids, and is mediated by the rotation and motion of the free electrons.

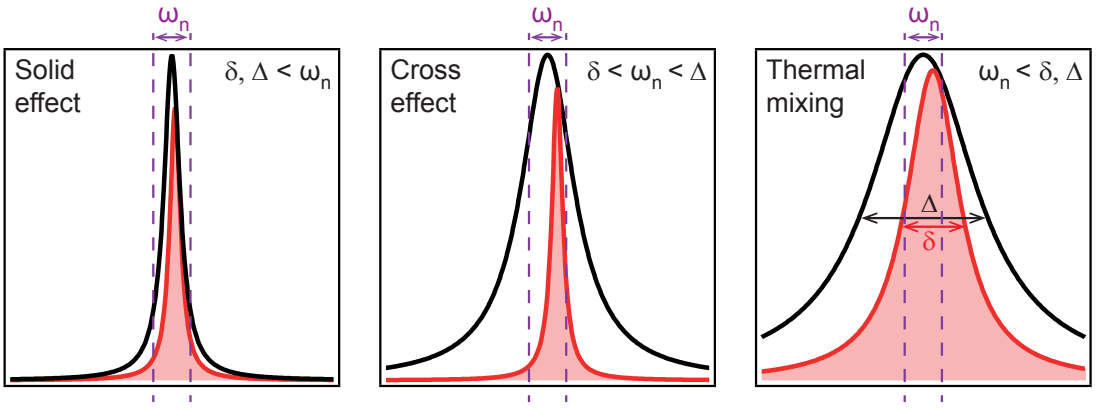

Figure 3.4: ESR linewidths governing DNP in dielectric solids. DNP occurs via three different mechanisms, depending on the homogeneous linewidth (δ, red) and inhomogeneous spectral breadth (Δ, black). When both linewidths are smaller then the nuclear Larmor frequency (ω_n, purple) hyperpolarization is governed by the solid effect ($\delta, \Delta < \omega_n$). If the nuclear Larmor frequency is larger than the homogenous linewidth while smaller than the spectral breadth ($\delta < \omega_n < \Delta$), then hyperpolarization is governed by the cross effect. If both the homogenous linewidth and spectral breadth are larger than the nuclear Larmor frequency ($\omega_n < \delta, \Delta$), hyperpolarization is governed by thermal mixing.

The solid effect is a two spin process between an electron and a nucleus. It is the dominant hyperpolarization mechanism in materials where electron concentrations are low, and the interaction between electron spins can be neglected. The solid effect applies in a material with a homogeneous EPR linewidth δ (the linewidth of a single electron component or orientation), and an inhomogeneous spectral breadth Δ (the full width of the entire EPR line) both smaller than the nuclear Larmor frequency ω_n ($\delta, \Delta < \omega_n$) [106–108], see Fig. 3.4 .

Dielectric solids with a high concentration of electron spins and an inhomogeneously broadened ESR line are polarized via the cross effect. The cross effect is a three spin process between two dipolar coupled electrons and one nuclear spin. It is the dominant hyperpolarization mechanism in a system with a narrow homogeneous linewidth but an inhomogeneous spectral breadth broader than the Larmor frequency, ($\delta < \omega_n < \Delta$) [109–114], see Fig. 3.4.

Finally, highly doped dielectric solids are hyperpolarized via thermal mixing. Thermal mixing makes use of spin temperature theory of the spin reservoirs in the

material. The theory considers coupling between the electron dipolar and the electron Zeeman spin baths [115], and the nuclear Zeeman reservoir [116]. Thermal mixing dominates when the spectral breadth and homogenous linewidth are both larger than the nuclear Larmor frequency ($\omega_n < \delta, \Delta$) [71, 97].

The mechanism governing the DNP experiment depends highly upon the electron system. The radicals can either be exogenous (such as TEMPO added to a urea solution) or endogenous (for example free electrons in diamond or silicon). Exogenous radicals can be attached to a matrix [117, 118] attached to nanoparticles [119] or dissolved in a solvent [120]. The most common exogenous radicals used for hyperpolarization are: trityl, BDPA, TEMPO, BTnE and TOTAPOL. Trityl and BDPA have three fold symmetry with narrow EPR lines and usually lead to solid effect DNP. TEMPO is a nitroxide based radical, resulting in cross effect DNP (or thermal mixing DNP at high concentrations) within solids and Overhauser effect in liquids. BTnE and TOTAPOL are biradicals and lead to cross effect DNP in solids and Overhauser effect DNP in liquids. Endogenous radicals can lead to hyperpolarization by any DNP mechanism.

Further explanations of the DNP mechanism are given in the following sections.

3.5 Overhauser effect

The Overhauser effect makes use of a relaxation process through dipolar and scalar hyperfine interactions to build up a nuclear polarization, see Fig. 3.5. Overhauser enhancement is mediated through the free electrons in metals and through molecular rotations and motion in liquids. This section details Overhauser enhancement in liquids.

Initially, when placed in a magnetic field, the electron spins are polarized, while the nuclear spin system remains mainly unpolarized, due to the difference in gyromagnetic ratios and Boltzmann polarization, see Fig. 3.5c.

Driving the system continuously at $f = \omega_e$ (ESR transition) saturates the electron spin system, and the electron polarization approaches zero (the number or spin-up electrons approaches the number of spin-down electrons). The combined electron-nuclear system can relax back via a combination of three transitions: the electronic transition (ESR), the zero quantum transition (occurring at rate Γ_0) and the double quantum transition (occurring at rate Γ_2). If the relaxation is dominated by dipolar interac-

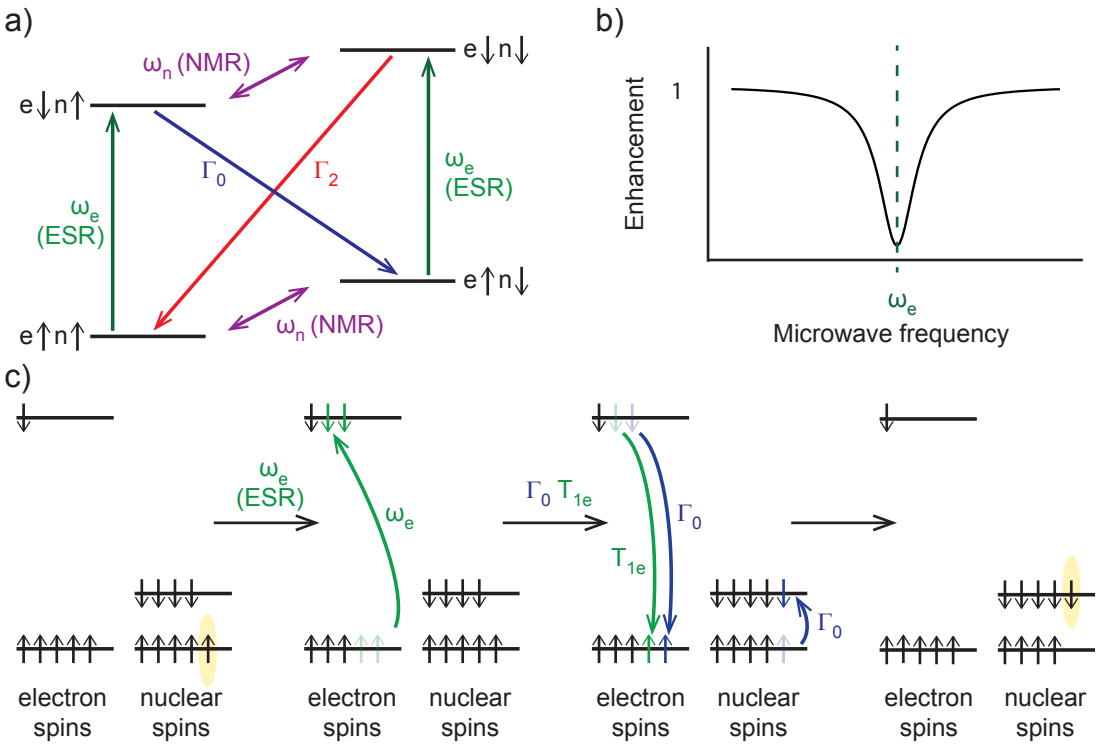

Figure 3.5: Schematic of the Overhauser effect. a) Energy level diagram, **b)** enhancement and **c)** schematic of the Overhauser effect for a coupled electron-nuclear spin system. After saturation of the ESR transition (green arrows), the system can relax via the zero (blue) or double (red) quantum transitions (at rates Γ_0 and Γ_2 respectively). If one of these occurs at a faster rate (e.g. $\Gamma_0 > \Gamma_2$) then a nuclear polarization will be built up, leading to a negative nuclear enhancement. If $\Gamma_0 < \Gamma_2$ a positive enhancement is obtained.

tions ($\Gamma_0 > \Gamma_2$), then the nuclear spin system polarizes, and a negative enhancement is obtained, see Fig. 3.5b. A positive enhancement is obtained if scalar interactions dominate and $\Gamma_2 > \Gamma_0$.

For effective Overhauser enhancement, the rotational correlation time of the electron (τ_e) must be smaller than the inverse nuclear frequency:

$$\omega_n \tau_e < 1 \tag{3.7}$$

This leads to a decrease in Overhauser effect with increasing magnetic field.

Theoretically, the maximum Overhauser enhancement is $\epsilon = \gamma_e/\gamma_n$ ($\epsilon = 660$ for ^{1}H), however saturation and relaxation rates play a role in the obtained enhancement. Experimentally the enhancement is given by [121]

$$\epsilon = 1 - \rho f S \frac{\gamma_e}{\gamma_n} \tag{3.8}$$

where

$$\begin{aligned} S &= \frac{S_0 - S_z}{S_0} \\ \rho &= \frac{\Gamma_2 - \Gamma_0}{\Gamma_0 + 2\Gamma_1 + \Gamma_2} \\ f &= \frac{\Gamma_2 - \Gamma_0 + 2\Gamma_1}{\Gamma_0 + 2\Gamma_1 + \Gamma_2 + \Gamma^0} \end{aligned} \tag{3.9}$$

S is the electron saturation factor, ($S = 1$ for a completely saturated system, incomplete ESR saturation can originate from multiple ESR lines or insufficient power), ρ is the coupling parameter ($\rho = -1$ or pure scalar coupling and $\rho = 0.5$ for pure dipolar coupling), and f is the leakage factor, describing the nuclear relaxation by electrons ($f = 0$ when there is no relaxation and $f = 1$ when all relaxation is mediated by electrons). Γ_0, Γ_1, Γ_2, Γ^0, are the rate of the zero quantum transition, electron T_1 relaxation, the double quantum transition and nuclear relaxation respectively.

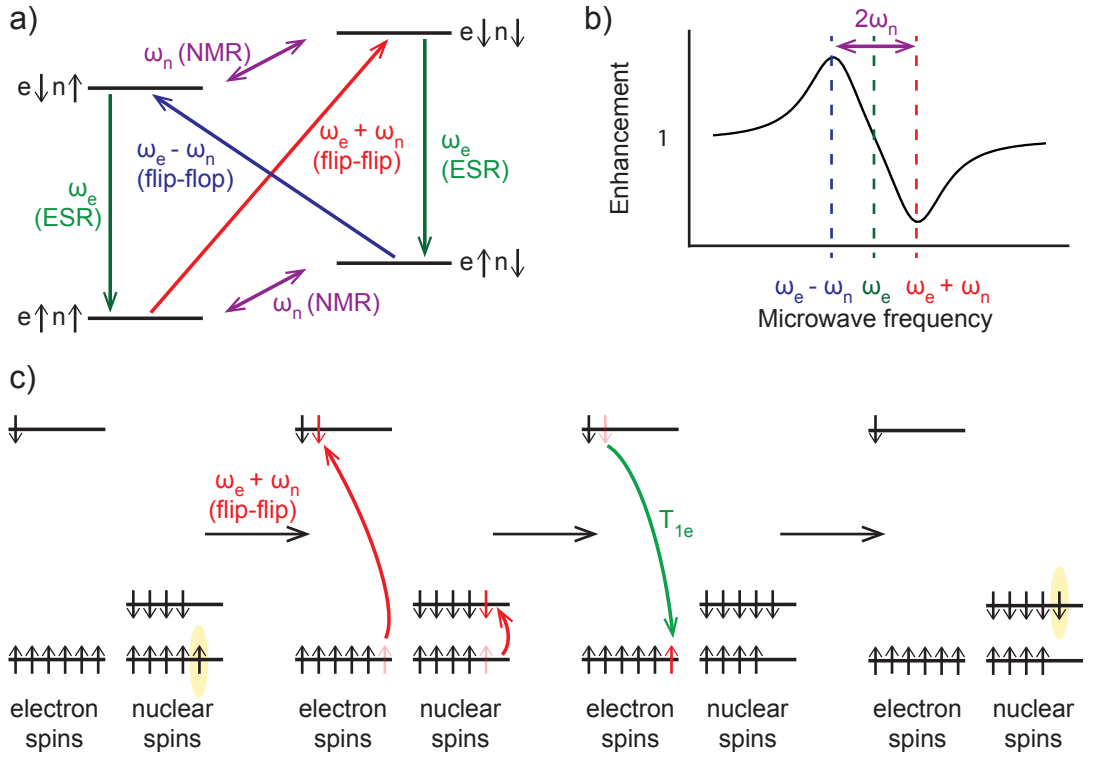

Figure 3.6: Schematic of the solid effect. **a)** Energy level diagram, **b)** theoretical enhancement, and **c)** schematic of solid effect hyperpolarization. Initially the electron system is highly polarized and the nuclear system is relatively unpolarized. Driving flip-flip transitions with microwaves at $f = \omega_e + \omega_n$ (red), simultaneously flips a nuclear and electron spin. The system then relaxes through an electronic T_{1e} transition. Continual pumping of these spin flips results in a negative nuclear polarization. Driving flip-flop transitions with microwaves at $f = \omega_e - \omega_n$ (blue) results in positive nuclear polarization.

3.6 Solid effect

The solid effect is the hyperpolarization mechanism in dielectric solids which dominates when the system has a dilute bath of isolated electronic defects, with a dipolar interaction between a single electron and nuclear spin, see Fig. 3.6.

At low temperatures and high magnetic fields the electron spins are highly polarized while the nuclear spins remain mainly unpolarized. This leaves the coupled 4-level energy system populated mainly in the lowest two energy states.

Dipolar interactions between the nuclei and electrons allow simultaneous electron

and nuclear flips (flip-flip transition, $|\uparrow_e\uparrow_n\rangle \longleftrightarrow |\downarrow_e\downarrow_n\rangle$) and reversals of the electron and nuclear spins (flip-flop transitions, $|\uparrow_e\downarrow_n\rangle \longleftrightarrow |\downarrow_e\uparrow_n\rangle$). In such transitions, the total energy of the system changes by $E = \hbar(\omega_e \pm \omega_n)$. These transitions can be driven by an external RF field at a frequency of $f = \omega_e \pm \omega_n$,

Driving the system at $f = \omega_e + \omega_n$ (forced flip-flip transitions), see Fig. 3.6c, simultaneously flips an electron and a nuclear spin. The system then relaxes through an electronic T_1 transition. The electron is able to undergo spin flips with successive nuclear spins, building up a negative nuclear polarization, see Fig. 3.6b. Driving the system at $f = \omega_e - \omega_n$ (forced flip-flop transitions) results in a positive enhancement.

Theoretically, the maximum nuclear polarization can approach the electron polarization $P_n = \pm P_e$, however the condition

$$\frac{N_n}{N_e}\frac{T_{1e}}{T_{1n}} << 1 \tag{3.10}$$

where N_e is the number of impurities and N_n the number of nuclear spins, must be met to ensure that electron relaxation rates T_{1e} are short enough and the nuclear relaxation rates T_{1n} are long enough such that hyperpolarization can accumulate.

For solid effect hyperpolarization, as the electronic spin system is dilute, most nuclear spins are far enough away from an electron that an interaction between the two is negligible. Bulk nuclear polarization is mediated by spin diffusion, which transfers polarization from nuclear spins close to the impurity to spins further away. The solid effect enhancement scales as B_0^{-2}, with the enhancement given by

$$\epsilon_{SE} \propto \frac{B_1^2}{B_0^2}\frac{N_e}{\delta}T_{1n} \tag{3.11}$$

where B_1 is the driving microwave power, B_0 is the static magnetic field, N_e is the number of electrons, δ is the homogeneous EPR linewidth and T_{1n} is the nuclear relaxation time.

If the ESR line is narrow compared with ω_n, (ie. $\delta, \Delta << \omega_n$) positive and negative polarization occur at separate frequencies. This is known as the well resolved

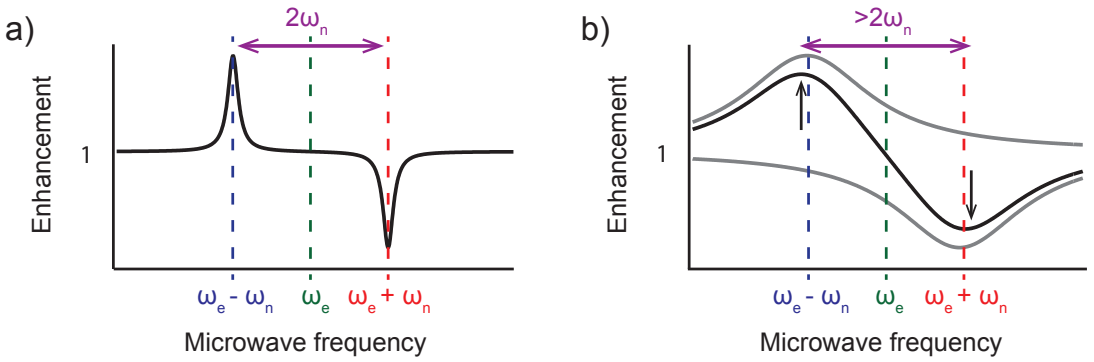

Figure 3.7: Schematic of the differential and well resolved solid effect. **a)** Schematic of the well resolved solid effect. The peak splitting is $f = 2\omega_n$. **b)** Schematic of the differential solid effect. If the ESR lines are broad, driving flip-flip transitions can also drive flip-flop transitions, leading to a broader hyperpolarization profile with less enhancement. The peak separation is $f > 2\omega_n$. Individual contributions from hyperpolarization are shown in grey and the sum is shown in black.

solid effect, see Fig. 3.7a, with a separation between positive and negative enhancement typically given by $f = 2\omega_n$. If the ESR line is not narrow compared to the nuclear Larmor frequency (ie. $\delta, \Delta \sim \omega_n$), then both the double and zero quantum transitions can occur simultaneously partially canceling the polarization. This is known as the differential solid effect, see Fig. 3.7b, and results in a separation between the positive and negative enhancement with $f > 2\omega_n$.

3.7 Cross effect

The cross effect is the dominant hyperpolarization mechanism in a dielectric solid with a high concentration of electron spins and an inhomogeneously broadened EPR line. Such a system can be considered as a series of dipolar coupled electron spin packets, each with a homogenous EPR line smaller than the nuclear Larmor frequency. The cross effect is a three spin process, using two dipolar coupled electron spins and one nuclear spin, see Fig. 3.8a.

Effective polarization occurs when the degeneracy condition is met and the fre-

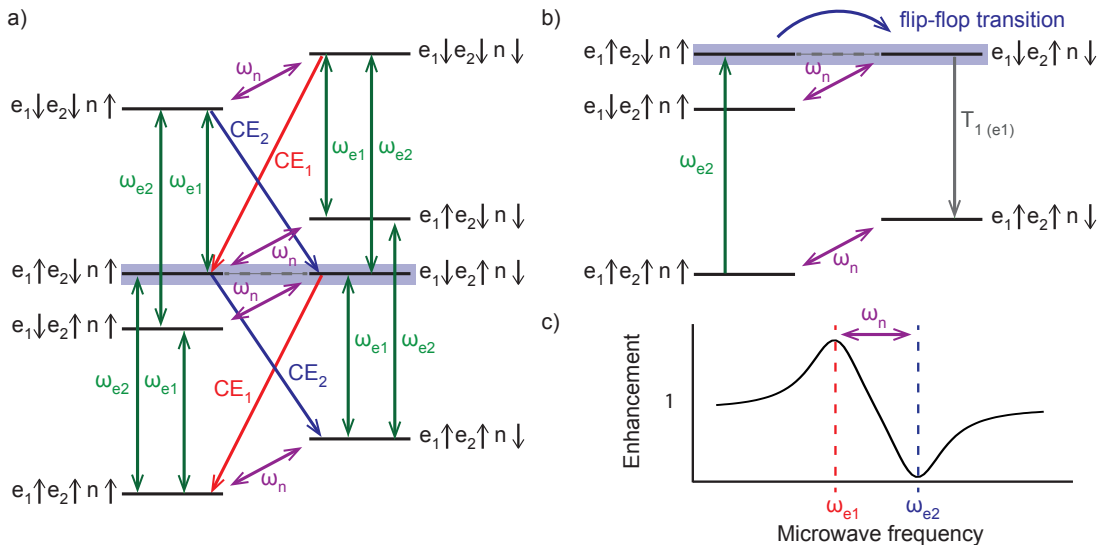

Figure 3.8: Schematic of the cross effect. a) Energy level diagram, **b)** schematic, and **c)** enhancement for two electron spins coupled to a nuclear spin in a degenerate system where $|\uparrow_{e1}\downarrow_{e2}\uparrow_n\rangle \longleftrightarrow |\downarrow_{e1}\uparrow_{e2}\downarrow_n\rangle$ (highlighted in grey). Electron transitions are shown in green, nuclear transition are shown in purple and cross effect transitions (CE_1 and CE_2) are shown in red and blue. After saturating one of the electron spins (at $f = \omega_{e2}$) the system can undergo flip-flop transitions $|\uparrow_{e1}\downarrow_{e2}\uparrow_n\rangle \longrightarrow |\downarrow_{e1}\uparrow_{e2}\downarrow_n\rangle$, flipping a nuclear spin. The system then relaxes through an electronic T_{1e} transition, resulting in a net nuclear polarization. Saturating the other electronic transition results in positive enhancement. The separation between peaks is $f = \omega_n$.

quency separation between electron pairs is given by the nuclear Larmor frequency:

$$|\omega_{e1} - \omega_{e2}| = \omega_n \tag{3.12}$$

The degeneracy condition means that two electrons can undergo flip-flop transitions providing a fluctuating magnetic field, which can flip a nuclear spin in an energy conserving process such that $|\uparrow_{e1}\downarrow_{e2}\uparrow_n\rangle \longleftrightarrow |\downarrow_{e1}\uparrow_{e2}\downarrow_n\rangle$.

At low temperatures and high magnetic fields the electron system is polarized while the nuclear system is relatively unpolarized. Microwave radiation at one of the ESR transitions (e.g. $f = \omega_{e2}$), saturates that electronic transition, see Fig. 3.8b. Dipolar flip-flops between electrons can then occur, and if the degeneracy condition is met, a nuclear spin is flipped. The system then relaxes through an electronic T_{1e} transition. Driving the system at $f = \omega_{e1}$ leads to a positive enhancement, while driving the system at $f = \omega_{e2}$ leads to a negative enhancement, with a separation of $f = \omega_n$ between the maximum positive and negative enhancement, see Fig. 3.8c. Provided that electron T_{1e} is faster than the nuclear spin T_{1n}, a significant nuclear polarization can be built up.

Realistically, the electron spin packets are not isolated from other spin packets, and the dipolar order can transfer to another pair of spins. This leads to additional nuclear polarization.

The enhancement due to the cross effect is given by

$$\epsilon_{CE} \propto \frac{\gamma_e}{\gamma_n}\frac{B_1^2}{B_0}\frac{N_e^2}{\delta^2}T_{1n} \tag{3.13}$$

where B_1 is the driving microwave power, B_0 is the static magnetic field, N_e is the number of electrons, δ is the homogeneous EPR linewidth and T_{1n} is the nuclear relaxation time.

The degeneracy condition is hard to satisfy at high magnetic fields, however the B_0^{-1} dependence means that the cross effect is more efficient at high magnetic fields than the solid effect.

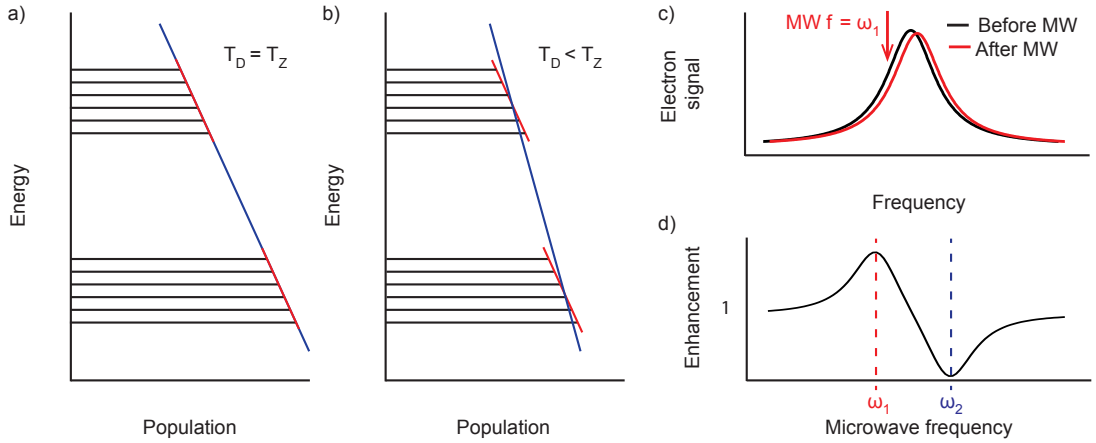

Figure 3.9: Schematic of thermal mixing. a,b) Population diagram of the ESR line. The bands represent two sections of the ESR line and the broadening represents electron-electron dipolar interactions. In a) the system is in thermal equilibrium and the dipolar and Zeeman systems are at the same temperature ($T_D = T_Z$). **b, c)** After cooling with off resonant microwave radiation (e.g. at $f = \omega_1$ below the central ESR line), a non-equilibrium polarization gradient is formed over the EPR line, shifting the ESR line, equivalent to cooling the dipolar reservoir ($T_D < T_Z$) and leading to a positive nuclear enhancement. Irradiation at $f = \omega_2$, above the central ESR line leads to negative nuclear enhancement. **d)** Theoretical nuclear polarization after thermal mixing.

3.8 Thermal mixing

Thermal mixing is the dominant hyperpolarization mechanism for solids with high electron concentrations, for example in highly electron doped materials. Thermal mixing can be thought of as an interaction between three spin baths - an electron Zeeman, an electron dipolar and a nuclear Zeeman. The electronic spin-spin interactions can be in good thermal contact with the distribution of electronic resonance frequencies and the nuclear Zeeman interactions, with each of the reservoirs at the same temperature, see Fig. 3.9a. Off resonant microwave radiation results in a polarization gradient across the EPR line, equivalent to cooling the electron dipolar spin bath, see Fig. 3.9b, c. Equilibration of the spin baths occurs in a three spin process similar to the cross effect.

The common spin temperature evolves towards a positive or negative value when the irradiation is below or above the electronic Larmor frequency respectively, leading to nuclear enhancement, see Fig. 3.9d.

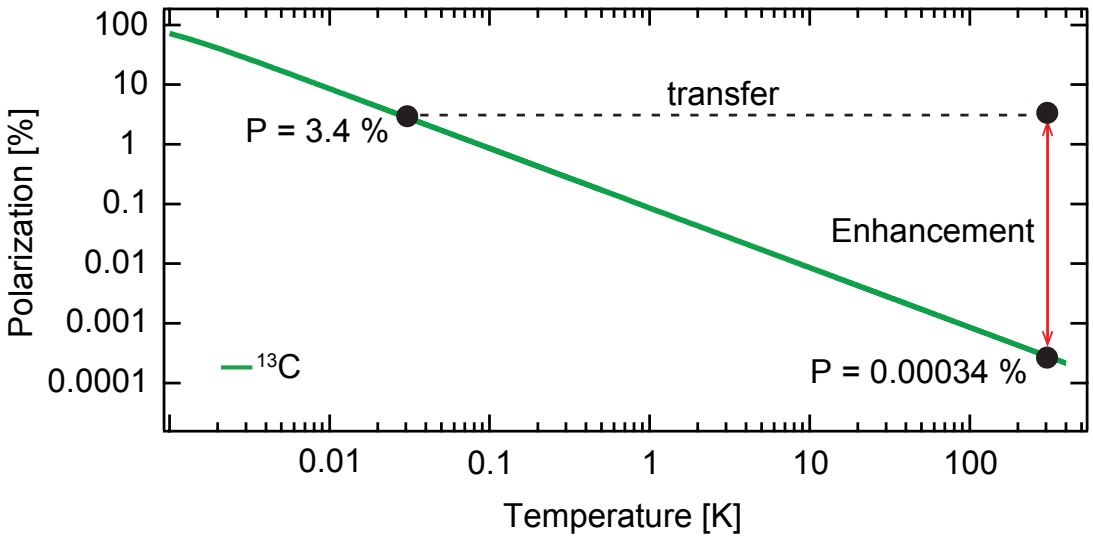

Figure 3.10: Schematic of brute force hyperpolarization. As the temperature is lowered to T = 30 mK the ^{13}C polarization increases. Removing the nanodiamonds quickly leads to a room temperature enhancement.

Thermal mixing scales as

$$\epsilon_{TM} \propto \frac{B_1^2}{B_0} \frac{N_e^2}{\delta^2} T_{1n} T_{1e} \tag{3.14}$$

where B_1 is the driving microwave power, B_0 is the static magnetic field, N_e is the number of electrons, δ is the homogeneous linewidth, T_{1n} is the nuclear relaxation time and T_{1e} is the electron relaxation time.

In general thermal mixing is more efficient than the solid effect but less efficient than the cross effect at high magnetic fields.

3.9 Brute force hyperpolarization

Brute force hyperpolarization makes use of high magnetic fields and low temperatures to achieve a high Boltzmann polarization. If the NMR sample is transferred to an environment where the thermal equilibrium polarization is lower, then while the sample is approaching the new equilibrium it is considered hyperpolarized, see Fig. 3.10.

The sample will equilibrate to the new temperature and magnetic field at the nuclear spin lattice relaxation time (T_{1n}). Care must be taken during the transfer process to retain a magnetic field on the NMR sample; if the magnetic field is too low the Zeeman states can mix, resulting in a complete loss of hyperpolarization. Additionally the nuclear T_{1n} can be much faster at low magnetic fields, resulting in a rapid depolarization during the transfer process.

3.10 Summary

In this thesis DNP techniques are used to polarize ND. As ND is a dielectric solid with a dilute electron spin bath, the solid effect is the dominant hyperpolarization mechanism, however, there may be contributions from other DNP mechanism. Each of the mechanisms, along with brute force hyperpolarization, has been explained. In ND, spin diffusion is largely suppressed, and transfer of polarization to spins further from the impurity is slow.

4

Experimental methods

Multiple experimental setups were used for the experiments detailed in this thesis. The W-band hyperpolarization at a frequency of $f = \sim 80$ GHz and a field of $B = 2.89\,\mathrm{T}$ is described in Section 4.1. The low field setup used for X-band hyperpolarization in the magnetic field range $B = 150$ - 500 mT is described in Section 4.2. The setup used for measuring polarization transferred between the hyperpolarizer and the detection magnet, and for measuring brute force hyperpolarization at $T \sim 30$ mK cryogenic temperatures in a dilution refrigerator is detailed in Section 4.3.

4.1 W-band hyperpolarization setup

Direct ^{13}C hyperpolarization in ND was measured in a setup at W-band frequencies at a magnetic field of $B = 2.89$ T at temperatures ranging between $T = 4$ K and 300 K. Measurements included enhancements, polarization build up times and decay times (T_1), decoherence measurements under Hahn echo and CPMG conditions (T_2), and signal enhancement as a function of driving microwave power and frequency. The cryostat and probe are on loan from Harvard University, and the probe has been modified for ^{13}C and ^{1}H measurements. Additional information about the construction of the probe and cryostat can be found in Ref. [122]. A schematic of the experimental setup is shown in Fig. 4.1, and photos of the setup are shown in Figs. 4.2, 4.3, and 4.4.

The magnetic field was provided by a 400 MHz Magnet[1] charged to a field of $B = 2.89$ T for compatibility with the microwave source. A flow cryostat[2] was used to obtain variable temperatures for hyperpolarization. The cryostat was run in continuous flow operation at either $T = 4$ K using liquid helium, or at $T = 77$ K using liquid nitrogen. A diaphragm pump[3] was attached to the return line of the transfer siphon. Pumping speed and temperature were controlled using a gas flow controller[4]. The cryostat and magnet setup is shown in blue in Fig. 4.1 and on the right in Fig. 4.2.

The NMR measurements of polarization at $B = 2.89$ T were made using a Redstone NMR system[5] for pulse generation and data acquisition, and TNMR software to create the pulse sequences. RF pulses were amplified using a power amplifier[6], and passed through a transducer and $\lambda/4$ cable to the NMR probe. The NMR signal returned through the transducer, was amplified with a pre-amplifier[7], filtered, and detected with the Redstone NMR system. Signal processing, such as filter functions and Fourier transforms were performed using Matlab. Data processing and analysis was performed in Matlab and IGOR Pro.

A Gunn oscillator[8] was used to produce the microwaves for hyperpolarization. The Gunn oscillator could be mechanically tuned over $f = 1$ GHz in the frequency range

[1] Oxford Instruments
[2] Oxford Instruments
[3] GAST RAA-V212-EB
[4] Oxford Instruments VC 31
[5] Tecmag Redstone
[6] TOMCO Technologies BT00500-gamma
[7] MITEQ AU-1114T
[8] Quinstar Technology QTM-811205AE

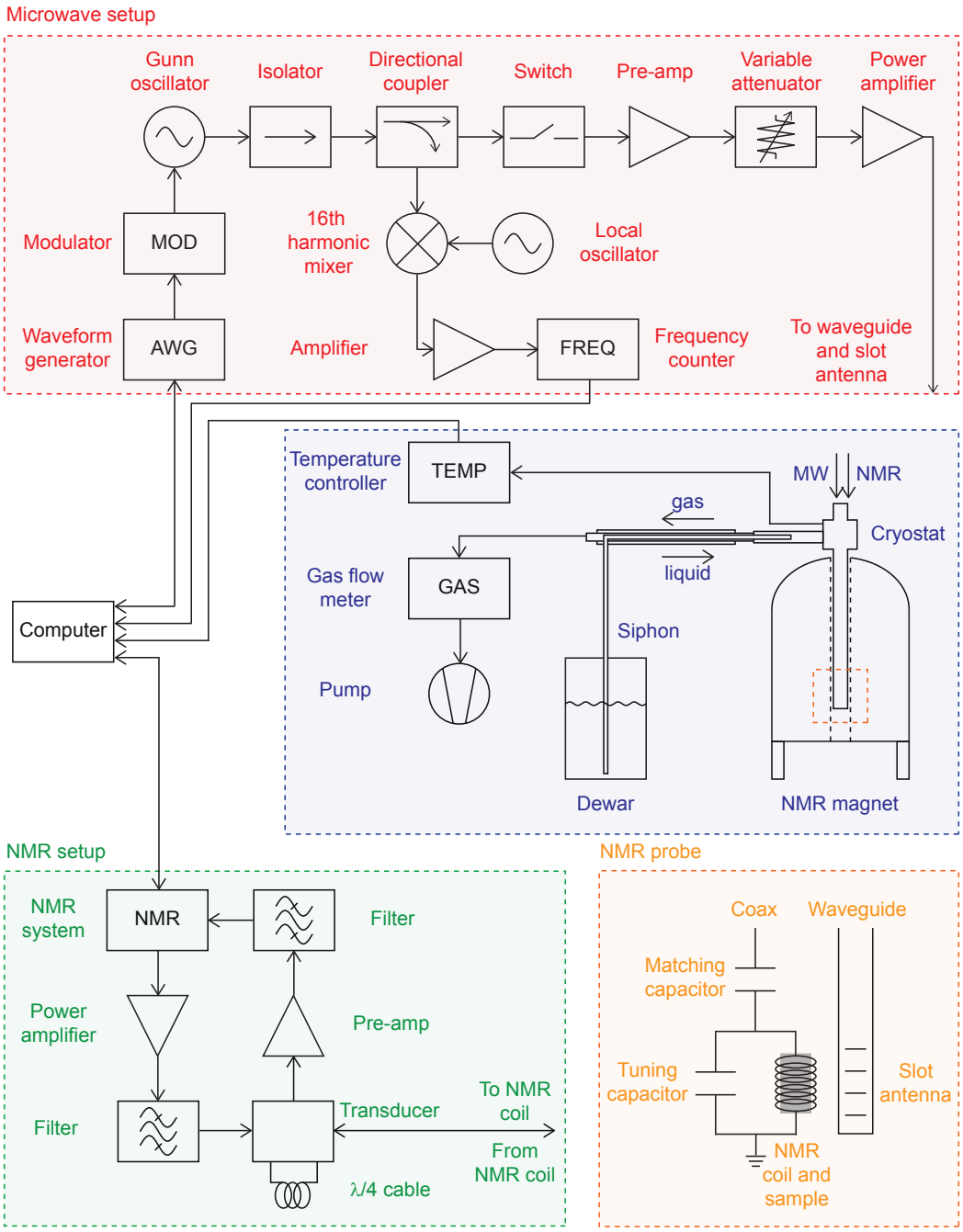

Figure 4.1: Schematic of the W-band hyperpolarizer. The microwave components used for hyperpolarization are shown in red, the NMR components used for ^{13}C signal detection are shown in green, the NMR probe and slot antenna are shown in orange, and the NMR magnet, cryostat and cooling setup are shown in blue.

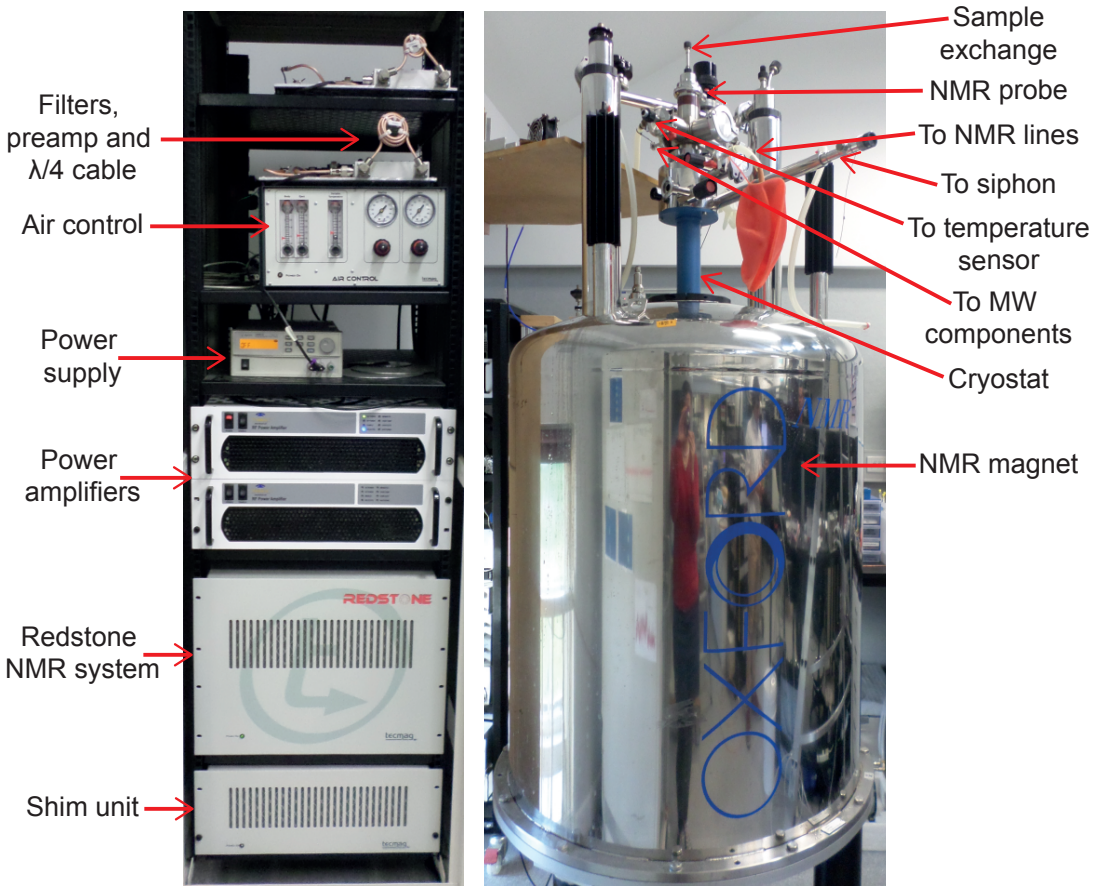

Figure 4.2: Photo of the W-band hyperpolarizer. Left: Photo of the NMR spectrometer, and Right: photo of the NMR magnet and hyperpolarizer used for W-band hyperpolarization.

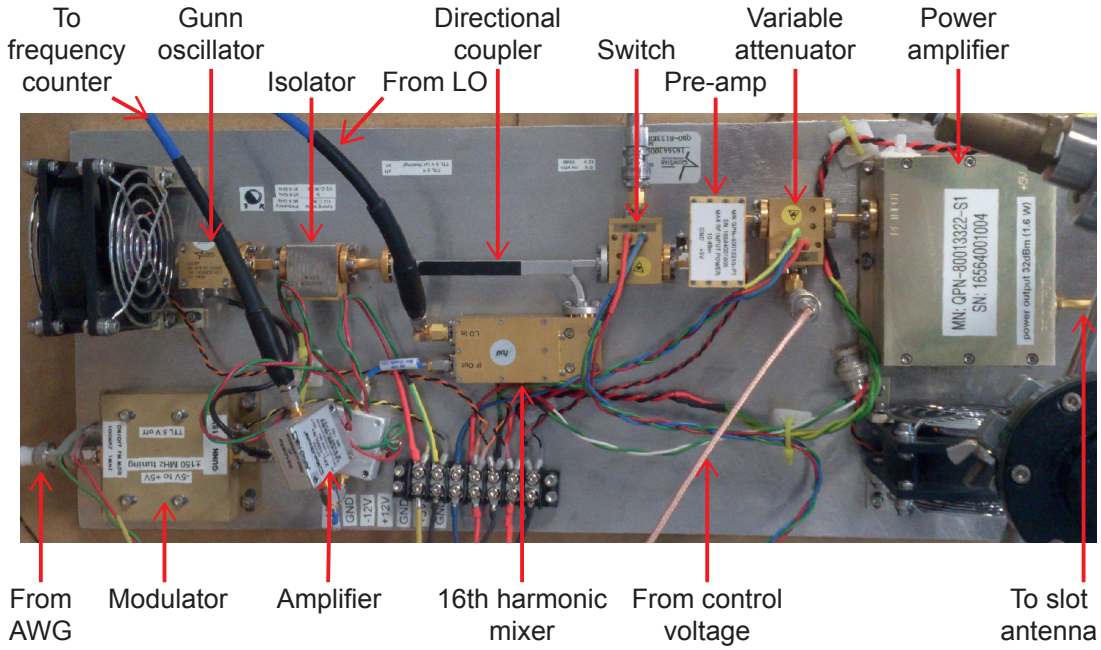

Figure 4.3: Photo of the W-band hyperpolarizer. Photo of the microwave components used for W-band hyperpolarization.

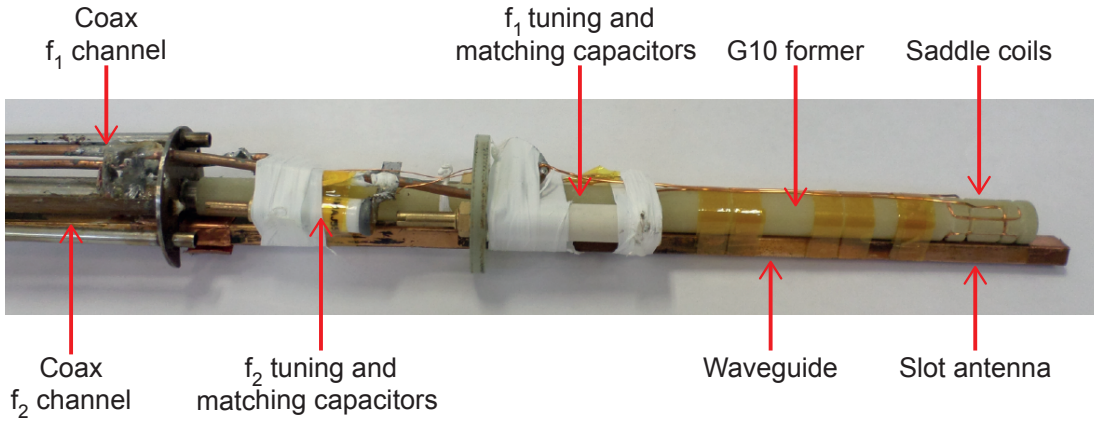

Figure 4.4: Photo of the W-band hyperpolarizer. Photo of the NMR probe showing the saddle coil, tuning and matching capacitors, and waveguide and slot antenna.

f = 80.5 - 81.5 GHz by changing the dimensions of the cavity. Additionally the cavity was tuned over a frequency of f = 500 MHz by applying a DC bias, using a modulator[1] and waveform generator[2].

The microwaves were amplified using a pre-amp[3] and a P = 2 W power amplifier[4]. An isolator[5] was used to prevent reflections damaging the Gunn oscillator. The microwave components are shown in red in Fig. 4.1 and a photo can be see in in Fig. 4.3.

The frequency of the microwaves was measured by sampling the microwaves using a 10 dB directional coupler[6], mixing this signal with a 4.9 GHz local oscillator[7] through a 16th Harmonic mixer[8], producing a signal in the frequency range f = 1.5 - 3 GHz which was amplified[9] and detected using a frequency counter[10].

Any microwave frequency shifts could be accounted for by changing the DC bias in a feedback loop, ensuring that the frequency stayed constant for the duration of the experiment.

The microwave radiation incident on the sample was controlled using a TTL switch[11] and a variable attenuator[12]. The Gunn oscillator was additionally switched on and off using a TTL voltage.

The waveguide of the microwave components was converted from WR12 to WR19 using a cylindrical waveguide transition and a bulkhead feedthrough with a mica optical window for a vacuum tight connection between the microwave components and the waveguide in the hyperpolarizer.

The NMR probe is a cryostat insert consisting of a stainless steel frame wired with two semi-rigid copper coaxial cables for ^{1}H and ^{13}C NMR detection and a WR19 gold plated copper waveguide and slot antenna for microwave irradiation. The waveguide is WR19 to reduce attenuation along the length of the cryostat. The NMR detection

[1] Quinstar Technology QCR-10MM00
[2] Agilent 33250A
[3] Quinstar Technology QPN-80012210-P1
[4] Quinstar Technology QPN-80013322-S1
[5] Quinstar Technology QJI-E
[6] Aerowave 12-3000/10
[7] HP 8350 B sweep oscillator
[8] HXI HHM12C04-066
[9] Mini circuits ZFL-1000LN+
[10] TTi TF930
[11] Millitech PSP-12-RIBSN
[12] Millitech VCA-12-RINSO

coils are copper saddle coils (offset by 90°), each tuned and matched by two capacitors[1] close to the coil, mounted on a fiberglass former.

Temperature changes can shift the capacitance and inductance of the components of the NMR probe, resulting in an untuned or unmatched resonant circuit. If the detection circuit detuned, then it could be externally tuned outside the cryostat using a tuning capacitor in parallel and a matching capacitor in series.

A slot antenna is used to irradiate the sample with microwaves. The slot antenna consists of four horizontal $\lambda/2$ length slots within the waveguide, with a vertical separation λ between slots starting a length 2λ from the end of the waveguide. The slot height is small compared to the wavelength. Matching between the waveguide and the slot antenna was achieved using a tunable stopper at the bottom of the waveguide. A schematic of the cryostat insert showing the NMR probe, waveguide and slot antenna is shown in orange in Fig. 4.1 and a photo is shown in Fig. 4.4.

ND samples could be loaded and removed rapidly from the hyperpolarizer while cold. This was done by placing the ND sample in a Teflon tube mounted onto the end of a G10 rod and loading it thorough a sample port at the top of the cryostat. The cryostat was over-pressurized during the sample exchange to ensure no water vapor entered the system.

The temperature of the hyperpolarizer was monitored using two temperature sensors: a Cernox sensor attached to the fiberglass former to measure the temperature at the sample using a 4 wire measurement and a built in thermometer in the cryostat connected to a temperature controller[2].

4.2 X-band hyperpolarization setup

Low field hyperpolarization was measured with a setup at X-band frequencies at magnetic fields ranging between $B = 100$ mT and 500 mT. This setup was used for measurements performed on liquid-nanodiamond mixtures, using ND surface electrons to polarize adsorbed liquids. More specifically, measurements included ^{1}H signal enhancements, polarization build up times, hyperpolarization decay times, and the T_1 relaxation times of liquids containing various ND concentrations.

[1] Voltronics NMA55HV-E
[2] Oxford Instruments ITC 5035

NMR signals were measured using a home-built probe and spectrometer based on a SpinCore system, and hyperpolarization was achieved by driving electron-nuclear transitions using microwave radiation and a horn-mirror cavity.

A schematic of the experimental setup is shown in Fig. 4.5 and a photo of the setup is shown in Fig. 4.6.

The magnetic field was provided by either an electromagnet[1] (B = 150 mT - 500 mT) or a permanent magnet[2] (B = 458 mT). The electromagnet was set to field using a power supply[3] and a gaussmeter[4]. The permanent magnet provided a higher field homogeneity than the electromagnet, however temperature shifts over the course of the day resulted in magnetic field shifts and loss of the matching condition for hyperpolarization. A frequency locking algorithm measuring the NMR resonance and readjusting the local oscillator and hyperpolarization frequency was used to account for these shifts.

Various NMR probes were constructed for use with X-band hyperpolarization and low field NMR detection. A schematic is shown in orange in Fig. 4.5 and a photo can be seen in Fig. 4.6. Probes were constructed from brass as it is non-magnetic and easy to machine. The NMR detection circuit consists of a doubly spaced solenoid coil made from copper wire, a tunable capacitor to ground for frequency tuning, and a tunable capacitor in series to impedance match the resonant circuit to the coaxial transmission line. The probe also contained a horn antenna[5] combined with a reflector to tune a magnetic field maximum at the sample. A horn reflector cavity was chosen as the magnetic field maximum covers a large volume, allowing for larger samples to be polarized. The double spacing of the NMR coil allowed the microwaves to pass through the coil and penetrate the sample. Any less spacing shielded the sample too much for effective microwave penetration and hyperpolarization.

NMR pulses were produced by a Spincore NMR system[6], amplified using a power amplifier[7], passed through series crossed diodes (protecting the output of the amplifier) and then passed to the NMR coil. A $\lambda/4$ cable combined with diodes to ground, acts

[1]Lakeshore model EM4-HVA electromagnet
[2]SpinCore Technologies, Inc.
[3]Lakeshore model 642 electromagnet power supply
[4]Lakeshore model 475 DSP gaussmeter
[5]Pasternack PE-9854-10 and PE-9856-10
[6]SpinCore Technologies Inc. ispin-NMR-mini
[7]Tomco Technologies BTM00250-AlphaS

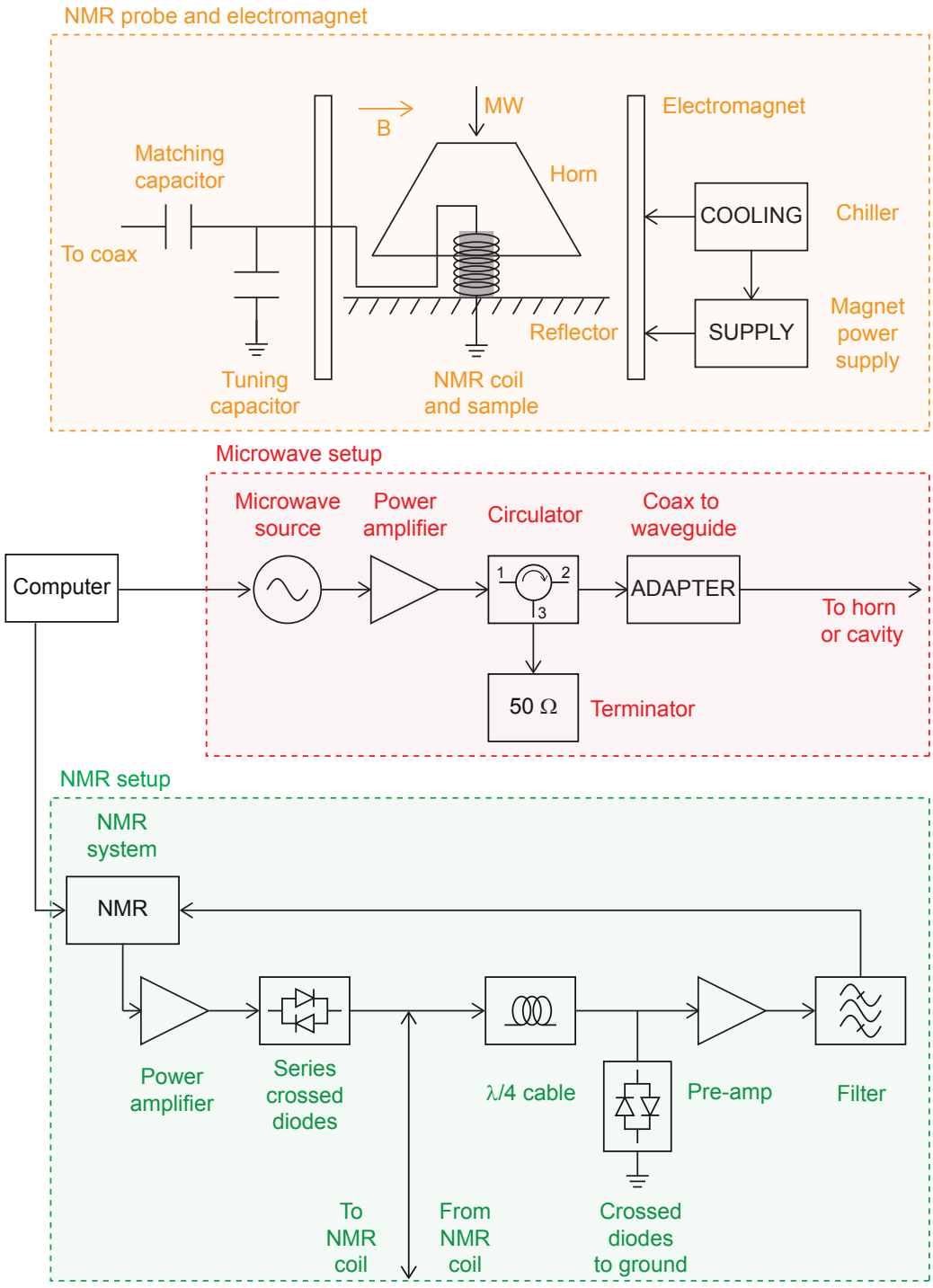

Figure 4.5: Schematic of the X-band hyperpolarizer. The NMR probe, horn antenna and electromagnet are shown in orange, the microwave components used for hyperpolarization are shown in red and the NMR components used to detect increased ^{1}H polarization are shown in green.

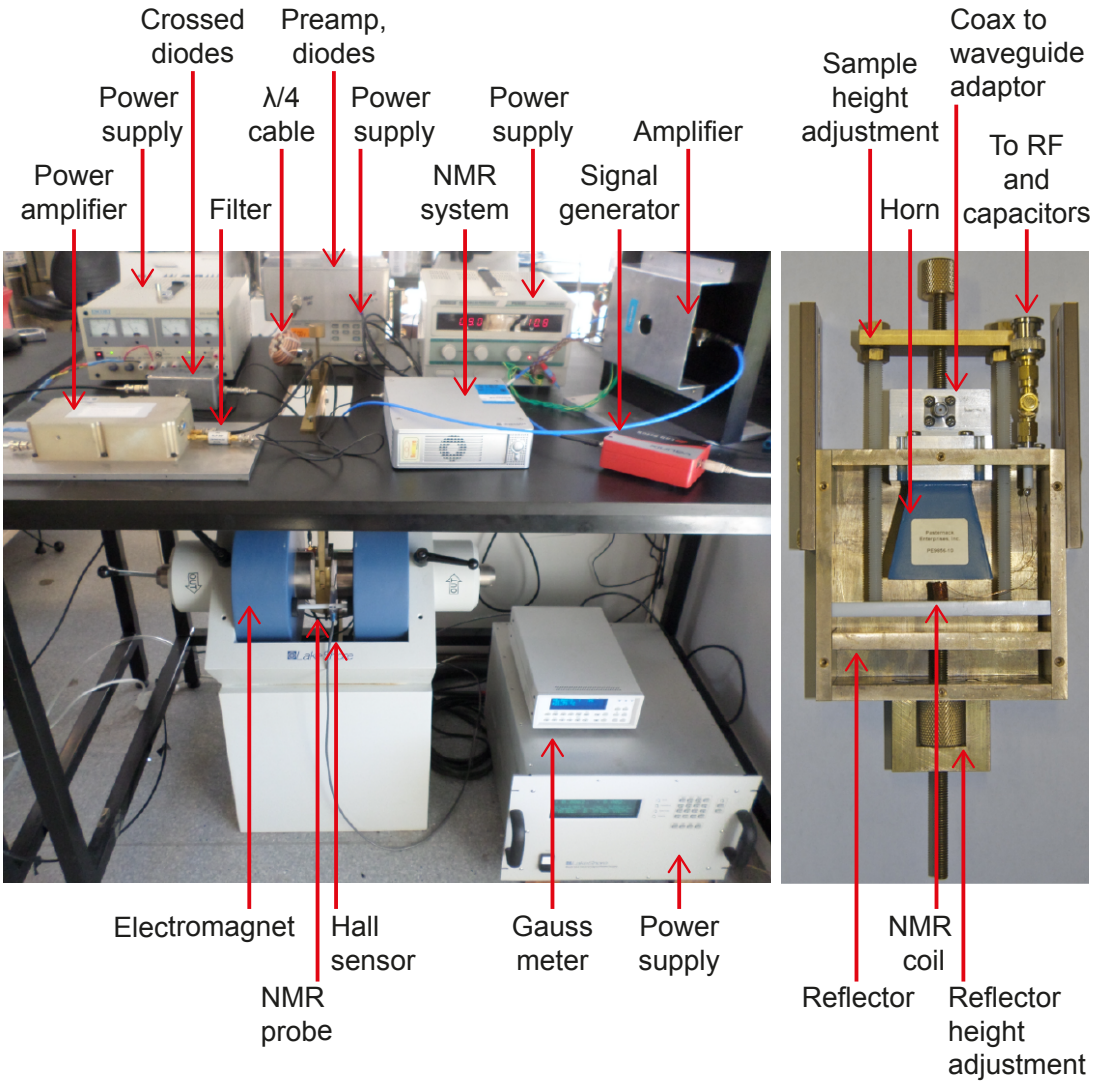

Figure 4.6: Photo of the X-band hyperpolarizer. Left: The microwave setup used for hyperpolarization and the NMR spectrometer are shown with the NMR probe in the electromagnet. Right: The NMR probe with a horn-mirror reflector cavity used for hyperpolarization. The detection circuit consisted of a doubly spaced solenoid coil and tuning and matching capacitors (not shown).

as a fast switch for high power pulses from the amplifier, transforming the short at the diodes to an open circuit, ensuring the pulses are directed to the NMR coil. NMR signals are amplified by a pre-amplifier[1], filtered, and then acquired by the SpinCore NMR console. A schematic of the NMR setup is shown in green in Fig. 4.5.

The X-band microwaves (f = 8 − 16 GHz) were produced by a signal generator[2], amplified to a maximum of $P = 10$ W using a power amplifier[3], transferred from coaxial to waveguide using an adapter and then passed to the horn antenna and sample. A schematic of the microwave components can be seen in red in Fig. 4.5.

The NMR console and microwave source (frequencies and pulse sequences) were controlled using an interface in IGOR Pro[4]. Data analysis and fitting were performed in IGOR Pro.

4.3 Polarization transfer and brute force hyperpolarization setup

Brute-force hyperpolarization was achieved using a dilution refrigerator combined with a hot swap probe. The ND sample was placed in a sample mount attached to a hot swap probe and placed into a dilution refrigerator. The hot swap probe was thermalized to each stage of the fridge. Photos of the sample mount, hot-swap probe and dilution refrigerator are shown in Fig. 4.7a.

The refrigerator was cooled to a temperature of $T = 4$ K, and then an electromagnet mounted on the bottom of the fridge was charged to a field of $B = 4$ T. The temperature was then lowered to $T = 35$ mK. The ND was allowed to equilibrate at these conditions for 3 days (4 days on the 2nd run). The ND was removed from the fridge by taking out the hot-swap probe (~ 30 seconds). The sample was then placed between two rare earth permanent magnets in a field of $B = 600$ mT, and transferred to a $B = 7$ T magnet for detection (~ 10 seconds, over a distance of 5 m). A schematic of the process is shown in Fig. 4.7b.

The ^{13}C NMR spectra of transferred polarization were acquired using an NMR spectrometer based on a National Instruments system with PXI modular components.

[1] Miteq AU-1565 and Miteq AU-1447
[2] Vaunix Lab brick LMS-163
[3] Quinstar Technology QPJ-06184045
[4] WaveMetrics

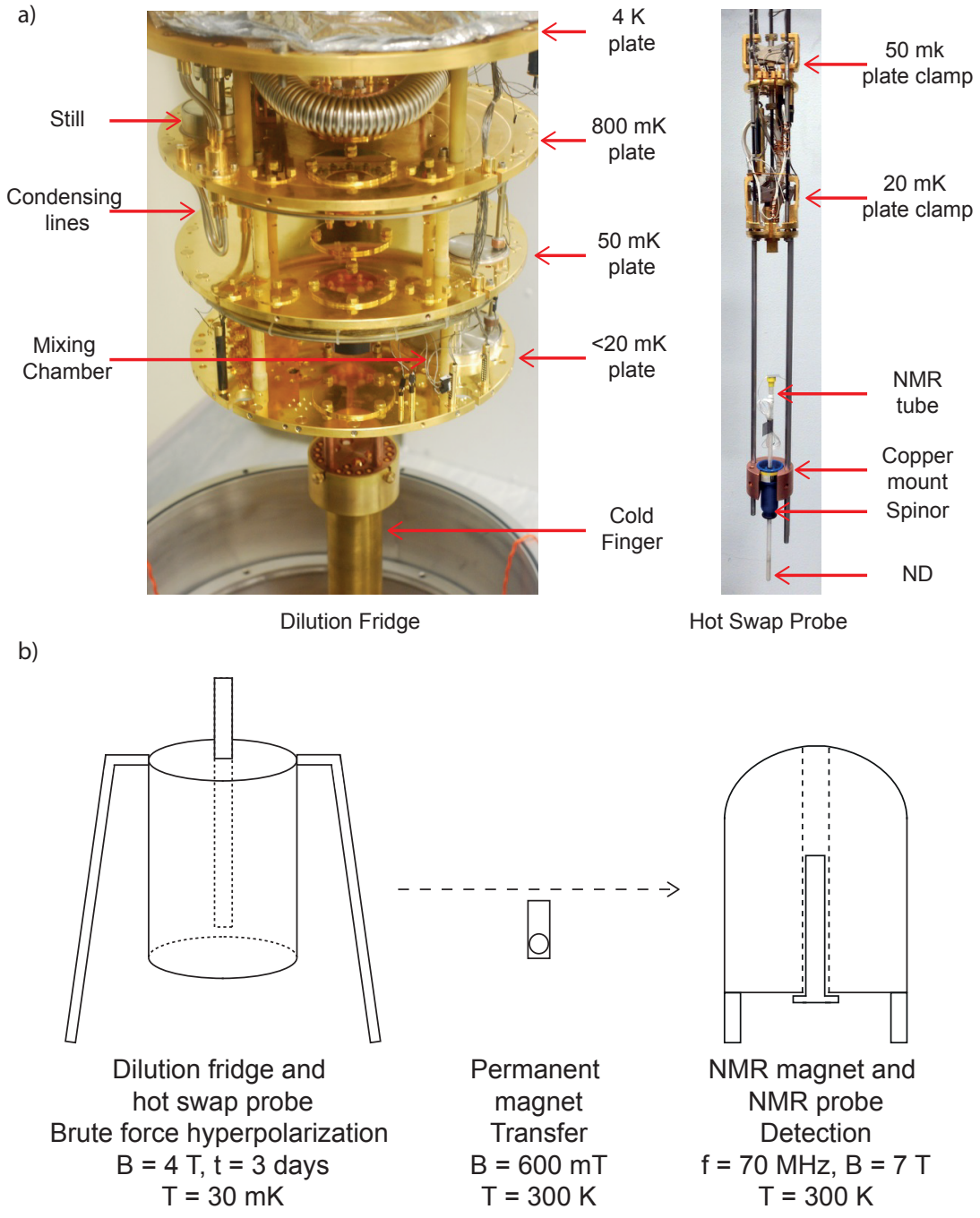

Figure 4.7: Dilution refrigerator brute force hyperpolarization setup. a) Photo of the dilution fridge (left) and hot swap probe with sample mount (right) used for brute-force hyperpolarization. **b)** Schematic of the process used for brute-force hyperpolarization to transfer polarization from a sample in a dilution refrigerator at a temperature of $T = 35\,\mathrm{mK}$ and magnetic field $B = 4$ T to an NMR magnet at $B = 7$ T and $T = 300$ K.

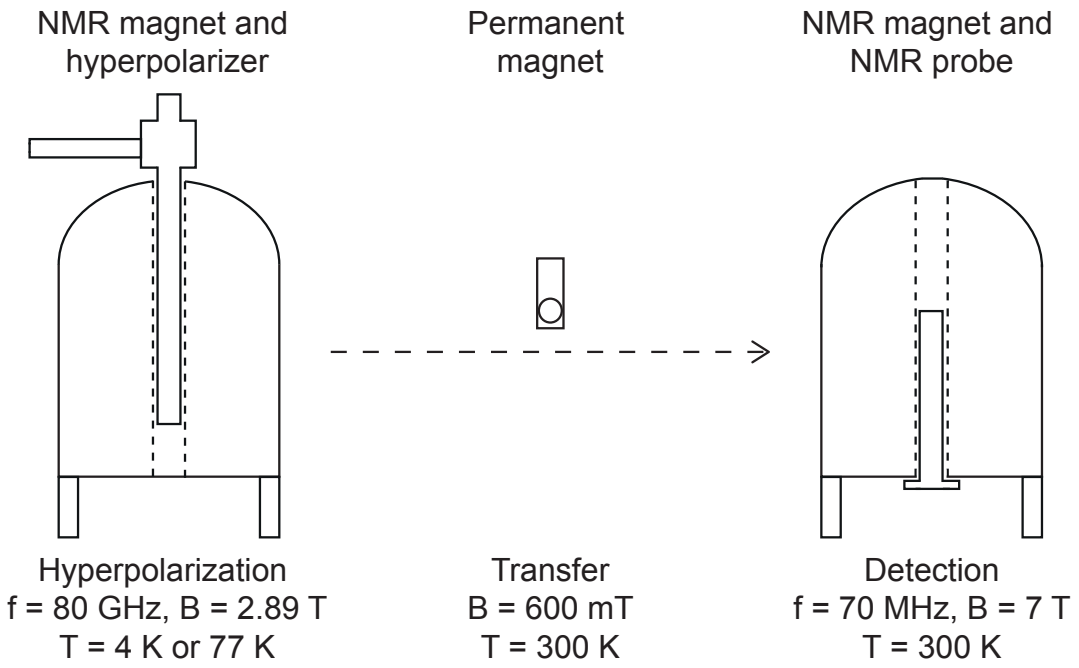

Figure 4.8: Schematic of polarization transfer. Schematic of the process used to transfer polarization from the hyperpolarizer to an NMR magnet.

Software for this spectrometer was based on IGOR Pro. Additional information about the spectrometer can be found in Ref. [122].

Measurements were made to determine how much polarization was retained during transfer between the polarizer and a separate magnet for detection. The NDs were polarized at a temperature of either $T = 4$ K or $T = 77$ K at a frequency $f \sim 80$ GHz. The cryostat was over-pressurized and the ND was removed using the sample exchange port at the top of the cryostat. The ND was placed between two rare earth magnets in a field of $B = 600$ mT, and transferred to a $B = 7$ T magnet for detection. The transfer process was over a distance of 3 m and took approx 10 seconds. A schematic of the process is shown in Fig. 4.8. The NMR signal was acquired using the spectrometer based on the National Instruments PXI components.

5

Nanodiamond characterization

Diamond is an interesting and unique material with outstanding mechanical, thermal, chemical, electrical and optical properties. Perhaps more interesting, however, are the crystallographic defects and colour centres in diamond which can change the material properties, leading to spin and optical properties which have found use in quantum information technology, high resolution magnetometry and biotechnology. This technological interest has led to the development of synthesis techniques for artificial diamond with tailored impurities and properties to fit the application.

This chapter gives a brief overview of properties and defects found in diamonds with emphasis on nanometer and micrometer sized diamonds. A description is given on how various synthesis methods can affect impurities and as a result the diamond properties. This chapter also details the characterization of nanodiamonds using NMR, ESR, Raman spectroscopy and SEM imaging[1].

[1]This chapter contains data from the supplementary material in Rej, E. et al. *Hyperpolarized nanodiamond with long spin-relaxation times.* Nature Communications 6, 8459 (2015) [123].

5.1 Diamond

5.1.1 Properties of diamond

Diamond is an allotrope of carbon with sp^3 hybridized orbitals. In diamond each carbon atom has four valence electrons which are equally distributed forming covalent bonds with neighboring carbon atoms. This makes a periodic structure, tetrahedral in shape, known as a diamond lattice, where nearest neighbor bonds are 0.154 nm long [124], see Fig. 5.1. The covalent bonds and tetrahedral arrangement lead to diamond being the hardest known natural mineral. The diamond lattice is weakly anisotropic (when properties vary in different crystalline directions) with $A = 1.21$, where A is the elastic anisotropy [125].

Several carbon isotopes make up diamond: ^{12}C (98.9%), ^{13}C (1.1%) and trace amounts of ^{14}C. The ^{13}C is a spin-1/2 particle and can be detected in an NMR or MRI experiment, the ^{12}C is a spin-0 atom and can not be detected, and the ^{14}C is a spin-3 atom with a radioactive half life of 5730 years. The ^{13}C nuclear spin has a gyromagnetic ratio $\gamma = 10.705$ MHz/T.

5.1.2 Defects found in diamond

Interesting spin dynamics and changes in the properties of diamond originate from the defects (or colour centres), either intrinsic of extrinsic, that disrupt the lattice structure. Over 500 different colour centres and crystallographic defects have been identified in diamond [127], the most famous being the NV centre [128, 129].

Two types of defects exist in diamond: intrinsic defects, where carbon atoms are displaced from their regular positions, and extrinsic defects, where elements other than carbon form substitutional or interstitial impurities embedded in the diamond lattice. Examples of intrinsic and extrinsic defects are shown in Fig. 5.2 on a 2-D plane.

Intrinsic defects include interstitial carbon atoms, where more than one carbon atom exists at one lattice site [130, 131] (Fig. 5.2a), vacancies [132–138] where carbon atoms are missing from a lattice site (Fig. 5.2b), dislocations, where broken bonds exist, platelets of regular arrays of carbon interstitial atoms [139–141] (Fig. 5.2c), and voidities, which are nanometer sized carbon clusters [142,143]. Intrinsic defects result in carbon-carbon dangling bonds (a chemical bond associated with a carbon atom, which does not join another carbon atom in the crystal), which are a spin-1/2 electronic

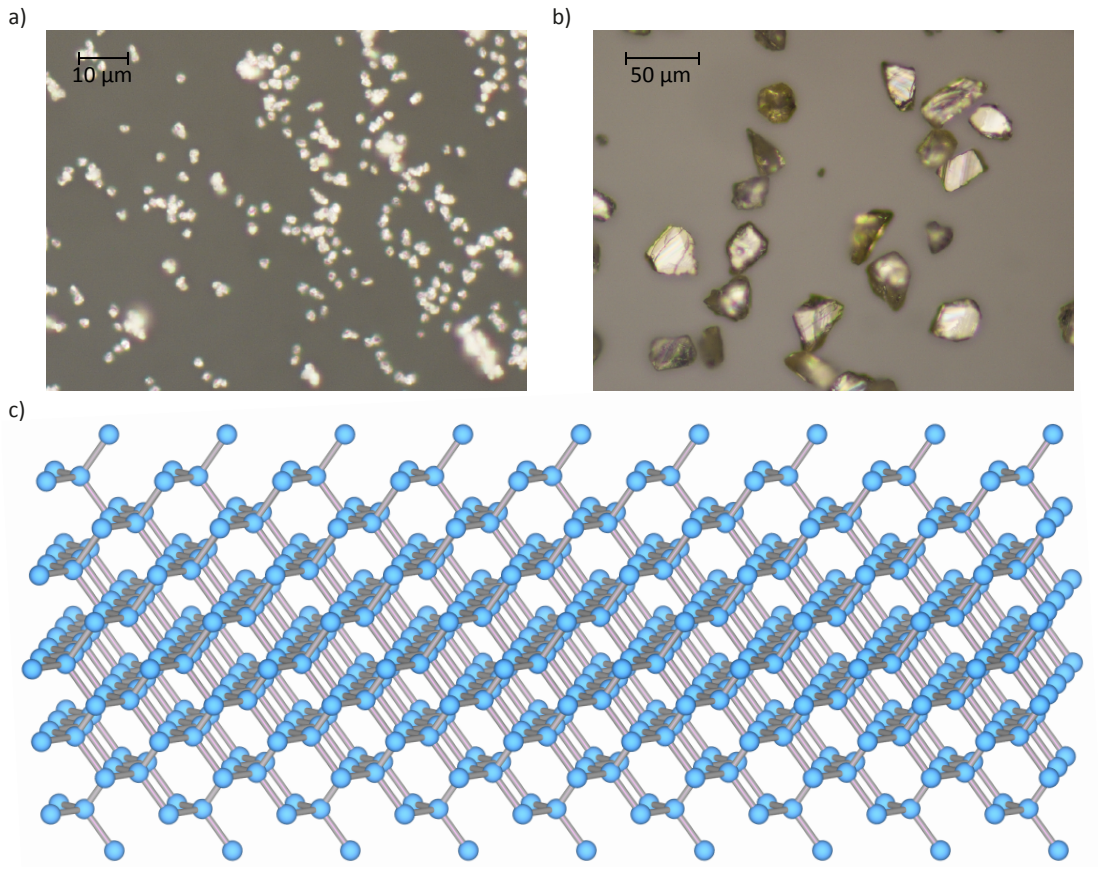

Figure 5.1: Optical images and lattice structure of diamond. a) Optical microscope image of 2 µm ND. **b)** Optical microscope image of 40 µm ND. **c)** Schematic of the tetrahedral diamond lattice structure. Carbon atoms are shown in blue and covalent bonds are shown in grey. The lattice structure were drawn with Vesta [126].

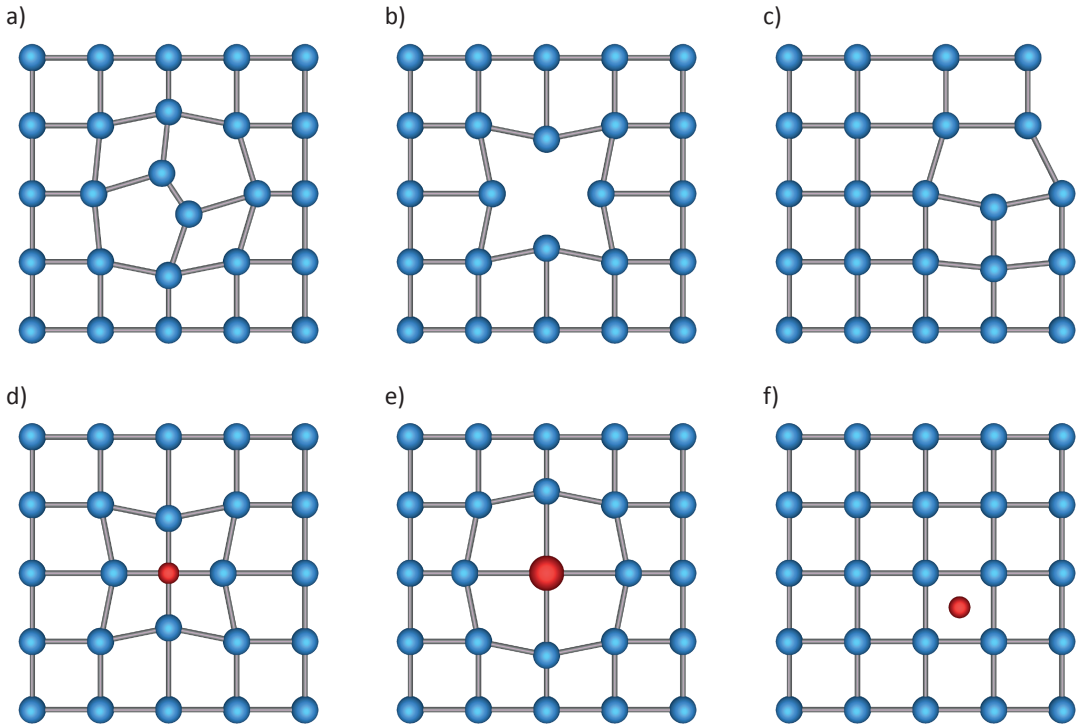

Figure 5.2: Two dimensional representation of defects found in the diamond lattice. Intrinsic defects include: **a)** self interstitial carbon atoms, where more than one carbon atom exists at one lattice site, **b)** vacancies, where one or more carbon atoms are missing from a lattice site, and **c)** dislocations in the diamond lattice. Extrinsic defects include: **d, e)** foreign substitutional atoms (such as nitrogen), either as isolated atoms or atomic clusters, and **f)** foreign interstitial atoms. Lattice atoms are shown in blue, impurities are shown in red, and chemical bonds are shown in grey. Images were drawn with Vesta [126].

defect. Carbon dangling bonds are also found on diamond surfaces.

Extrinsic defects can be foreign substitutional atoms (Fig. 5.2d, 5.2e) or foreign interstitial atoms (Fig. 5.2f) embedded in the carbon lattice. They can be isolated atoms or small atomic clusters either dispersed through the diamond or artificially introduced into specific spots, for example by ion implantation or during the diamond growth process. The most common extrinsic impurity is substitutional nitrogen which makes up various nitrogen related defects in diamond, however elements including H, He, Li, B, N, O, Ne, P, Si, As, Ti, Cr, Ni, Co, Zn, Zr, Ag, W, Xe, and Tl [127, 135, 136, 144, 145] have been found as defects in the diamond lattice.

The defects can occur in different charge states, depending upon surrounding donor and acceptor defects. A typical donor atom is nitrogen, which has one more electron than carbon, and a typical acceptor atom is boron, which has one less electron than carbon.

Historically, diamonds were classified based upon their nitrogen defect concentration, according to their ultraviolet and infrared transmission. Diamonds with nitrogen concentrations $>$ 20 ppm are classed as type I, while diamond with nitrogen concentrations $<$ 20 ppm are classed as type II. Type II diamonds are further classed into diamond with boron impurities (type IIb) and without boron impurities (type IIa).

Nitrogen defects make up the majority of defects found in diamond, see Fig. 5.3. The most common defect found in natural diamond is the A-centre, which consists of two substitutional nearest neighbor nitrogen atoms with a double bond between them, see Fig. 5.3a. Diamonds containing predominantly A-centre impurities are classified as type IaA. The B-centre is another nitrogen defect that can occur in diamond, consisting of four nitrogen atoms surrounding a vacancy, see Fig. 5.3b. Diamonds with predominant B-centre impurities are classed as type IaB. Diamonds with similar concentrations of A-centre and B-centre aggregates are classed as type IaAB.

The most common defect in synthetically produced diamond is the C-centre (also known as the P1 centre) which consists of an electrically neutral substitutional nitrogen atom in the diamond lattice, see Fig. 5.3c. The P1 centre is an electron paramagnetic system with electron spin angular momentum $S = 1/2$ in the ground state [146], originating from the nitrogen atom having one more electron than the carbon atom that it substitutes. Diamonds predominantly containing C-centre impurities are classed as type Ib.

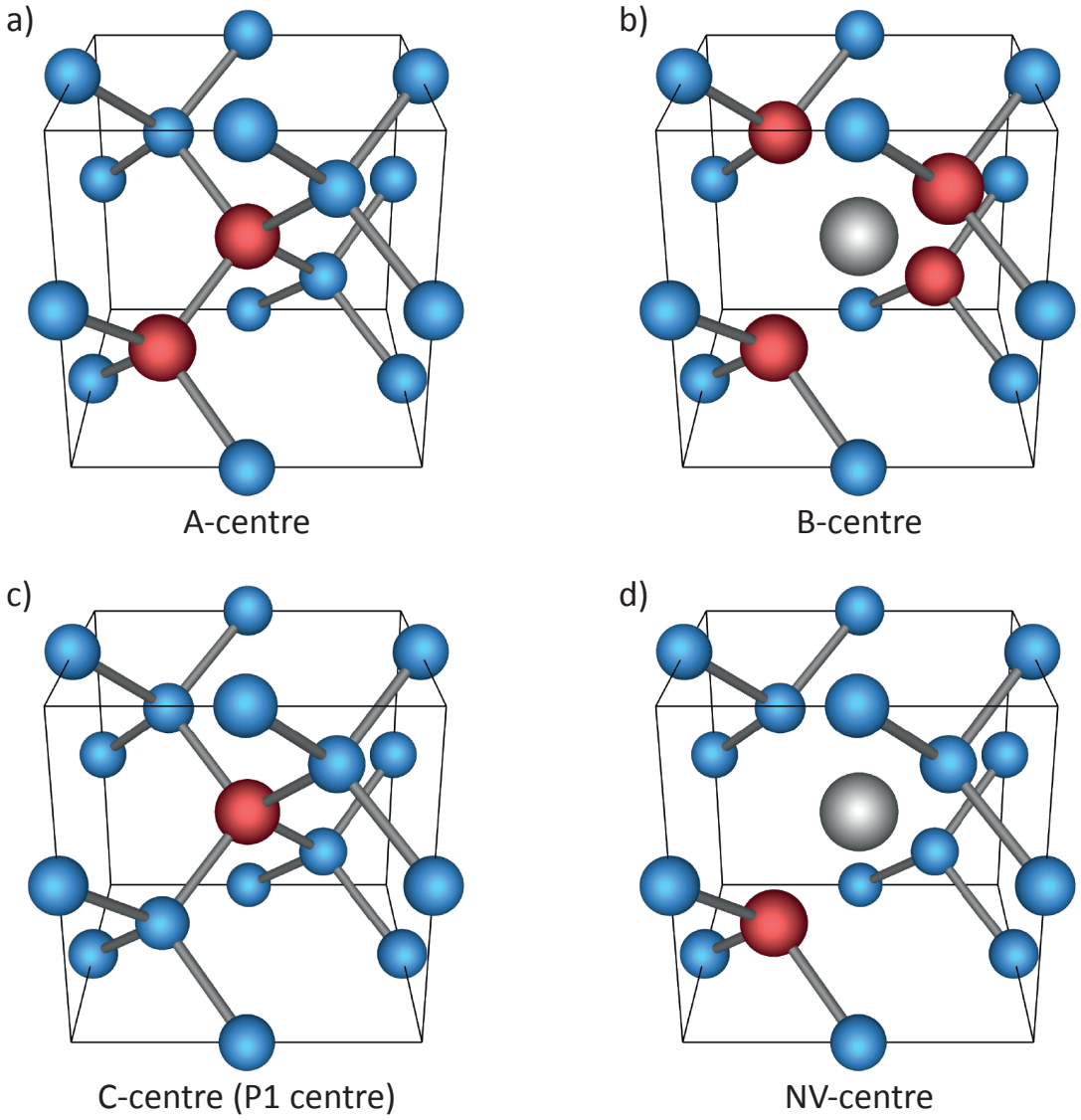

Figure 5.3: Schematic of nitrogen defects found in diamond. a) A-centre defect, consisting of two nitrogen substitutional atoms on adjacent lattice sites. **b)** B-centre defect, consisting of four nitrogen atoms surrounding a vacancy in the lattice. **c)** C-centre (P1 centre) defect, consisting of a single substitutional nitrogen in the lattice. **d)** NV centre defect, consisting of a substitutional nitrogen atom next to a vacancy in the lattice. Carbon atoms are shown in blue, nitrogen atoms are shown in red, vacancies are shown in grey and chemical bonds are shown as grey sticks. Images were drawn with Vesta [126].

Probably the best known and most studied nitrogen defect in diamond is the nitrogen-vacancy centre (or NV centre), which consists of a substitutional nitrogen atom next to a vacancy in the diamond lattice. The NV centre (in the negative charge state) is a spin-1 system, which can be polarized optically into the ground state, and has easily addressable optical and microwave spin states at room temperature [147]. When combined with long spin coherence times [128, 129, 148, 149], NV centres are a promising system for applications such as magnetometry [27, 28] and quantum information [150, 151]. Coherent coupling of NV centres and surrounding spins have led to selective addressing and manipulation of single spins such as ^{13}C [152], ^{14}N [153] and other NV centres [154]. Additionally NV centres show florescence and can be used for biolabelling [26, 155–158].

While all these defects exist in the diamonds studied in this work, the predominant defects are P1 centres and carbon-carbon dangling bonds, both electron spin-1/2 systems, which can be addressed using microwave radiation.

5.1.3 Synthetic production of diamond and nanodiamond

Diamonds are produced naturally in high temperature and high pressure conditions in the Earth's crust, and can also be produced synthetically in conditions that mimic the geological processes.

Three methods exist for manufacturing synthetic diamonds: the high pressure high temperature (HPHT) technique, the detonation technique and chemical vapor deposition (CVD).

HPHT mimics the phase transition of graphite to diamonds in carbon containing materials at high temperatures ($T > 1500$°C) and high pressures ($P > 5$ GPa) [159]. At high temperatures a solvent metal (usually iron, nickel, or both) working as a catalyst, melts and dissolves a high purity carbon source (typically graphite), producing a supersaturated mixture which precipitates and crystallizes onto diamond seed crystals. The catalyst significantly lowers the temperature and pressure conditions (provided by a press [160]) as compared to that needed for natural diamond to form (diamond melts at a temperature $T = 4500$ K and the graphite/diamond/liquid triple point occurs at a temperature of $T = 4200$ K and a pressure of $P = 11$ GPA [161]. Temperature gradients within the vessel are able to lower the operating temperature further [162].

Nitrogen is the most common contaminant, originating from the gas found in

the press, the carbon source, or the solvent/catalyst, and usually result in P1 centre impurities [163].

Improvements in the manufacturing process have allowed for the control of impurity concentrations and tailored properties of diamond. Nitrogen getters for example can be used to minimize the nitrogen in the press [163–165], producing type IIa diamonds [166]. Impurities can also be added to tailor material properties for example HPHT diamond has been heavily doped with Boron, producing superconducting diamond for use in electronics [167].

Another way to synthesize diamond is through CVD. A combination of methane gas (acting as a carbon source) and hydrogen gas is injected into a growth chamber under controlled temperature and pressure conditions, where it is heated and ionized. The radicals react and form diamond crystals on a substrate or seed crystals, producing either single crystal or polycrystalline diamond respectively. The hydrogen plasma etches away non-diamond carbon during the growth process. As with HPHT diamond synthesis, impurities can be well controlled in the CVD process. Doping CVD diamond with nitrogen or phosphorous results in n-type semiconductors and doping with boron results in p-type semiconductors. The high break down voltages make doped diamond a well suited material when high frequencies, powers, temperatures or voltages are required for electrical applications [168].

The third common way to make diamond is using the detonation process. Carbon containing explosives are detonated in a detonation chamber. The high temperatures and pressures at the shock front during the detonation process allow for the thermodynamically favorable creation of diamond. Detonation NDs are typically less than 5 nm in size [169], and have an sp^3 hybridized core surrounded by an sp^2 hybridized shell [170].

Nanoscale diamonds can be made in a small size distribution with uniform shape by grinding down larger diamonds, such as natural diamond offcuts, CVD films, or larger HPHT diamonds. A typical way to do this is to use a ball mill combined with a centrifuge. A ball mill is a grinder, working with friction and impact forces, consisting of a rotating hollow cylinder, partially filled with zirconia balls. Size reduction of a sample fed into the mill occurs as the balls drop from near the top of the rotating cylinder. The milling process can introduce metal and non-diamond carbon impurities.

Impurities in the core of diamonds can be modified or added in several ways.

Irradiation by ion or electron beams can produce vacancies, which can lead to NV centres forming after annealing [171]. Ion implantation can also be used to create defects, for example diamond can be irradiated with N^+ ions to form nitrogen defects.

The surface structure of diamond depends strongly on the conditions under which the diamond was created. NDs that have been created from grinding down larger diamonds exhibit the surface structure typical to larger diamonds. Detonation diamonds usually have many surface functional groups from reactions of dangling bonds and the gases used in the production [172]. The most characteristic surface groups are carboxyl, hydroxyl, lactones, anhydrides and ketone functional groups [173].

The ND surface can be controlled through acid cleaning which removes the majority of non-carbon impurities such as those introduced during ball milling, and can remove functional groups from the ND surface [174]. Surface functionalization with molecules such as hydrogen, hydroxyl, carboxyls or ketone groups can then be used to produce diamonds with specific surface properties, [19, 172]. Specific compounds can also be attached to a nanodiamond, for example fluorophores for optical tracking, or doxorubicin, a chemotherapeutic for drug delivery in medicine [24].

5.2 Characterization of nanodiamond

The properties of electron and nuclear spins in diamond are examined through nuclear magnetic resonance (NMR), electron spin resonance (ESR), Raman spectroscopy and scanning electron microscope (SEM) studies. Diamonds synthesized using different techniques and in various sizes were examined and characterized.

5.2.1 Types of diamonds studied

Three types of diamonds are studied in this work:

- HPHT ND: Diamonds produced by the HPHT technique, between 18 nm and 40 μm in size, purchased from Microdiamant[1]. Throughout this study these diamonds are referred to as HPHT ND.
- AO ND: HPHT diamonds were air oxidized (AO) to burn off the outer layer of carbon and to modify the surface electronic defects. The HPHT ND was spread in

[1] http://www.microdiamant.com

a thin layer in ceramic crucibles and placed in a furnace[1]. The furnace was heated to 550°C (∼ 1 hr), left at 550°C for 1 hour and then cooled to room temperature (∼ 20 min). The NDs are expected to decrease in size by approximately $4-5$ nm (the etch rate for diamonds is 4 nm/hr at 550°C and 1 nm/hr at 500°C [175]). AO ND in the size range 18 nm to 2 μm were examined. Throughout this study, these diamonds are referred to as AO ND.

- NAT ND: Natural diamonds in the size range 125 nm - 2 μm were examined. Throughout this study these diamonds are referred to as NAT ND. These diamonds were purchased from Microdiamant.

A list of the ND particles that were used in this study with median particle size and size range can be found in Appendix A.

5.2.2 SEM studies

Scanning electron microscope[2] images of a range of NDs were acquired in scanning mode to examine the shape, surfaces, and aggregation, and in transmission mode to analyze the size of the NDs, see Fig. 5.4.

Suspensions of ND in water were shaken and sonicated to break up diamond aggregates and a drop of the solution was placed on a TEM grid and allowed to dry. At least 15 images of different regions of each ND were taken.

The images were analyzed using ImageJ[3], to confirm the size of the NDs. Histograms of the size distributions are shown in Fig. 5.5. ND particle areas were calculated as a number of pixels and converted to particle diameters (shown in dots), assuming spherical particles. In the case of larger diamonds, which are more angular than spherical, this assumption can result in an underestimate of the particle diameter by up to 10%. The size distributions were consistent with that stated by the supplier.

Small NDs ($<$ 50 nm) can be found in the 210 nm, 500 nm and 2 μm diamond images. It should be noted, that although there are quite a few NDs in this size range, the volume they take up is much smaller than the volume taken up by the larger NDs.

We observe a size difference between the 25 nm HPHT and 25 nm AO NDs, consistent with the amount etched away by the air oxidation process.

[1] Fetlow Melbourne Furnace
[2] Zeiss Ultra Plus Gemini
[3] imagej.net

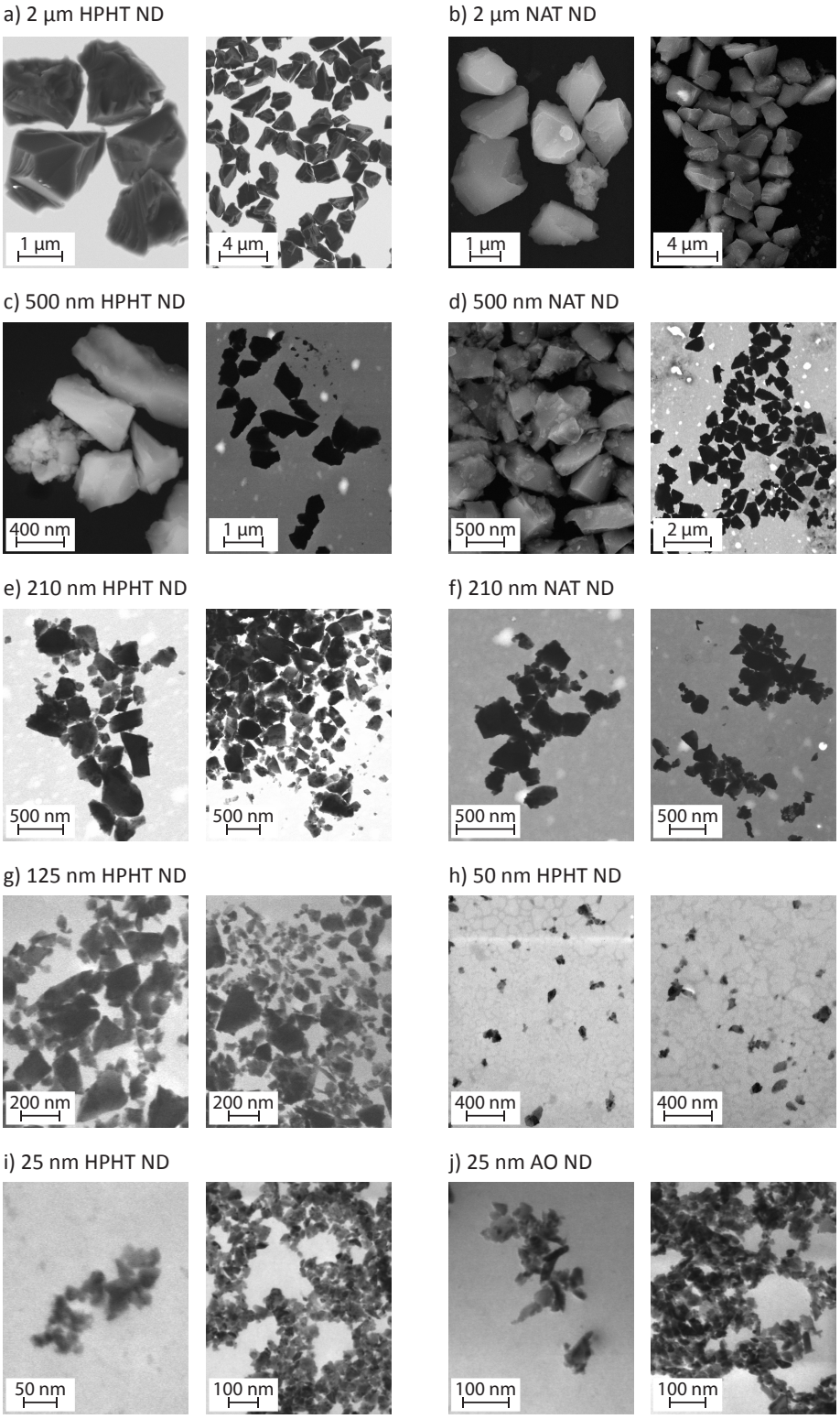

Figure 5.4: SEM images of NDs. a) 2 µm HPHT ND, **b)** 2 µm NAT ND, **c)** 500 nm HPHT ND, **d)** 500 nm NAT ND, **e)** 210 nm HPHT ND, **f)** 210 nm NAT ND, **g)** 125 nm HPHT ND, **h)** 50 nm HPHT ND, **i)** 25 nm HPHT ND, **j)** 25 nm AO ND.

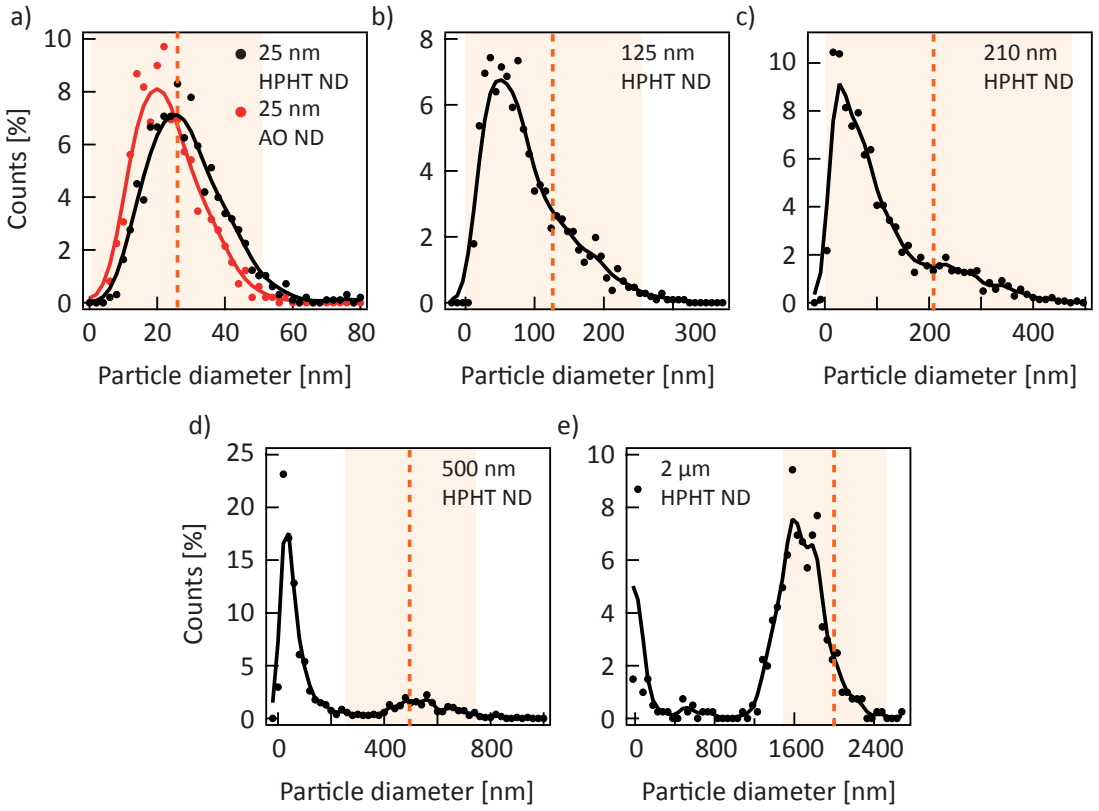

Figure 5.5: SEM size distributions of NDs. Histograms of **a)** 25 nm HPHT ND (black) and 25 nm AO ND (red), **b)** 125 nm HPHT ND, **c)** 210 nm HPHT ND, **d)** 500 nm HPHT ND, and **e)** 2 µm HPHT ND. ND particle areas were measured from SEM micrographs using image analysis software and converted to particle diameters (dots) assuming spherical particles. The solid line is a guide to the eye. The orange shaded region is the size range, and the dashed orange line is the median particle size as specified by the supplier.

5.2.3 NMR studies

The tetrahedral lattice structure in diamond, combined with the low abundance of ^{13}C (1.1%) within a lattice of non-spinful ^{12}C atoms, leads to a long T_1 relaxation time in bulk diamond. Spin diffusion between the ^{13}C nuclear spins is largely suppressed.

Several authors have considered the problem of spin relaxation of nuclei in a crystal containing paramagnetic impurities, in the case of limited spin diffusion between the nuclear spins [101, 176–179]. Nuclear relaxation is attributed to the coupling between the magnetic moment of the paramagnetic ion and the magnetic moment of the nuclei in the crystal through dipole-dipole interactions. Initially, after the bulk magnetization is disturbed, any local magnetization of a nuclear spin will be dominated by the nearest paramagnetic ion and changes will be most rapid close to the paramagnetic impurity. This leads to a spatial distribution of magnetization [179]. It should be noted, however, that nuclear spins very close to the paramagnetic ion have shifted Larmor frequencies, and do not contribute to the NMR line or undergo spin flip-flop transitions with the remaining nuclei in the bulk diamond. For a system such as diamond, with limited spin diffusion, the presence of paramagnetic impurities, and a high magnetic field, the growth of magnetization follows a stretched exponential behavior [176]:

$$M \propto e^{-At^{\alpha}} \tag{5.1}$$

where M is the magnetization, A is a constant, t is the time and α is a constant which depends on the concentration and distribution of the paramagnetic centres. The stretched exponential component α depends upon both the sample space dimensionality (D) and whether the individual nuclear spins are affected by many impurities (homogenous distribution of spins) or one impurity (inhomogeneous distribution of spins).

For a homogeneous distribution of spins $\alpha = D/6 = 1/2$, (in this case $D = 3$ for a 3D crystal), and the magnetization build up follows:

$$M/M_0 = 1 - e^{-(t/T_1)^{1/2}} \tag{5.2}$$

where T_1 is the spin-lattice relaxation time, and M_0 is the equilibrium magnetization.

For an inhomogeneous distribution of spins, the system can be considered as a series of subsystems packed in the D-dimensional space, each consisting of a paramagnetic impurity surrounded by nuclei. In this case the dimensionality of the magnetic moment (d) must be considered and $\alpha = (D + d)/6 = 2/3$ (in this case $d = 1$, as all the magnetic moments are aligned in the direction of the high external magnetic field, and $D = 3$ for a 3D crystal). The magnetization build up follows:

$$M/M_0 = 1 - e^{-(t/T_1)^{2/3}} \tag{5.3}$$

The T_1 relaxation times can range from many hours in bulk diamond to a few hundred milliseconds in detonation ND. HPHT and CVD diamonds have T_1 relaxation times in between. The T_1 relaxation time has been found to be dependent upon ND size, the method used for synthesis, type of impurities, the concentration of impurities, and the concentration of ^{13}C spins in the diamond. A summary of some of the relaxation times can be found in Table 5.1.

The T_1 relaxation times of a range of HPHT nanodiamond samples used in this study were measured at a magnetic field of $B = 7$ T using a saturation recovery pulse sequence. Measurements were made using a Bruker probe and a Redstone Tecmag NMR system for pulse generation and NMR signal acquisition.

The magnetization build up curves for three representative NDs can be seen in Fig. 5.6. Small NDs in the size range 18 nm to 350 nm (see Fig 5.6a) are well described by a stretched exponential magnetization build up with an exponent $\alpha = 0.66$, indicating an inhomogeneous distribution of paramagnetic impurities within the ND.

In contrast, NDs larger than 350 nm (see Fig. 5.6b, and Fig. 5.6c) are better fitted by a double exponential function than a stretched exponential function. We attribute this to ^{13}C spins on the surface of the ND relaxing quickly and ^{13}C spins in the core of the ND relaxing on a longer time scale. When fitted with a stretched exponential, the exponent is $\alpha = 0.5$, corresponding to a homogenous distribution of spins, where each nuclear spin is affected by more than one electron spin. The T_1 build up times and stretched exponents α are summarized in Fig. 5.7.

ND particle	Size	T_1	reference	notes
Gem	600 mg	3.5 days	[180]	
Gem (IIa)	-	10 min	[181]	
Gem (Ib)	-	7.14 min	[181]	
Gem (Ib)	6.75 mg	300 s	[182]	
Nat (Ib)	380 mg	40 s	[95]	
Nat (Ia)	700 mg	11 hrs	[183]	
Nat (IIa)	680 mg	19 hrs	[183]	
Semiconducting (IIb)	3.1 g	4 hrs	[46]	
CVD	$\sim$ 15 µm	67 s	[184]	
CVD	$\sim$ 15 µm	17 s	[184]	50% ^{13}C
CVD	$\sim$ 15 µm	8 s	[184]	100% ^{13}C
S.C.	100 - 500 nm	12 - 45 s	[185]	
HPHT	30 mg	14 - 17 s	[186]	99% ^{13}C
HPHT	30 mg	up to 5000 s	[187]	99% ^{13}C
HPHT	$\sim$ µm	460 s	[51]	
HPHT	400 - 600 µm	220 s	[98]	
d-ND	10 - 30 nm	1.8 s	[51]	
d-ND	5 nm	300 ms	[188]	
d-ND	5 nm	140 - 170 ms	[189]	
d-ND	5 nm	370 - 600 ms	[51]	
d-ND	5 nm	$<$ 1 s	[170]	
d-ND	4.3 nm	22 - 450 ms	[190]	

Table 5.1: T_1 relaxation times of different types of diamonds in the size range between 12 mm and 5 nm. S.C. are shock compression diamonds, CVD are chemical vapor deposition thin films, Gem are natural gem cut diamonds, and Nat are natural diamonds. The type of diamond is given in brackets when specified. Assuming a spherical diamond: 30 mg diamonds are $\sim$ 2.5 mm, 650 mg are $\sim$ 7.0 mm, 6.75 mg are $\sim$ 1.5 mm, and 3.1 g are 11.9 mm large.

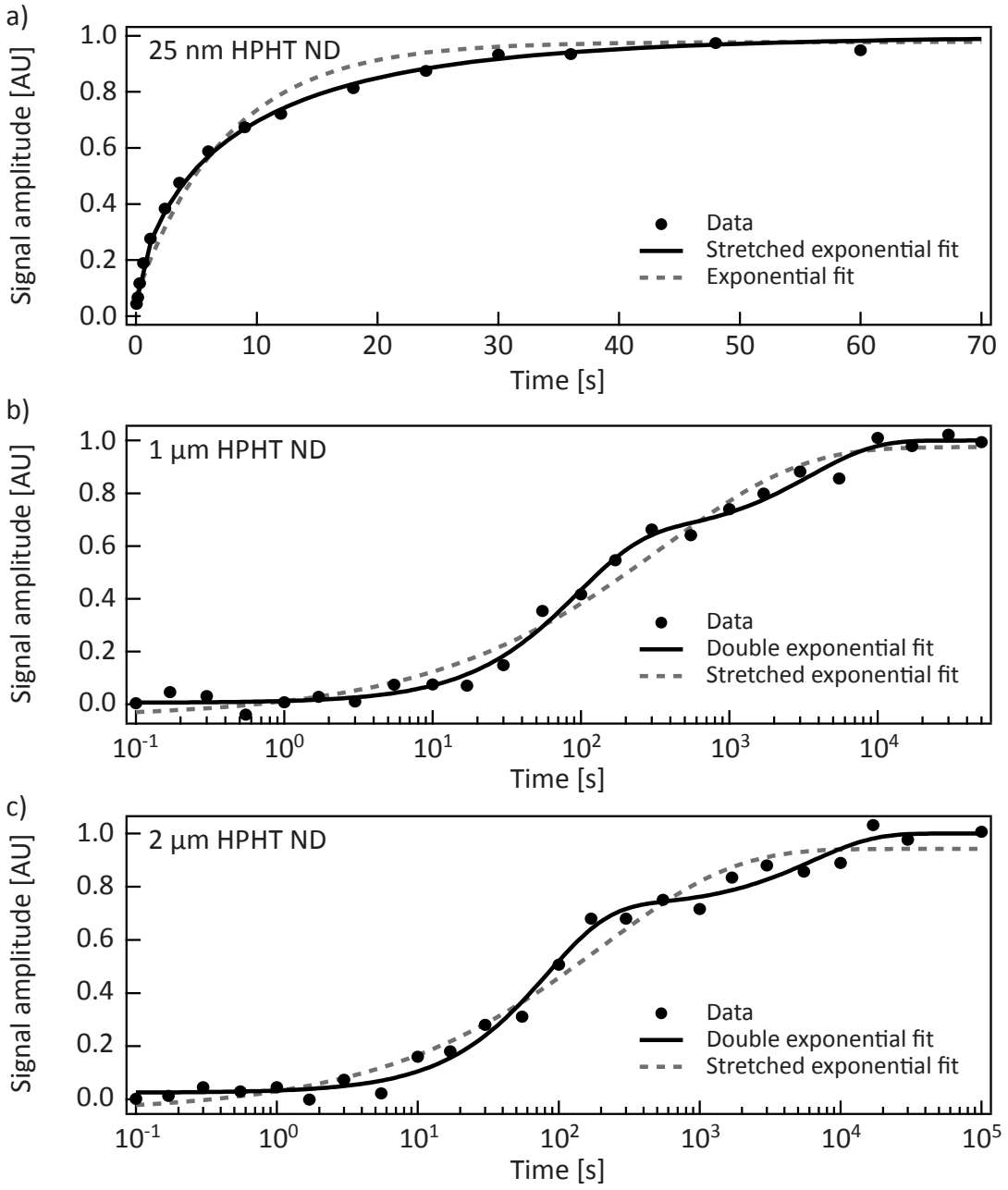

Figure 5.6: T_1 magnetization build up in ND measured using a saturation recovery pulse sequence at $B = 7$ T. a) Comparison between a stretched exponential fit (solid black line) and exponential fit (grey dashed line) to the magnetization build up (black dots) of 25 nm HPHT ND. The stretched exponential is a better fit for small NDs. **b, c)** Comparison between a double exponential fit (solid black line) and a stretched exponential fit (grey dashed line) for **b)** 1 µm HPHT ND and **c)** 2 µm HPHT ND (black dots). For larger ND particles the double exponential fit has a smaller variation from the data than a stretched exponential fit. Errors are smaller than the symbols.

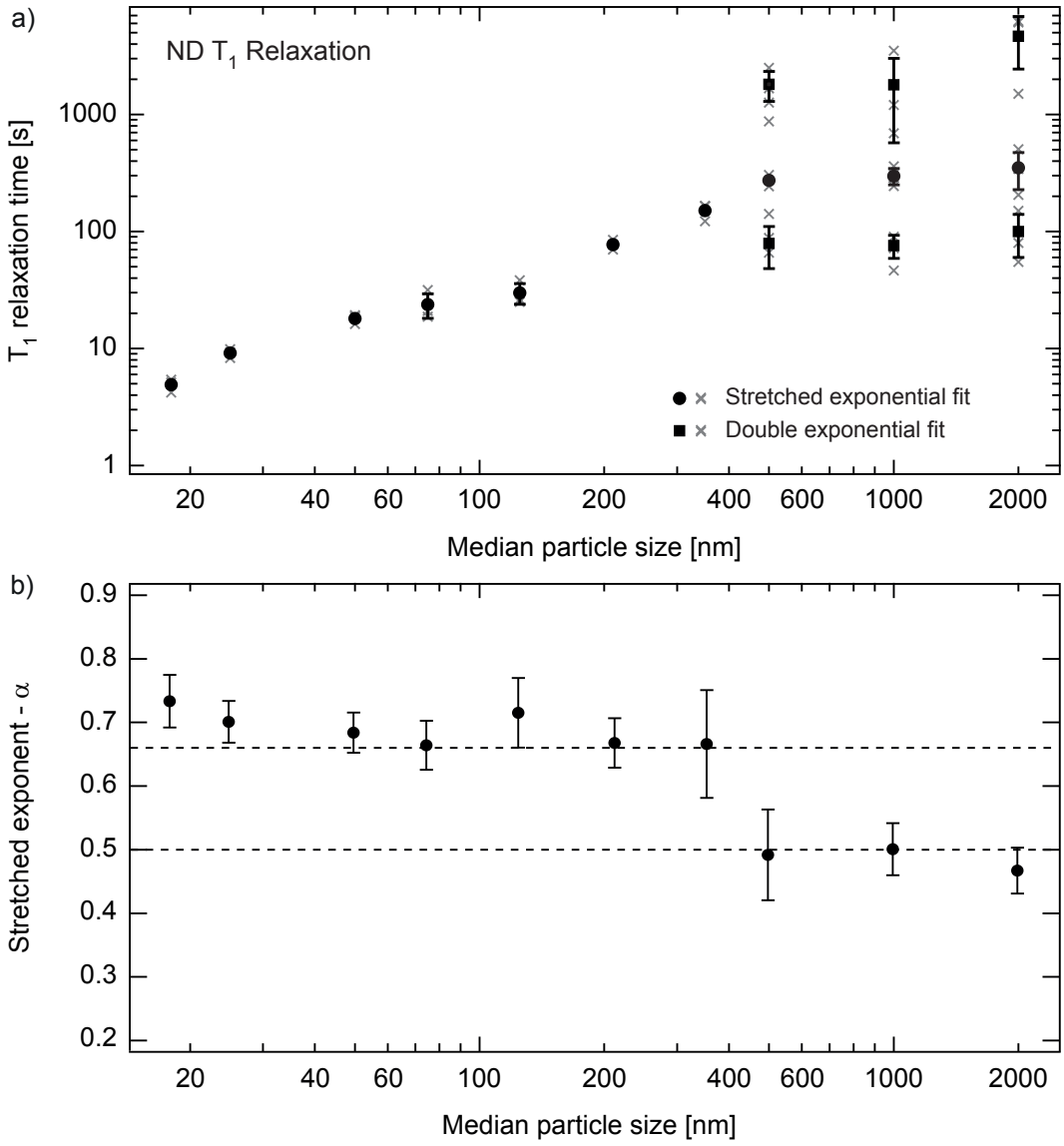

Figure 5.7: T_1 relaxation time and stretched exponential component α for HPHT NDs. a) The T_1 relaxation time (grey crosses) extracted from the best fit to $M/M_0 = 1 - \exp(-(t/T_1)^\alpha)$ for the T_1 build up measured using a saturation recovery sequence for HPHT NDs. Three repetitions were taken for each ND and the average is shown in black dots. Larger NDs were better fitted by a double exponential with a fast and a slow component, which we attribute to surface spins and core spins respectively. The two components of the double exponential are shown in grey crosses and the average is shown in black squares. **b)** Stretched exponential component, α, extracted from the best fit to $M/M_0 = 1 - \exp(-(t/T_1)^\alpha)$ of T_1 relaxation data of HPHT NDs. Small NDs exhibit a build up with $\alpha = 2/3$ (corresponding to an inhomogeneous distribution of spins). When fitted with a stretched exponential, larger NDs have stretched exponential components of $\alpha = 0.5$ (corresponding to impurity mediated relaxation from a homogenous distribution of spins). Error bars are given by the standard deviation and are shown when they exceed the size of the data point.

The T_1 relaxation times ranged between $T_1 = 6$ s for 18 nm ND to $T_1 = 1$ hr for 2 μm ND. The long T_1 relaxation times measured in the nanodiamonds, indicate that the hyperpolarized state, especially in the core of the nanodiamond, may also have long T_1 relaxation times. These T_1 build up times also indicate how long it may take to build up a hyperpolarized nuclear state when driving with microwaves.

5.2.4 Magic angle spinning studies

Magic angle spinning is a technique used to enhance solid state NMR spectroscopy. Line broadening in solid samples, mainly originating from dipolar interactions, chemical shift anisotropy and quadrupolar interactions, can result in featureless and very wide lines. The dipole-dipole interactions in solids are direction dependent and can be averaged to zero by spinning the sample (at frequencies up to $f = 100$ kHz), at the magic angle $\theta^\circ = 54.74$ about the magnetic field B_0. This narrows the NMR lines, increasing the resolution and allowing for better analysis of NMR spectra. Magic angle spinning was first described by Andrew, Bradbury and Eades in 1958 [191], and independently by Lowe in 1959 [192].

NMR measurements were performed under MAS conditions to examine NMR linewidths and T_1 relaxation times using an MAS probe in a 400 MHz magnet and a Bruker spectrometer. NDs were spun at $f = 13$ kHz and NMR measurements were made using a saturation recovery pulse sequence.

MAS spectra of HPHT NDs are shown in Fig. 5.8. The NMR peak, corresponding to sp^3 hybridized carbon (found at 33 ppm), is well described by two lorentzian components; a broad and a narrow component. No sp^2 hybridized carbon (at 120 ppm) is observed. We attribute the broad Lorentzian component of the NMR line to ^{13}C spins near the surface of the diamond, and the narrow Lorentzian component of the NMR line to ^{13}C spins in the core of the diamond.

The line widths of the broad and narrow Lorentzian components stayed approximately constant over the ND size range measured. No comparison can be made about the composition of the broad and narrow components as the diamonds have different T_1 relaxation times and the spectra were not measured at maximum magnetization.

A comparison of the NMR peaks of AO ND and HPHT ND shows that while the narrow Lorentzian component remains constant, the broad Lorentzian component is narrower and decreases, see Fig. 5.9 and Table 5.2. The air oxidation process burns

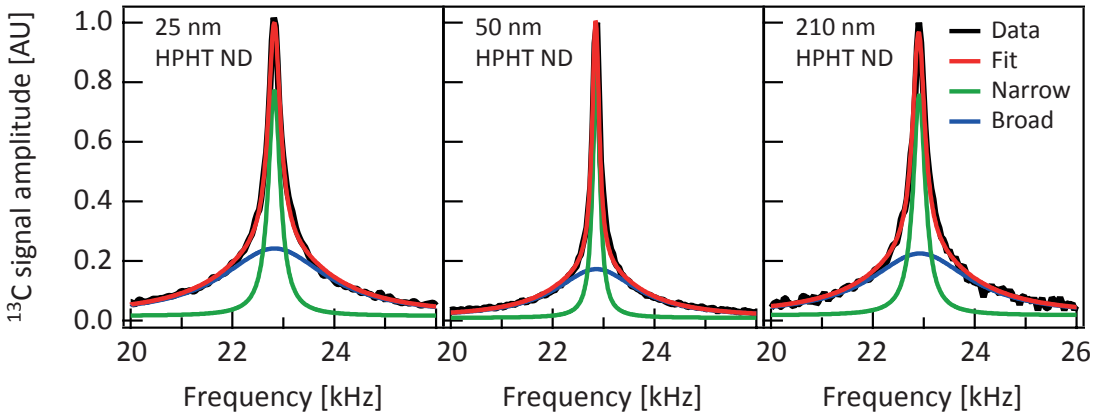

Figure 5.8: MAS NMR spectra of HPHT NDs. From left to right: MAS NMR spectra of 25 nm HPHT ND, 50 nm HPHT ND, and 210 nm HPHT ND. NMR signals were acquired after 1000 s of magnetization build up, and have been normalized. Data is shown in black, a double-Lorentzian best fit to the data is shown in red, and the two Lorentzians comprising the fit are shown in green (narrow component) and blue (broad component).

off the outer layer of ND, decreasing the signal from surface ^{13}C spins.

The MAS T_1 relaxation time was compared for small HPHT and AO NDs, see Fig. 5.9. The total magnetization (dots) has been decomposed into the broad (squares) and narrow (crosses) components of the NMR peak. The T_1 build up times for the AO NDs are slightly shorter than the HPHT NDs, see Table 5.3. We observe a faster T_1 relaxation time for the broad Lorentzian component than the narrow Lorentzian component.

The broad and narrow components comprising the NMR line were examined for a medium sized ND, see Fig. 5.10. The widths of the narrow and broad components do not change with increasing magnetization build up time. Initially 40% of the NMR signal is made up of the broad Lorentzian component, attributed to surface spins and 60% narrow Lorentzian component, originating from core spins, and after a long polarization build up time, 85% of the NMR signal is made up of core spins and 15% of surface spins, see inset Fig. 5.10b. We observe a double exponential T_1 build up for each of the Lorentzian components, see Table 5.3.

Similarly to results under static conditions, the T_1 relaxation time increases with particle size however the T_1 relaxation time measured under MAS conditions are longer

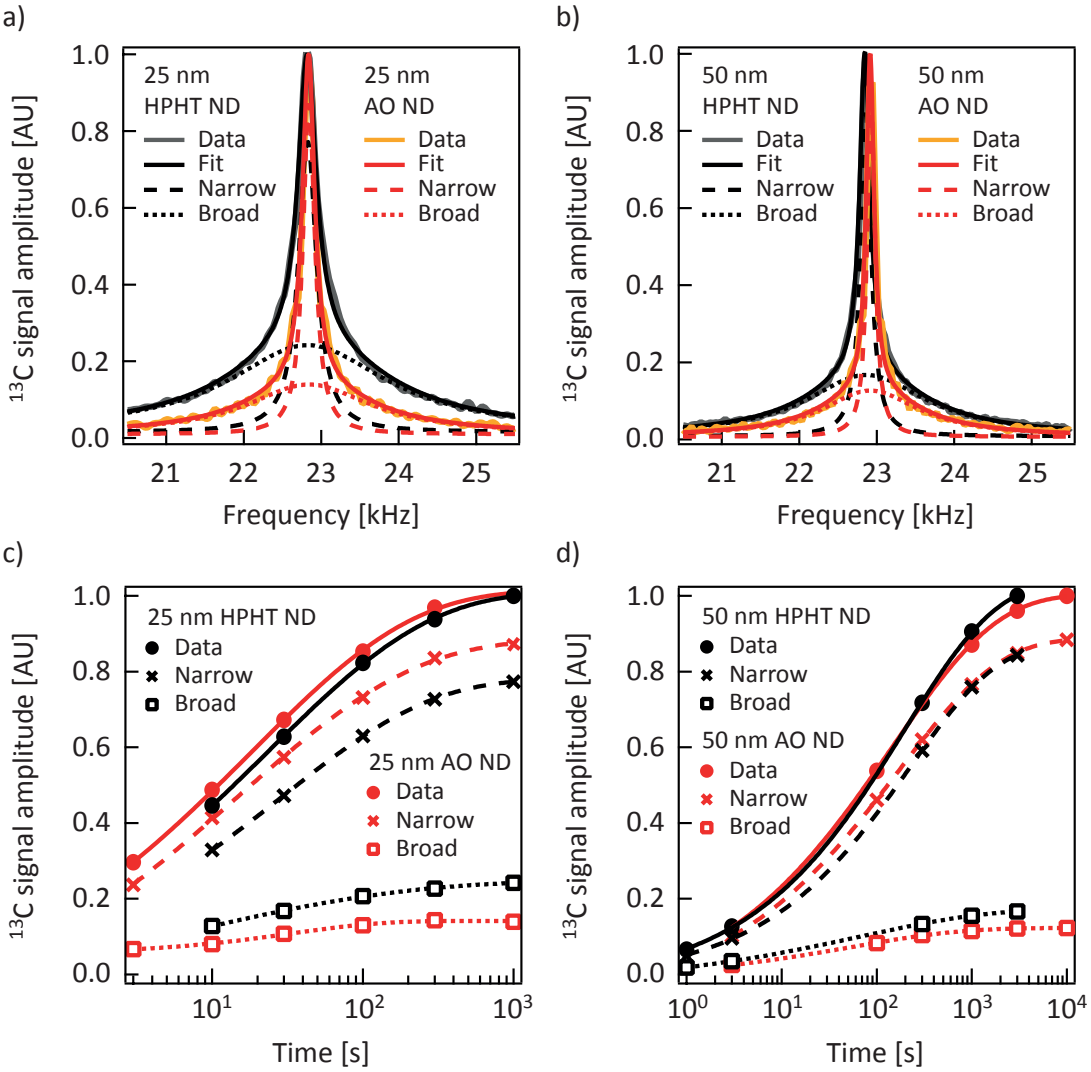

Figure 5.9: MAS NMR spectra and T_1 comparison between small HPHT and AO NDs. a, b) Comparison of the MAS NMR spectra of HPHT ND (grey) and AO ND (orange) for **a)** 25 nm ND, and **b)** 50 nm ND. The double lorentzian fit is shown in black for HPHT ND and red for AO ND. The best fit is shown as a solid line, the broad Lorentzian component is shown as a dotted line, and the narrow Lorentzian component is shown as a dashed line. The largest difference in the spectra comes from a reduction in the broad component for AO ND. **c, d)** Comparison of the T_1 MAS magnetization build up for HPHT ND (black) and AO ND (red) for **c)** 25 nm ND, and **d)** 50 nm ND. The total magnetization is shown in dots, the magnetization of the narrow Lorentzian component is shown in crosses and the magnetization of the broad component is shown in squares. Lines are stretched exponential fits to the data. Data has been normalized to one for comparison, and errors are smaller than the symbols used.

ND particle	Linewidth (narrow) [kHz]	Linewidth (broad) [kHz]
25 nm HPHT	0.285	2.50
25 nm AO	0.187	1.96
50 nm HPHT	0.167	1.95
50 nm AO	0.123	1.53
210 nm HPHT	0.290	2.37

Table 5.2: Linewidths of NDs measured under MAS conditions. Line widths of the broad and narrow Lorentzian components of the ^{13}C NMR signal after 1000 s of magnetization build up.

ND particle	Total		Narrow		Broad	
	T_1 [s]	α	T_1 [s]	α	T_1 [s]	α
25 nm HPHT	24	0.40	29	0.44	5.0	0.27
25 nm AO	19	0.42	15	0.37	34	0.74
50 nm HPHT	190	0.45	220	0.47	65	0.32
50 nm AO	150	0.40	170	0.40	55	0.38
ND particle	Total		Narrow		Broad	
	τ_1 [s]	τ_2 [s]	τ_1 [s]	τ_2 [s]	τ_1 [s]	τ_2 [s]
210 nm HPHT	8900	320	9300	350	7400	270

Table 5.3: Summary of the T_1 relaxation times measured under MAS conditions. T_1 relaxation times for the broad and narrow Lorentzian components and total magnetization measured under MAS conditions. Stretched exponential curves were fitted to the 25 nm and 50 nm NDs (T_1 and α values tabulated) and a double exponential was fitted to the 210 nm ND (with two build up times τ_1 and τ_2 tabulated). We see an increase of T_1 with particle size, a small decrease in the T_1 of AO NDs, and a shorter T_1 of the broad component than the narrow component.

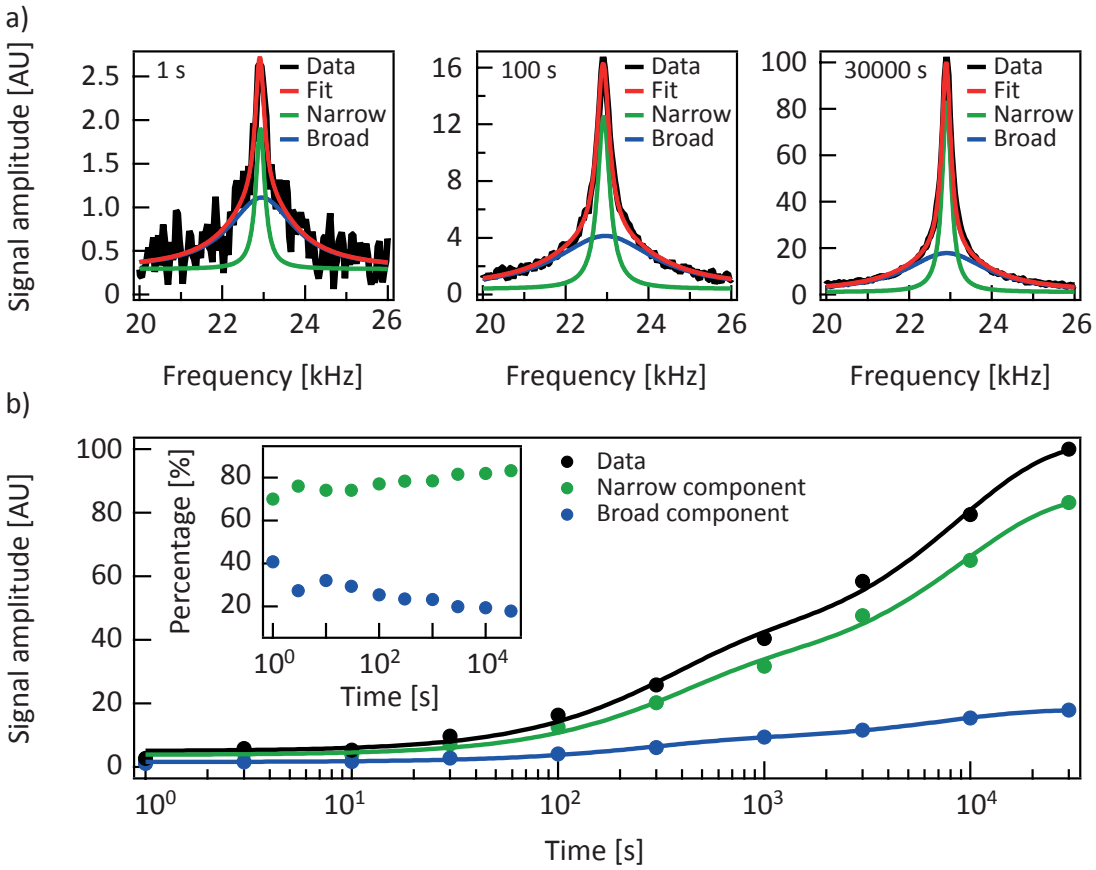

Figure 5.10: MAS NMR spectra and T_1 build up of 210 nm HPHT ND. a) NMR spectra of 210 nm HPHT ND. From left to right: NMR spectrum at 1 s, 100 s, and 30,000 s. **b)** MAS T_1 build up. Solid lines are double exponential fits to the data. Inset: Percentage of the total NMR signal that is made up by the broad Lorentzian component and the narrow Lorentzian component. Errors are smaller than the symbols. Same colour scheme as in Fig. 5.8.

than those measured under static conditions. This could be either due to MAS measured at a higher field ($B = 10$ T compared to static NMR measured at $B = 7$ T), or due to the suppression of spin diffusion under MAS conditions.

The longer T_1 relaxation times indicate that while spin diffusion is largely suppressed in the nanodiamond lattice, there is still some transfer of energy through this pathway. This is important for understanding relaxation mechanisms in hyperpolarized nanodiamonds, and how spin polarization can be transferred from the impurity to spins in the core of the diamond.

5.2.5 ESR studies

Electron spin resonance is a spectroscopic technique used to study the free electrons in atoms and molecules by observing the resonance frequencies of the paramagnetic species. The concepts behind ESR are analogous to those of NMR. When placed in a magnetic field, electronic Zeeman splitting occurs, and the paramagnetic species absorb energy at the resonance frequencies. ESR was first observed independently by Zavoisky [193] and Bleaney [194] in 1944.

To measure an ESR spectrum, typically a sample is placed in a magnetic field, and microwaves are applied at a fixed frequency f to probe the energy levels. The magnetic field is varied, which changes the energy splitting of the Zeeman levels. When the energy gap matches the microwave frequency, spins are driven between the two energy levels, and a resonance condition is observed. The change in absorbed microwave power (measured as a cavity response) as a function of the change in magnetic field is recorded, and constitutes an ESR spectrum. Integrating the spectrum results in the power absorbed by the paramagnetic species, and integrating the absorption spectrum results in the number of spins making up the feature. Most ESR spectra are measured at X-band frequencies (between $f = 9$ and 10 GHz) at a magnetic field of approximately $B = 0.35$ T.

The width and position of the ESR line yield information about the electron's environment and how free the electron is (denoted by the g-factor) respectively. In particular, for this work, ESR studies yield information about the defects found in nanodiamonds, and the particular energy and frequency of the electronic transitions ($f = \omega_e$), which in turn yields information about which frequencies can be used to drive electron-nuclear flip-flop transitions and hyperpolarize the diamond ($f = \omega_e \pm \omega_n$).

Additionally to being the source of hyperpolarization, the defect sites are the primary source of ^{13}C T_1 relaxation, and a detailed understanding of the electronic defects is important for maximizing hyperpolarization conditions with minimal relaxation.

The ESR measurements were performed on a Bruker EMX-plus X-Band ESR spectrometer, with a Bruker rectangular cavity at room temperature. Approximately 100 mg of each ND (as a dry powder) was placed in a 4 mm diameter suprasil tube. The cavity was tuned for each sample, and the Q-factor ranged from $Q = 5000$ (for small NDs) to $Q = 10000$ (for large NDs). The spectrometer frequency ranged between $f = 9.852 - 9.854$ GHz. To ensure no signal distortion or power broadening, spectra were acquired with parameters: modulation amplitude $B_{\mathrm{mod}} = 1$ Gs, modulation frequency $f_{\mathrm{mod}} = 100$ kHz, conversion time $t = 15.06$ ms, time constant $t = 0.01$ ms and power $P = 0.25$ µW (59 dB attenuation).

All NDs exhibited features at $B \sim 348$ mT, $B \sim 351.5$ mT, and $B \sim 355$ mT, see Fig. 5.11. The ESR spectra comprise three components: a broad spin-1/2 lorentzian component (black), attributed to carbon dangling bonds near the surface of the diamond, a narrow spin-1/2 lorentzian component (yellow), attributed to defects within the diamond lattice, see Fig. 5.2, and a P1 centre component (green), see Fig. 5.3c. The P1 centre component has three peaks (the central $m_I = 0$ transition and two hyperfine transitions $m_I = \pm 1$) due to the hyperfine coupling between the ^{14}N spin-1 nucleus and the free electron of the substitutional nitrogen atom.

Each component was simulated in Easy Spin [195] and added together to make the final simulated spectrum (red). The linewidth, g-factor and amplitude, of each component, were varied and the best fit was found using a least squares analysis. The g-factors remained constant over all HPHT NDs measured, with $g_{P1\ centre} = 2.0016$, and $g_{narrow} = g_{broad} = 2.0023$.

The total number of spins in the NDs decreased as particle size increased, see Fig. 5.12a. This trend is also seen for the surface spins (broad spin-1/2 component) and for the defects within the diamond (narrow spin-1/2 component). In contrast the number of P1 centre defects increases as particle size increases. This can be explained by smaller diamonds having a higher surface to volume ratio (with more surface spins and less core spins) than larger diamonds.

The line widths of the three components comprising the ESR spectra, remained constant across all particle sizes, indicating that all NDs show similar electronic defects,

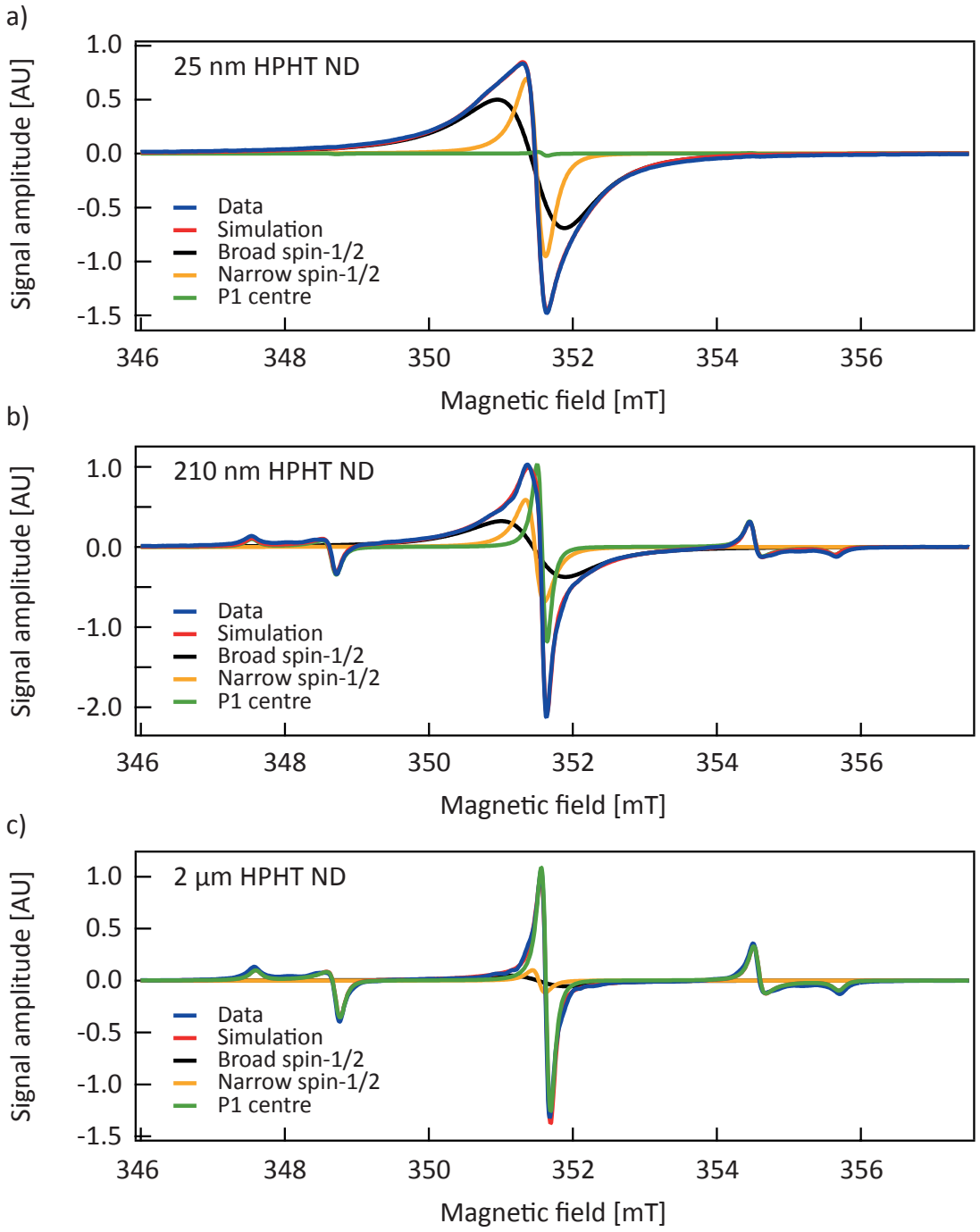

Figure 5.11: ESR spectra of HPHT NDs. ESR spectrum of **a)** 25 nm HPHT ND **b)** 210 nm HPHT ND and, **c)** 2 µm HPHT ND. Data (blue) is simulated (red) with three components: a broad spin-1/2 component (black) a narrow spin-1/2 component (yellow) and a P1 centre component (green). Fit parameters are linewidth, relative intensity and g-factor. The spectrometer frequency was $f = 9.853$ GHz (25 nm ND, 210 nm ND), or $f = 9.854$ GHz (2 μm ND).

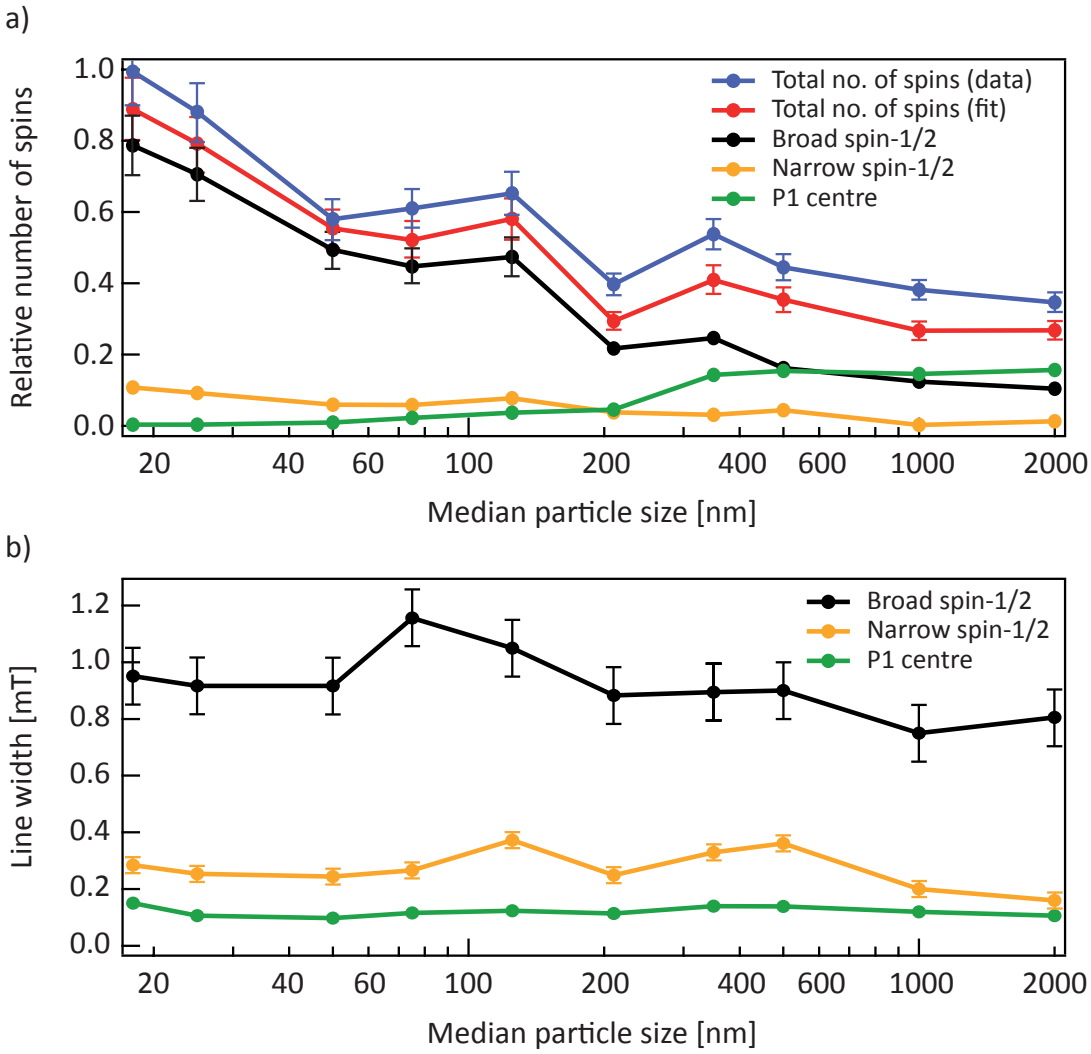

Figure 5.12: ESR spectra simulation results of HPHT NDs. a) Relative number of spins a function of particle size. Individual components (same colour scheme as in Fig. 5.11) were integrated to determine the number of spins. The total number of spins, the broad spin-1/2 component and the narrow spin-1/2 component decreases with increasing particle size while the number of P1 centres increases as ND particle size increases. Data was normalized to the highest electron signal (18 nm ND). **b)** Line widths of the simulated components of the ESR spectra. The linewidths stay constant over the particle size range measured. Error bars (shown when larger than the data points) are extracted from the best fit to the ESR data, and are approximately 10%.

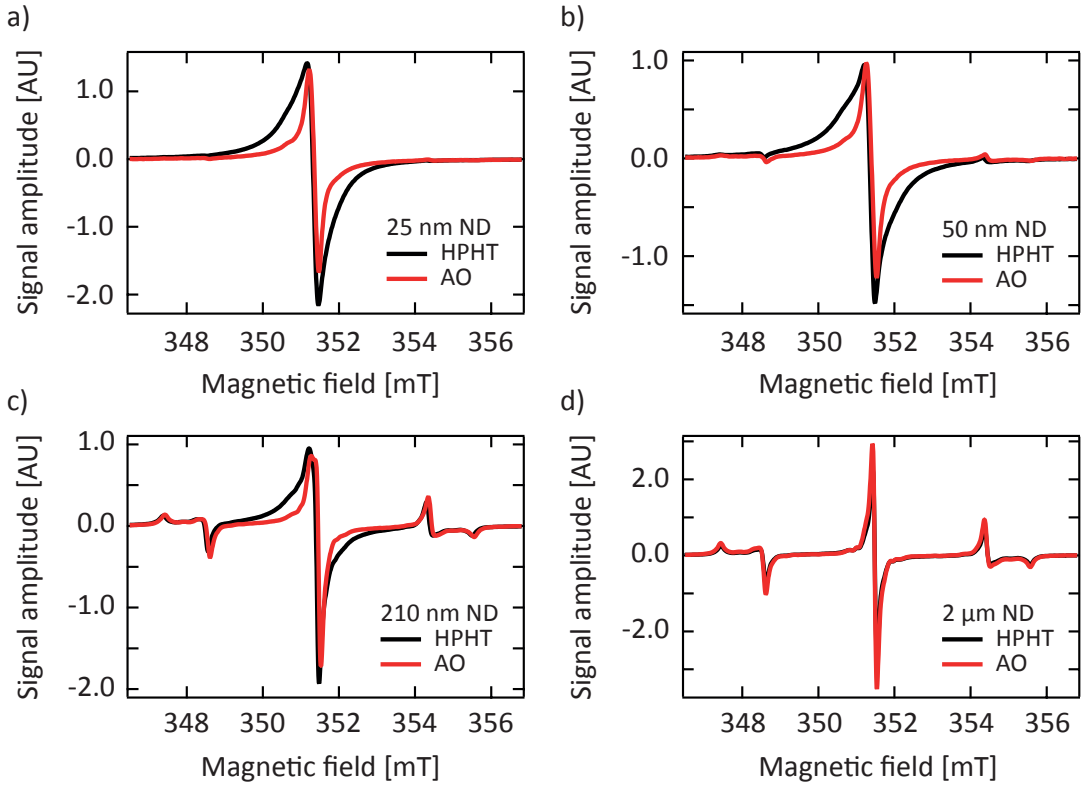

Figure 5.13: Comparison of ESR spectra of HPHT and AO NDs. ESR spectra of HPHT ND (black) and AO ND (red) compared for **a)** 25 nm ND, **b)** 50 nm ND, **c)** 210 nm ND, and **d)** 2 µm ND. For small NDs, the AO ND ESR spectra are narrower than the HPHT ND spectra, while for larger NDs there is no difference between the ESR spectra of HPHT and AO NDs. The spectrometer frequency was $f = 9.852\,\mathrm{GHz}$ (25 nm ND), or $f = 9.853\,\mathrm{GHz}$ (50 nm ND, 210 nm ND, 2 μm ND).

see Fig. 5.12b.

The air oxidation process etches away the surface of the nanodiamond, removing surface spins, reducing the total number of free electrons and narrowing the ESR spectra, see Fig. 5.13 and Fig. 5.14.

The largest difference in ESR spectra is seen for small NDs, such as the 25 nm ND, while no difference is seen for large NDs such as the 2 µm ND. For small NDs the relative amount of broad component is reduced by a factor of 3 in the case of AO ND compared to HPHT ND. The narrow component decreases slightly, and the P1 centre component does not change after air oxidation. The change is most evident for small diamond due to the large surface to volume ratio and abundance of surface spins.

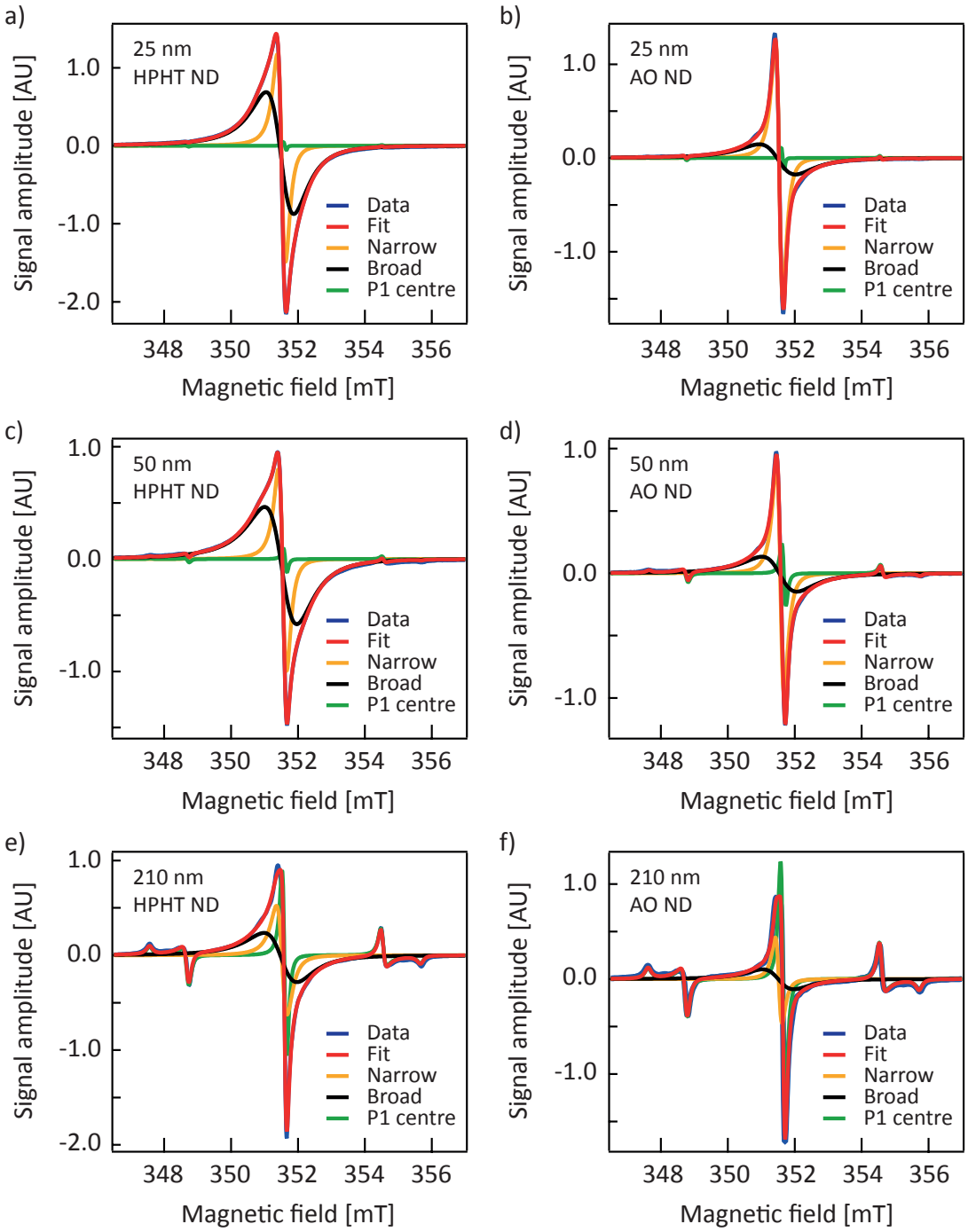

Figure 5.14: Comparison of the components comprising the ESR spectra of small HPHT and AO NDs. ESR spectra of **a)** 25 nm HPHT ND, **b)** 25 nm AO ND, **c)** 50 nm HPHT ND, **d)** 50 nm AO ND, **e)** 210 nm HPHT ND, and **f)** 210 nm AO ND. Same colour scheme as in Fig. 5.11. The AO process reduced the amount to surface spins (as can be seen in the decrease of the broad spin-1/2 component). The narrow spin-1/2 component changed only slightly, and the P1 centre component remained unchanged. See Fig. 5.13 for the spectrometer frequency used.

ND particle	Narrow spin-1/2			Broad spin-1/2			P1 centre		
	g	spins	lw [mT]	g	spins	lw [mT]	g	spins	lw [mT]
25 nm HPHT	2.0023	0.14	0.236	2.0023	0.86	0.817	2.0016	0.001	0.041
25 nm AO	2.0024	0.11	0.211	2.0024	0.30	1.08	2.0016	0.002	0.040
50 nm HPHT	2.0023	0.09	0.234	2.0023	0.76	0.951	2.0017	0.005	0.078
50 nm AO	2.0025	0.08	0.215	2.0025	0.24	1.04	2.0017	0.015	0.098
210 nm HPHT	2.0024	0.07	0.270	2.0024	0.42	0.930	2.0017	0.090	0.120
210 nm AO	2.0025	0.06	0.243	2.0025	0.14	1.109	2.0017	0.089	0.116

Table 5.4: Summary of the fit component parameters for AO and HPHT NDs. A comparison of the g-factor, relative number of spins and linewidth (lw) of the three components (broad spin-1/2, narrow spin-1/2 and P1 centre) comprising the ESR spectrum for HPTH and AO NDs.

The linewidths of the three components do not change significantly after air oxidation, and the g-factors for the broad and narrow spin-1/2 components increased slightly, see Table 5.4.

An understanding of the ESR spectrum is important for hyperpolarization and choosing the pumping frequency for negative or positive polarization. Changes in the ESR spectrum, such as with air oxidation, can result in changes in the hyperpolarization spectrum of the NDs, and different T_1 and T_2 relaxation pathways for the ^{13}C spins.

An estimate of the electron T_1 relaxation time can be made by measuring the peak to peak signal amplitude of the ESR line as a function of driving microwave power [196]. As the ND ESR spectra comprise three components with different g-factors and linewidths contributing to different parts of the spectra, each component must be examined separately. The peak to peak signal amplitude for the three components are shown in Fig. 5.15. Peak to peak signal saturation is not observed for either the broad or the narrow spin-1/2 components, and we are unable to estimate the electron T_1 relaxation times for any of the spin species. We infer from the saturation curves that the P1 centre has the longest T1 relaxation time, followed by the narrow spin-1/2 component, and then the broad component. AO NDs require more power for saturation, indicating that the electrons have shorter relaxation times in AO NDs than in HPHT NDs, see Fig. 5.15a.

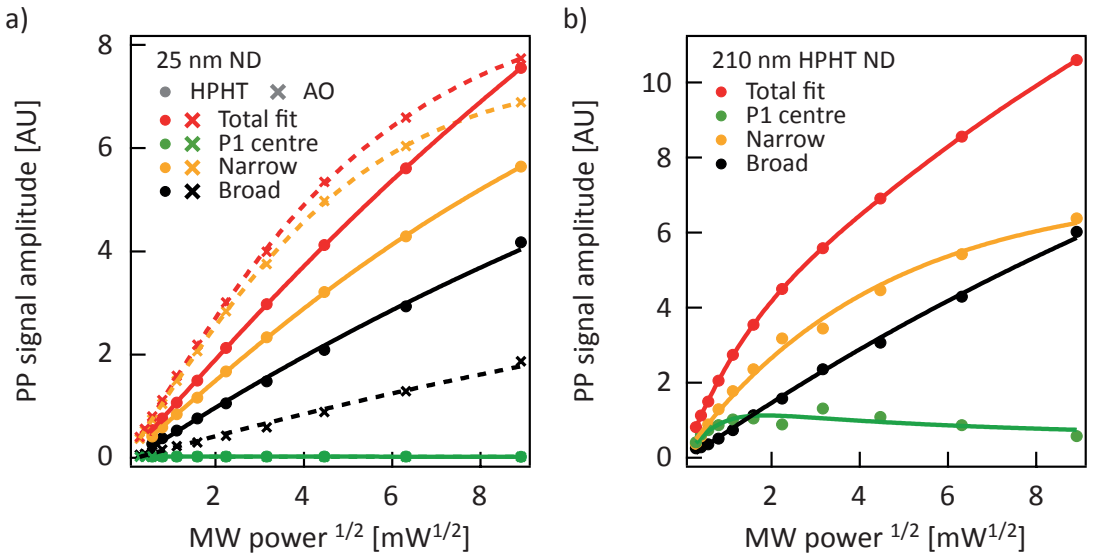

Figure 5.15: Power saturation of the ESR spectrum of ND. The peak to peak signal amplitude as a function of microwave power is shown for **a)** 25 nm HPHT ND (dots) and 25 nm AO ND (crosses), and **b)** 210 nm HPHT ND. The total peak to peak amplitude is shown in red, and the peak to peak signal amplitude of the broad spin-1/2 component, narrow spin-1/2 component, and P1 centre component are shown in black, yellow and green respectively. Lines are a guide to the eye. A difference is seen in the saturation behavior between the AO and HPHT ND. The curves do not reach saturation with the maximum power available.

An understanding of electron relaxation times can give clues to which DNP mechanism will dominate when hyperpolarizing nanodiamonds.

5.2.6 Raman studies

Raman spectroscopy [197] is a spectroscopic technique used to observe vibrational and rotational modes in a molecule or compound. When a system is subject to monochromatic light, the light (usually from a laser) interacts with molecular vibrations, phonons, or other excitations in the system, resulting in inelastic scattering, and thus shifts in the laser frequency. These shifts in energy give direct information about the vibrational modes in the system.

In Raman spectroscopy, a sample is illuminated with laser light, and scattered light is collected with a lens and monochromator and dispersed onto a detector.

Raman spectroscopy was used to examine the vibrational modes in NDs, in par-

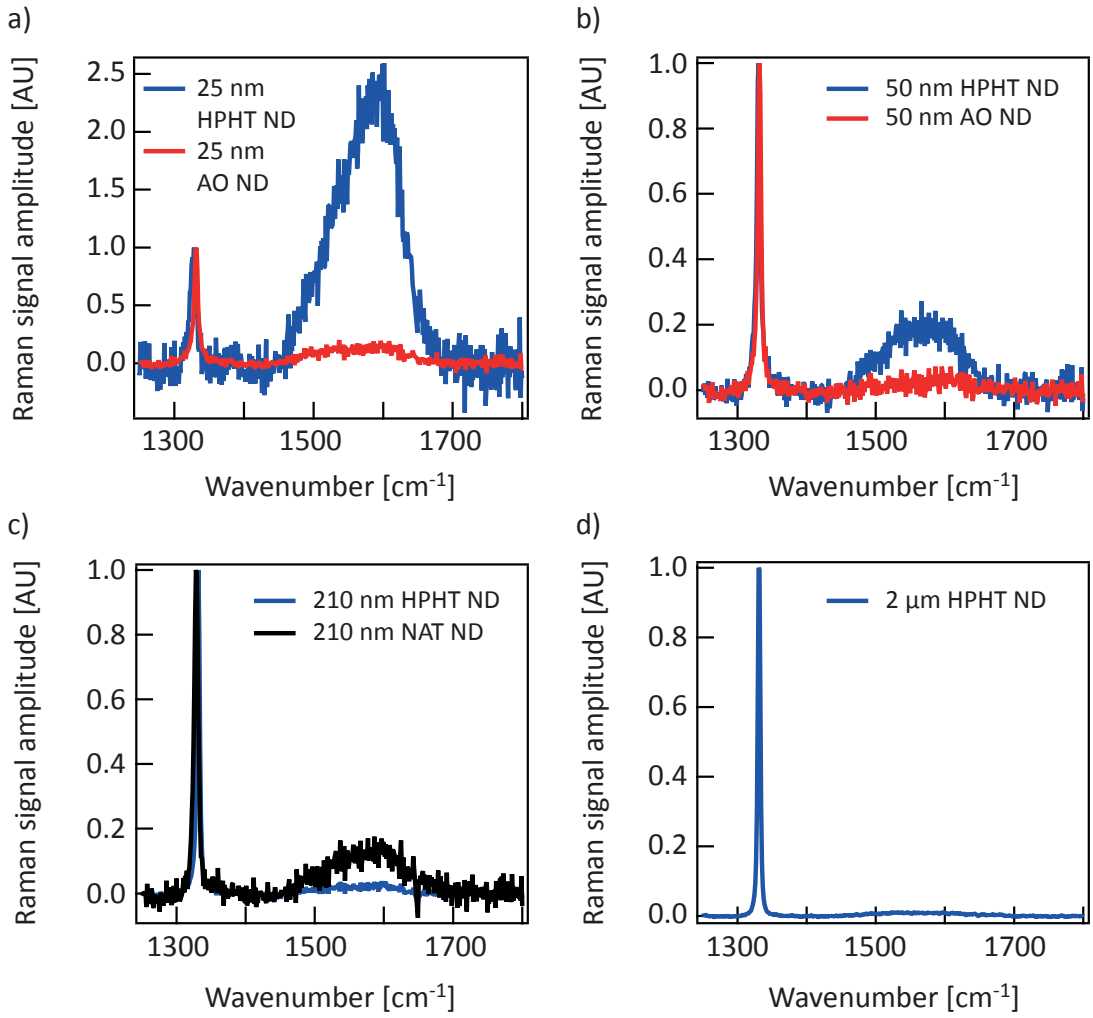

Figure 5.16: Raman spectroscopy of ND. a) Comparison of 25 nm AO (red) and 25 nm HPHT (blue) ND and **b)** comparison of 50 nm AO (red) and 50 nm HPHT (blue) ND. For both the 25 nm ND and 50 nm ND, the AO ND has a much smaller signal from sp^2 hybridized carbon, found on the surface of ND. **c)** Comparison of 210 nm HPHT ND (blue) and 210 nm NAT ND (black). **d)** Raman spectrum of 2 µm HPHT ND. A baseline subtraction was performed on the spectra to remove signal from the fluorescence of diamond, and the spectra are normalized to the sp^3 hybridized peak at $\tilde{\nu} \sim 1330$ cm^{-1}.

ticular to examine the sp^2 and sp^3 phase composition and surface groups, see Fig. 5.16. A Renishaw inVia Raman microscope with laser light at an excitation wavelength $\lambda = 488\,\text{nm}$ and power $P = 50\ \mu\text{W}$ was used to measure the Raman spectra.

The peaks at $\tilde{\nu} \sim 1330\ \text{cm}^{-1}$ and $\tilde{\nu} \sim 1590\ \text{cm}^{-1}$ correspond to sp^3 hybridized (tetrahedral) nanodiamond, and sp^2 hybridized nanodiamond respectively [20]. Although there is more sp^3 hybridized carbon than sp^2, the cross sectional area for sp^2 hybridized diamond is larger than that for sp^3 hybridized diamond (50-250 times at $\lambda = 514.5\,\text{nm}$ [198–200]), resulting in a more prominent peak.

The ratio of sp^2/sp^3 hybridized diamond decreases as particle size increases, as the sp^2 hybridized diamond is mainly found on the surface of the ND, and smaller NDs have a higher surface to volume ratio than larger NDs.

The air oxidation process etches away the diamond surface, removing sp^2 hybridized carbon from the diamond surface, see Fig. 5.16a, 5.16b, resulting in more diamond phase in the NDs and a cleaner diamond surface. The amount of sp^2 hybridized carbon dropped by a factor of 15 for 25 nm ND and a factor of 5 for 50 nm ND.

We observe that the NAT ND has a higher sp^2/sp^3 ratio than HPHT ND, see Fig. 5.16c, which could be due to surface treatments that were performed on the diamonds after the ball-milling size reduction process.

The Raman spectroscopy confirms that the AO process is etching away the surface of the diamond, while leaving the core of the diamond unchanged. The Raman spectrum also confirms that we have crystalline diamond in the HPHT, AO and NAT NDs, with minimal graphitic carbon.

5.3 Summary

NMR, ESR, MAS, SEM and Raman studies were performed to characterize various NDs. T_1 relaxation in ND is dominated by paramagnetic impurities. Small NDs have a T_1 relaxation behavior well described by a stretched exponential, corresponding to relaxation by an inhomogeneous distribution of defects, while large NDs have a relaxation better described by a double exponential. T_1 relaxation times of up to 1 hour are measured. The main defects in NDs are P1 centres, spin-1/2 surface defects and spin-1/2 core defect. Air oxidation of the ND etches away the surface and removes surface spin-1/2 defects. MAS studies showed a double Lorentzian line shape to the

NMR peak, attributed to ^{13}C surface spins and ^{13}C core spins. Raman studies showed sp^2 hybridized carbon on the surface of the ND that can be removed with air oxidation. Understanding the electronic and nuclear characteristics in important for understanding polarization build up and relaxation pathways of the hyperpolarized state, and hyperpolarization mechanisms.

6

Hyperpolarized nanodiamond with long spin-relaxation times

E. Rej, T. Gaebel, T. Boele, D.E.J. Waddington and D. J. Reilly

ARC Centre of Excellence for Engineered Quantum Systems, School of Physics, The University of Sydney, Sydney, NSW 2006, Australia

The use of hyperpolarized agents in magnetic resonance (MR), such as ^{13}C-labeled compounds, enables powerful new imaging and detection modalities that stem from a 10,000-fold boost in signal. A major challenge for the future of the hyperpolarization technique is the inherently short spin relaxation times, typically less than 60 seconds for ^{13}C liquid-state compounds, which limit the time that the signal remains boosted. Here, we demonstrate that 1.1% natural abundance ^{13}C spins in synthetic nanodiamond (ND) can be hyperpolarized at cryogenic and room temperature without the use of free-radicals, and, owing to their solid-state environment, exhibit relaxation times exceeding 1 hour. Combined with the already established applications of NDs in the life-sciences as inexpensive fluorescent markers and non-cytotoxic substrates for gene and drug delivery, these results extend the theranostic capabilities of nanoscale diamonds into the domain of hyperpolarized MR[1].

[1]This chapter is adapted from Rej et al. *Hyperpolarized nanodiamond with long spin-relaxation times.* Nature Communications **6**, 8459 (2015).

6.1 Introduction

Nanoparticles, having found use in the treatment of cancers [1,2], the study of autoimmune diseases [3], and cardiovascular affections [4], are currently of interest as theranostic agents needed for the advent of personalised medicine [201]. These nanoscale systems are expected to integrate imaging, tracking, and monitoring capabilities with targeted delivery of compounds to tumours, cellular functions and processes, or specific organs. Especially powerful is the modality established by combining high-resolution magnetic resonance imaging (MRI) with nanoparticles that have been hyperpolarized to act as contrast agents, as has been achieved recently using silicon compounds [38, 202].

Nanodiamonds (ND) are well-suited to act as theranostic platforms, having demonstrated an innate compatibility with biological environments and low toxicity in comparison to other nanoscale structures [17, 18]. The readily modifiable surface, which is easily functionalized [19], has enabled NDs to be conjugated to specific molecules [21], opening a plethora of biomedical applications that include pharmaceutical delivery [18,23,24,203] and intracellular tracking [26] based on the unique optical properties of defects in the diamond lattice [21]. A particular defect, the nitrogen-vacancy (NV) colour centre, has also established a sensitive means of detecting minute magnetic fields on the nanoscale using methods pioneered in controlling quantum devices [27,28,204]. Beyond luminescence-based techniques however, approaches to non-invasively detect and image diamond nanoparticles in vivo have to date, been lacking.

Standard MRI modalities (operating at few Tesla magnetic fields) are not well suited to resolving weak concentrations of ND in vivo since diamond is a dilute spin system (1.1% ^{13}C) and carbon has a small gyromagnetic ratio. This limitation can, in principle, be overcome using hyperpolarization techniques [44] which can result in a 10,000-fold boost in signal over that from typical thermal polarization conditions [36, 37]. Hyperpolarized molecular compounds such as [1-^{13}C]pyruvate, for example, have recently been used to study tumour metabolism in humans by first transferring electron spin polarization to ^{13}C nuclei at cryogenic temperatures [43].

In these liquid-state compounds, hyperpolarized ^{13}C spins typically relax to thermal equilibrium on timescales T_1 less than 60 seconds [44]. In contrast, bulk, high-purity diamond can exhibit ^{13}C T_1 times of many hours [46] and recent work using optical techniques to manipulate NV centres [47–50] has produced significant polarization in

large single-crystal samples. The challenge therefore is to maintain these long spin lifetimes even when diamond is produced in nanoparticle form and in sufficient quantities to be of clinical relevance. Addressing this challenge requires a detailed understanding of particle size effects, the structure of internal crystal defects, contaminants, and spin-relaxation channels that arise from the nanoparticle surface [51, 52, 189, 190]. Balancing these constraints, the hyperpolarization mechanism also requires the presence of unpaired electrons which, in the case of liquid ^{13}C compounds are typically added to the agent in the form of organic free-radicals.

In the present work we extend the opportunity for deploying nanodiamond in life-science applications by demonstrating its suitability as a MR marker and contrast agent for MRI. Using electron spin resonance (ESR) we observe that inexpensive commercially available ND, produced via the high pressure high temperature (HPHT) process, surprisingly exhibits a suitable balance of paramagnetic centres from defects and surface dangling bonds to allow both hyperpolarization and the preservation of long spin relaxation times. In comparison to previous results on detonation ND [189, 190], the ^{13}C relaxation data reported here exhibits a 1,000-fold extension in T_1 together with signal enhancements that compare favorably with hyperpolarized ^{13}C liquid-state compounds. Particle size is found to significantly effect both the relaxation time and amount of achievable hyperpolarization, opening the possibility of selectively detecting NDs of a particular size distribution.

In addition to showing significant hyperpolarization at $T = 4$ K, we demonstrate that a sizeable signal enhancement is also possible at liquid nitrogen (77 K) and room temperature using dynamic nuclear polarization (DNP), alleviating the need for expensive liquid helium and potentially enabling new in vivo modalities. Finally, we examine the spin dynamics of the ND core and its surface using hyperpolarized states to resolve new phenomena associated with defects in this versatile material system.

6.2 ESR spectra and nuclear spin relaxation

Turning to the experimental results, SEM images (see Fig. 6.1a, Fig. 5.4, and Fig. 5.5) and the ESR spectrum and simulation results (see Fig. 6.1b) for a representative ND sample are shown. The ESR spectrum, which indicates the predominant types of defects available for use in hyperpolarization, can be seen to comprise three components

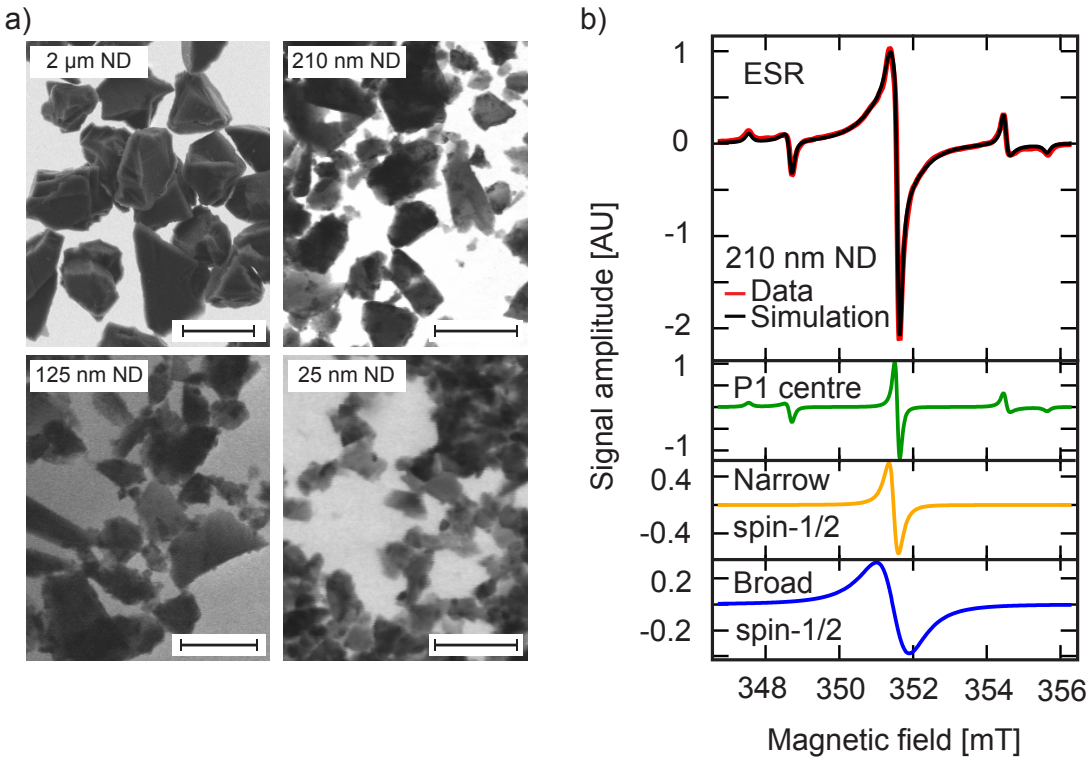

Figure 6.1: ESR and SEM of nanodiamond. **a)** Electron micrographs of various sized NDs used in this work. Top left: scale bar = 2 μm, top right: scale bar = 400 nm, bottom left: scale bar = 200 nm, bottom right: scale bar = 100 nm. **b)** ESR spectrum of 210 nm ND (red). The black line is a simulated spectrum consisting of three components: a narrow spin-1/2 component (yellow) a broad spin-1/2 component (blue) and a P1-centre component (green). Each of the three components were simulated separately using Easyspin [195] and added together to make the final spectrum.

that sum to produce the black simulation curve in Fig. 6.1b. These are a broad spin-1/2 Lorentzian component (blue trace) attributed to carbon dangling bonds near the surface of the ND, a narrow spin-1/2 Lorentzian component (yellow trace) attributed to defects within the diamond lattice, and a component associated with P1-colour centres (green trace) which constitutes a substitutional nitrogen atom with the extra electron hyperfine coupled to the ^{14}N spin-1 nucleus. The number of P1 centre impurities, which lead to central ($m_{\mathrm{I}} = 0$) and hyperfine transitions ($m_{\mathrm{I}} = \pm 1$), increases as ND size increases, while the number of spin-1/2 impurities (broad and narrow spectra) decreases as ND size increases (see Fig. 5.11 and Fig. 5.12).

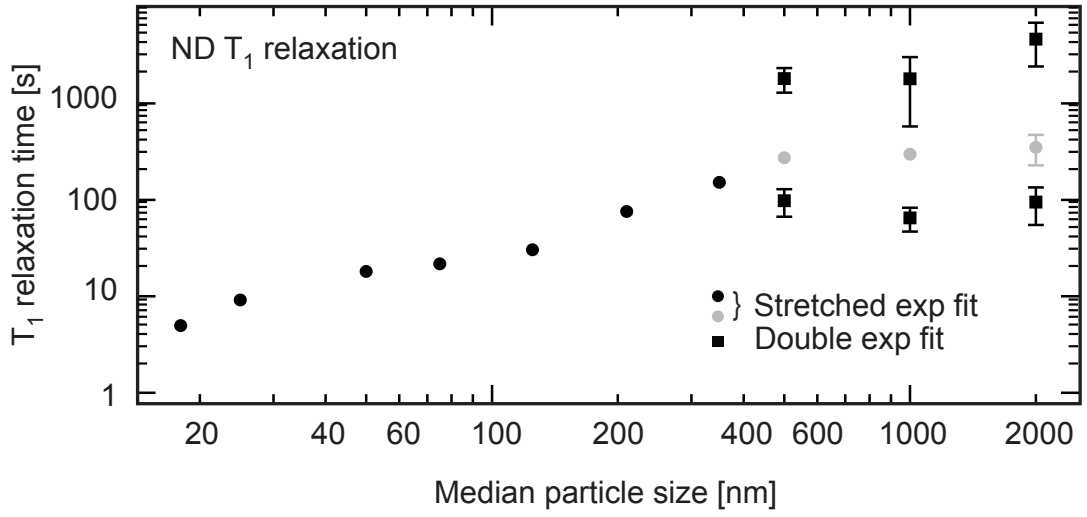

Figure 6.2: Room temperature ^{13}C relaxation times, T_1, as a function of diamond particle size at $B = 7$ T. Relaxation times were measured using the saturation recovery method with build-up time of magnetization M determined by fitting a stretched exponential $\mathrm{M} = M_0(1-\exp(-(t/T_1)^{\alpha})$ or double exponential. Small NDs exhibit a buildup with $\alpha = 2/3$ (black circles), with larger NDs better fitted by a stretched exponential with $\alpha = 1/2$ (grey circles) or double exponential fits with a long and short component shown as black squares. Error bars are given by the standard deviation and are shown when they exceed the size of the data point.

These defect sites also provide the primary mechanism for ^{13}C nuclear spin relaxation in ND. We find that the T_1 relaxation time grows with increasing particle size, as shown in Fig. 6.2. In determining these T_1 times, the spin polarization build-up for smaller diamonds is well described by models [176,179] in which the dipolar interaction of nuclear spins with paramagnetic impurities dominates over nuclear spin diffusion, leading to polarization curves that follow a stretched exponential form [see Section 6.8]. Diamond particles with average diameter approaching 1 μm however, are better characterized by a double exponential in their polarization build-up with time. For 2 μm diamonds the longer component of the double exponential yields a T_1 time of 63 min (see Section 6.8, Fig. 5.6 and Fig. 5.7).

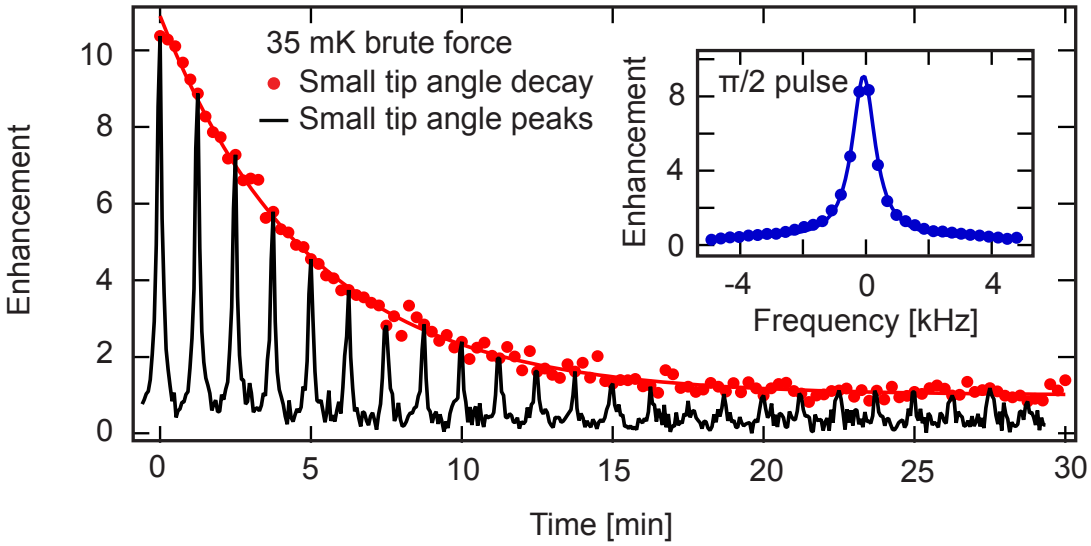

Figure 6.3: Brute force hyperpolarization of ND. Enhanced signal following brute-force hyperpolarization of 2 μm ND at $T = 35$ mK and $B = 4$ T for 3 days in a dilution refrigerator. Following a 40 s transfer in a field of 630 mT, detection is at $B = 7$ T, via a $\pi/2$-pulse (inset) with decay ($T_1 \sim 53$ min) measured via a sequence of small tip angles (main panel).

6.3 Brute-force hyperpolarization

The simplest method of increasing the MR signal from ND is to first cool the system to low temperatures in a high magnetic field to increase the Boltzmann population difference in the nuclear spins, a process termed brute-force polarization. If the NDs are subsequently moved to a different magnetic field and temperature, the spin system can be considered hyperpolarized until it thermalizes on timescale T_1. Using the brute force method we hyperpolarize 2 μm ND at $T = 35$ mK and $B = 4$ T in a dilution refrigerator fitted with a rapid sample exchange system that allows fast (< 1 min) transfer of the ND sample to a room temperature $B = 7$ T spectrometer for detection. A $\pi/2$ pulse applied immediately after transfer produces a signal (see inset Fig. 6.3) that is enhanced by an order of magnitude when compared to the signal from 2 μm ND at thermal equilibrium and $B = 7$ T. To measure the relaxation time a series of small tip-angles is used to destroy the polarization over 0.5 hours, as indicated by the decaying signal in Fig. 6.3. The decay is a combination of the T_1 relaxation of spins in the ND

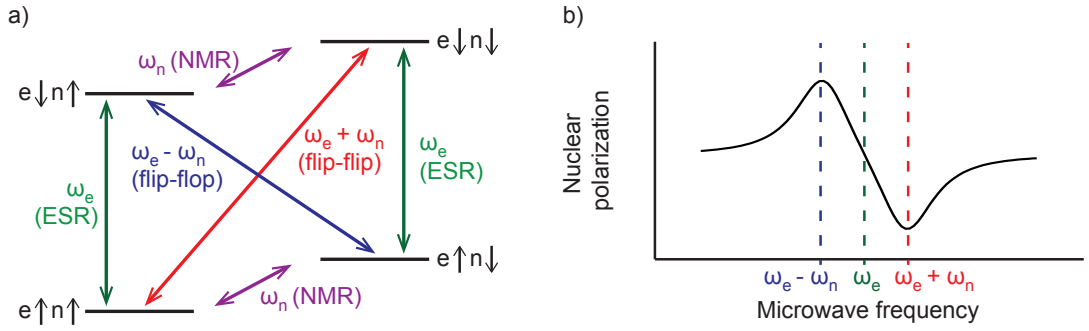

Figure 6.4: DNP via the solid effect used to hyperpolarize ND. a) Energy level diagram for a dipolar coupled electron spin-1/2 and a nuclear spin-1/2 system in a magnetic field. The ESR, NMR, flip-flop and flip-flip transitions are shown. Driven flip-flop transitions (blue) at a frequency $f = \omega_e - \omega_n$ involve a mutual electron flip and a nuclear flop resulting in a positive nuclear polarization, shown in b). Driven flip-flip transitions (red) result in a negative nuclear polarization.

($T_1 \sim 53$ min) and polarization lost from the tipping pulses (see Section 6.8 for details).

6.4 Hyperpolarization via the solid effect

To achieve even higher polarizations and larger signals, DNP [71] can be used to transfer electron polarization to the ^{13}C nuclear spins in the diamond [46]. As described above, the source of these unpaired electrons in ND are paramagnetic centres in the lattice, dipolar coupled to a surrounding nuclear spin bath. Application of a microwave magnetic field slightly below the electron spin resonance frequency can drive spin flip-flops between nuclear and electron spins associated with centres, leading to a net transfer of spin polarization from the electrons to the nuclei near the impurities in a process known as the solid effect (see Fig. 6.4).

Turning to the main results of our work, we demonstrate that DNP can be used to hyperpolarize commercially available NDs, which as we have shown above, also exhibit long relaxation times. In the case of the largest diameter diamonds (2 µm) a $T = 4$ K signal enhancement of ~ 400 is achieved over thermal equilibrium, corresponding to a nuclear polarization of ~ 8 %, as shown in Fig. 6.5. Comparing this hyperpolarized signal to the thermal signal at room temperature gives an enhancement of 13,500 similar to what has been demonstrated with isotopically labeled ^{13}C liquid compounds [44]. We

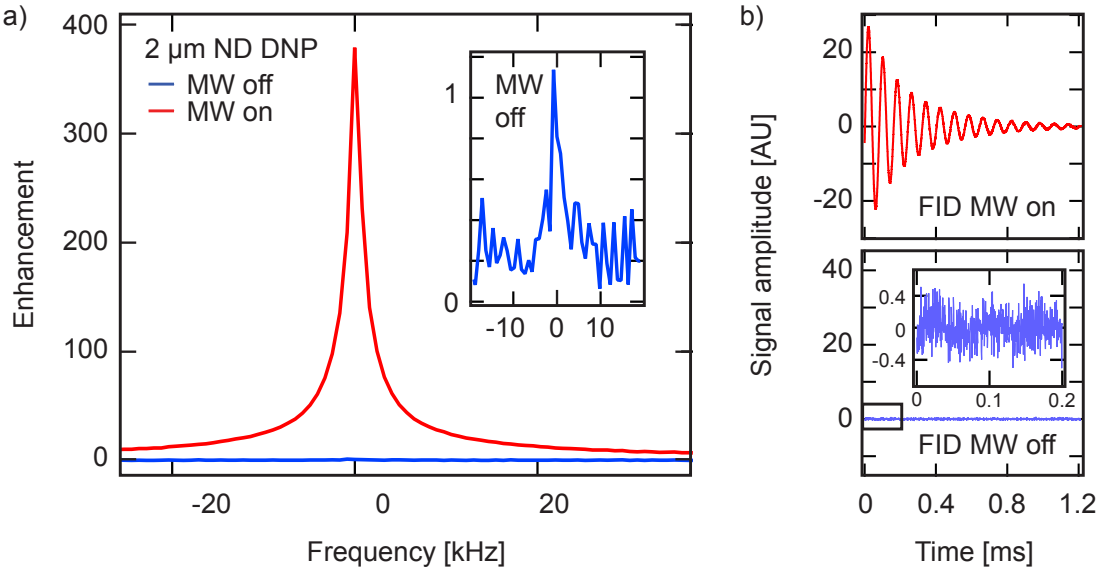

Figure 6.5: NMR signal of hyperpolarized nanodiamond. a) Hyperpolarized signal enhancement of 380 times for 2 µm ND at $T = 4$ K. Inset: Zoom of NMR signal taken at thermal equilibrium ($T = 4$ K) with no microwaves. **b)** NMR free induction decay of 2 µm ND after a $\pi/2$-pulse at $T = 4$ K. Top: Signal after hyperpolarization. Bottom: Thermal polarization signal.

estimate that for a ND concentration of 1 mg mL^{-1}, this amount of hyperpolarization leads to a spatial resolution better than 2 mm × 2 mm in a preclinical MRI scanner (see Section 6.10.1). Note that ND exceeding this concentration has already been used for therapeutic delivery in vivo [24].

It is possible that by hyperpolarizing the nuclear spin system using DNP, new relaxation channels are created that shorten the relaxation time. We test this possibility by first polarizing 2 µm ND for 1 hr and then allowing it to decay for 1 hr at field. The resulting signal, shown in Fig. 6.6a, indicates a T_1 comparable to measurements performed at thermal equilibrium. As a further demonstration of the potential for hyperpolarized ND, we show in Fig. 6.6b that the enhanced polarization can be maintained during transfer of the sample from a lower field polarizer to a high field MR detection system (see Section 6.8 for details).

Unlike hyperpolarized molecular compounds, the use of nanoparticles opens a new modality that links MR signal strength (and relaxation time) to particle size. For hyperpolarized ND, we determine a significant size dependence to the signal enhance-

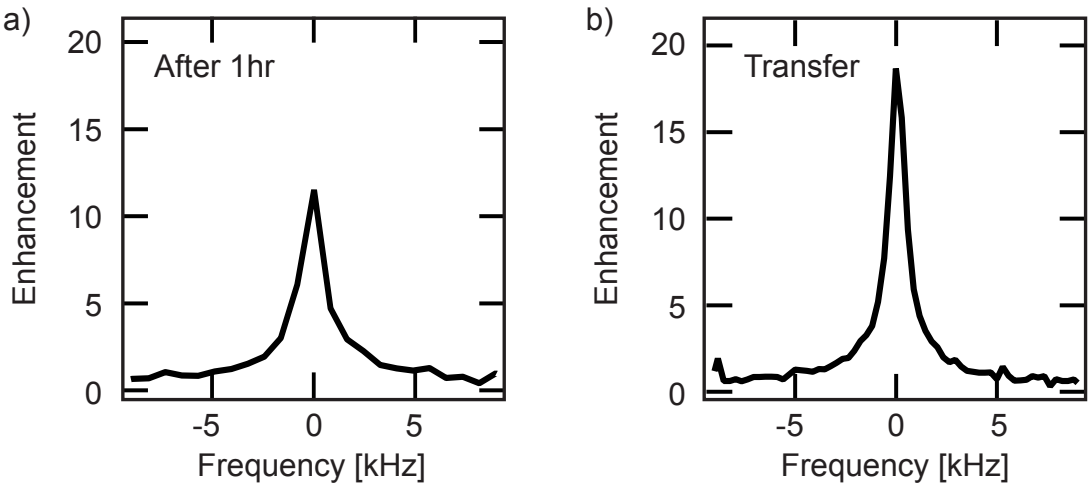

Figure 6.6: Polarization transfer. a) Signal enhancement of 2 μm ND that was polarized for 1 hr and then allowed to decay at field ($B = 3$ T) for 1 hr. **b)** 2 μm ND signal enhancement after transfer from the polarizer to a $B = 7$ T magnet for detection. The 2 μm ND was polarized for 15 min at $T = 4$ K. The transfer took place in a field of $B = 730$ mT and took approximately 15 s.

ment, as shown in Fig. 6.7. This dependence is most prominent for particle sizes below $\sim$300 nm, where the larger rate of spin relaxation competes with the rate at which hyperpolarization from DNP occurs. We suggest that this dependence on the diameter of NDs opens a means of selectively tracking particles based on their size distribution, potentially of use in determining the integrity of permeable barriers and epithelium membranes.

For potential clinical use of hyperpolarized MRI, a major drawback of the technique is the need for liquid helium to cool sample agents during the polarization phase. This drawback is particularly significant for applications that require MR in remote locations, for instance in battlefield MRI using ultra-low magnetic fields. In the case of hyperpolarized ND however, we find that sizeable enhancements are possible at liquid nitrogen temperatures (77 K) (see Fig. 6.7), where cryogens are readily available. Extending this idea, Fig. 6.7 also shows that hyperpolarization is possible at room temperature, doing away with cryogens altogether.

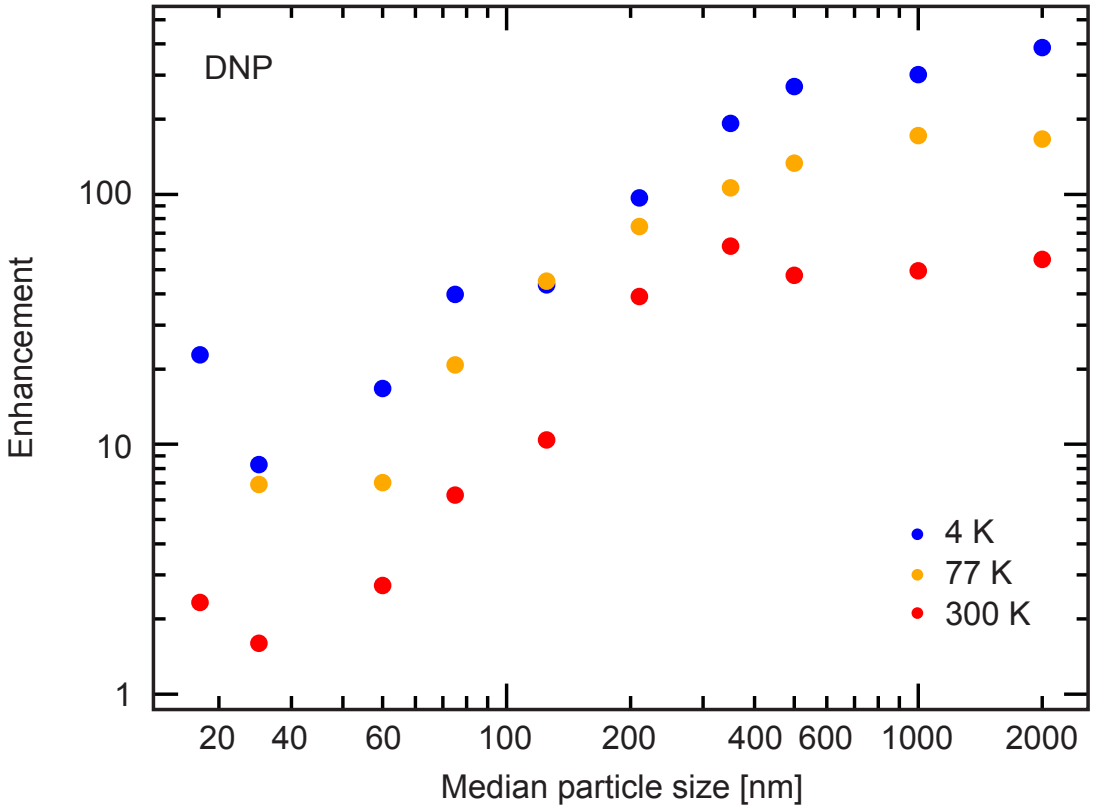

Figure 6.7: DNP enhancement of ND. Signal enhancement as a function of particle size and temperature at $T = 4$ K (blue), 77 K (yellow) and 300 K (red). The enhancement is given by the hyperpolarized signal divided by the thermal signal at each temperature.

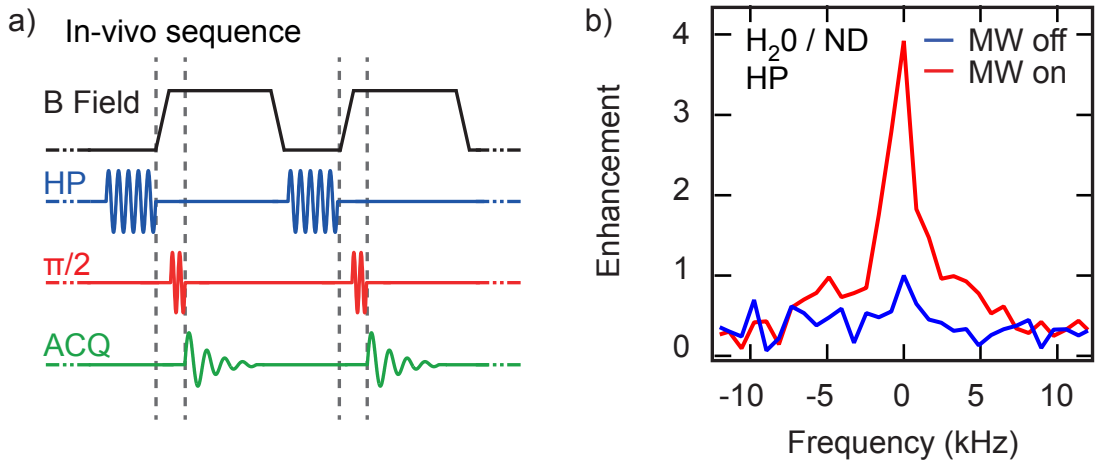

Figure 6.8: Room temperature hyperpolarization in the presence of water. **a)** The combination of room temperature signal enhancement and long relaxation times opens the possibility of in vivo hyperpolarization using a magnetic field shuttling technique. With the ND agents already administered to the bio-system, hyperpolarization is performed at low-field where microwave heating is reduced. The field is then ramped on a timescale much shorter than T_1 to enable imaging and detection of the hyperpolarized ND. Figure shows a repeated sequence with radio frequency $\pi/2$ -pulses and acquisition window (ACQ). **b)** Hyperpolarization in the presence of water, mimicking in vivo conditions. Even at the high microwave frequency of 80 GHz, we observe an enhanced signal (red) of ~ 4 times compared to the thermal polarization (blue).

6.5 Hyperpolarization in the presence of water

Room temperature hyperpolarization, even for modest enhancements, opens the possibility of new modalities that polarize and detect compounds in vivo. The significant barrier to this technique is the heating of water and surrounding tissue during the application of microwaves needed to perform DNP. Polarizing at low magnetic field and microwave frequency however, can significantly reduce heating but requires sufficiently long T_1 times to enable magnetic field ramping between polarization and high-field detection conditions [205]. Hyperpolarized nanodiamond appears well suited to explore this modality, since for example, the signal from 350 nm ND (as a dry powder) can be enhanced by a factor of 40 at room temperature and exhibits a T_1 of several minutes (long enough for field ramping). Since the polarize and detection sequence can be cycled many times in vivo (see Fig. 6.8a), background noise can be averaged well below

the limits imposed by one-shot polarize and detect methods.

To test this modality we hyperpolarize a slurry of 125 nm ND and water (200 μL water with ∼ 50 mg ND) at room temperature. Even in the presence of ∼80 GHz microwaves, we observe a 4-fold enhancement of ^{13}C MR signal from the diamond with little discernible heating of the water (see Fig. 6.8b). This enhancement, which corresponds to a halving of the signal relative to the case without water, suggests that such modalities may be possible for small animals.

6.6 ND impurity selection and surface modification

The results presented so far are for ND samples readily obtained commercially, without further treatment or surface modification. We now turn to examine the role that surface impurities play in both hyperpolarization and relaxation, noting that there is significant scope to tailor the surface chemistry via passivation and treatment [206]. Our approach is to effectively perform ESR spectroscopy at the magnetic field used for DNP ($B \sim 3$ T), by monitoring the NMR signal enhancement as a function of microwave frequency, see Fig. 6.9a and Fig. 6.10. At room temperature we observe enhancement spectra consisting of four peaks that are in agreement with the low-field ESR data shown in Fig. 6.1b. The position of these peaks correspond to DNP processes at $f = \omega_e \pm \omega_n$. As the temperature is lowered, these distinct peaks become dipolar broadened. The high field DNP spectra are similarly broadened as the particle size is increased, as shown in Fig. 6.9b.

Modifying the defects or the types of defects within the nanodiamonds can change the DNP spectra, leading to enhanced polarization and longer relaxation times. We find that burning off the outer layer of ND using air oxidation (AO) processes [175] removes some of the broad spin-1/2 component associated with impurities near the surface of the ND. This can be seen in Fig. 6.9c where we compare the hyperpolarization spectra of 25 nm AO ND (black) with standard 25 nm ND (grey) (see Fig. 6.11 for larger NDs). The oxidation process leads to a suppression of the two central lines (f_2, f_3) in the spectrum, consistent with removing some of the surface impurities that would otherwise contribute to the signal.

By adjusting the microwave frequency for DNP, we can select different impurity

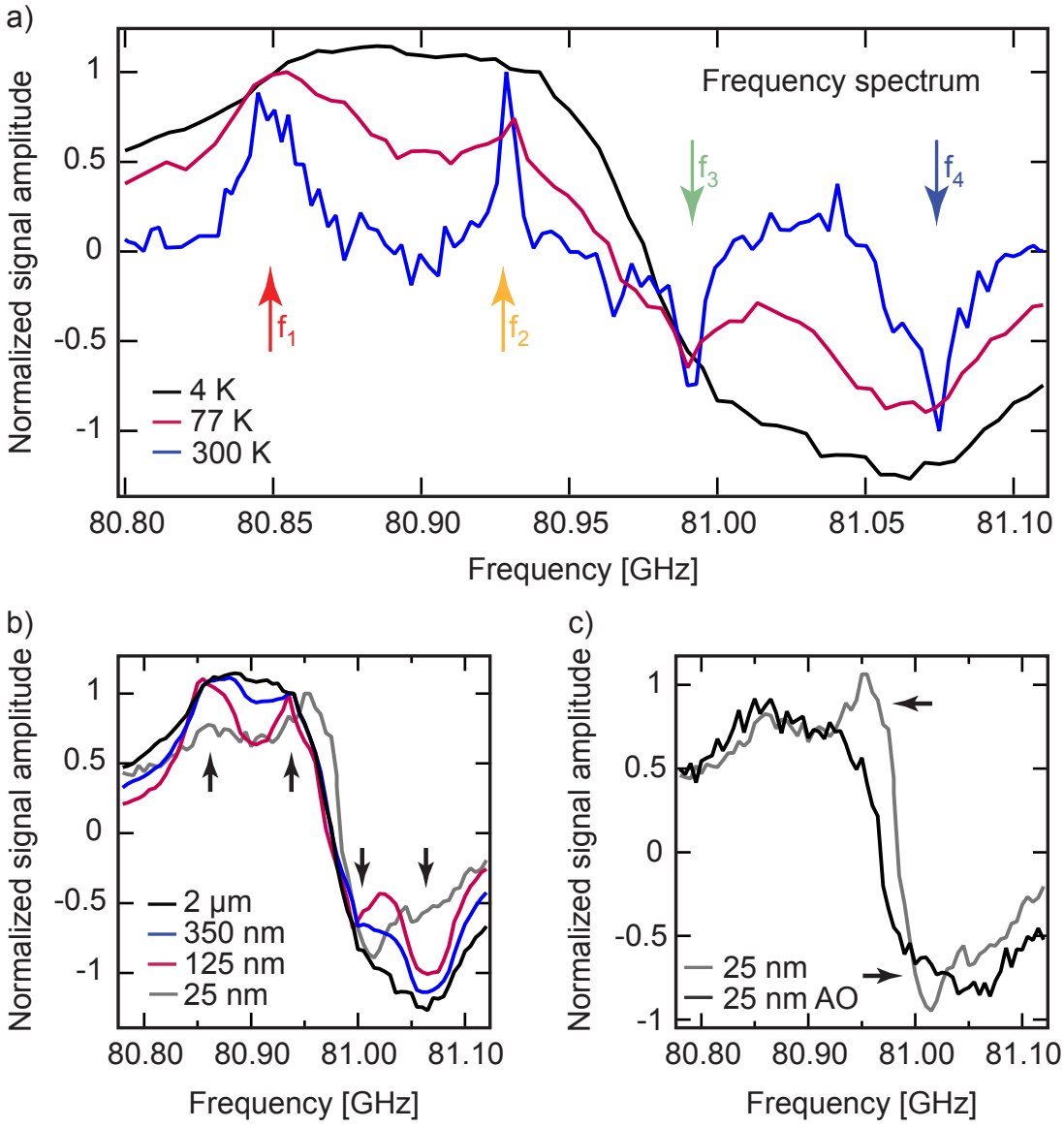

Figure 6.9: ND impurity selection and surface modification. a) Hyperpolarized signal of 2 µm ND as a function of polarization frequency at $T = 4$ K (black), 77 K (purple) and 300 K (blue). The arrows indicate the four frequencies at which polarization build up and decay were examined. The traces were normalized to 1. Note the features broaden as temperature decreases. **b)** Normalized hyperpolarized signal of 2 µm ND (black), 350 nm ND (blue), 125 nm ND (purple), and 25 nm ND (grey) at $T = 4$ K as a function of microwave frequency. More features are visible as the particle size decreases. **c)** Comparison of the hyperpolarized signal amplitude as a function of frequency for 25 nm ND and 25 nm AO ND.

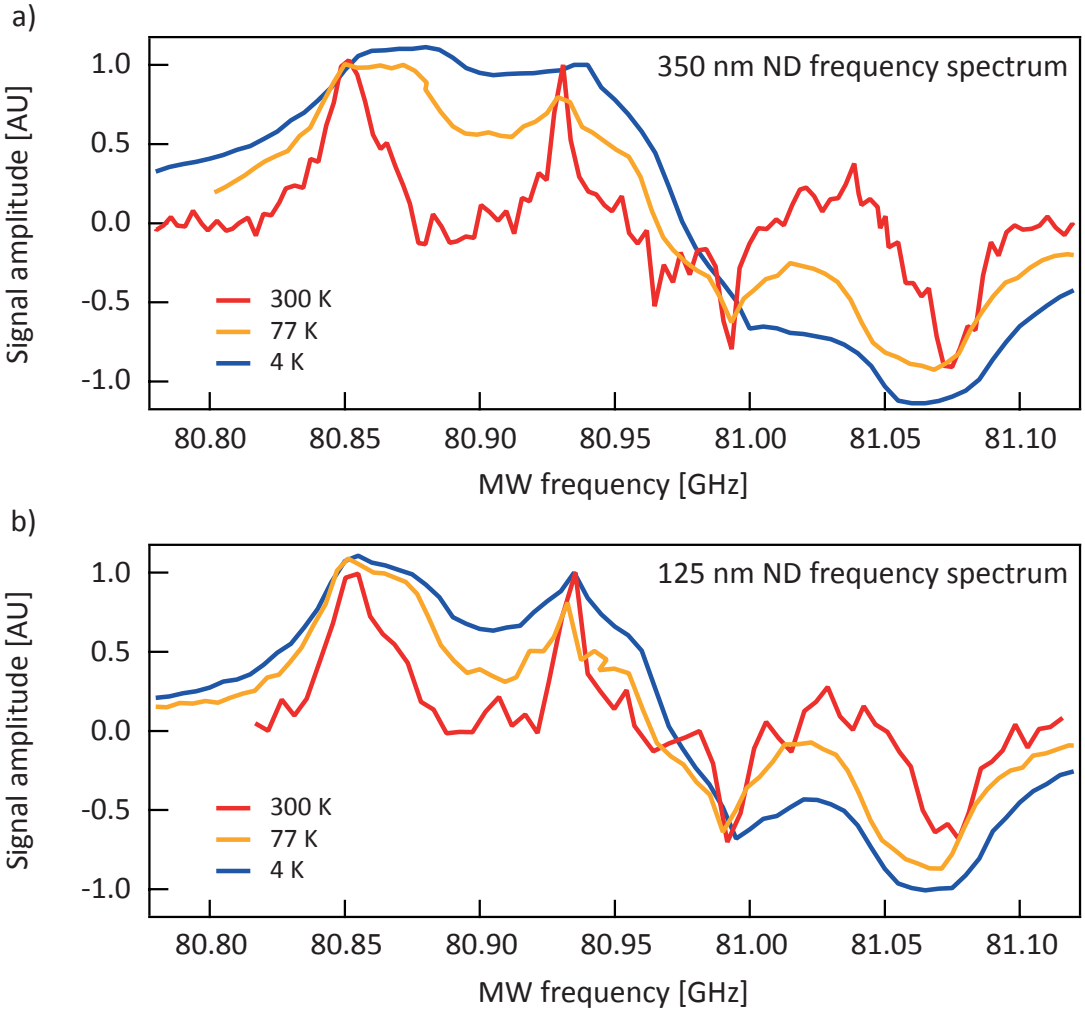

Figure 6.10: Hyperpolarized signal as a function of polarization frequency at various temperatures. Hyperpolarized spectra of **a)** 350 nm ND, and **b)** 125 nm ND at $T = 300$ K (red), 77 K (yellow), and 4 K (blue). The traces have been normalized to 1. The features appear at the same frequencies for all NDs examined. The peaks broaden with decreasing temperature, and broaden as particle size increases.

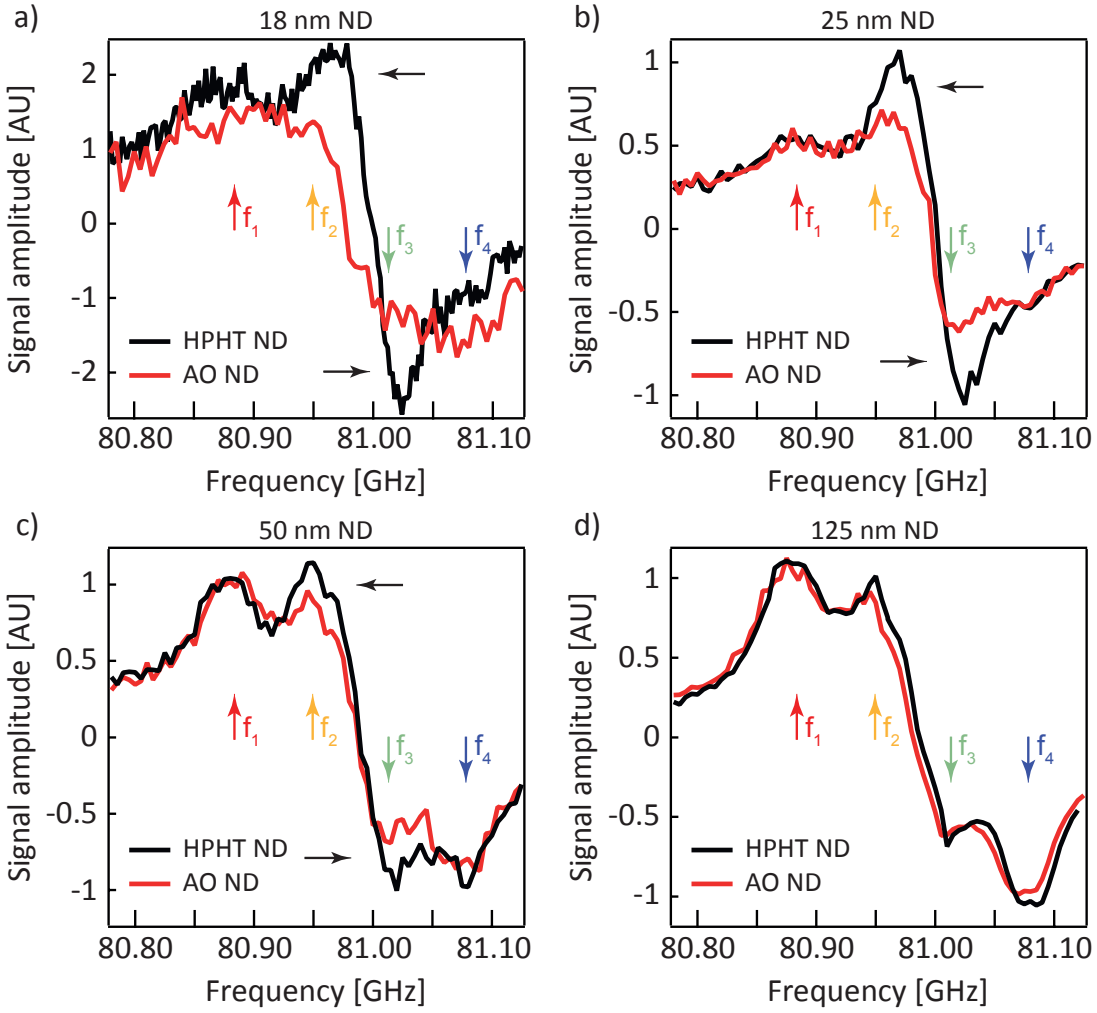

Figure 6.11: Comparison of the hyperpolarization spectrum for small HPHT and AO NDs. ^{13}C signal amplitude were measured at $T = 4$ K after 30 seconds of polarization of HPHT NDs (black) and AO NDs (red). The signals have been normalized to the peak at $f = 80.880$ GHz. Differences in the hyperpolarization spectra at the central transitions (yellow and green) are more pronounced for smaller NDs (18 nm and 25 nm) and not present for larger diamonds (125 nm ND). Frequency shifts between the spectra are due to the differing g-factors and concentrations of paramagnetic impurities in the AO NDs.

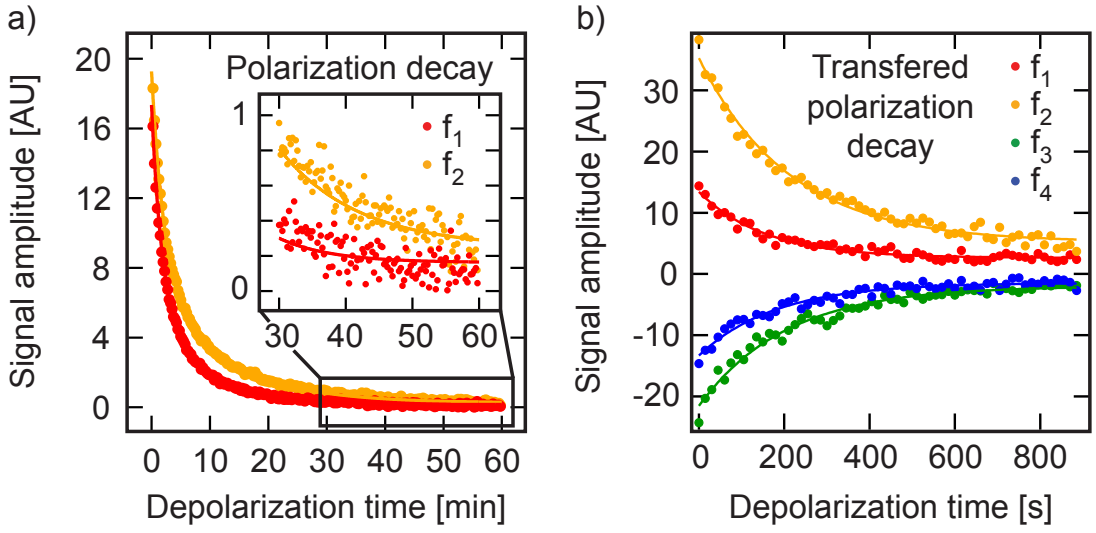

Figure 6.12: Depolarization of the hyperpolarized signal. a) Depolarization of the hyperpolarized signal of 350 nm ND at $T = 4$ K using a small tip angle pulse sequence ($\theta = 3.5°$, $TR = 15$ s). The ND was polarized for 180 minutes at the frequencies indicated by the arrows in Fig. 6.9a. We see a difference in the decay times of the red trace ($f_1 = 80.870$ GHz, $T_1 = 12$ s, 2.1 s) and the yellow trace ($f_2 = 80.930$ GHz, $T_1 = 16$ s, 2.5 s). Data has been multiplied by $cos(\theta)^{n-1}$ to take into account the polarization lost due to the small tip angle. Fits to the data (solid lines) are double-exponential decay curves. **b)** Depolarization of the signal from 350 nm ND after hyperpolarization for 15 min at $T = 4$ K at the four frequencies indicated by arrows in Fig. 6.9a and transfer to a $T = 7$ T magnet for detection. The decay was examined using a small tip angle sequence ($\theta = 8°$, $TR = 15$ s). Data is shown in red ($f_1 = 80.870$ GHz, $T_1 = 157$ s), yellow ($f_2 = 80.925$ GHz, $T_1 = 250$ s), green ($f_3 = 80.990$ GHz, $T_1 = 190$ s) and blue ($f_4 = 81.050$ GHz, $T_1 = 157$ s).

sites for use in hyperpolarization. Polarization via the P1 centres, for instance, can be selected by irradiating at the frequencies corresponding to the outer peaks (f_1, f_4) in Fig. 6.9a. This is in contrast to irradiating at the inner peaks (f_2, f_3) which also comprise both narrow and broad components from spin-1/2 sites (see discussion of Fig. 6.1b).

Surprisingly, we find that hyperpolarization due to microwave driving at the inner peaks takes longer to build up and is retained longer than when driving at the outer peaks associated with the P1 centres. This behaviour is seen in Fig. 6.12a and Fig. 6.13, where for 350 nm ND, we compare the decay of hyperpolarization established by driving at peak f_1 or peak f_2 in Fig. 6.9a (polarization build up at various frequencies can

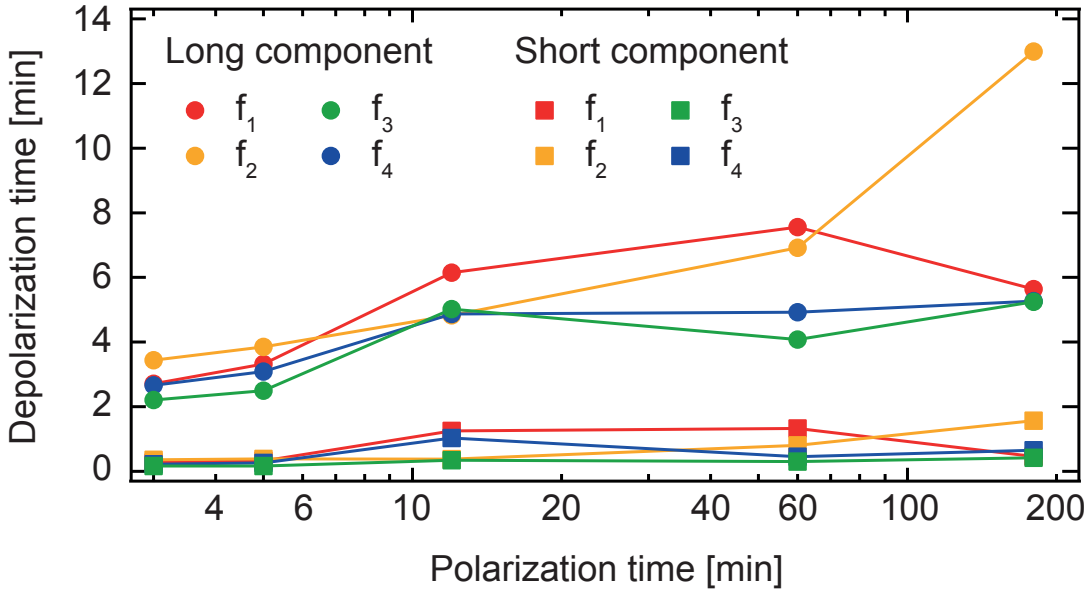

Figure 6.13: Depolarization of hyperpolarized nanodiamond. Depolarization time of the hyperpolarized signal in 350 nm ND at T = 4 K, measured using a small tip angle pulse sequence (θ = 3.5°, TR = 15 s) after the ND was polarized for various times at $f_1 = 80.87$ GHz (red), $f_2 = 80.93$ GHz (yellow) $f_3 = 80.99$ GHz (green) and $f_4 = 81.05$ GHz (blue). The depolarization data was fitted with a double exponential function, taking into account polarization lost due to the small tip angle, with the best fit parameters τ_1 (squares) and τ_2 (circles) plotted. We observe an increase in depolarization time for longer polarization times.

be seen in Fig. 6.14, Fig. 6.15, Table 6.1 and Table 6.2, and a comparison of ND and AO ND can be seen in Fig. 6.16). These results suggest that nuclear spin diffusion is somewhat suppressed in these systems, since relaxation appears dominated by the particular impurities selected for polarization via the choice of microwave frequency.

Beyond examining the spin dynamics of ND, these results are of practical interest in optimizing conditions for maximum signal enhancement with minimal relaxation. As an example, we compare the signal from 350 nm ND, initially irradiated with microwaves at the four distinct frequencies indicated in Fig. 6.9a and then subsequently transferred to a $B = 7$ T system for detection. Following sample transfer, the relaxation data in Fig. 6.12b show that a larger polarization is maintained if the nuclei were polarized using the two central spectra peaks (f_2 and f_3), in comparison to the outer peaks associated with the P1 centres (f_1 and f_4).

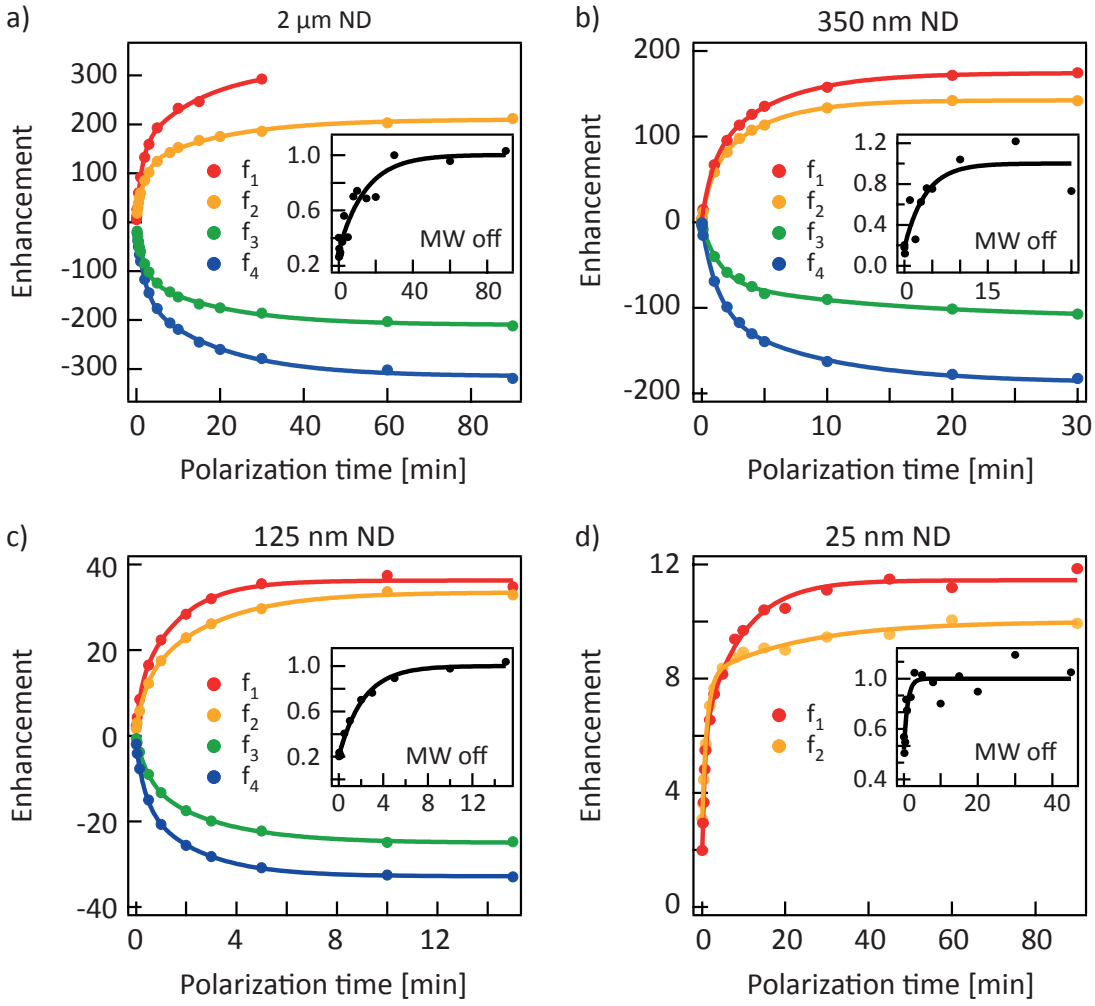

Figure 6.14: Hyperpolarization build up in ND at T = 4 K. Enhancement as a function of polarization time, normalized to the saturated magnetization taken with no microwave power (insets) in ND. Polarization build up was measured using a saturation recovery pulse sequence at the four frequencies f_1 (red), f_2 (yellow), f_3 (green), and f_4 (blue) indicated by arrows in Fig. 6.9a. Data is shown for **a)** 2 µm ND, **b)** 350 nm ND, **c)** 125 nm ND, and **d)** 25 nm ND. Data is shown in dots and double exponential fits to the data are shown in solid lines. T_1 relaxation times are summarized in Table. 6.1.

Particle size	Frequency [GHz]	$T_{1,\text{short}}$ [min]	$T_{1,\text{long}}$ [min]
2 µm ND	$f_1 = 80.880$	1.3	16
	$f_2 = 80.940$	1.9	19
	$f_3 = 81.000$	1.9	19
	$f_4 = 81.060$	2.0	19
	MW off	$T_1 = 14$	
350 nm ND	$f_1 = 80.870$	0.8	5.2
	$f_2 = 80.940$	0.7	4.2
	$f_3 = 81.000$	1.4	14
	$f_4 = 81.060$	1.0	6.0
	MW off	$T_1 = 4$	
125 nm ND	$f_1 = 80.880$	0.2	1.6
	$f_2 = 80.945$	0.4	2.8
	$f_3 = 81.005$	0.48	2.8
	$f_4 = 81.075$	0.34	2.2
	MW off	$T_1 = 2.2$	
25 nm ND	$f_1 = 80.880$	0.6	9
	$f_2 = 80.955$	1.1	22
	MW off	$T_1 = 1.0$	

Table 6.1: Hyperpolarization build up using saturation recovery. Summary of the fit parameters for hyperpolarization build up in ND at $T = 4$ K using a saturation recovery pulse sequence.

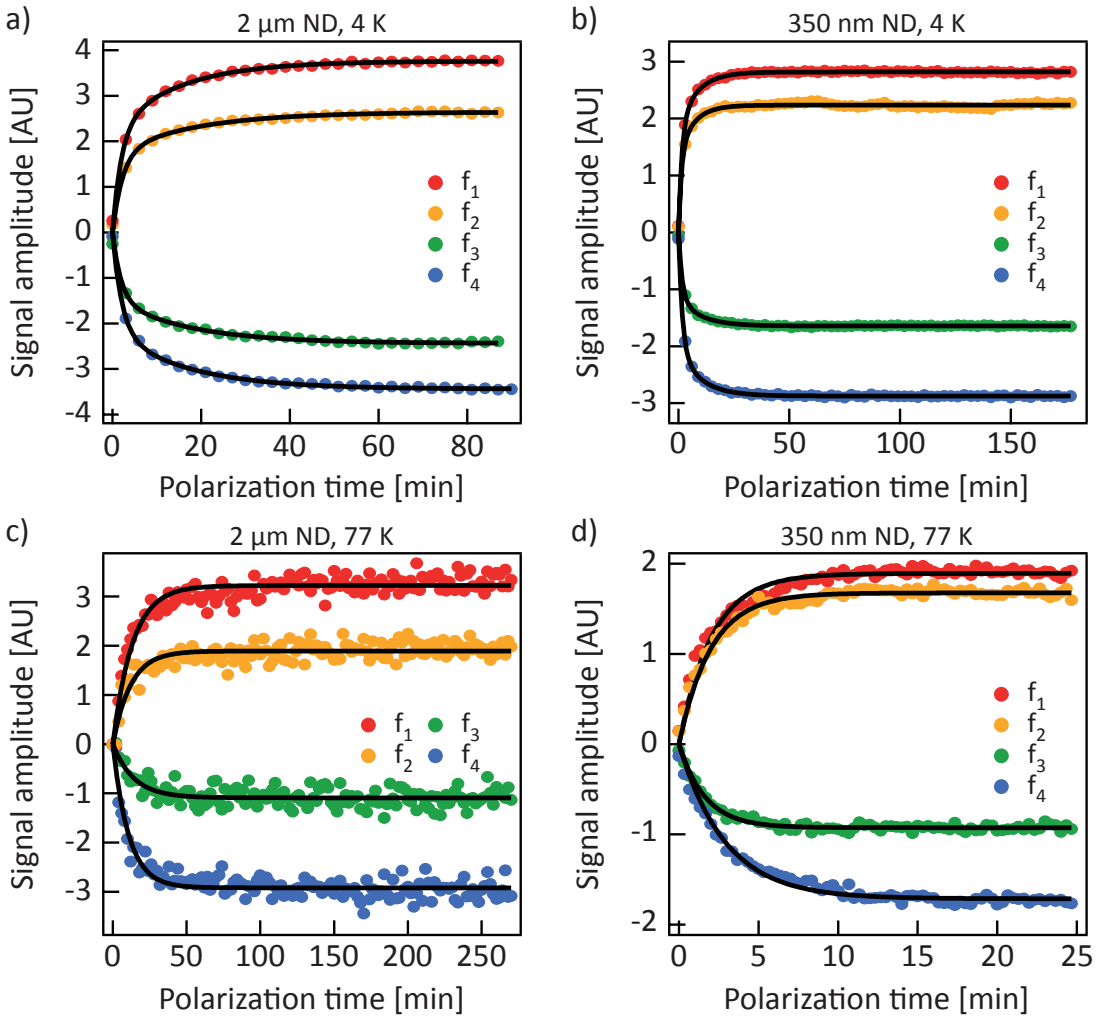

Figure 6.15: Small tip angle hyperpolarization build up in ND. Signal amplitude as a function of polarization time in **a)** 2 µm ND at $T = 4\,\mathrm{K}$, **b)** 350 nm ND at $T = 4\,\mathrm{K}$, **c)** 2 µm ND at $T = 77$ K, and **d)** 350 nm ND at $T = 77$ K. Polarization build up was measured at the four frequencies f_1 (red), f_2 (yellow), f_3 (green), and f_4 (blue) indicated by arrows in Fig. 6.9a. Data is shown in dots and solid lines are fits to the data (see Section 6.8 for details). T_1 relaxation times are summarized in Table. 6.2.

Particle size	Parameters	Frequency [GHz]	$T_{1,\text{short}}$ [min]	$T_{1,\text{long}}$ [min]
2 µm ND	$T = 4$ K	$f_1 = 80.880$	2.0	16
	$\theta = 9°$	$f_2 = 80.940$	2.3	20
	$TR = 3$ min	$f_3 = 81.000$	1.9	18
		$f_4 = 81.060$	2.1	18
350 nm ND	$T = 4$ K	$f_1 = 80.870$	1.5	8.4
	$\theta = 9°$	$f_2 = 80.940$	1.3	7
	$TR = 3$ min	$f_3 = 81.000$	1.6	10.2
		$f_4 = 81.060$	1.7	10.2

Particle size	Parameters	Frequency [GHz]	T_1 [min]
2 µm ND	$T = 77$ K	$f_1 = 80.880$	15.2
	$\theta = 11.25°$	$f_2 = 80.930$	13.5
	$TR = 2$ min	$f_3 = 80.990$	16.5
		$f_4 = 81.075$	12.0
350 nm ND	$T = 77$ K	$f_1 = 80.860$	2.1
	$\theta = 4.5°$	$f_2 = 80.930$	2.0
	$TR = 20$ s	$f_3 = 80.993$	1.7
		$f_4 = 81.064$	3.0

Table 6.2: Hyperpolarization build up using a small tip angle pulse sequence. Summary of the fit parameters for hyperpolarization build up in ND using a small tip angle pulse sequence.

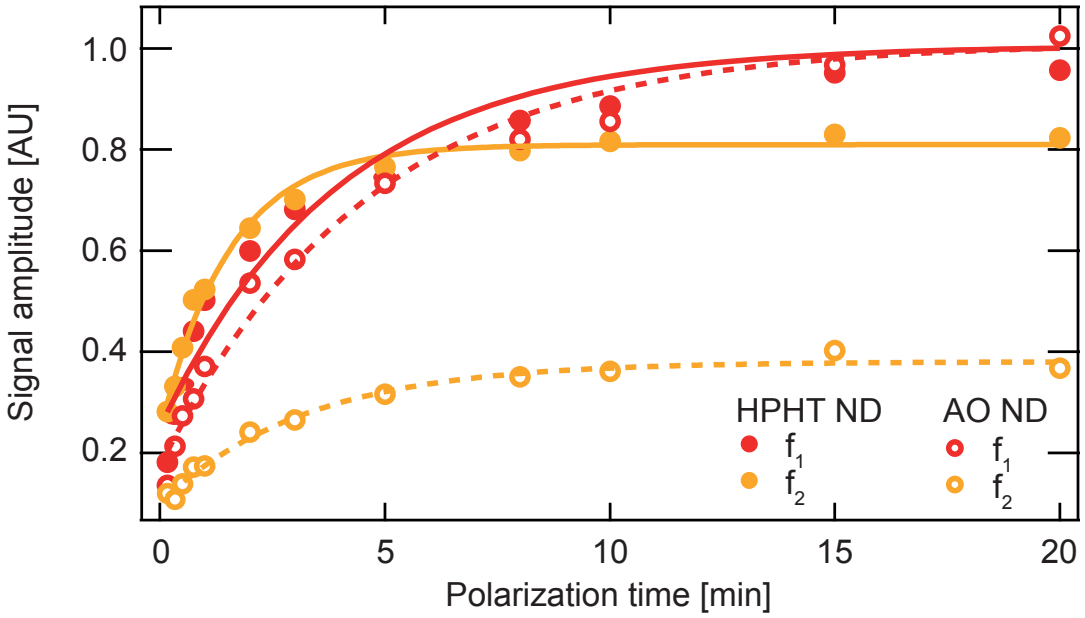

Figure 6.16: Polarization build up comparison for HPHT and AO NDs. The normalized ^{13}C signal amplitude as a function of polarization time for 25 nm HPHT ND (solid dots) and 25 nm AO ND (open circles) at $f_1 = 80.88$ GHz (red) and $f_2 = 80.97$ GHz (yellow). Lines are exponential fits to the data with best fit polarization build up times: HPHT ND: f_1: $\tau = 4.0$ min, f_2: $\tau = 1.5$ min, AO ND: f_1: $\tau = 4.6$ min, f_2: $\tau = 3.2$ min. We observe no difference when polarizing at the P1-centre hyperfine transition (red) and a decrease in the signal and longer polarization times when polarizing at a central transition (yellow) consistent with removing surface impurities from the diamond.

6.7 Discussion

There is significant scope to further enhance the degree of hyperpolarization in ND. In particular, by adding microwave capability to our brute force hyperpolarizer at mK temperature (based on a dilution refrigerator), much larger polarizations appear possible. Eliminating isolated defects via surface passivation techniques [206] will also likely result in longer relaxation times. Another direction is to work with isotopically enriched ^{13}C NDs to increase the number of spins that contribute to the signal and enhance spin diffusion from polarization sites on the surface to the spins in the core. Finally, we mention the possibility of using NDs for long time storage of nuclear polarization that is transferred to the hydrogen nuclei in an aqueous environment using cross-polarization sequences [207,208]. Although the efficiency for polarization transfer

is yet to be experimentally explored, this modality may enable life-science applications in which nanodiamond is tracked and imaged using standard MRI technology [208].

6.8 Methods

Nanodiamonds. The nanodiamonds used in these experiments were HPHT NDs purchased from Microdiamant. See Appendix A for a list of the NDs used.

Brute force T_1 measurements. The decay of brute force hyperpolarization in Fig. 6.3 (red dots) was measured using a small tip angle detection sequence ($\theta = 17°$, $TR = 15$ s). The solid red line is a fit to $M = M_0\cos(\theta)^{n-1}e^{-(n-1)TR/T_1}$ resulting in a T_1 of 53 min. The decay is a combination of the T_1 decay of the particles and the signal lost due to RF induced polarization loss with tip angle θ where n is the nth pulse and TR is the repetition time. Every fifth peak is shown in black.

Hyperpolarization measurements. Measurements were made at a field of $B = 2.88$ T with a Redstone Tecmag system and a in-house constructed NMR probe (design details can be found in Section. 4.1 and Ref [122]) inside an Oxford Instruments flow cryostat. The microwave source was a tuneable Gunn Oscillator ($f = 80.5$ - 81.5 GHz) combined with a power amplifier. Microwaves were coupled to the sample using a waveguide. Polarization transfer measurements were determined using an in-house constructed NMR spectrometer based upon a National Instruments system and an NMR probe at a field of $B = 7$ T. Before polarization the signal was saturated with $64 \times \pi/2$ pulses to null any signal. Enhancement: Measurements were made by hyperpolarizing the ND at $f = 80.855$ GHz (4 K, 77 K) and 80.85 GHz (300 K) and then detecting the signal with a $\pi/2$ pulse. The hyperpolarized signal was compared to the NMR signal with no microwaves and the same polarization build up time. Frequency sweeps: The frequency was swept between 80.78 and 81.12 GHz in discrete steps of 5 MHz and polarization was measured at every point. The 2 μm ND was polarized for 30 s, 3 min and 3 min at $T = 4$ K, 77 K, and 300 K respectively. The spectra have been normalized to 1 for easier comparison. Small tip angle polarization build up: At $T = 4$ K data was fitted with a double exponential taking into consideration the polarization lost due to the detection pulses: $M = M_0\cos(\theta)^{n-1}(A_1e^{-(n-1)TR/\tau_1} + A_2e^{-(n-1)TR/\tau_2})$. At $T = 77$ K data was fitted with a single exponential taking into account polarization lost due to the small tip angle: $M = M_0\cos(\theta)^{n-1}e^{-(n-1)TR/T_1}$.

Depolarization. Measurements at $B = 7$ T: the ND was polarized for 15 min at four frequencies ($f = 80.87$, 80.925, 80.99 and 81.05 GHz in successive experiments) and then transferred to a $B = 7$ T magnet for detection. The transfer was performed in a field of $B \sim 0.7$ T, created from rare-earth permanent magnets and took ~ 20 s. A small tip angle pulse sequence with 8° pulses was used to detect the signal. Enhancement is compared to ND at thermal equilibrium at $B = 7$ T. Measurements at $B = 2.88$ T: The ND was polarized for 180 minutes at two frequencies and the decay was monitored with small tip angle pulses (every 15 s). Depolarization data was multiplied by $\cos(\alpha)^{(n-1)}$ to take into account RF induced depolarization. The resulting data was fitted with a double exponential.

6.9 Acknowledgements

We thank M. Cassidy for technical contributions in the construction of the hyperpolarization probe and M. Cassidy, and C. Marcus for useful discussions. For SEM measurements the authors acknowledge the facilities and technical assistance of the Australian Centre for Microscopy & Microanalysis at the University of Sydney. For ESR measurements the authors acknowledge the staff and facilities at the Nuclear Magnetic Resonance Facility at the Mark Wainwright Analytical Centre at the University of New South Wales. This work is supported by the Australian Research Council Centre of Excellence Scheme (Grant No. EQuS CE110001013) ARC DP1094439, and the Lockheed Martin Corporation.

6.10 Additional measurements

6.10.1 Feasibility of imaging with hyperpolarized nanodiamonds

We expect to perform hyperpolarized ND imaging in a preclinical scanner with a small tip angle 2D fast spin echo (FSE) sequence, with ^{1}H-^{13}C co-registration. Overlaying ^{13}C images of functionalized nanodiamonds on high resolution ^{1}H anatomical images would provide information in a similar format to those seen in PET/MRI [209]. Here, we present calculations estimating a pixel signal-to-noise ratio (SNR) of ~ 11 for a nanodiamond concentration of $1\,\mathrm{mg\,mL^{-1}}$. This SNR value is for $2\,\mathrm{mm} \times 2\,\mathrm{mm}$ sized

pixels in a 5 mm slice assuming significant polarization loss during transfer from polarizing cryostat to imager. We note that nanodiamond concentrations of 2 mg mL^{-1} have previously been used in vivo [24].

First, we consider the fundamental limit to MRI resolution set by the observed transverse coherence time T_2^*, which is reached when the frequency line-width of the signal is approximately equal to the frequency separation between each pixel [210]:

$$dz \sim \frac{1}{\gamma G \pi T_2^*} \tag{6.1}$$

where dz is the pixel length, γ the nuclear gyromagnetic ratio and G is the peak gradient strength. Our nanodiamond samples have $T_2^* \sim 250$ µs, which corresponds to a fundamental resolution limit of 0.25 mm in a preclinical scanner or 2.5 mm in a whole body MRI scanner (assuming typical peak gradient strengths for these systems of $G = 500\,\mathrm{mT\,m^{-1}}$ and $G = 50\,\mathrm{mT\,m^{-1}}$ respectively).

Next, we consider the pixel SNR that would be possible from our hyperpolarized nanodiamond samples in an imaging experiment. Our 2 µm ND samples have a polarization after DNP at 4 K, P_{DNP}, of $\sim 8\%$. The thermal polarization, P_{thermal}, at $B_0 = 7$ T and $T = 300$ K, is 0.0006%, as given by the Boltzmann distribution:

$$P = \frac{h\gamma B_0}{2k_{\mathrm{B}}T} \tag{6.2}$$

where γ is the gyromagnetic ratio and k_{B} is Boltzmann's constant. The free induction decay (FID), after a $\pi/2$ pulse, from a 0.1 g, thermally polarized, 2 µm ND sample was acquired in our 7 T spectroscopic probe under the matched filter condition, $t_{\mathrm{acq}}/T_2^* = \pi/2$, where t_{acq} is the acquisition time. The Fourier transform of this FID has $\mathrm{SNR}_{\pi/2\text{-thermal}} = 35$. Preliminary transfer measurements between the hyperpolarizer and 7 T detection magnet have shown a sample transfer efficiency, η, of 10%. Hence, we predict that, after sample transfer of a hyperpolarized sample to our 7 T spectrometer,

we will have an SNR post transfer, $\mathrm{SNR}_{\pi/2\text{-PT}}$, of 45,000,

$$\mathrm{SNR}_{\pi/2\text{-PT}} = \eta\, \mathrm{SNR}_{\pi/2\text{-thermal}}\, P_{\mathrm{DNP}}/P_{\mathrm{thermal}} \tag{6.3}$$

Scaling this SNR value to give an expected sensitivity in a preclinical imaging experiment is inherently nontrivial due to the difficultly of estimating noise associated with coil resistance and losses arising from the sample [211–213]. Here we make an SNR estimate for a preclinical scanner on the assumption that our SNR is limited primarily by coil resistance, which is generally true at $B = 7$ T for mouse coils [214].

The SNR of a pickup coil scales as:

$$\mathrm{SNR} \propto \frac{B_{\mathrm{r}}}{I_{\mathrm{r}}} \frac{1}{\sqrt{4k_{\mathrm{B}}TR_{\mathrm{c}}}} \tag{6.4}$$

where $\frac{B_{\mathrm{r}}}{I_{\mathrm{r}}}$ is the magnetic field strength of the pickup coil per unit current, T is the coil temperature and R_{c} is the coil resistance. $\frac{B_{\mathrm{r}}}{I_{\mathrm{r}}}$ at the centre of an optimized saddle coil is given by:

$$\frac{B_{\mathrm{r}}}{I_{\mathrm{r}}} = \frac{\sqrt{3}\mu_0 N}{\pi d} \frac{l}{\sqrt{l^2 + d^2}} \tag{6.5}$$

where N is the number of turns in the coil, μ_0 is the permeability of free space, l is the coil length, and d is its diameter [215]. If all power dissipation occurs in the coil, then we can estimate the coil resistance from

$$Q = \frac{\omega_0 L_{\mathrm{c}}}{R_{\mathrm{c}}} \tag{6.6}$$

where L_{c} is the coil inductance and ω_0 is the resonance frequency. Typically Q is ∼100 at 75 MHz for preclinical imaging and spectroscopic NMR probes. Assuming a homogeneous field across the saddle coil, we estimate from Faraday's law that the

coil's inductance scales approximately as [215, 216]

$$I_{\mathrm{c}} \sim \frac{Nl^2}{\sqrt{l^2+d^2}} \tag{6.7}$$

Assuming a 1 turn 40 mm diameter, 60 mm long saddle coil is used for mouse imaging, the ratio $\frac{B_{\mathrm{r}}}{I_{\mathrm{r}}}$ is reduced by 95% compared to the 2 turn 6 mm diameter, 13 mm long coil in our spectroscopic NMR probe. Therefore, the expected SNR after DNP and transfer to the imager is $\mathrm{SNR}_{\pi/2\text{-imager}} = 2{,}100$. This result is very similar to that obtained when the resistance is simply scaled by the ratio of the wire lengths in the coils.

We envision using a small tip angle 2D FSE sequence, similar to that used in Ref. [38], to image ^{13}C. When using a CPMG sequence, our nanodiamond samples have demonstrated T_2 values of approximately 100 ms, which would then allow for many echoes, making a FSE sequence feasible. Based on previous calculations for a 2D gradient-recalled echo (GRE) sequence, we estimate the pixel SNR of a 2D FSE imaging sequence to be [217, 218]

$$\mathrm{SNR}_{\mathrm{pixel}} = \frac{N}{N_0^2}\left(\mathrm{SNR}_{\pi/2\text{-imager}}\right)\sin\theta \tag{6.8}$$

where N is the number of pixels across an $N \times N$ image, N_0 is the number of pixels across the object, θ is the tip angle (setting the acquisition time $t_{\mathrm{acq}} \sim T_2^*$). If the 0.1 g of ND powder in our sample is uniformly distributed through a 40 mm × 40 mm × 5 mm phantom there is a ND concentration of $16\,\mathrm{mg\,mL^{-1}}$. For a 32 × 32 pixel image with 2 mm × 2 mm resolution and 5 mm slice thickness, $N = 32$, $N_0 = 20$. For tip angles 10° and 90°, this gives $\mathrm{SNR}_{\mathrm{pixel}} = 30$ and $\mathrm{SNR}_{\mathrm{pixel}} = 170$ respectively. Normalizing this value, we predict $\mathrm{SNR}_{\mathrm{pixel}} = 11$ at $1\,\mathrm{mg\,mL^{-1}}$ for a 90° tip angle.

Hence, we estimate that there will be sufficient SNR for hyperpolarized nanodiamond imaging. In practice, the measured SNR will deviate from these values depending on the actual sensitivity of the detection coil and polarization lost during sample transfer. We have also not considered the loss of spin coherence due to T_2 effects during

the acquisition sequence. These effects will cause some degradation of the SNR at higher spatial frequencies. A range of linewidth narrowing sequences developed for solid imaging may also help to improve image quality [210].

6.10.2 Hyperpolarization build up in ND at off resonant MW frequencies

By adjusting the microwave frequency we can select which impurity is used for hyperpolarization. This results in different polarization build up times and decay times, depending on the driving frequency, see Fig. 6.12, Fig. 6.13, Fig. 6.14, Fig. 6.15, Table 6.1, and Table 6.2. For example, when polarizing with spin-1/2 impurities, polarization takes longer to build up and is retained longer than when polarizing with P1 centre impurities. Testing this further, the polarization build up time was measured as a function of microwave frequency over the entire hyperpolarization frequency spectrum, see Fig. 6.17.

The slowest polarization build up occurs at the hyperpolarization peaks, where maximum polarization occurs (indicated by arrows in Fig. 6.9a). At intermediate frequencies, we obtain less polarization, which saturates at a faster rate. This polarization is attributed to defects making up the broad spin-1/2 ESR component. The broad spin-1/2 component of the ESR trace is wide enough to drive hyperpolarization over the entire frequency range measured.

We again observe that the two central frequencies (due to surface and core spin-1/2 impurities as well as the P1-centre impurity) have build up that occurs at a faster rate than the build up at the two outer peaks (due to only the P1-centre impurities). Lastly, we note that although the hyperpolarization off resonance of the main four hyperpolarization peaks occurs at a faster rate, the amount of polarization is lower, and there is no net enhancement gain.

6.10.3 Depolarization of the hyperpolarized signal in a stray magnetic field.

Hyperpolarized MRI involves hyperpolarizing nanoparticles in a polarizer, followed by transfer to another NMR or MRI magnet for detection. Although this transfer process is usually fast, the low magnetic fields can lead to significant polarization loss.

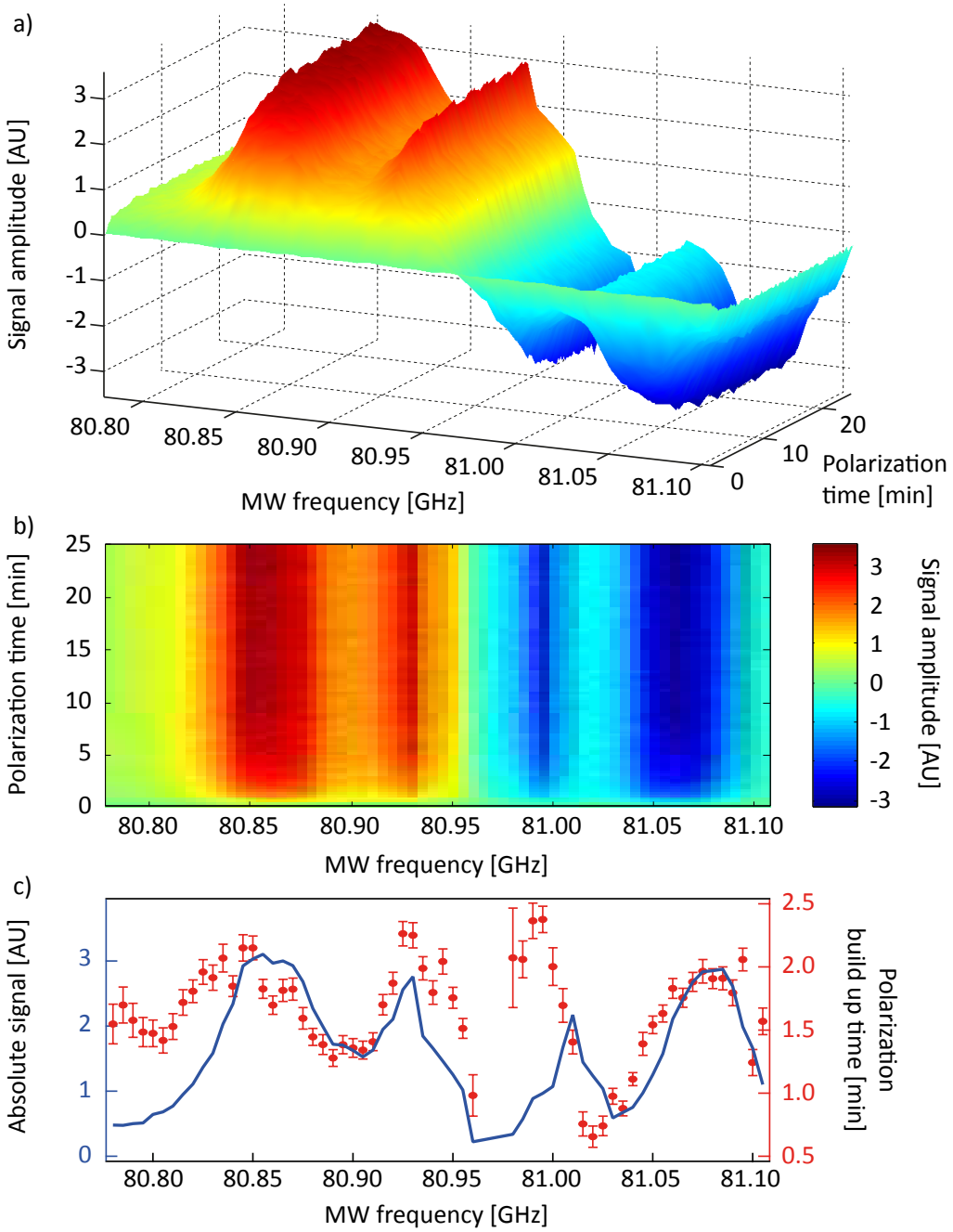

Figure 6.17: ^{13}C polarization build up as a function of microwave frequency. **a)** A 3D-plot and **b)** a surface plot of the ^{13}C signal amplitude of 350 nm ND at $T = 77\,\mathrm{K}$, as a function of driving microwave frequency. The ^{13}C signals were measured using a small tip angle pulse sequence, ($\theta = 1.66°$ with detection pulses every 15 sec). **c)** The polarization build up time (red dots) when fitted with an exponential function taking into account polarization lost due to the tip angle. Error bars are from the fit. The frequency spectrum at 25 min of polarization (blue) is overlayed.

In our initial polarization transfer measurements, we lost $\sim 90\%$ of the hyperpolarized signal, see Fig. 6.3and Fig. 6.12a. Even with this significant signal loss, the polarizations are still high enough to be detected in an MRI scan, however, any additional signal would lead to more sensitivity, a higher signal to noise ratio and longer imaging times.

Here we examine the magnetic field dependence of the polarization loss (in the stray field of the hyperpolarizer), in order to improve the polarization transfer process, see Fig. 6.18.

At both $T = 300$ K and 77 K, there is no significant loss of hyperpolarization above $B \sim 500$ mT. After that there is a steady decrease in the ^{13}C signal and ~ 90 % signal is lost at $B = 5$ mT (the field at the top of the cryostat).

It is possible that at $B = 50$ mT and $B = 100$ mT there could be additional depolarization from the coupling of the NV-centre and ^{13}C spins systems (due to the LACs at these two fields). However we observe no additional depolarization. This could be due to the low concentration of NV centres in our NDs, or that the coupling happens on a longer time scale than the T_1 depolarization.

Similarly as for depolarization measurements at high magnetic fields, see Fig. 6.12a, we see more polarization retained when polarizing at the central peaks (due to P1-centre and spin-1/2 impurities, shown in yellow) than at the outer peaks (due to only P1-centre impurities, shown in red), indicated by arrows in Fig. 6.9a.

Although during polarization transfer, the ND was kept in a field of $B = 500$ mT made from permanent magnets, the ND was in a low field of $B \sim 5$ mT at the top of the hyperpolarizer and detection magnet. Ideally we would like to keep a magnetic field $B > 200$ mT throughout the entire transfer to retain as much polarization as possible. Such a field could be implemented by constructing a magnetic tunnel [219] between the polarizer and MRI magnet.

6.10.4 Hyperpolarizing nanodiamond using frequency modulation

All ND hyperpolarization reported involved continuously driving the system at a set frequency. However, if the ESR linewidths are broad, this only excites a small section of the spectral breadth, and hence not all electrons take part in hyperpolarization. Frequency modulation [122, 220, 221] of the driving microwave radiation can excite multiple sections of the ESR line, leading to additional flip-flop interaction and more

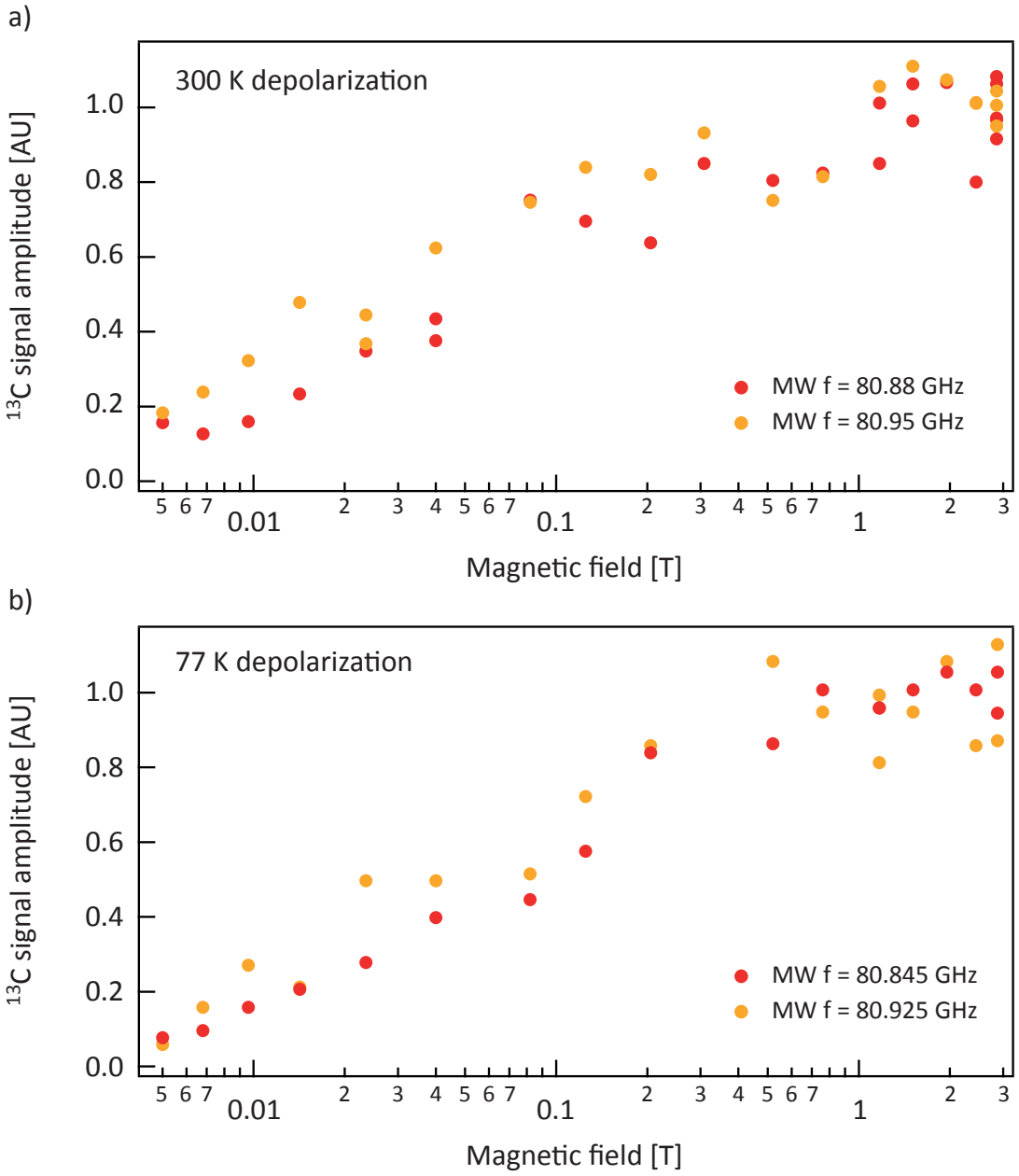

Figure 6.18: Depolarization of the hyperpolarized signal in a stray magnetic field. ^{13}C signal amplitude of 2 µm HPHT NDs after 15 min of polarization and 2 sec of depolarization in the stray field of the $B = 3$ T magnet at **a)** $T = 300$ K and **b)** $T = 77$ K. After depolarization the ND was lowered back to the centre of the magnet for detection. The microwaves were switched off during detection and depolarization. Signals have been normalized to the signal with no depolarization. We observe no significant depolarization above $B \sim 500$ mT, and a decrease to 10% of the signal at $B = 5$ mT. More polarization is retained when polarizing using spin-1/2 and P1 centre defects (yellow dots) than when polarizing using only P1 centre defects (red dots).

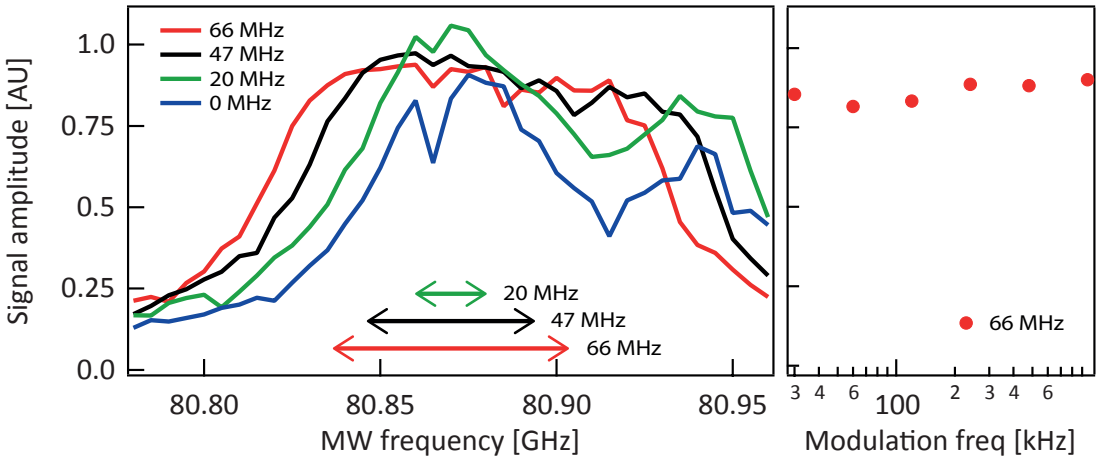

Figure 6.19: Hyperpolarizing nanodiamond using frequency modulation. Left: ^{13}C signal from 350 nm ND at T = 300 K as a function of driving microwave frequency, f, for modulations: f (no modulation) (blue), $f \pm 66$ MHz (red), $f \pm 47$ MHz (black), and $f \pm 20$ MHz (green). The ND was polarized for 2 min at a sweep rate of 60 kHz. We observe no additional hyperpolarization, however we see a broadening of the hyperpolarization features. Right: Modulating at $f \pm 66$ MHz, as a function of sweep rate. Increasing this rate did not lead to additional signal enhancement.

hyperpolarization. Here we examine the signal enhancement as a function of the driving microwave frequency modulation, see Fig. 6.19.

We see no additional signal enhancement with modulation, however we observe a broadening of the frequency spectrum with increasing modulation, consistent with exciting a broader section of the ESR line. Increasing the sweep rate of the modulation did not increase the signal enhancement. This could be due to the combination of the sweep rate and electron T_1 relaxation times being too fast to build up additional polarization. Decreasing the temperature could result in a decrease of the electron T_1, and hence enhancement through frequency modulation.

6.10.5 Spin-spin interactions in diamond

For MRI using nanoparticles, a thorough understanding of the spin-spin interactions is necessary, as this limits both pulse sequences and image acquisition windows that can be used to acquire a hyperpolarized MRI image. While the T_2 spin-spin relaxation time in dilute crystalline lattices is typically very short, ($T_2 \sim$ ms), providing con-

siderable challenges for acquiring an MRI image, an interesting phenomenon has been observed, which can extend T_2 through multiple spin echoes. Usually the transverse magnetization decoheres to zero, however when measuring under CPMG conditions, the decoherence can approach a steady non-zero value [222, 223]. This long tail of spin echoes can be used to increase the MRI imaging acquisition window, boosting the signal to noise and allowing for MRI images of nanoparticles.

The T_2 relaxation times of various NDs were measured under Hahn echo conditions, see Fig. 6.20a. We found that at $B = 7$ T and $T = 300$ K the T_2 relaxation time ranged from $T_2 = 3$ ms for small NDs to $T_2 = 1.5$ ms for larger NDs. We attribute the T_2 relaxation to P1 centre defects in the core of the NDs, with larger NDs having more P1 centre and hence shorter T_2 relaxation. We saw no significant difference between AO NDs and HPHT NDs.

The T_2 relaxation time, when measured using a Hahn echo pulse sequence, did not change after hyperpolarizing, see Fig. 6.20b. The T_2 relaxation time at $T = 77$ K and $B = 3$ T stayed at $T_2 \sim 1$ ms irrespective of the polarization frequency (when polarizing using P1 centres at f_1, or when polarizing using P1 centres and spin-1/2 defects at f_2) or polarization time.

When measuring the T_2 relaxation time under CPMG conditions, we observe long tails in the echo trains that persist for a much longer time, similar to those observed in silicon [122, 222, 223] We see an increase of two orders of magnitude in T_2 from $T_2 \sim 1$ ms under Hahn echo to a long tail with $T_2 \sim 100$ ms under CPMG conditions, see Fig. 6.21a. We observe an increase in both the amplitude and relaxation time of the long tail with increasing polarization time, see Fig. 6.21b.

Surprisingly, we observe larger and longer echo tails when polarizing using spin-1/2 and P1 centre impurities (at one of the central transitions, f_2 and f_3 in yellow and green) than when polarizing at a P1 centre transition (f_1, f_4, in red and blue), the frequencies indicated by arrows in Fig. 6.9a. Although this phenomenon is not yet completely understood, several explanations have been proposed.

These long T_2 tails are not believed to be a long coherence, but pseudo tails arising as a consequence of the formation of stimulated echoes, which can exist up to the spin-lattice relaxation time T_1. Although stimulated echoes are not expected in a CPMG pulse sequence, they can be generated by the pulse angle distribution present in an inhomogeneously broadened NMR line. Under conditions where inhomogeneities

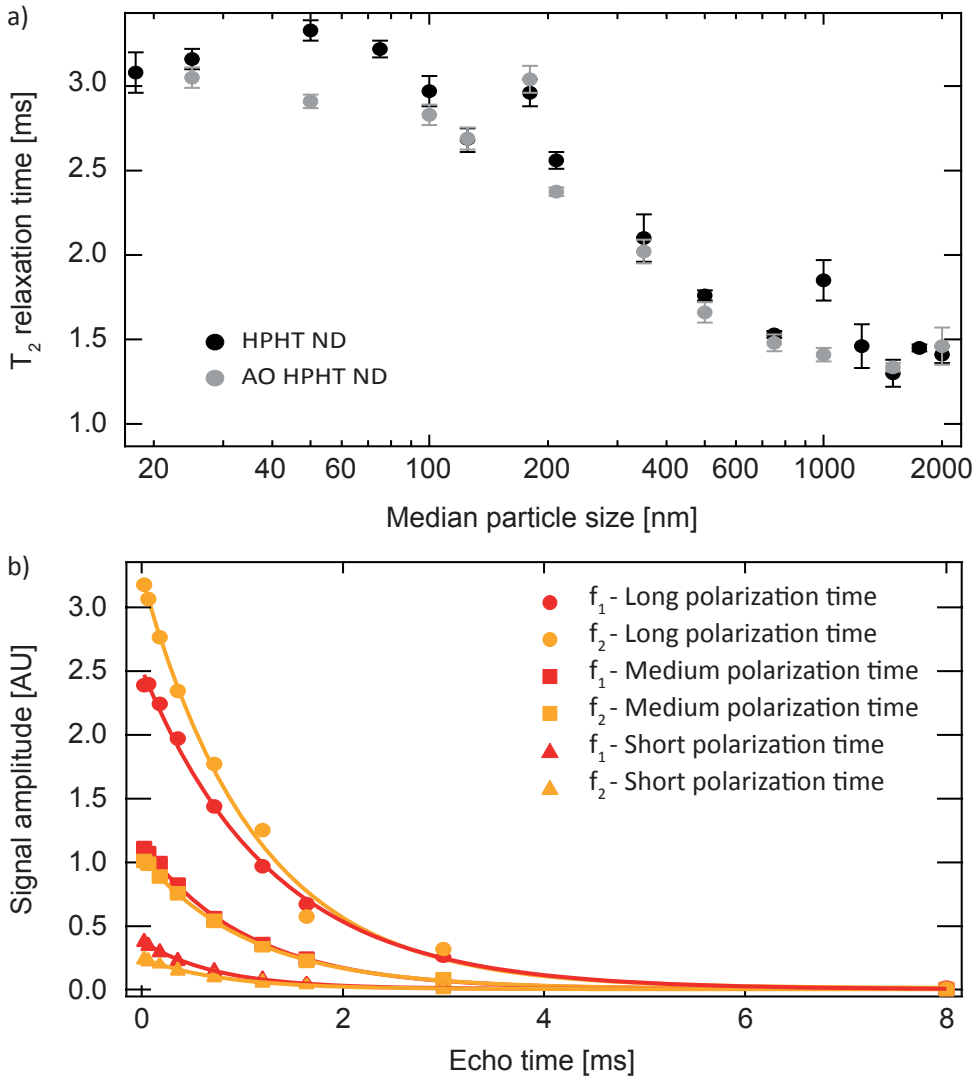

Figure 6.20: Spin-spin T_2 relaxation in ND measured under Hahn echo conditions. a) T_2 relaxation time at $B = 7$ T and $T = 300$ K. The relaxation times are the average of three Hahn echo measurements fitted with an exponential decay. The error bars are the standard deviation. No difference is seen between HPHT NDs (black) and AO NDs (grey) over the size range measured. Diamonds were allowed to equilibrate in the magnetic field before the Hahn echo measurement was taken. We see a decrease in T_2 from $T_2 = 3$ ms for small NDs to $T_2 = 1.5$ ms for larger NDs, which we attribute to P1 centre defects. **b)** T_2 relaxation time of 2 µm HPHT ND at $T = 77$ K and $B = 3$ T for various polarization times measured using a Hahn echo pulse sequence. T_2 relaxation was measured when polarizing using P1 centres (red) and when polarization using spin-1/2 defects and P1 centres (yellow). The T_2 relaxation time did not change and stayed at $T_2 \sim 1$ ms for short polarization times (t_{pol} = 30 s, f_1: T_2 = 0.74 ms, f_2: T_2 = 0.8 ms), medium polarization times (t_{pol} = 3.5 min, f_1: T_2 = 1.0 ms, f_2: T_2 = 1.1 ms) and long polarization times ($t_{pol} = 50$ min, f_1: T_2 = 1.3 ms, f_2: T_2 = 1.1 ms).

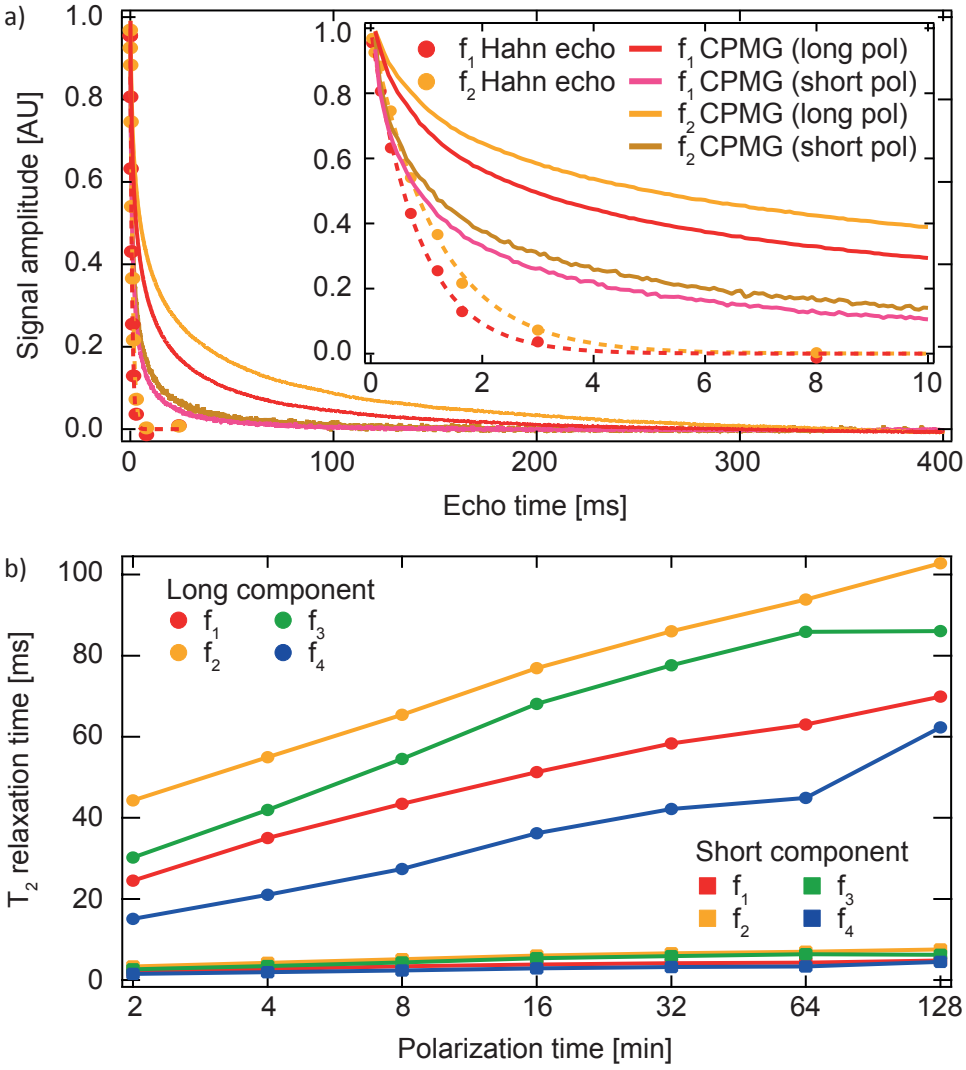

Figure 6.21: Spin-spin T_2 relaxation in ND measured under CPMG conditions. **a)** Comparison of T_2 measured with a Hahn echo sequence (dots) and CMPG sequence (solid lines) for 2 µm ND at $T = 300$ K and $B = 3$ T. NDs were polarized for $t_{pol} = 30$ s (for Hahn echo) and for $t_{pol} = 2$ min (short polarization time) and $t_{pol} = 128$ min (long polarization time) (for CPMG) at both the P1 centre (f_1, red) and P1 centre and spin-1/2 defects (f_2, yellow). When measuring under CPMG conditions we see a long echo tail which persists out to 400 ms, two orders of magnitude longer than when measuring under Hahn echo conditions. Inset: Zoom of the short echo times. **b)** T_2 relaxation time as a function of polarization time when measured under CPMG conditions at $T = 300$ K and $B = 3$ T. The ND was polarized at the four frequencies indicated by arrows in Fig. 6.9a. We observe an increase in T_2 as a function of polarization time at all four frequencies and we observe a longer tail when polarizing at one of the central transitions due to P1 centres and spin-1/2 defects (f_2, f_3) than when polarizing at the outer transitions due to P1 centres (f_1, f_4). For the CPMG sequence: $\pi/2 = 8.5$ µs, $\tau = 40$ µs, with 5000 echoes.

produce different tipping angles in different sites of the sample, and in a system with suppressed spin diffusion, the different tipping angles do not average to a π pulse, leaving a perpendicular component that behaves like a stimulated echo [224, 225]. We observe an increase in T_1 with polarization time, which could lead to an increase in T_2 with polarization time if we have stimulated echoes that exist for a time proportional to T_1. Another explanation involves longer decoherence times due to highly polarized nuclear states very close to the paramagnetic impurities [226]. Further studies involving stimulated echoes are needed to understand the cause of the increasing T_2 time.

7

Hyperpolarized nanodiamond surfaces

The biological function and application of nanoparticles stem from their surface properties. Understanding these properties, especially the adsorption and desorption mechanisms, is important for the design of nanoparticle systems capable of targeted drug delivery and triggered release. Characterizing the surface structure of nanoparticles is challenging due to typical low concentrations of surface functional groups. Here, we demonstrate that free electrons on the nanodiamond surface can be used to hyperpolarize adsorbed liquids, giving information about the ND surface. We differentiate between adsorbed liquids and non-adsorbed liquids through examining spin-lattice relaxation and hyperpolarization build up times. These results extend the available methods of monitoring desorption of chemotherapeutics for targeted delivery[1].

[1]This chapter is adapted from Rej et al. *Hyperpolarized nanodiamond surfaces.* Submitted to Nano Letters.

7.1 Introduction

Bio-functionalized nanoparticles are emerging as highly versatile platforms upon which to develop the new theranostic and tailored imaging modalities needed in the era of personalized medicine [1, 2, 201, 227]. These nanoscale agents, comparable in size to the machinery of the cell, open the prospect of detecting and examining a spectrum of diseases with enhanced sensitivity, and offer a means of targeting the delivery and controlled release of pharmaceutical payloads. Underpinning these powerful applications is the need to develop a detailed understanding of the interface between a nanoparticle and its complex environment. The chemistry of the functionalized nanoparticle surface configures their interaction with, for instance, the extracellular matrix, disease processes, or tumour microenvironment.

Magnetic resonance (MR) techniques are well-placed for probing bio-chemical reactions between a nanoparticle and its environment, but challenging in the limit where the nanoparticle interfacial surface contributes only a fraction of the signal relative to the core [228,229]. The difficulty in isolating surface signals has lead to new techniques based on dynamic nuclear polarization (DNP), to enhance the sensitivity of MR spectroscopy, mostly via the use of surface-bound radicals [230–234]. These techniques have been extended to polarizing liquids surrounding the NPS using both extrinsic [235,236] and intrinsic defects [202].

Nanodiamonds (NDs) are emerging as a promising carbon nanomaterial for drug delivery applications [18, 23, 24, 203], as their biocompatible, non-toxic nature [17, 18] with rich surface chemistry allows for a wide range of small molecules such as proteins, therapeutics, and antibodies to bind to the surface [19]. NDs can be non-invasively tracked using optical techniques based on the NV centre fluorescence, providing cellular imaging [21, 26], and magnetic field detection [27, 28] and through hyperpolarized MRI [51,52,123] detecting ^{13}C nuclear signals. As these nanoparticles become more complex, a thorough understanding of the surface and the interplay with the environment is important for understanding in-vivo behaviour [237].

Here, we explore how ND surface interactions can be used to enhance the applications of NDs in-vivo. We demonstrate that naturally occurring defects on the ND surface can be used as a non-toxic dopant for hyperpolarizing molecules adsorbed on the ND surface. We observe ^{1}H signal enhancements consistent with the solid effect, for

a range of magnetic fields at X-band frequencies. At higher magnetic fields we observe a cross effect contribution to the hyperpolarization mechanism. Enhancements are observed for a wide range of liquids with differing polarities, and we find that enhancement decreases with ND particle size, consistent with surface defect hyperpolarization.

We are able to distinguish between adsorbed liquid and non-adsorbed liquids by measuring the T_1 relaxation behaviour of the nuclear spins, observing two distinct spin baths with differing relaxation times. Combined with measurements of the enhancement, we are able to monitor when the nanoparticle surface is saturated, and when adsorption and desorption occur. These techniques could be used to monitor and examine chemotherapeutic adsorption and desorption on ND surfaces.

Additionally we demonstrate how these surface defects affect the T_1 relaxation time of ^{1}H nuclear spins in solutions surrounding the NDs for T_1 weighted imaging, and contrast in MRI.

7.2 Nanodiamond surfaces

The nanodiamonds used in these experiments are manufactured using the high pressure high temperature (HPHT) technique and purchased from Microdiamant. A micrograph of a small ND is shown in Fig. 7.1a. Measurements were made on diamonds in a size range between 18 nm and 2 μm. Adsorption of the liquids onto the ND surface occurred passively when diamonds were mixed and sonicated with various liquids.

We observe two phases of carbon in our NDs, sp^2 hybridized carbon, attributed to carbon on the surface of the diamond, at $\nu = 1580\,\mathrm{cm}^{-1}$, and sp^3 hybridized carbon, attributed to carbon in the core of the diamond, at $\nu = 1332\,cm^{-1}$, see Fig. 7.1b. The sp^2 carbon phase results in free electrons and provides a surface for liquid adsorption. We observe more sp^2 hybridized carbon on smaller NDs than for larger NDs, due to the much higher surface to volume ratio. Air oxidation [175] of the NDs etches away the ND surface removing sp^2 hybridized carbon and surface electrons.

NDs contain intrinsic impurities and free electrons that provide the dominant pathway for ^{13}C T_1 relaxation [176], and ^{13}C hyperpolarization [123]. For small ND, the dominant electronic defects are surface spins, contributing to a broad spin-1/2 component (black) in an ESR spectrum, attributed to carbon dangling bonds on the surface of the ND, see Fig. 7.1c. Air oxidation of the NDs removes surface electrons,

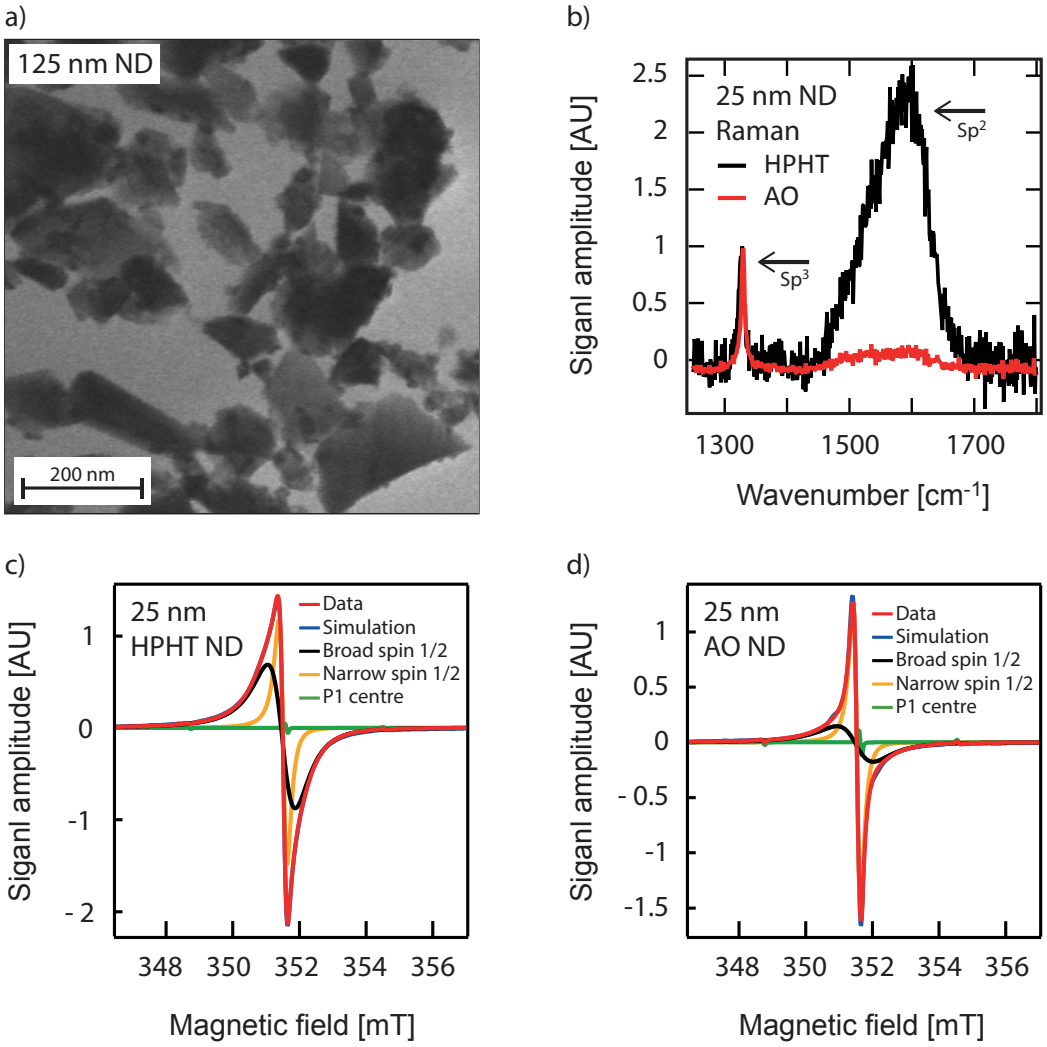

Figure 7.1: SEM, Raman and ESR spectra of small NDs. a) Electron micrograph of 125 nm ND. **b)** Comparison of Raman spectra for HPHT ND (black) and AO ND (red). Raman spectrum show sp^2 hybridized carbon from the surface of the diamond and sp^3 hybridized carbon from the core of the diamond. The sp^2 Raman cross section is 150 times larger than the sp^3 Raman cross section leading to a comparatively larger peak. The fluorescence of the diamond has been subtracted using a baseline correction, and spectra have been normalized to the sp^3 hybridized peak. **c,d)** Comparison of the ESR spectrum of 25 nm HPHT ND and 25 nm AO ND. The data (red) is simulated (blue) using three components: a narrow spin-1/2 Lorentzian component (yellow), a broad spin-1/2 Lorentzian component (black) and a P1 centre component (green).

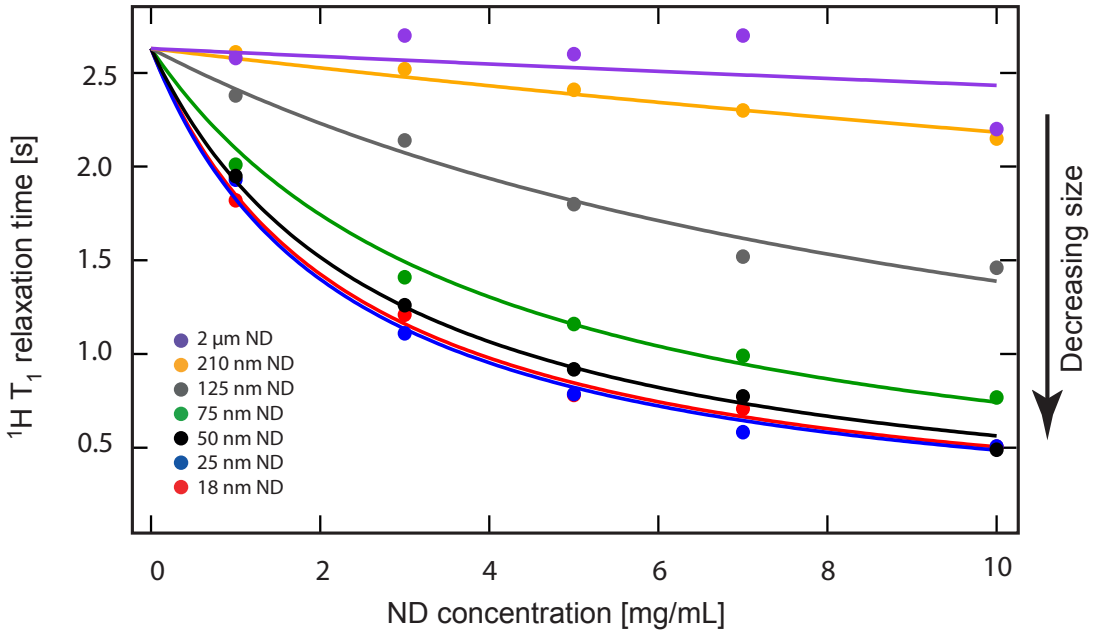

Figure 7.2: ND as a ^{1}H T$_1$ contrast agent. The ^{1}H T$_1$ relaxation time of water in water-ND mixtures as a function of ND size and concentration. Data points are fits to the ^{1}H T$_1$ build up performed using an inversion recovery sequence at $B = 330$ mT. The solid lines are fits to the relaxivity equation [see Section 7.6]. Smaller NDs (25 nm ND, blue dots, $R = 0.17$ mg^{-1}mL^{-1}s^{-1}) have a larger effect upon the T$_1$ relaxation time of water than larger NDs (2 µm ND, purple dots, $R = 0.003$ mg^{-1}mL^{-1}s^{-1}), where R is the relaxivity of the ND.

seen as a decrease in the broad spin-1/2 component of the ESR trace, see Fig. 7.1d. Other components of the ESR spectrum include a narrow spin-1/2 component (yellow), attributed to defects in the core of the ND and a P1 centre component (green) which is a substitutional nitrogen atom with the electron hyperfine coupled to the ^{14}N spin. As the surface to volume ratio decreases with increasing ND particle size, the amount of broad and narrow spin-1/2 defects decrease, while the number of P1 centre defects increases, with small NDs having very few P1-centre defects, see Fig. 5.12.

In addition, the intrinsic free electrons on the surface of the NDs interact with surrounding water, and act as centres for ^{1}H T$_1$ relaxation, see Fig. 7.2, Fig. 7.3, Fig. 7.4 and Fig. 7.5. In much the same way as gadolinium contrast agents add contrast to MRI by modifying the T$_1$ relaxation of surrounding tissues, the T$_1$ relaxation time of water

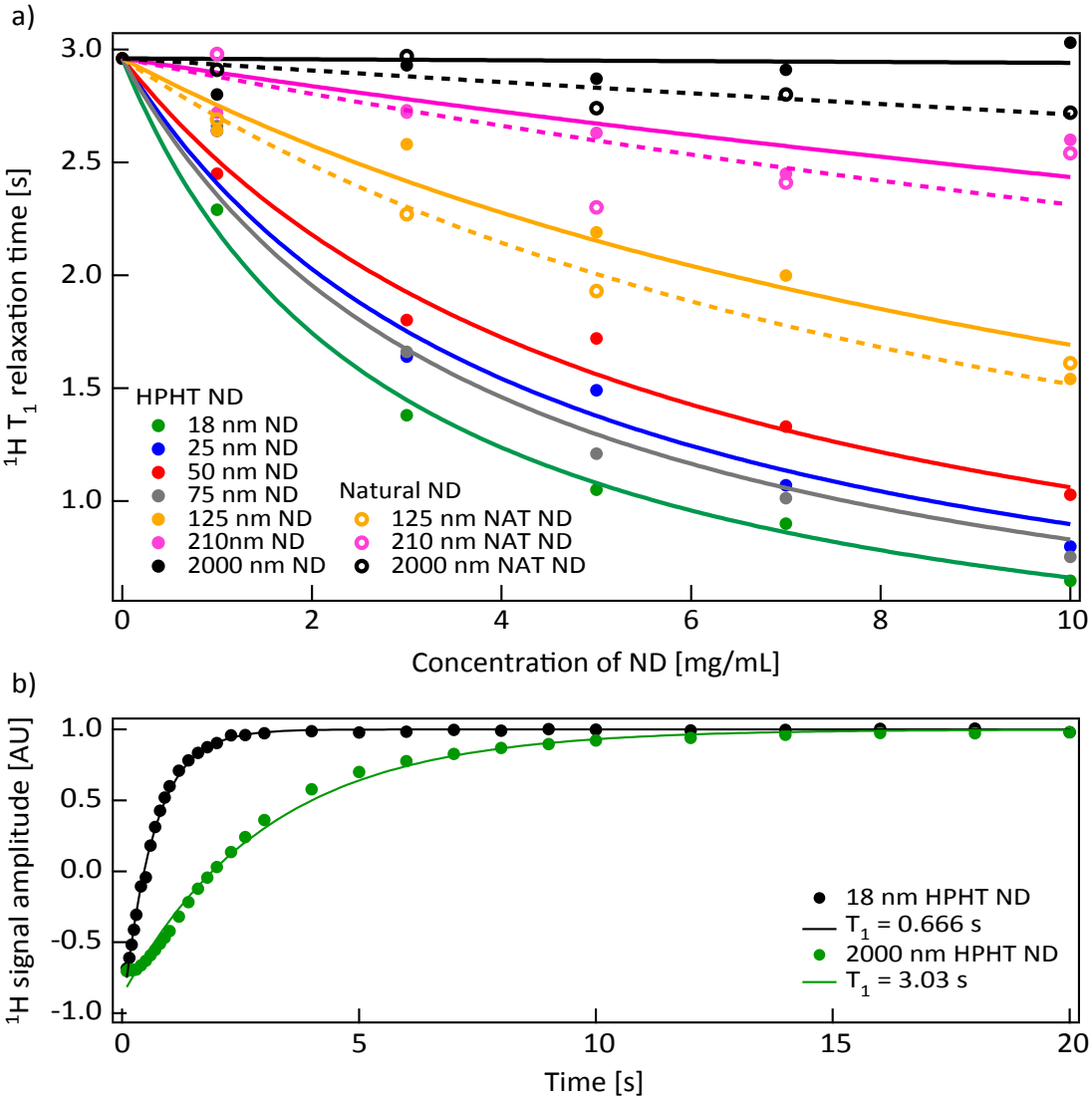

Figure 7.3: ND as a T_1 contrast agent at B = 7 T. a) The ^{1}H T_1 relaxation time in water from a water-ND mixture as a function of ND size and concentration for HPHT ND (solid dots) and NAT ND (empty circles). Data points are fits to the ^{1}H T_1 build up. Lines are fits to the relaxivity equation (solid lines for HPHT ND, and dashed lines for NAT ND) [see Section 7.6]. We see a similar relaxivity for NAT ND as for HPHT ND, with NAT ND being a slightly better relaxant than HPHT ND. **b)** Comparison of the T_1 relaxation time of ^{1}H from a ND-water mixture (10 mg ND/mL) for 18 nm ND (black) and 2 μm HPHT ND (green).

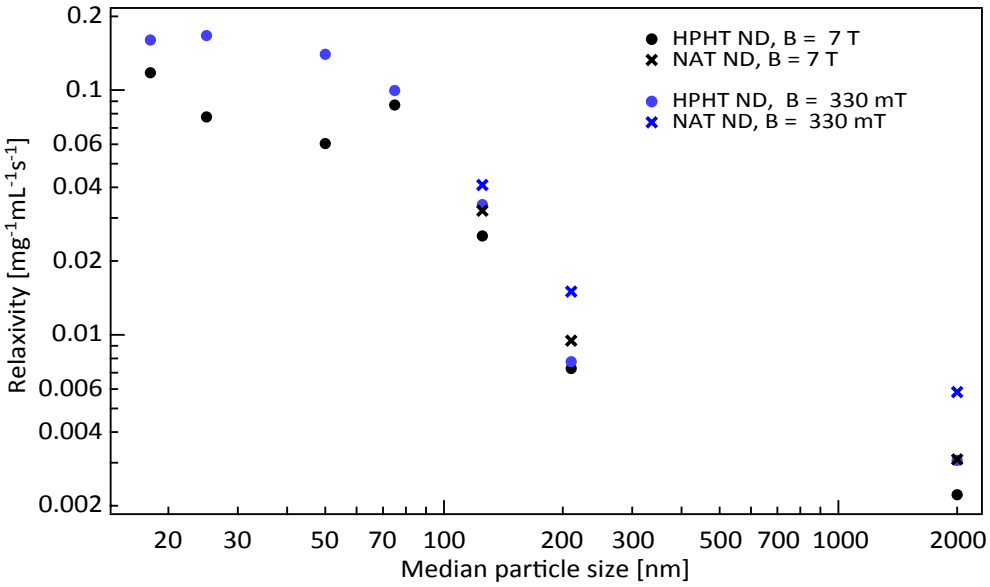

Figure 7.4: Relaxivity of ND. Summary of the relaxivity of HPHT ND (dots) and NAT ND (crosses) at $B = 7$ T (black) and $B = 330$ mT (blue). The relaxivity of ND does not change between $B = 7$ T and $B = 330$ mT, and is similar for NAT and HPHT NDs.

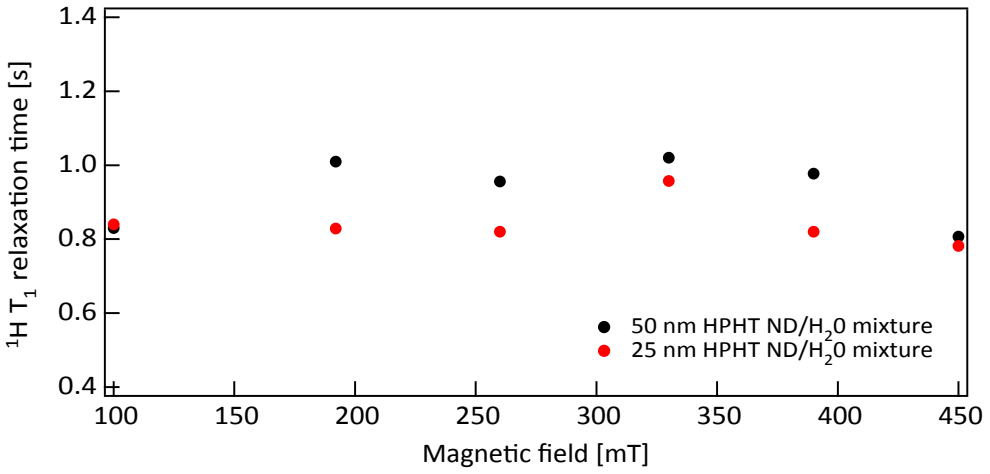

Figure 7.5: ^{1}H T$_1$ relaxation in water-ND mixtures at low fields. ^{1}H T$_1$ relaxation time as a function of magnetic field for ND-water mixtures for 25 nm HPHT ND (black) and 50 nm HPHT ND (red) at a ND concentration of 5 mg/mL. Data points are exponential fits to the ^{1}H T$_1$ decay. No change is seen in the T$_1$ relaxation time over the range $B = 100$ mT - 450 mT.

depends upon the nanodiamond concentration. The relaxivity effect is more prominent for small NDs, which have a large surface to volume ratio, and more surface spins, and decreases until there is no effect for 2 μm ND. Although the relaxivity is small when compared to metal conjugates [238], the effect is large enough to be detected in-vivo, and could be used as a new way to indirectly detect nanodiamonds.

Measuring the T_1 relaxation time of ^{1}H spins in ND-liquid mixtures can also be used as a method of analyzing surface impurities. Combining this modality with hyperpolarization techniques using ND surface spins to polarize surrounding liquids, gives new information about nanoparticle surfaces and the nanoparticle-liquid interface.

7.3 ND as a hyperpolarizing agent

Hyperpolarization can occur via several different mechanisms depending on the electron-nuclear couplings. Hyperpolarization occurs via the Overhauser effect in liquids, however in adsorbed liquids, if the primary nuclear relaxation is via the same electrons used for polarizing [239–241], then hyperpolarization occurs via the solid effect, cross effect or thermal mixing.

For solid effect hyperpolarization, the combined electron-nuclear dipolar coupled system, can be driven at one of the two forbidden transitions ($f = \omega_e \pm \omega_n$), where ω_e and ω_n are the electron and nuclear resonance frequencies respectively, creating positive nuclear polarization when driven at $f = \omega_e - \omega_n$ and negative polarization when driven at $f = \omega_e + \omega_n$, see Fig. 7.6a, b. The cross effect is a three spin process relying on energy conserving flip-flops between two electrons separated by $f = \omega_n$ and one nuclear spin. The hyperpolarization profile has a characteristic separation of $f = \omega_n$ between positive and negative enhancement. The Overhauser effect relies on scalar and dipolar relaxation pathways to build up a nuclear polarization when driving at $f = \omega_e$, resulting in positive or negative enhancement depending on the electron-nuclear coupling.

Using the natural defects found on the ND surface as the hyperpolarizing agent, signal enhancements were measured for ^{1}H spins in oil (Sigma O1514) adsorbed onto the surface of 25 nm ND, see Fig 7.6c. We observed behavior consistent with the solid effect in the ^{1}H hyperpolarized signal with a positive signal enhancement when driving at $f = \omega_e - \omega_n$ and a negative signal enhancement at $f = \omega_e + \omega_n$. No enhancement is seen at $f = \omega_e$, ruling out any Overhauser effect contribution. We conclude that we

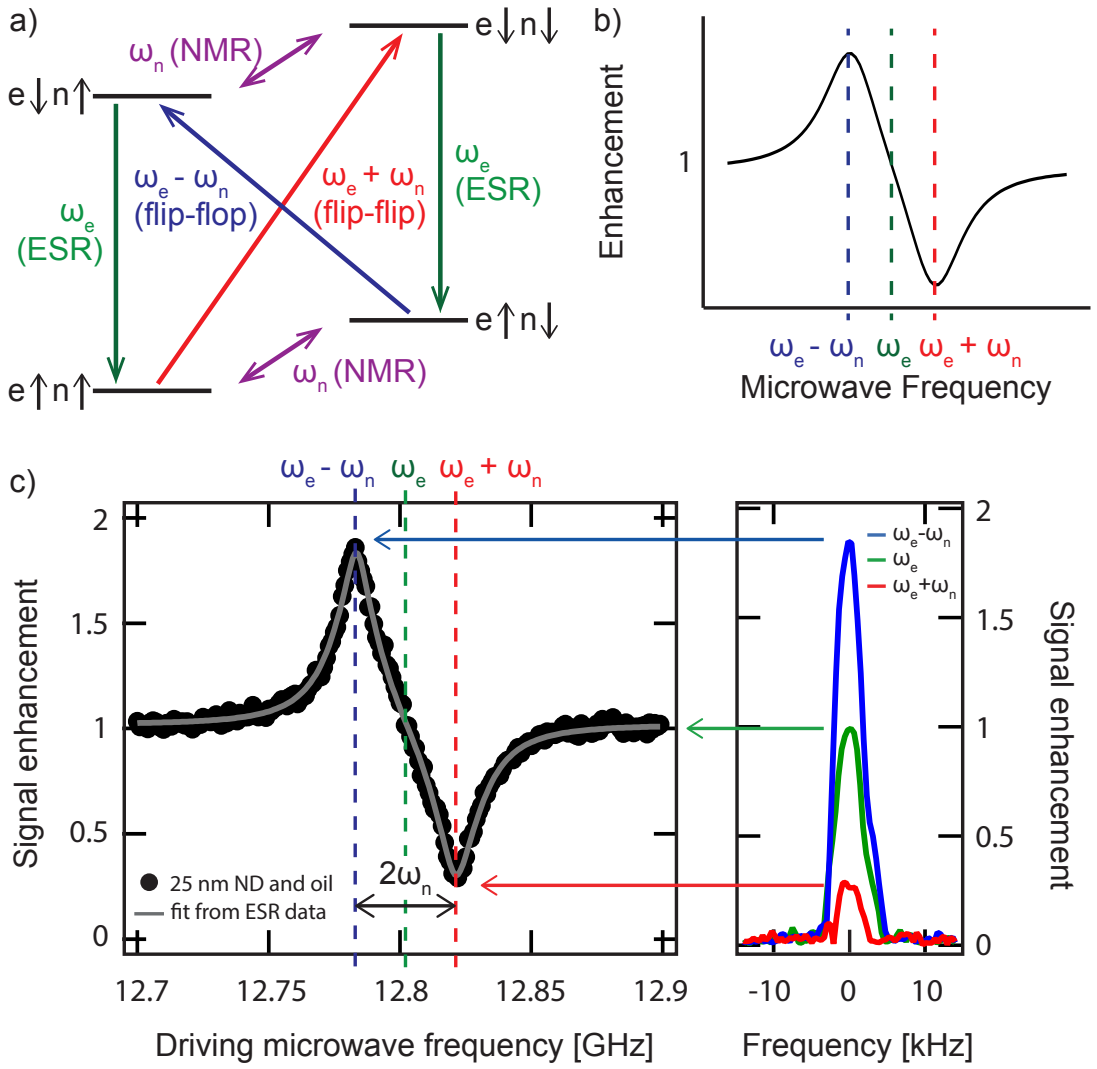

Figure 7.6: Solid effect enhancement of adsorbed liquids on ND. a,b) Energy level diagram for a dipolar coupled electron and nuclear spin-1/2 system in a magnetic field. The ESR (green), NMR (purple), flip-flip (red) and flip-flop (blue) transitions are shown. Driven flip-flop transitions (blue) at a frequency $f = \omega_e - \omega_n$ involve a mutual electron flip and nuclear flop resulting in a positive nuclear polarization, shown in b. Driven flip-flip transitions (red) result in a negative nuclear polarization. **c)** ^{1}H signal enhancement as a function of driving microwave frequency at $B = 458$ mT (black dots). The fit to the data (grey line) is based on the ESR trace linewidths for the broad and narrow spin-1/2 impurities in the ND. The hyperpolarization spectrum is consistent with that given by the solid effect. Enhancement is given by the hyperpolarized signal divided by the signal with microwaves off.

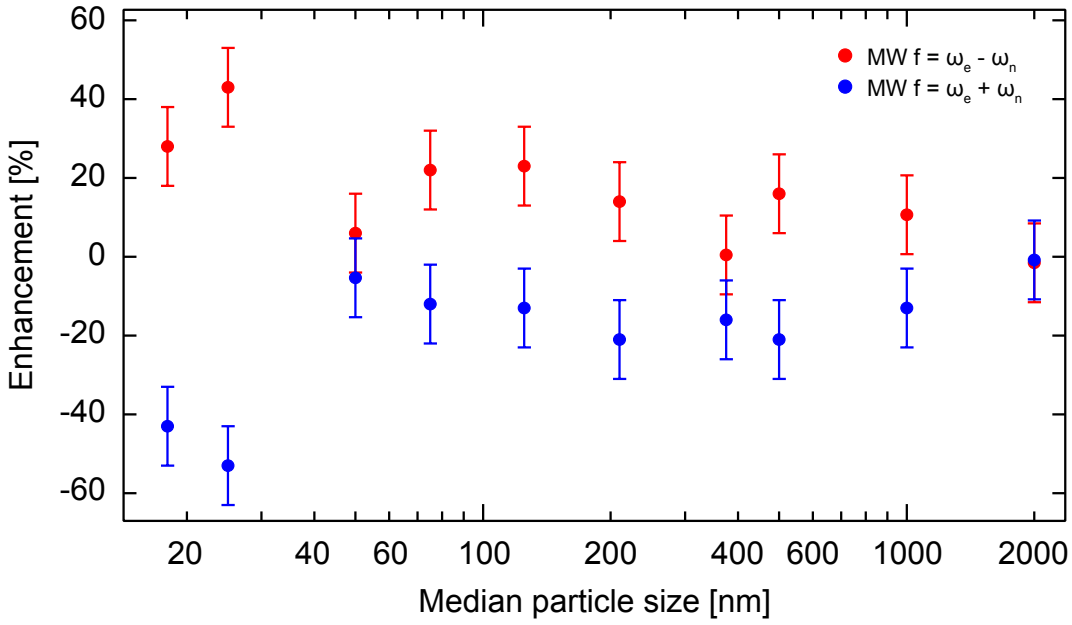

Figure 7.7: ^{1}H enhancement in oil-ND solutions. The ^{1}H NMR enhancement from an oil-ND mixture at $B = 500$ mT when polarized at $f = \omega_e - \omega_n$ (red) and at $f = \omega_e + \omega_n$ (blue). Enhancement is given as a percentage by comparing to the NMR signal with off-resonant driving microwaves. Error bars represent the error in the signal amplitude. We see the largest enhancement for the two smallest nanodiamonds used, moderate enhancement for nanodiamonds in the range 50 nm - 1000 nm, and no enhancement for 2 μm ND.

are observing adsorbed ^{1}H spins on the surface of the nanoparticle.

We observe a decrease in ^{1}H enhancement as ND particle size increases, with no enhancement for 2 µm ND, consistent with surface defect hyperpolarization, see Fig. 7.7. There is no enhancement in liquid solutions without NDs. Similar behavior for ^{1}H in water-ND mixtures, acetic acid-ND mixtures, and glycerol-ND mixtures is seen, and we note that although these liquids have different polarities, they are all adsorbed onto the ND surface, see Fig. 7.8.

The hyperpolarization spectrum was measured at magnetic fields in the range $B = 300$ mT - 500 mT, see Fig 7.9a. The position of the hyperpolarization peaks follow $f = \omega_e - \omega_n$ and $f = \omega_e + \omega_n$ with a peak splitting of $f = 2\omega_n$ (black dashed lines) at low magnetic fields, see Fig. 7.9b. We see a deviation from the predicted value of the peak splitting at higher magnetic fields, indicating that the cross effect or thermal mixing mechanism may be contributing to the hyperpolarization, and the solid effect

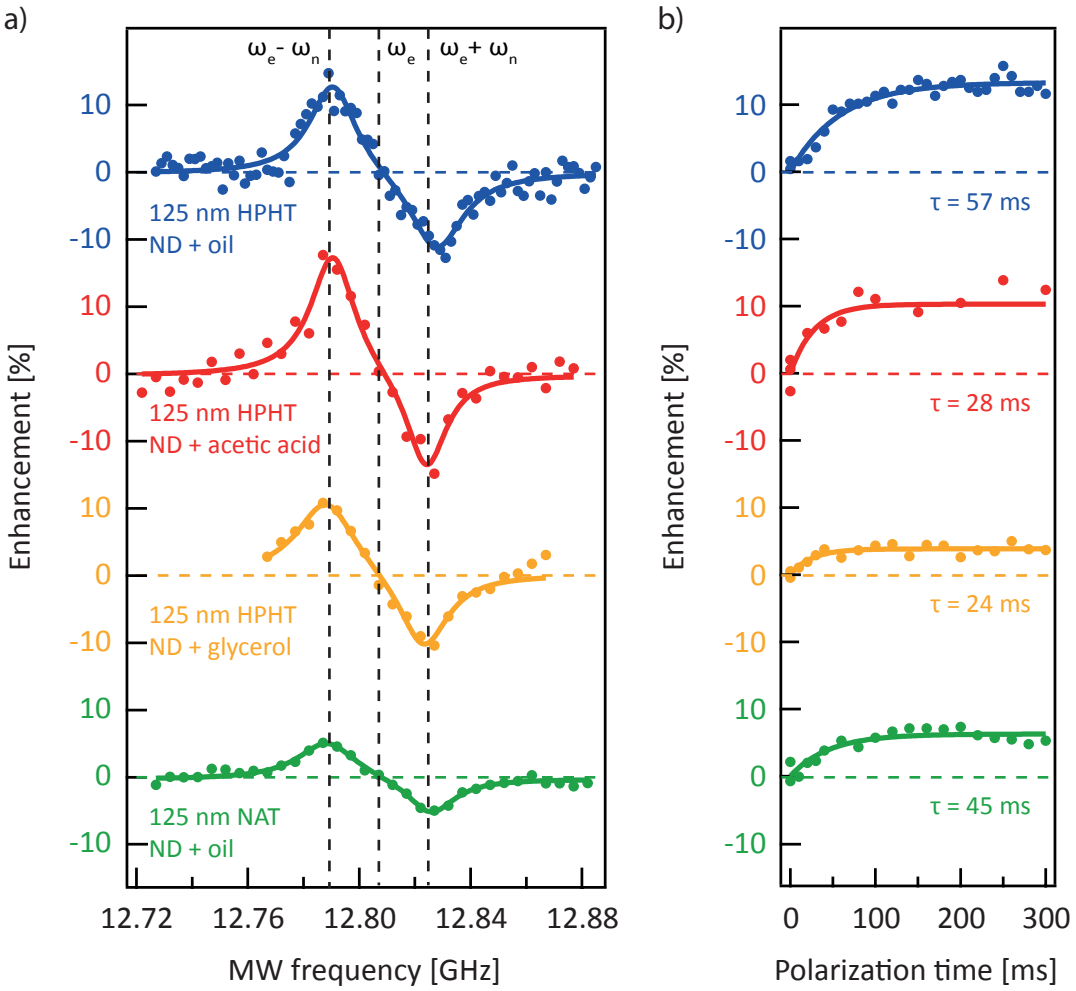

Figure 7.8: Solid effect enhancement in liquid-ND mixtures. a) ^{1}H signal enhancement as a function of driving microwave frequency and **b)** polarization build up at $B = 458$ mT for 125 nm HPHT ND mixed with oil (blue), acetic acid (red) and glycerol (yellow), and for 125 nm NAT ND mixed with oil (green). We always observe a positive enhancement when driving at $f = \omega_e - \omega_n$, a negative enhancement when driving at $f = \omega_e + \omega_n$, and no enhancement at $f = \omega_e$. Polarization build up was measured when driving at $f = \omega_e - \omega_n$. Solid lines in the hyperpolarization spectrum are double Lorentzian fits [see Section 7.6], and solids lines in the polarization build-up are exponential fits, with τ as the fit parameter.

may not be sufficient to explain the hyperpolarization profile.

Surprisingly we observe that the ^{1}H NMR signal enhancement increases as magnetic field increases, see Fig. 7.9c. As the solid effect enhancement has a $\epsilon \propto 1/B^2$ dependence and thermal mixing and cross effect enhancement have a $\epsilon \propto 1/B$ dependence, we may expect to see a higher enhancement at lower magnetic fields, however the cross effect is more efficient than the solid effect at lower powers and may be contributing more at higher magnetic fields, resulting in increasing enhancement with increasing magnetic field.

7.4 Adsorption and desorption onto ND

Now we turn to measuring the relaxation behavior of the hyperpolarized liquid, to determine how much of a liquid has been adsorbed onto the nanodiamond. These techniques can be used to probe conditions (e.g. pH or temperature) which lead to chemotherapeutic desorption for targeted delivery. Here we examine two ways that we can characterize adsorption and desorption on the ND surface.

Firstly we examine the T_1 relaxation time of the adsorbed and non adsorbed liquids. Five ^{1}H T_1 relaxation rates can occur within a hyperpolarized sample, see Fig. 7.10. An inversion recovery experiment (black) affects all the ^{1}H spins in the liquid. Hyperpolarizing at $f = \omega_e \pm \omega_n$ for positive (red) or negative (orange) enhancement and then observing how this polarization returns back to thermal equilibrium examines the relaxation properties of the ^{1}H spins close to the ND surface. Hyperpolarizing at $f = \omega_e \pm \omega_n$ (blue and green), and then inverting the spins reveals information about how both the polarized spins and the non-polarized spins return back to thermal equilibrium.

When these T_1 relaxation times are examined in a oil-ND mixture, we observe two distinct spin baths, one of hyperpolarized spins adsorbed onto the ND surface and one of non-hyperpolarized spins in a liquid surrounding the ND. Limited spin diffusion or molecular diffusion between the two spin baths is observed for short polarization times, see Fig. 7.11a.

We observe a single exponential decay with a short relaxation time ($\tau \sim 100\,\mathrm{ms}$) for spins adsorbed on the NDs. When the spins are inverted we observe a double-exponential return to thermal equilibrium, with a short T_1 corresponding to spins

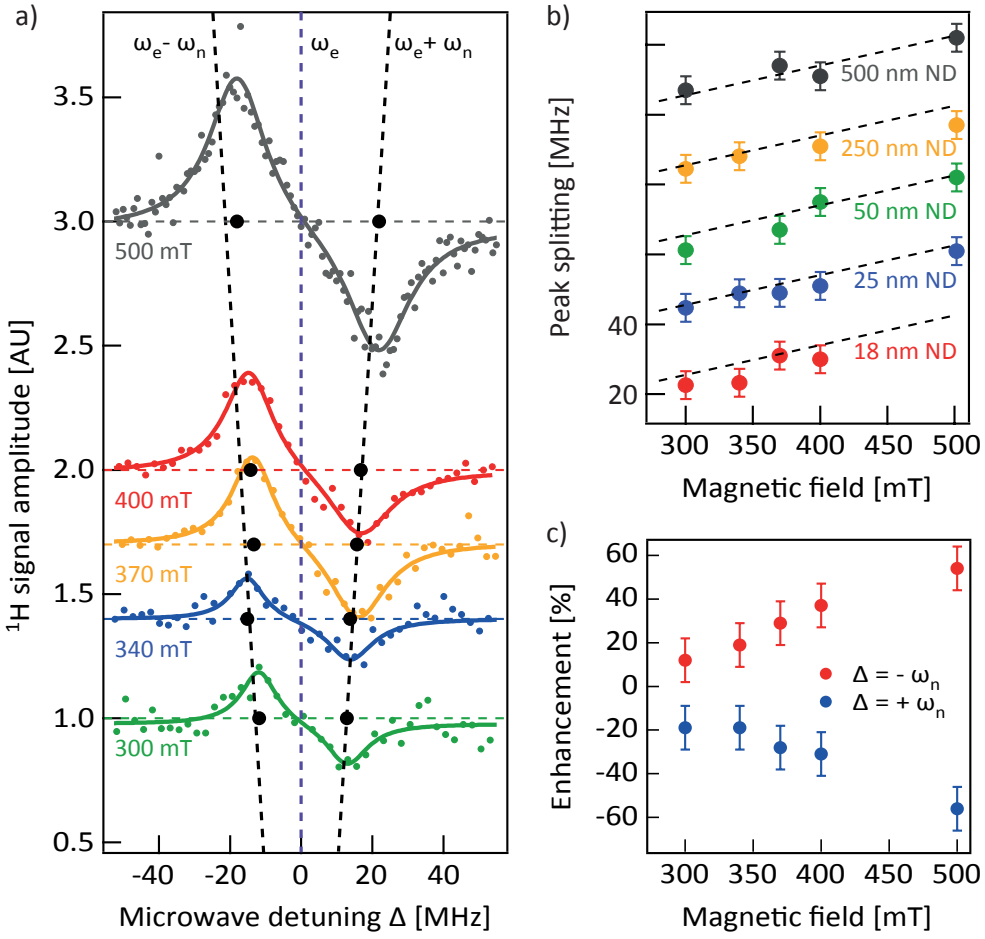

Figure 7.9: Hyperpolarization behavior at various magnetic fields. a) The hyperpolarized ^{1}H NMR signal in oil adsorbed onto 25 nm ND as a function of driving microwave frequency at magnetic fields between $B = 300$ mT and $B = 500$ mT ($B = 300$ mT in green, 340 mT in blue, 370 mT in yellow, 400 mT in red and 500 mT in grey). The solid lines are bi-Lorentzian fits to the data [see section 7.6]. The positions of the peaks (black dots) follow the lines $f = \omega_e - \omega_n$ and $f = \omega_e + \omega_n$ (black dashed lines). We see no hyperpolarization at $f = \omega_e$. The traces have been offset by the magnetic field scaling for clarity. **b)** The frequency splitting between the maximum and minimum ^{1}H signal from oil adsorbed on the ND surface for 18 nm ND (red), 25 nm ND (blue), 50 nm ND (green), 210 nm ND (yellow), and 500 nm ND (grey). The splitting follows the predicted value for the solid effect of $f = 2\omega_n$ (dashed lines) at low magnetic fields and deviates at high magnetic fields. Error bars are 10 % of the Lorentzian fit to the hyperpolarization data. Traces have been offset for clarity. **c)** The ^{1}H signal enhancement as a percentage of the non-polarized signal at magnetic fields between $B = 300$ mT - $B = 500$ mT for a 25 nm ND and oil mixture. Positive enhancement at $f = \omega_e - \omega_n$ is shown in red and negative enhancement at $f = \omega_e + \omega_n$ is shown in blue. Data points are the saturation value of an exponential fit to a polarization build up divided by the signal with detuned microwaves, and error bars reflect the noise in the signal amplitude.

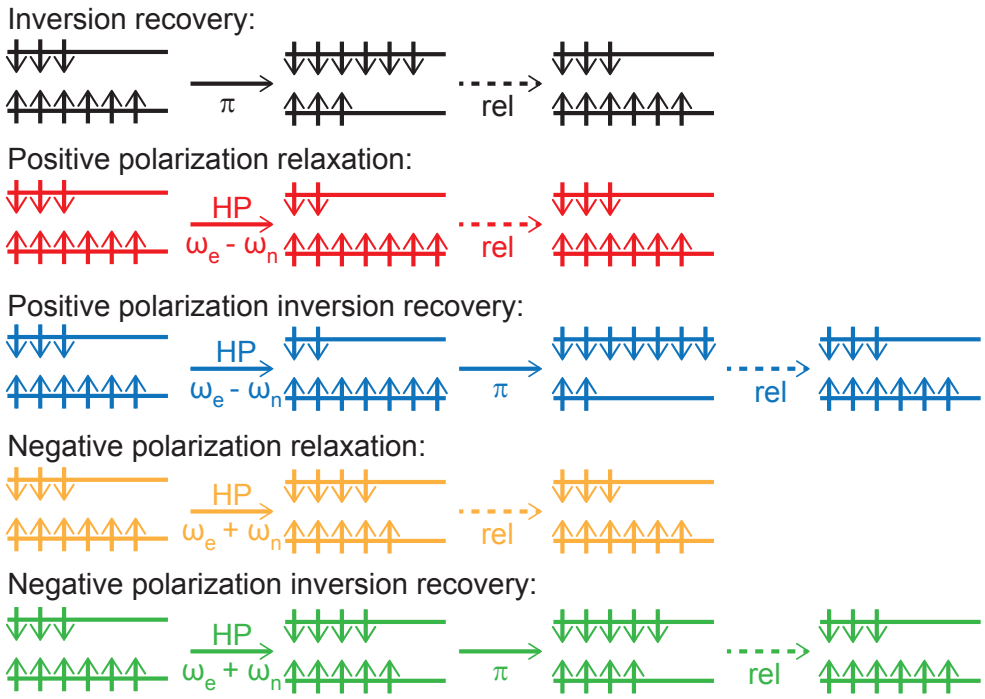

Figure 7.10: Schematic of the T_1 relaxation in adsorbed hyperpolarized liquids. Schematic of the five relaxations that are measured in a hyperpolarized liquid sample. Inversion recovery (black), hyperpolarization at $f = \omega_e + \omega_n$ (yellow) or $f = \omega_e - \omega_n$ (red) and relaxation to thermal equilibrium, and hyperpolarization at $f = \omega_e + \omega_n$ (green) or $f = \omega_e - \omega_n$ (blue) inversion and then relaxation to thermal equilibrium are shown. Rel stands for relaxation, π represents a 180° inversion pulse and HP stands for hyperpolarization.

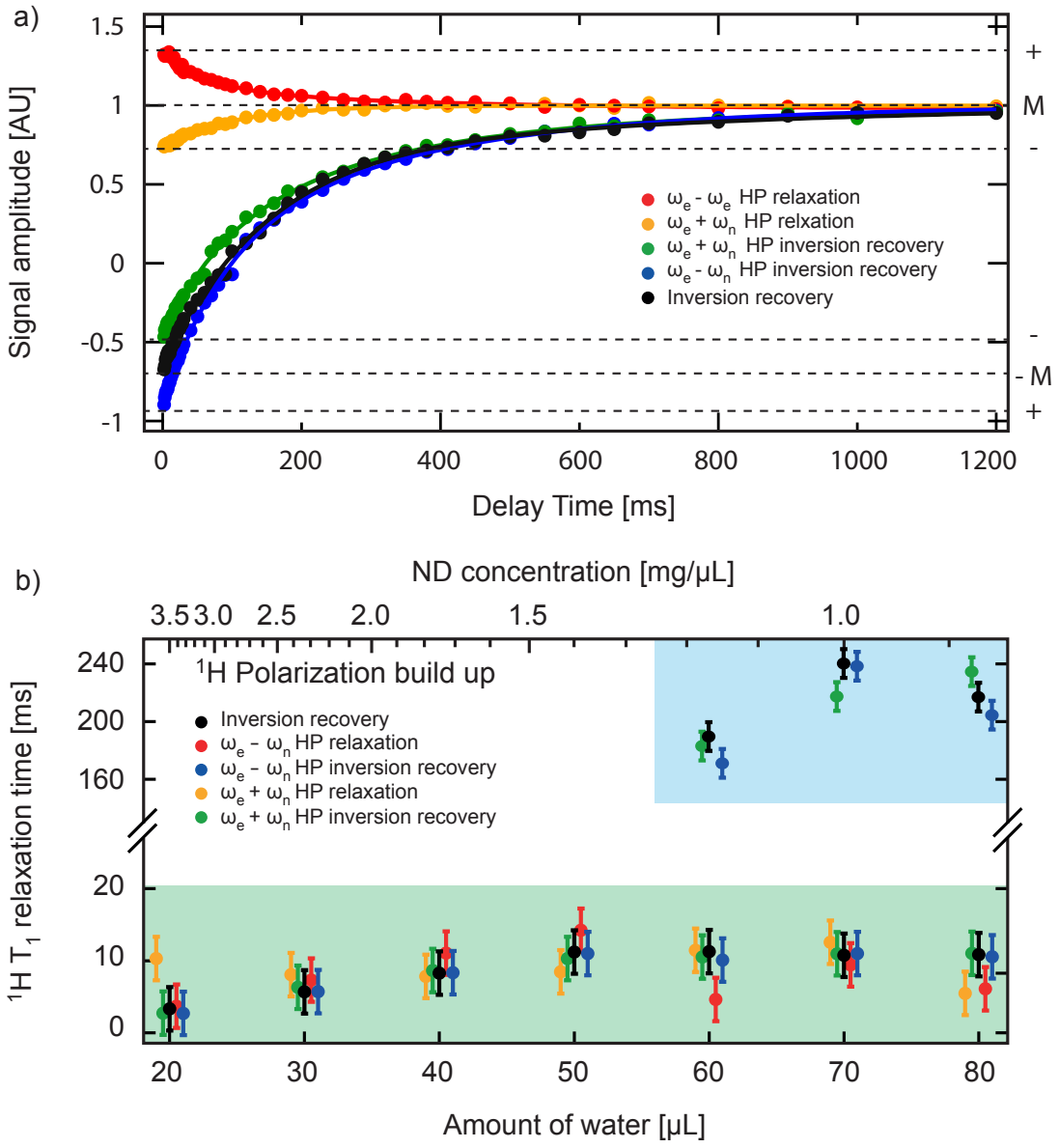

Figure 7.11: T_1 relaxation in adsorbed liquids. a) The ^{1}H signal amplitude (dots) as a function of delay time for an oil-ND mixture for the five relaxation sequences shown in Fig. 7.10. The solid lines are either exponential fits (red, orange) or double exponential fits (black, green and blue) to the data (dots) with relaxation times: red: $\tau = 100$ ms, yellow: $\tau = 104$ ms, blue: $\tau_1 = 90$ ms, $\tau_2 = 318$ ms, green: $\tau_1 = 85$ ms, $\tau_2 = 286$ ms, and black: $\tau_1 = 149$ ms, $\tau_2 = 1181$ ms. **b)** The ^{1}H T_1 relaxation time in a water-ND mixture as a function of water concentration. We always observe a short component to the relaxation ($\tau_1 \sim 10$ ms) and we begin to observe a long component ($\tau_2 \sim 200$ ms) in inversion experiments after 50 μL of water is added to the ND (dashed line). Data points are exponential and double exponential fits to the five relaxation experiments outlined in Fig. 7.10. Error bars are from the uncertainty in the exponential fit. Data points have been separated horizontally for clarity.

adsorbed on the ND surface, and a long T_1 from spins further away from the ND.

The amount of liquid that can be adsorbed onto the ND can be examined by measuring the ^{1}H T_1 relaxation times of the two spin baths as a function of liquid added, see Fig. 7.11b. Initially only one spin bath is seen for all five T_1 relaxation experiments. We observe a second spin bath with a longer relaxation time once the NP surface is saturated.

By examining the relaxation time of the adsorbed liquid, we are able to differentiate between water and oil adsorbed on the ND surface.

Next we explore the liquid adsorbed onto the ND surface by measuring the ^{1}H hyperpolarized signal amplitude and enhancement of the adsorbed liquid, see Fig. 7.12. We see that the amount of hyperpolarized signal, $S = S_{MWon} - S_{MWoff}$ (red), initially increases as oil is added until the ND surface is saturated, after which adding additional oil does not increase the hyperpolarized signal. The enhancement, $\epsilon = S_{MWon}/S_{MWoff}$ (blue), decreases steadily as oil is added, as adding additional unpolarized oil decreases the observed enhancement. We expect this saturation amount to change based upon the adsorbed liquid and ND particle size. These two techniques could be used to examine adsorption and desorption onto NDs in biological environments.

Examining hyperpolarized ND surfaces also gives us a tool for examining dynamics of ND-liquid mixtures, including spin diffusion and molecular diffusion.

When measuring the ^{1}H polarization build up in oil-ND mixture, we see different behaviour based on ND particle size, see Fig. 7.13. We see diffusion in the oil for small NDs sizes, where we see a continual increase of the ^{1}H signal with polarization time and no signal saturation, while we see saturation behavior and no diffusion for larger NDs. The signal increase could either be spin diffusion between adsorbed and non-adsorbed ^{1}H spins, sample diffusion, or hyperpolarized oil desorbing from the ND surface. We observe this behavior at long polarization times ($t_{pol} > 1s$) after heating of the ND-oil mixtures due to the hyperpolarization microwaves. We were unable to polarize longer than for 5 s due to heating effects on the samples.

7.5 Discussion

The spin dynamics of hyperpolarized molecules adsorbed onto the nanodiamond surface are examined using DNP. Hyperpolarization is mediated by the solid effect, with

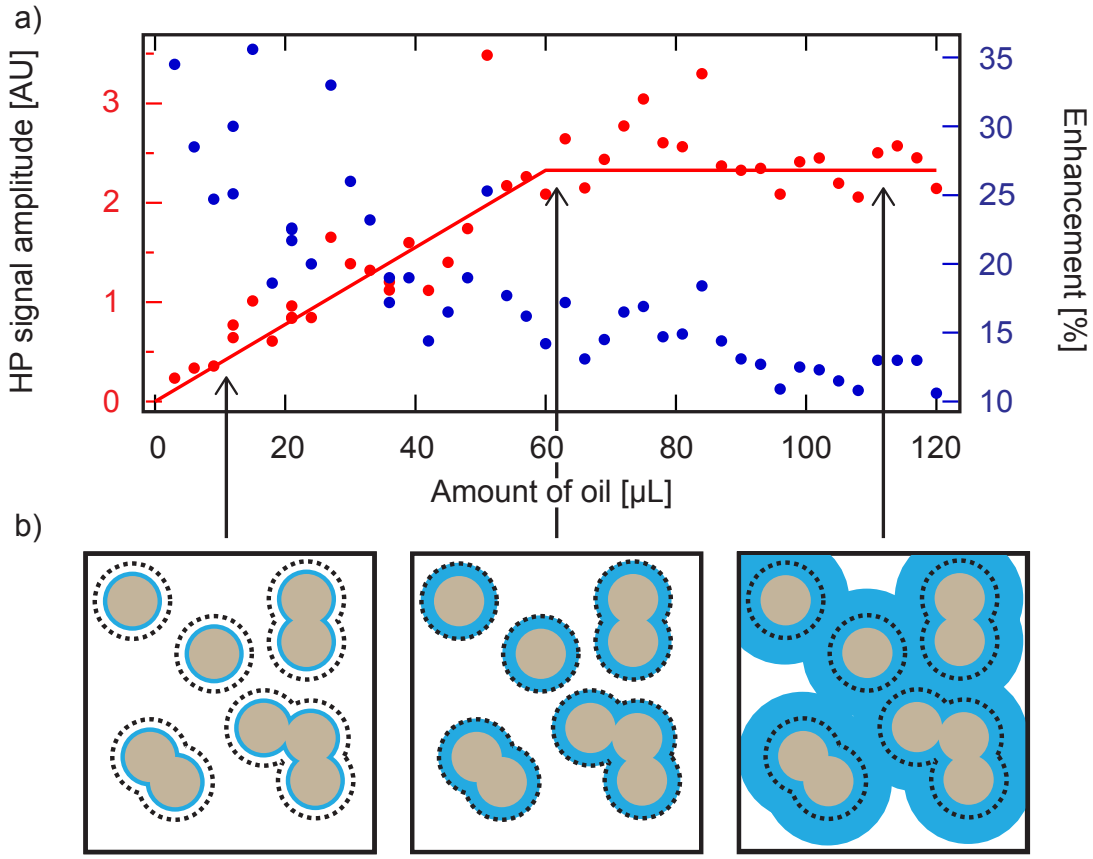

Figure 7.12: Probing adsorption using enhancement. a) Hyperpolarized ^{1}H signal amplitude (red) and enhancement (blue) for oil-ND mixture as a function of oil concentration. Saturation of the ND surface occurs after 60 µL of oil is added. The data points are the saturation values of polarization build up curves (at $f = \omega_e - \omega_n$). The solid red line is a guide to the eye. **b)** Schematic demonstrating liquid that is adsorbed onto the ND surface and hyperpolarized, until the ND surface is saturated. ND is shown in grey, liquid is shown in blue, and the hyperpolarization radius is indicated in black.

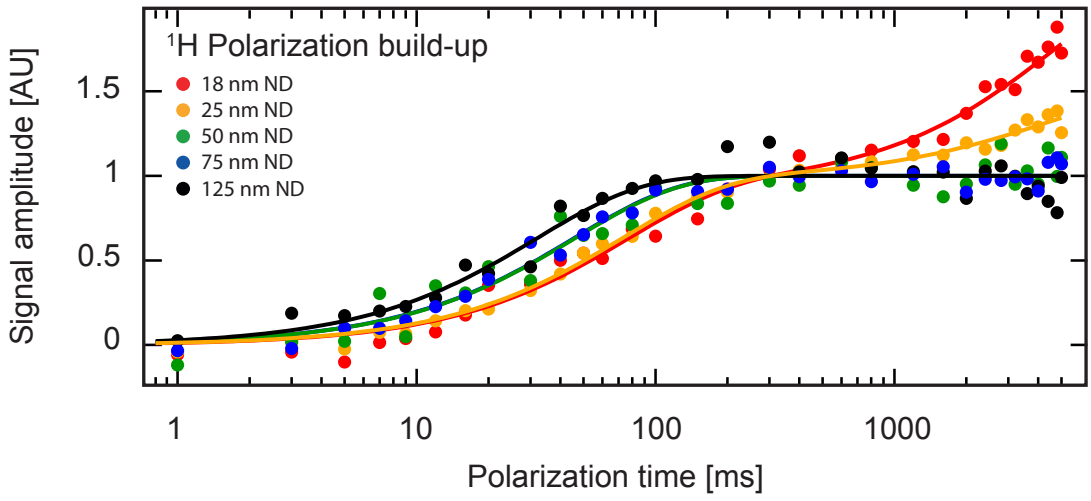

Figure 7.13: Hyperpolarization dynamics of adsorbed liquids. ^{1}H Polarization build up at $f = \omega_e - \omega_n$ in an oil-ND mixture for 18 nm ND (red), 25 nm ND (yellow), 50 nm ND (green), 75 nm ND (blue), and 125 nm ND (black). Solid lines are either exponential fits (50 nm, 75 nm and 125 nm ND) or double exponential fits (18 nm and 25 nm ND) to the data. The data has been corrected for heating effects [see Section 7.6]. The polarization build up times are: 18 nm ND: $\tau_1 = 72$ ms, $\tau_2 = 4.7$ s; 25 nm ND: $\tau_1 = 72$ ms, $\tau_2 = 4.4$ s; 50 nm ND: $\tau = 46$ ms; 75 nm ND: $\tau = 45$ ms; 125 nm ND: $\tau = 32$ ms. Data has been normalized such that 0 corresponds to the signal with no microwaves, and 1 corresponds to saturation of the fast component of the polarization build-up.

possible contributions from the cross effect at higher magnetic fields. T_1 relaxation times, hyperpolarization build up times and enhancement measurements allow for adsorbed liquids to be differentiated from non-adsorbed liquids surrounding the NDs. These methods can be used as a probe of adsorption and desorption mechanisms for nanoparticle bioagents with targeted delivery of chemotherapeutics.

DNP of nanodiamond surfaces could additionally be used as a spectroscopic technique to determine which compounds are attached to the ND. This method would be of particular interest in characterizing preferential adsorption.

The same defects on the ND surface have been used to both hyperpolarize ^{13}C spin in the ND and ^{1}H spins on the ND surface. These electrons may be used to mediate polarization transfer between ^{13}C and ^{1}H spins. This could enable a modality where polarization is stored in the ^{13}C spins in the ND and transferred to the ^{1}H spins for detection.

7.6 Methods

Nanodiamonds used. The nanodiamonds used in these experiments were purchased from Microdiamant. See Appendix A for a list of the NDs used.

Air Oxidation. HPHT NDs were spread in a thin layer and placed in a furnace at 550°C for 1 hr (with 1 hr of heating to reach 550°C and 20 min to return to room temperature).

Adsorption. Initially NDs were heated on a hot plate to remove any adsorbed water. The NDs were mixed with various liquids and sonicated. Adsorption occurred passively. The ND remained suspended in solution for the duration of the experiments.

Experimental setup. Signals were acquired with a single spaced solenoid coil in a home built NMR probe in a magnetic field range of $B = 300$ mT - 500 mT provided by either a permanent magnet ($B = 460\ mT$) or an electromagnet. X-band microwave irradiation was amplified to $P = 10$ W and coupled to the sample using a horn antenna and reflector. NMR signals were measured by initially polarizing the sample, then detecting the polarized signal using either a $\pi/2$ pulse or an echo ($\pi/2 - \tau - \pi$) pulse, and finally waiting for the polarization to return to thermal equilibrium. Data was acquired using either a Redstone NMR system (Tecmag) or a Spincore NMR system. Data processing and fitting was performed using IGOR pro, see Section 4.2.

SEM images. SEM measurements were made using a Zeiss Ultra Plus Gemini SEM spectrometer working in transmission mode. Suspensions were made of NDs in water and a small amount of the suspension was placed upon a TEM grid.

ESR measurements. ESR measurements were recorded using a Bruker EMX-plus X-Band ESR Spectrometer. ESR spectra were taken at 0.25 µW, (within the linear regime of the saturation curves of the impurities) at a modulation amplitude of 1 Gs, a modulation frequency of 100 kHz, and a Q-factor of 5,000. Each of the three components were simulated separately using Easyspin [195] and added together to make the final spectrum. Linewidth, signal amplitude and g-factor were varied. The best fit to the data was performed using a least squares analysis.

Raman spectra. Raman spectra were acquired with a Renishaw inVia Raman Microscope at $\lambda = 488$ nm and $P = 50$ µW.

Relaxivity Measurements. The T_1 polarization build up curves were fitted with an exponential fit $M/M_0 = 1 - 2e^{-t/T_1}$, where M is the Magnetization, M_0

is the equilibrium magnetization, T_1 is the spin lattice relaxation time and t is the polarization build up time. Relaxivity data was fitted with the curve for relaxivity $T_1 = 1/(1/T_{1pure} + R[C])$ where C is the concentration of nanodiamond, T_{1pure} is the T_1 relaxation time of pure (undoped) water and R is the relaxation rate. The water had a T_1 relaxation time of 2.6 s measured at 300 mT.

Hyperpolarization spectra of ND-liquid mixtures. For the ND-oil mixtures, approximately 50 mg of ND was mixed with 60 µL of oil. The mixtures were polarized for 300 ms, at $B = 458$ mT and for 1 s at other fields in the range $B = 300$ mT - 500 mT. For the ND-liquid mixtures in Fig. 7.8, 50 mg of ND was mixed with 30 µL of liquid. Mixtures were polarized for 300 ms. Solid lines are double lorentzian fits to $y = y_0 + \frac{a_1}{(x-x_1)^2+B_1} + \frac{a_2}{(x-x_2)^2+B_2}$.

T_1 relaxation. ND-oil mixtures: 70 mg of 18 nm ND was mixed with 60 µL of oil. Mixtures were polarized for 300 ms. ND-water mixtures: 70 mg of 18 nm ND was mixed with de-ionized water. Mixtures were polarized for 300 ms.

Enhancement as a function of oil concentration. 75 mg of 125 nm ND was mixed incrementally with oil. Polarization build up was measured out to 1 second and fitted with an exponential curve. All the curves reached saturation.

Polarization build up. 70 mg of ND was mixed with 40 µL of oil. With off-resonant microwaves, a signal decrease of 6% due to heating effects was seen after 1 second of polarization. Data with on-resonant microwaves was corrected for this heating effect.

7.7 Acknowledgments

For SEM measurements the authors acknowledge the facilities and technical assistance of the Australian Centre for Microscopy & Microanalysis at the University of Sydney. For Raman measurements the authors acknowledge the staff and facilities at the Vibrational Spectroscopy Core Facility at the University of Sydney. For ESR measurements the authors acknowledge the staff and facilities at the Nuclear Magnetic Resonance Facility at the Mark Wainwright Analytical Centre at the University of New South Wales. This work is supported by the Australian Research Council Centre of Excellence Scheme (Grant No. EQuS CE110001013) ARC DP1094439, and the Lockheed Martin Corporation.

7.8 Additional measurements

7.8.1 Hyperpolarization as a function of microwave frequency and polarization time.

Solid effect behavior is observed in the hyperpolarization spectra of ND-liquid mixtures at saturated polarization. Here we examine the hyperpolarization spectra to determine if there is a cross effect or Overhauser effect contribution at shorter polarization times. Hyperpolarization spectra were acquired for various polarization times ranging between $t_{pol} = 1$ μs and $t_{pol} = 300$ ms, see Fig. 7.14. The solid effect characteristics of a $f = 2\omega_n$ splitting between maximum and minimum polarization are present at all polarization times. A cross effect contribution would result in a narrower splitting, approaching $f = \omega_n$. Additionally we observe no evidence of polarization at $f = \omega_e$, ruling out any Overhauser contribution. We conclude that even for short polarization times, the hyperpolarization is dominated by the solid effect mechanism.

7.8.2 Polarization build up for various microwave powers.

The polarization build up time of adsorbed liquids was measured as a function of driving microwave power in order to examine the spin-dynamics of the nuclear spins under low power hyperpolarization conditions, see Fig. 7.15. The cross effect can be more efficient than the solid effect at low driving powers, and testing the polarization build up times as a function of power may determine if this hyperpolarization mechanism is contributing to the signal enhancement.

We observe no change in polarization build up time over the range of measured powers spanning two orders of magnitude. We observe heating effects for longer polarization times, and the maximum ^{1}H signal amplitude occurs for medium polarization times. We see a decrease in enhancement with decreasing power, however the maximum enhancement does not occur at the maximum power, probably due to heating effects leading to signal loss at the highest microwave powers. We observe no evidence for an additional hyperpolarization mechanism other than the solid effect.

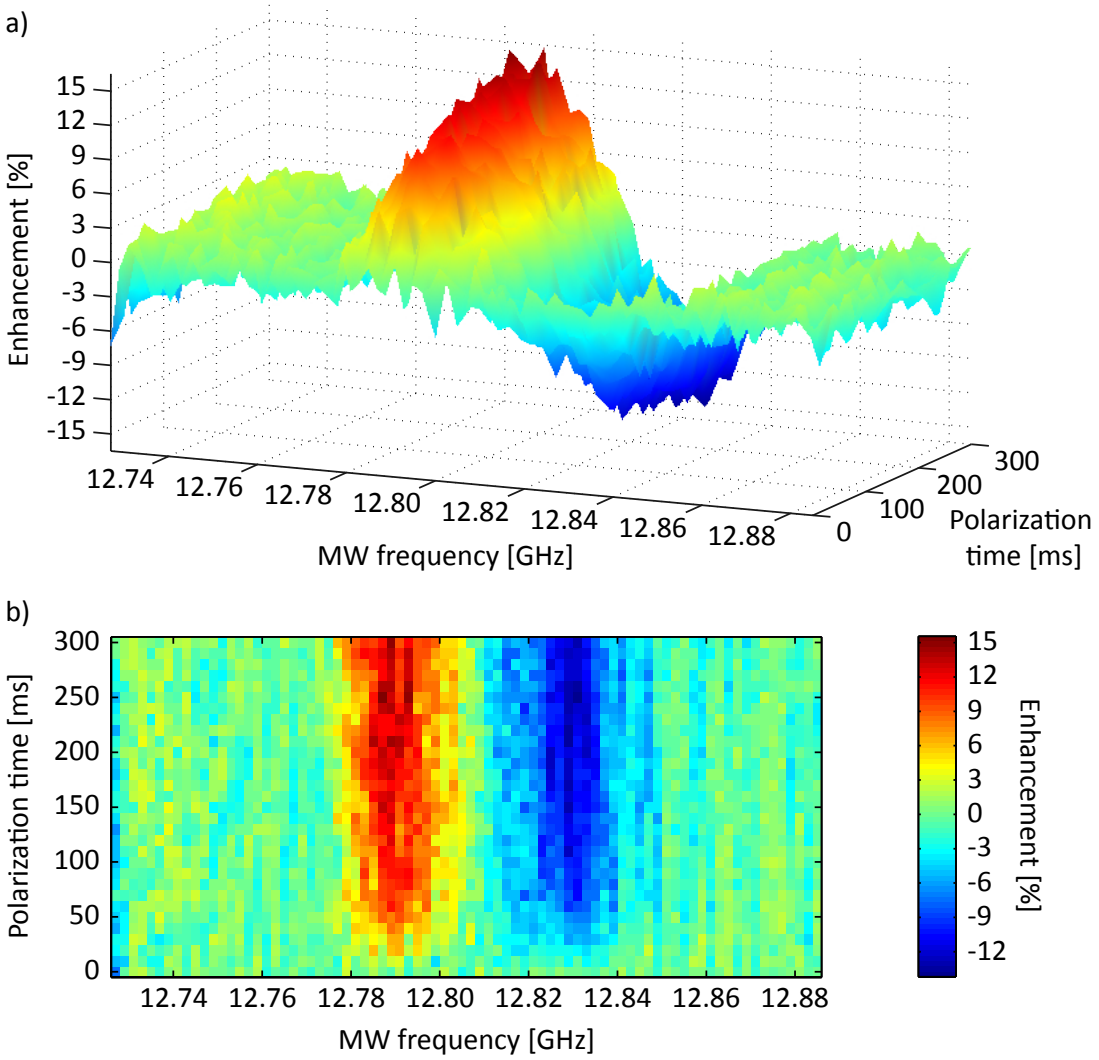

Figure 7.14: Hyperpolarization as a function of microwave frequency and polarization time. a) A 3D plot and **b)** a surface plot of the ^{1}H NMR signal enhancement from an oil-ND mixture with 125 nm HPHT ND as a function of driving microwave frequency and polarization time at $B = 458$ mT. Red corresponds to positive enhancement, green corresponds to no enhancement and blue corresponds to negative enhancement. Data has been normalized to the signal with no driving microwaves.

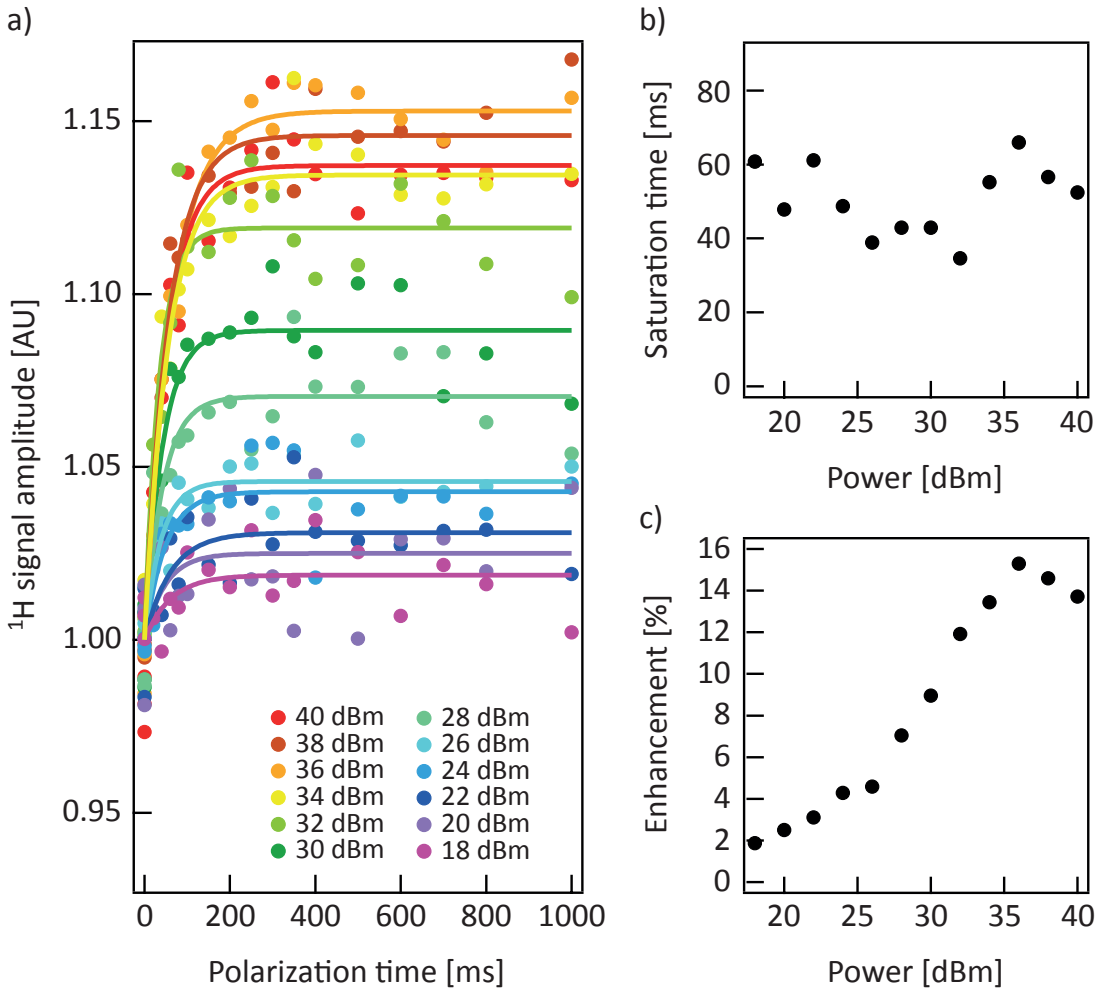

Figure 7.15: Polarization build up as a function of microwave power. a) Polarization build up in an acetic acid-ND mixture with 70 mg of 125 nm ND mixed with 30 µL of acetic acid. Polarization build up was measured at $B = 458$ mT, driving the system for positive polarization enhancement at $f = \omega_e - \omega_n$. Solid lines are exponential fits to the data (dots). **b)** Polarization build up time and **c)** enhancements are extracted from an exponential fit to the polarization build up curves. Enhancement is given by the saturation value of the exponential divided by the signal with no microwaves. The power stated is the power at the output of the power amplifier. We expect some loss from propagation through the waveguide and coupling from the horn antenna.

7.8.3 Quenching of the ^{1}H signal in a water-ND mixture

The free electrons on the surface of the NDs shift the Zeeman energies of nearby nuclear spins. These spins will have shifted resonance frequencies and will not contribute to an NMR line, see Fig. 3.6. This quenching behavior will effect both ^{13}C spins in the ND and nuclear spins such as ^{1}H in liquids surrounding the NDs. A measure of the amount of quenched NMR signal from ^{1}H spins surrounding the ND gives an indication of the amount of impurities on the ND surface.

Quenching of the ^{1}H NMR signal was more evident for small NDs, such as in the 18 nm ND-water mixture where 50 % of the ^{1}H NMR signal was lost, than for large NDs, such as the 1 μm ND-water mixture where almost no quenching was seen, see Fig. 7.16.

Small NDs have a larger surface to volume ratio, and more surface spins than large NDs (see Fig. 5.12a) and as a result more ^{1}H spins will be within the quenching radius of the small NDs. This difference in surface spins and proximal water for small and large NDs is illustrated in a schematic in Figs. 7.16c, d.

Adding 10 μL of water to 25 mg of ND was sufficient to saturate the ND surface, and no additional quenching was seen when more water was added.

The ^{1}H signal lost when adding water to ND as a probe of surface spins is consistent with ESR and Raman studies, showing that smaller NDs have more surface impurities, and hence have more of an effect on water than larger NDs.

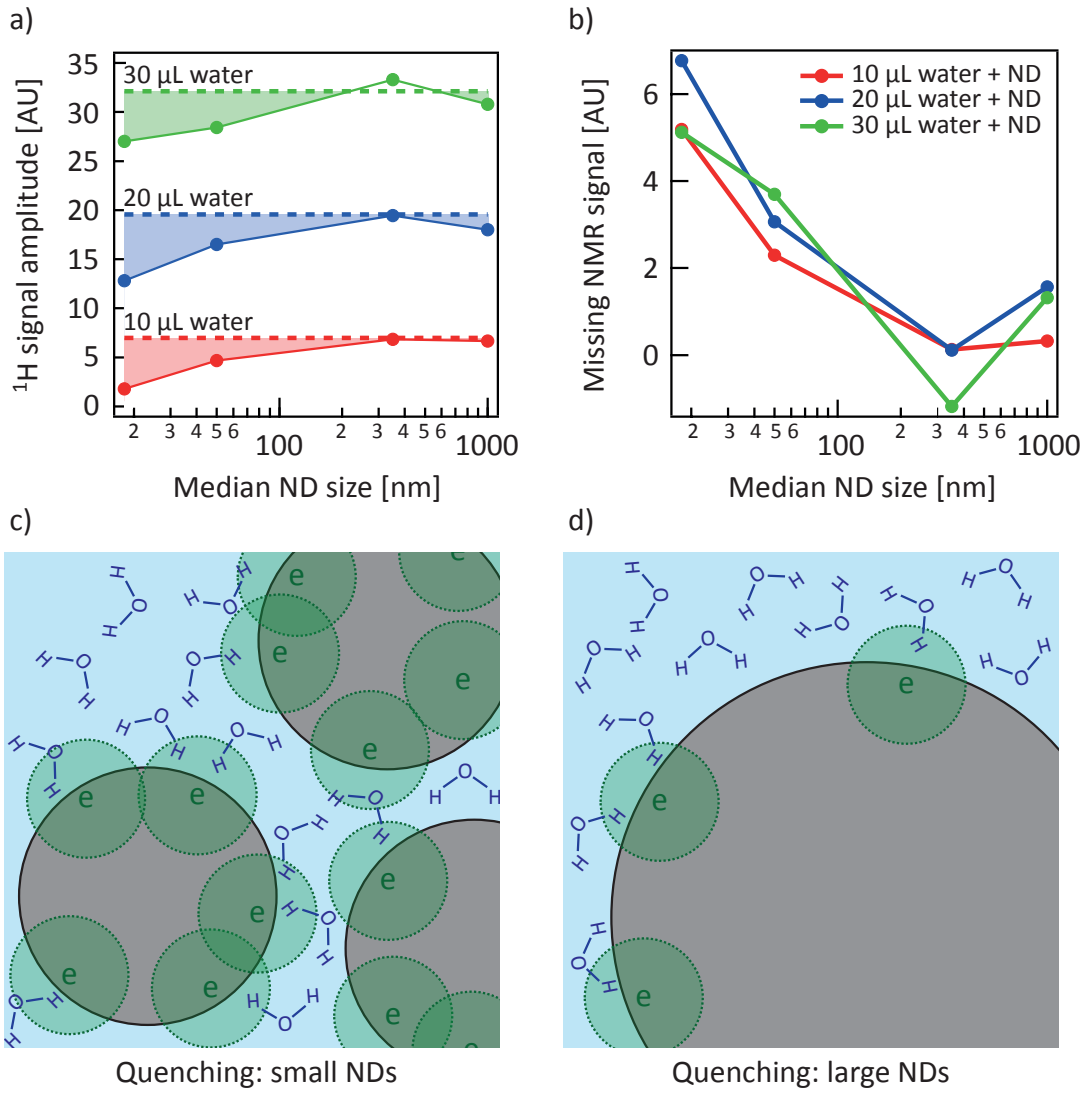

Figure 7.16: Quenching of ^{1}H signal in a water-ND mixture. a) The ^{1}H signal amplitude from water mixed with 25 mg of ND, with 10 µL of water (red dots), 20 µL of water (blue dots), and 30 µL of water (green dots). The signal from water with no ND is shown as a dashed line. The quenched NMR signal is shaded in and shown in b). NMR measurements were acquired at $B = 460$ mT and each data point is the average of three measurements. We see more quenching for small NDs and almost no signal loss for large NDs. **c, d)** Schematic of ND-water mixtures. ND is shown in grey, the quenching radius around surface electrons (e) is shown in green and water is shown in blue.

8

Conclusion and future outlook

When this project started the field of hyperpolarized magnetic resonance imaging was beginning to emerge. Liquid state metabolites had been polarized [36] and had recently been used to detect tumor response in a mouse [37]. This field has since grown considerably, and has resulted in the first human trials of hyperpolarized ^{13}C metabolites [43]. Commercial sterile polarizers are now available, making in-vivo hyperpolarization studies easier and more common place in research institutes around the world.

The idea to use solid nanoparticles with longer relaxation times had just been proposed using ^{29}Si [45], and the first silicon nanoparticle hyperpolarization experiments were underway [45, 242]. Now, the first in-vivo MRI images of hyperpolarized silicon nanoparticle have been demonstrated [38], with use in applications such as catheter tracking [243].

At the time this project started, nanodiamonds were emerging as a new bioagent. Within the last few years they had been found to be non-toxic [17], had been surface functionalized [19], and been used for medical applications in-vivo [18]. Bulk diamond hyperpolarization using DNP techniques, and magnetization relaxation pathways, were well understood [95], and other bulk diamond hyperpolarization techniques involving optical pumping had recently been demonstrated [47]. None of these hyperpolarization techniques had yet to be applied to nanodiamonds. Over the past few years, significant effort has been made to polarize ND, with demonstrations using DNP techniques [51,52] and proposals using optical techniques [50, 92].

In this thesis we set out to demonstrate ND's suitability as a contrast agent for hyperpolarized MRI. This project has been a success with ND demonstrating all the

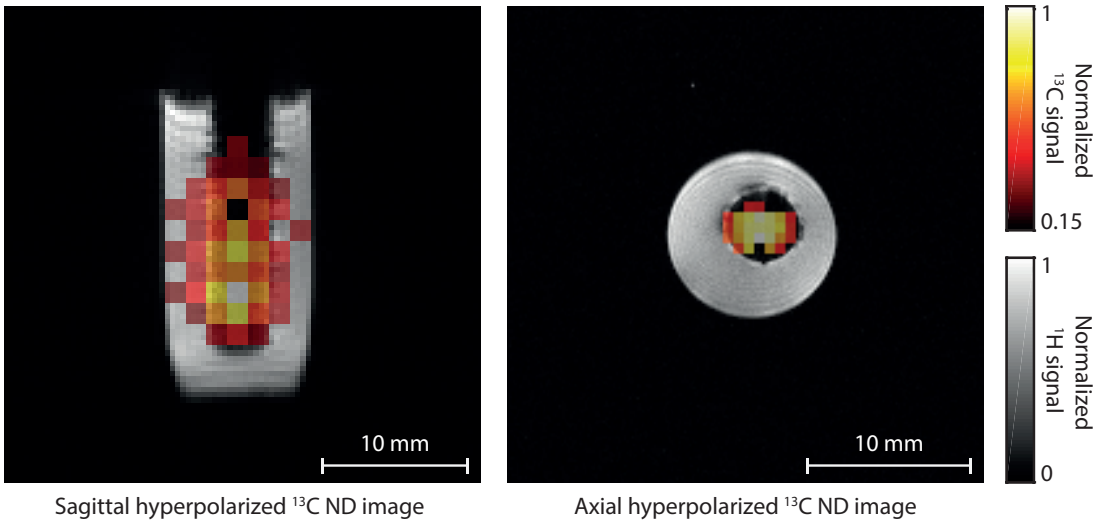

Figure 8.1: Co-registered ^{1}H/^{13}C MRI image of hyperpolarized ND in a phantom. Sagittal and axial ^{13}C (colour scale) and ^{1}H (black and white scale) images of a phantom. The phantom consists of a 4 mm tube of hyperpolarized ND surrounded by a 10 mm tube of water. ND was polarized at $T = 4$ K for 20 min at $f = 80.89$ GHz before being transferred to the MRI imager for signal detection. Imaging capability was established by David Waddington and Torsten Gaebel. MRI images are courtesy of David Waddington, Torsten Gaebel and Thomas Boele.

necessary aspects for a suitable bioagent.

We demonstrated that the intrinsic free electrons in ND can be used to drive electron nuclear flip-flops, producing a ^{13}C nuclear polarization comparable to that used in liquid state hyperpolarization experiments ($\epsilon \sim 13{,}500$ when compared to room temperatures signals). The NDs have long T_1 relaxation times, and as a result the hyperpolarized state exists for a long time (~ 1 hr), even when transferred from the polarizer. These results lay the groundwork for demonstrating ^{13}C ND hyperpolarized MRI. Towards this goal, the hyperpolarizer in this thesis has been combined with microimaging capabilities, and we have demonstrated the first hyperpolarized ^{13}C ND MRI imaging in a phantom, see Fig. 8.1. Next steps involve demonstrating hyperpolarized ^{13}C ND MRI in-vivo.

One of the main challenges of solid nanoparticle MRI is ensuring sufficient spatial resolution, despite the short T_2 relaxation times inherent in solids. We found that this limitation can be overcome in ND by using CPMG, which extends the T_2 relaxation

time, and imaging window for MRI. How hyperpolarization affects these long tails is not yet understood, and we are continuing measurements to observe this phenomenon, both for MRI pulse sequence design, and to gain an understanding of the spin-spin dynamics in the system.

Surprisingly we found that we could still achieve moderate polarization in ND at room temperature. This opens the possibility of direct in-vivo hyperpolarization. To demonstrate this new imaging modality, we demonstrated room temperature ND hyperpolarization in the presence of water, with plans to directly polarize and detect ND in tissues at low magnetic fields.

Improvements in the hyperpolarization process and the polarization transfer will lead to larger ND polarizations and hence larger signal amplitudes, and longer imaging windows for MRI. Using lower temperatures, higher driving microwave powers, microwave cavities, and frequency modulation can all lead to increased polarization. The transfer process can be improved using permanent magnet tunnels to keep a high field on the ND during transfer. Although a significant engineering challenge, incorporating the hyperpolarization setup with a dilution refrigerator and hot swap probe for DNP at mK temperatures could lead to significantly larger polarizations.

These experiments were performed using commercially available nanodiamonds, and it is perhaps surprising that these diamonds have the right concentration of impurities to both polarize the nuclear spins, while still retaining long nuclear relaxation times. There is scope however, to modify both the electron defect concentration and the $^{13}C/^{12}C$ ratio. Although increasing the ^{13}C concentration will lead to a larger NMR signal, T_1 and T_2 will likely shorten for high ^{13}C concentrations, and the system will move from one with limited spin diffusion, to one where spin diffusion plays a larger role in polarization transfer. Decreases in T_2 will make imaging applications harder, and will reduce signal amplitudes. A ^{13}C concentration 'sweet spot' for T_1, T_2, and enhancement, for a certain defect concentration, will exist, and this would be a very interesting study to perform. Additionally ND could be a good system to study spin diffusion, hyperpolarization dynamics, and T_1 and T_2 mechanisms, as a function of electron defect concentrations.

For nanodiamonds to be an effective bioagent, the nanoparticle characteristics after functionalization must be controlled and monitored. For this we have examined the nanodiamond surface through solid effect hyperpolarization of ^1H in adsorbed liquids

using intrinsic electrons on the surface of ND. We can distinguish between molecules adsorbed onto the ND from surrounding liquid molecules based on hyperpolarization enhancement, T_1 build up and relaxation times. These techniques could aid in characterizing ND surface functionalization and desorption mechanisms for targeted drug delivery. We also demonstrate how ND can be used as a contrast agent to modify the T_1 relaxation time of water, with ongoing work demonstrating ND as a T_1 and T_2 contrast agent currently underway.

Over the past ten years, there have been vast advances in both the fields of hyperpolarized MRI and DNP of nanoparticles. May the next ten show an overlap of these two very interesting and developing fields.

Appendix A

Nanodiamonds used in this thesis

A summary of the NDs used in this study are listed in the following tables. HPHT and NAT diamonds were purchased from Microdiamant[1]. AO NDs were HPHT NDs purchased from Microdiamant, which were air oxidized to remove surface defects.

[1] http://www.microdiamant.com

ND	Size range (μm)	Median size (μm)	Product
18 nm HPHT	0-0.03	0.018	MSY 0-0.03
25 nm HPHT	0-0.05	0.025	MSY 0-0.05
50 nm HPHT	0-0.1	0.050	MSY 0-0.1
75 nm HPHT	0-0.15	0.075	MSY 0-0.15
90 nm HPHT	0-0.2	0.090	MSY 0-0.2
125 nm HPHT	0-0.25	0.125	MSY 0-0.25
180 nm HPHT	0-0.35	0.180	MSY 0-0.35
210 nm HPHT	0-0.5	0.210	MSY 0-0.5
350 nm HPHT	0.25-0.5	0.350	MSY 0.25-0.5
500 nm HPHT	0.25-0.75	0.500	MSY 0.25-0.75
710 nm HPHT	0.5-1	0.71	MSY 0.5-1
1 μm HPHT	0.75-1.25	1.00	MSY 0.75-1.25
1.19 μm HPHT	1-1.5	1.19	MSY 1-1.5
1.42 μm HPHT	1-2	1.42	MSY 1-2
1.69 μm HPHT	1.25-2.25	1.69	MSY 1.25-2.25
2 μm HPHT	1.5-2.5	2.00	MSY 1.5-2.5
40 μm HPHT	35-45	40.0	MSY 35-45

Table A.1: HPHT NDs. List of HPHT ND powders used in these experiments.

ND	Size range (μm)	Median size (μm)	Product
18 nm AO	0-0.03	0.018	MSY 0-0.03
25 nm AO	0-0.05	0.025	MSY 0-0.05
50 nm AO	0-0.1	0.050	MSY 0-0.1
90 nm AO	0-0.2	0.090	MSY 0-0.2
125 nm AO	0-0.25	0.125	MSY 0-0.25
180 nm AO	0-0.35	0.180	MSY 0-0.35
210 nm AO	0-0.5	0.210	MSY 0-0.5
350 nm AO	0.25-0.5	0.350	MSY 0.25-0.5
500 nm AO	0.25-0.75	0.500	MSY 0.25-0.75
710 nm AO	0.5-1	0.71	MSY 0.5-1
1 μm AO	0.75-1.25	1.00	MSY 0.75-1.25
1.42 μm AO	1-2	1.42	MSY 1-2
2 μm AO	1.5-2.5	2.00	MSY 1.5-2.5

Table A.2: AO NDs. List of air oxidized ND powders used in these experiments.

ND	Size range (μm)	Median size (μm)	Product
125 nm NAT	0-0.25	0.125	NAT 0-0.25
210 nm NAT	0-0.5	0.210	NAT 0-0.5
500 nm NAT	0.25-0.75	0.500	NAT 0.25-0.75
2 μm NAT	1.5-2.5	2.00	NAT 1.5-2.5

Table A.3: NAT NDs. List of natural ND powders used in these experiments.

References

[1] Wang, M. & Thanou, M. Targeting nanoparticles to cancer. *Pharmacological Research* **62**, 90–99 (2010). 1, 100, 136

[2] Li, C. A targeted approach to cancer imaging and therapy. *Nature materials* **13**, 110–115 (2014). 1, 100, 136

[3] Getts, D. R. *et al.* Therapeutic inflammatory monocyte modulation using immune-modifying microparticles. *Science translational medicine* **6**, 219ra7 (2014). 1, 100

[4] Gupta, A. S. Nanomedicine approaches in vascular disease: a review. *Nanomedicine: Nanotechnology, Biology and Medicine* **7**, 763–779 (2011). 1, 100

[5] Singh, N. *et al.* Bioresponsive mesoporous silica nanoparticles for triggered drug release. *Journal of the American Chemical Society* **133**, 19582–19585 (2011). 1

[6] Sun, X. *et al.* Nano-graphene oxide for cellular imaging and drug delivery. *Nano research* **1**, 203–212 (2008). 1

[7] Liu, Z. *et al.* Drug delivery with carbon nanotubes for in vivo cancer treatment. *Cancer research* **68**, 6652–6660 (2008). 1

[8] Choi, J. *et al.* Core-shell silica nanoparticles as fluorescent labels for nanomedicine. *Journal of biomedical optics* **12**, 064007 (2007). 1

[9] Soppimath, K. S., Aminabhavi, T. M., Kulkarni, A. R. & Rudzinski, W. E. Biodegradable polymeric nanoparticles as drug delivery devices. *Journal of controlled release* **70**, 1–20 (2001). 1

[10] Tang, B. C. *et al.* Biodegradable polymer nanoparticles that rapidly penetrate the human mucus barrier. *Proceedings of the National Academy of Sciences* **106**, 19268–19273 (2009). 1

[11] Tasciotti, E. *et al.* Mesoporous silicon particles as a multistage delivery system for imaging and therapeutic applications. *Nature nanotechnology* **3**, 151–157 (2008). 1

[12] Park, J.-H. *et al.* Biodegradable luminescent porous silicon nanoparticles for in vivo applications. *Nature materials* **8**, 331–336 (2009). 1

[13] Matsumura, Y. & Maeda, H. A new concept for macromolecular therapeutics in cancer chemotherapy: mechanism of tumoritropic accumulation of proteins and the antitumor agent smancs. *Cancer research* **46**, 6387–6392 (1986). 1

[14] Jain, R. K. Delivery of molecular medicine to solid tumors. *Science* **271**, 1079 (1996). 1

[15] Bakowicz-Mitura, K., Bartosz, G. & Mitura, S. Influence of diamond powder particles on human gene expression. *Surface and Coatings Technology* **201**, 6131–6135 (2007). 1

[16] Schrand, A. M. *et al.* Are diamond nanoparticles cytotoxic? *The journal of physical chemistry B* **111**, 2–7 (2007). 1

[17] Liu, K.-K., Cheng, C.-L., Chang, C.-C. & Chao, J.-I. Biocompatible and detectable carboxylated nanodiamond on human cell. *Nanotechnology* **18**, 325102 (2007). 1, 100, 136, 161

[18] Huang, H., Pierstorff, E., Osawa, E. & Ho, D. Active nanodiamond hydrogels for chemotherapeutic delivery. *Nano letters* **7**, 3305–3314 (2007). 1, 2, 100, 136, 161

[19] Krüger, A., Liang, Y., Jarre, G. & Stegk, J. Surface functionalisation of detonation diamond suitable for biological applications. *Journal of Materials Chemistry* **16**, 2322–2328 (2006). 1, 73, 100, 136, 161

[20] Mochalin, V. N., Shenderova, O., Ho, D. & Gogotsi, Y. The properties and applications of nanodiamonds. *Nature nanotechnology* **7**, 11–23 (2012). 1, 96

[21] Say, J. M. *et al.* Luminescent nanodiamonds for biomedical applications. *Biophysical Reviews* **3**, 171–184 (2011). 1, 100, 136

[22] Zhang, X.-Q. *et al.* Polymer-functionalized nanodiamond platforms as vehicles for gene delivery. *ACS nano* **3**, 2609–2616 (2009). 2

[23] Chen, M. *et al.* Nanodiamond-mediated delivery of water-insoluble therapeutics. *ACS Nano* **3**, 2016–2022 (2009). 2, 100, 136

[24] Chow, E. K. *et al.* Nanodiamond therapeutic delivery agents mediate enhanced chemoresistant tumor treatment. *Science translational medicine* **3**, 73ra21 (2011). 2, 73, 100, 106, 123, 136

[25] Kossovsky, N. *et al.* Surface-modified diamond nanoparticles as antigen delivery vehicles. *Bioconjugate chemistry* **6**, 507–511 (1995). 2

[26] McGuinness, L. *et al.* Quantum measurement and orientation tracking of fluorescent nanodiamonds inside living cells. *Nature nanotechnology* **6**, 358–363 (2011). 2, 71, 100, 136

[27] Maze, J. *et al.* Nanoscale magnetic sensing with an individual electronic spin in diamond. *Nature* **455**, 644–647 (2008). 2, 71, 100, 136

[28] Balasubramanian, G. *et al.* Nanoscale imaging magnetometry with diamond spins under ambient conditions. *Nature* **455**, 648–651 (2008). 2, 71, 100, 136

[29] Bhallamudi, V. P. & Hammel, P. C. Nitrogen-vacancy centres: Nanoscale MRI. *Nature nanotechnology* **10**, 104–106 (2015). 2

[30] Rugar, D. *et al.* Proton magnetic resonance imaging using a nitrogen–vacancy spin sensor. *Nature nanotechnology* **10**, 120–124 (2015). 2

[31] Häberle, T., Schmid-Lorch, D., Reinhard, F. & Wrachtrup, J. Nanoscale nuclear magnetic imaging with chemical contrast. *Nature nanotechnology* **10**, 125–128 (2015). 2

[32] Brenneis, A. *et al.* Ultrafast electronic readout of diamond nitrogen–vacancy centres coupled to graphene. *Nature nanotechnology* **10**, 135–139 (2015). 2

[33] DeVience, S. J. *et al.* Nanoscale NMR spectroscopy and imaging of multiple nuclear species. *Nature nanotechnology* **10**, 129–134 (2015). 2

[34] Popovtzer, R. *et al.* Targeted gold nanoparticles enable molecular CT imaging of cancer. *Nano letters* **8**, 4593–4596 (2008). 2

[35] Devaraj, N. K., Keliher, E. J., Thurber, G. M., Nahrendorf, M. & Weissleder, R. ^{18}F labeled nanoparticles for in vivo PET-CT imaging. *Bioconjugate chemistry* **20**, 397–401 (2009). 2

[36] Ardenkjær-Larsen, J. H. *et al.* Increase in signal–to–noise ratio of > 10,000 times in liquid–state NMR. *Proceedings of the National Academy of Sciences* **100**, 10158–10163 (2003). 2, 100, 161

[37] Day, S. E. *et al.* Detecting tumor response to treatment using hyperpolarized ^{13}C magnetic resonance imaging and spectroscopy. *Nature medicine* **13**, 1382–1387 (2007). 2, 3, 100, 161

[38] Cassidy, M., Chan, H., Ross, B., Bhattacharya, P. & Marcus, C. M. In vivo magnetic resonance imaging of hyperpolarized silicon particles. *Nature nanotechnology* **8**, 363–368 (2013). 2, 3, 100, 125, 161

[39] Fain, S. B. *et al.* Functional lung imaging using hyperpolarized gas MRI. *Journal of Magnetic Resonance Imaging* **25**, 910–923 (2007). 3, 30

[40] Zacharias, N. M., Chan, H. R., Sailasuta, N., Ross, B. D. & Bhattacharya, P. Real–time molecular imaging of tricarboxylic acid cycle metabolism in vivo by hyperpolarized 1-^{13}C diethyl succinate. *J. Am. Chem. Soc.* **134**, 034–943 (2012). 3

[41] Keshari, K. R. *et al.* Hyperpolarized ^{13}C dehydroascorbate as an endogenous redox sensor for in vivo metabolic imaging. *PNAS* **108**, 18606–18611 (2011). 3

[42] Gallagher, F. A., Kettunen, M. I., Day, S. E., Hu, D. & Larsen, J. H. A. Magnetic resonance imaging of pH in vivo using hyperpolarized ^{13}C-labelled bicarbonate. *Nature* **453**, 940–943 (2008). 3

[43] Nelson, S. J. *et al.* Metabolic imaging of patients with prostate cancer using hyperpolarized [1-^{13}C] pyruvate. *Science translational medicine* **5**, 198ra108 (2013). 3, 100, 161

[44] Keshari, K. R. & Wilson, D. M. Chemistry and biochemistry of ^{13}C hyperpolarized magnetic resonance using dynamic nuclear polarization. *Chemical Society Reviews* **43**, 1627–1659 (2014). 3, 100, 105

[45] Aptekar, J. *et al.* Hyperpolarized long-T_1 silicon nanoparticles for magnetic resonance imaging. *arXiv preprint arXiv:0902.0269* (2009). 3, 161

[46] Hoch, M. & Reynhardt, E. Nuclear spin-lattice relaxation of dilute spins in semiconducting diamond. *Physical Review B* **37**, 9222 (1988). 3, 37, 79, 100, 105

[47] King, J. P., Coles, P. J. & Reimer, J. A. Optical polarization of ^{13}C nuclei in diamond through nitrogen vacancy centers. *Physical Review B* **81**, 073201 (2010). 3, 32, 100, 161

[48] Fischer, R., Jarmola, A., Kehayias, P. & Budker, D. Optical polarization of nuclear ensembles in diamond. *Physical Review B* **87**, 125207 (2013). 3, 32, 100

[49] Álvarez, G. A. *et al.* Local and bulk ^{13}C hyperpolarization in nitrogen-vacancy-centred diamonds at variable fields and orientations. *Nature communications* **6**, 8456 (2015). 3, 32, 100

[50] King, J. P. *et al.* Room-temperature in situ nuclear spin hyperpolarization from optically pumped nitrogen vacancy centres in diamond. *Nature communications* **6**, 8965 (2015). 3, 32, 100, 161

[51] Casabianca, L. B., Shames, A. I., Panich, A. M., Shenderova, O. & Frydman, L. Factors affecting DNP NMR in polycrystalline diamond samples. *The Journal of Physical Chemistry C* **115**, 19041–19048 (2011). 3, 33, 79, 101, 136, 161

[52] Dutta, P., Martinez, G. V. & Gillies, R. J. Nanodiamond as a new hyperpolarizing agent and its ^{13}C MRS. *The journal of physical chemistry letters* **5**, 597–600 (2014). 3, 33, 101, 136, 161

[53] Rabi, I. I., Zacharias, J. R., Millman, S. & Kusch, P. A new method of measuring nuclear magnetic moment. *Phys. Rev.* **53**, 318–318 (1938). 7

[54] Bloch, F. Nuclear induction. *Phys. Rev.* **70**, 460–474 (1946). 7

[55] Bloch, F., Hansen, W. W. & Packard, M. The nuclear induction experiment. *Phys. Rev.* **70**, 474–485 (1946). 7

[56] Bloembergen, N., Purcell, E. M. & Pound, R. V. Relaxation effects in nuclear magnetic resonance absorption. *Phys. Rev.* **73**, 679–712 (1948). 7

[57] Purcell, E. M., Torrey, H. C. & Pound, R. V. Resonance absorption by nuclear magnetic moments in a solid. *Phys. Rev.* **69**, 37–38 (1946). 7

[58] Lauterbur, P. C. Image formation by induced local interactions: examples employing nuclear magnetic resonance. *Nature* **242**, 190–191 (1973). 7

[59] Lauterbur, P. C. Magnetic resonance zeugmatography. *Pure and Applied Chemistry* **40**, 149–157 (1974). 7

[60] Hutchinson, J. M. S., Edelstein, W. A. & Johnson, G. A whole-body NMR imaging machine. *Journal of Physics E: Scientific Instruments* **13**, 947–955 (1980). 7

[61] Smith, F. *et al.* Clinical application of nuclear magnetic resonance. *The Lancet* **317**, 78–79 (1981). 7

[62] Pollet, J. E., Smith, F. W., Mallard, J. R., Ah-See, A. K. & Reid, A. Whole–body nuclear magnetic resonance imaging: The first report of its use in surgical practice. *British Journal of Surgery* **68**, 493–494 (1981). 7

[63] Slichter, C. P. *Principles of Magnetic Resonance* (Springer, New York, 1990). 7

[64] Abragam, A. *The Principles of Nuclear Magnetism* (Oxford, Clarendon, 1962). 7

[65] Keeler, J. *Understanding NMR spectroscopy* (John Wiley & Sons, England, 2005). 7

[66] Corvaja, C. *Electron Paramagnetic Resonance, A practitioner's Toolkit, Introduction to Electron Paramagnetic Resonance* (John Wiley & Sons, New Jersey, 2009). 7

[67] Hahn, E. L. Spin echoes. *Phys. Rev.* **80**, 580–594 (1950). 25

[68] Carr, H. Y. & Purcell, E. M. Effects of diffusion on free precession in nuclear magnetic resonance experiments. *Phys. Rev.* **94**, 630–638 (1954). 27

[69] Meiboom, S. & Gill, D. Modified spinecho method for measuring nuclear relaxation times. *Review of Scientific Instruments* **29**, 688–691 (1958). 27

[70] Wenckebach, W. The solid effect. *Appl. Magn. Reson.* **34**, 227–237 (2008). 29

[71] Abragam, A. & Goldman, M. Principles of dynamic nuclear polarisation. *Reports on Progress in Physics* **41**, 395 (1978). 29, 39, 105

[72] Goldman, M. Overview of spin temperature, thermal mixing and dynamic nuclear polarization. *Applied Magnetic Resonance* **34**, 219–226 (2008). 29

[73] Goldman, M. *Spin Temperature and Nuclear Magnetic Resonance in Solids* (Oxford University Press, Great Britain, 1970). 29

[74] Maly, T. *et al.* Dynamic nuclear polarization at high magnetic fields. *The Journal of Chemical Physics* **128**, 052211 (2008). 29

[75] Bowers, C. R. & Weitekamp, D. P. Parahydrogen and synthesis allow dramatically enhanced nuclear alignment. *Journal of the American Chemical Society* **109**, 5541–5542 (1987). 30

[76] Blankenship, R., McGuire, A. & Sauer, K. Chemically induced dynamic electron polarization in chloroplasts at room temperature: evidence for triplet state participation in photosynthesis. *Proceedings of the National Academy of Sciences* **72**, 4943–4947 (1975). 30

[77] Harrison, J., Sellars, M. & Manson, N. Measurement of the optically induced spin polarisation of N-V centres in diamond. *Diamond and Related Materials* **15**, 586 – 588 (2006). 30

[78] Manson, N. B., Harrison, J. P. & Sellars, M. J. Nitrogen-vacancy center in diamond: Model of the electronic structure and associated dynamics. *Phys. Rev. B* **74**, 104303 (2006). 30

[79] Walker, T. G. & Happer, W. Spin-exchange optical pumping of noble-gas nuclei. *Rev. Mod. Phys.* **69**, 629–642 (1997). 30

[80] Hartmann, S. R. & Hahn, E. L. Nuclear double resonance in the rotating frame. *Phys. Rev.* **128**, 2042–2053 (1962). 31

[81] Pines, A., Gibby, M. G. & Waugh, J. S. Proton enhanced nuclear induction spectroscopy. A method for high resolution NMR of dilute spins in solids. *The Journal of Chemical Physics* **56**, 1776–1777 (1972). 31

[82] Conte, P., Spaccini, R. & Piccolo, A. State of the art of CPMAS ^{13}C–NMR spectroscopy applied to natural organic matter. *Progress in Nuclear Magnetic Resonance Spectroscopy* **44**, 215 – 223 (2004). 31

[83] London, P. *et al.* Detecting and polarizing nuclear spins with double resonance on a single electron spin. *Phys. Rev. Lett.* **111**, 067601 (2013). 31, 32

[84] Henstra, A., P, D., Schmidt, J. & Wenckeback, W. T. Nuclear spin orientation via electron spin locking (NOVEL). *Journal of Magnetic Resonance* **77**, 389–393 (1988). 31

[85] Sanada, H. *et al.* Gate control of dynamic nuclear polarization in GaAs quantum wells. *Phys. Rev. Lett.* **94**, 097601 (2005). 31

[86] Ono, K., Austing, D. G., Tokura, Y. & Tarucha, S. Current rectification by pauli exclusion in a weakly coupled double quantum dot system. *Science* **297**, 1313–1317 (2002). 31

[87] Ono, K. & Tarucha, S. Nuclear-spin-induced oscillatory current in spin-blockaded quantum dots. *Phys. Rev. Lett.* **92**, 256803 (2004). 31

[88] Bornet, A. *et al.* Boosting dissolution dynamic nuclear polarization by cross polarization. *The Journal of Physical Chemistry Letters* **4**, 111–114 (2013). 31

[89] Navon, G., Song, Y., Room, T., Appelt, S. *et al.* Enhancement of solution NMR and MRI with laser-polarized xenon. *Science* **271**, 1848 (1996). 31

[90] Fischer, R. *et al.* Bulk nuclear polarization enhanced at room temperature by optical pumping. *Phys. Rev. Lett.* **111**, 057601 (2013). 32

[91] Wang, H. J. *et al.* Sensitive magnetic control of ensemble nuclear spin hyperpolarization in diamond. *Nature Communications* **4**, 1940 (2013). 32

[92] Chen, Q., Schwarz, I., Jelezko, F., Retzker, A. & Plenio, M. B. Optical hyperpolarization of ^{13}C nuclear spins in nanodiamond ensembles. *Phys. Rev. B* **92**, 184420 (2015). 32, 161

[93] Scheuer, J. *et al.* Optically induced dynamic nuclear spin polarisation in diamond. *New Journal of Physics* **18**, 013040 (2016). 32

[94] Reynhardt, E. C. & High, G. L. Dynamic nuclear polarization of diamond. II. nuclear orientation via electron spin-locking. *Journal of Chemical Physics* **109**, 4100–4107 (1998). 32

[95] Reynhardt, E. C. & High, G. L. Dynamic nuclear polarization of diamond. I. solid state and thermal mixing effects. *The Journal of chemical physics* **109**, 4090–4099 (1998). 33, 37, 79, 161

[96] Reynhardt, E. C. & High, G. L. Dynamic nuclear polarization of diamond. III. paramagnetic electron relaxation times from enhanced ^{13}C nuclear magnetic resonance signals. *Journal of Chemical Physics* **113**, 744–750 (2000). 33

[97] Wind, R., Duijvestijn, M., van der Lugt, C., Manenschijn, A. & Vriend, J. Applications of dynamic nuclear polarization in ^{13}C NMR in solids. *Progress in Nuclear Magnetic Resonance Spectroscopy* **17**, 33 – 67 (1985). 33, 39

[98] Duijvestijn, M. *et al.* ^{13}C NMR spectroscopy in diamonds using dynamic nuclear polarization. *Chemical physics letters* **102**, 25–28 (1983). 33, 79

[99] Zhou, J. *et al.* Study of natural diamonds by dynamic nuclear polarization-enhanced ^{13}C nuclear magnetic resonance spectroscopy. *Solid State Nuclear Magnetic Resonance* **3**, 339 – 351 (1994). 33

[100] Fang, K. *et al.* Study of diamond film by dynamic nuclear polarization-enhanced ^{13}C nuclear magnetic resonance spectroscopy. *Applied Magnetic Resonance* **29**, 211–219 (2005). 33

[101] Bloembergen, N. On the interaction of nuclear spins in a crystalline lattice. *Physica* **15**, 386 – 426 (1949). 36, 77

[102] Khutsishvili, G. R. Spin diffusion. *Soviet Physics Uspekhi* **8**, 743 (1966). 36, 37

[103] Overhauser, A. W. Polarization of nuclei in metals. *Phys. Rev.* **92**, 411–415 (1953). 37

[104] Carver, T. R. & Slichter, C. P. Polarization of nuclear spins in metals. *Phys. Rev.* **92**, 212–213 (1953). 37

[105] Carver, T. R. & Slichter, C. P. Experimental verification of the overhauser nuclear polarization effect. *Phys. Rev.* **102**, 975–980 (1956). 37

[106] Abragam, A. & Proctor, W. G. Dynamic polarization of atomic nuclei in solids. *Compt. Rend.* **246**, 2253–2256 (1958). 38

[107] Erb, E., Motchane, J. L. & Uebersfeld, J. Effect of nuclear polarization in liquids and gas adsorbed on charcoal. *Compt. Rend.* **243**, 2121–2123 (1958). 38

[108] Jeffries, C. D. Polarization of nuclei by resonance saturation in paramagnetic crystals. *Phys. Rev.* **106**, 164–165 (1957). 38

[109] Kessenikh, A., Lushchikov, V., Manenkov, A. & Taran, Y. V. Proton polarization in irradiated polyethylenes. *Soviet Phys.-Solid State (English Transl.)* **5** (1963). 38

[110] Kessenikh A V, M. & Pyatnitskii, A. A. On explanation of experimental data on dynamic polarization of protons in irradiated polyethylenes. *Sov.Phys. Solid State* **6**, 641–643 (1964). 38

[111] Hwang, C. F. & Hill, D. A. Phenomenological model for the new effect in dynamic polarization. *Phys. Rev. Lett.* **19**, 1011–1014 (1967). 38

[112] Hwang, C. F. & Hill, D. A. New effect in dynamic polarization. *Phys. Rev. Lett.* **18**, 110–112 (1967). 38

[113] Wollan, D. S. Dynamic nuclear polarization with an inhomogeneously broadened ESR line. I. theory. *Phys. Rev. B* **13**, 3671–3685 (1976). 38

[114] Wollan, D. S. Dynamic nuclear polarization with an inhomogeneously broadened ESR line. II. experiment. *Phys. Rev. B* **13**, 3686–3696 (1976). 38

[115] Provotorov, B. Magnetic resonance saturation in crystals. *Sov. Phys. JETP* **14**, 1126–1131 (1962). 39

[116] Borghini, M. Spin-temperature model of nuclear dynamic polarization using free radicals. *Phys. Rev. Lett.* **20**, 419–421 (1968). 39

[117] Dorn, H., Wang, J., Allen, L., Sweeney, D. & Glass, T. Flow dynamic nuclear polarization, a novel method for enhancing NMR signals in flowing fluids. *Journal of Magnetic Resonance* **79**, 404 – 412 (1988). 39

[118] McCarney, E. R., Armstrong, B. D., Lingwood, M. D. & Han, S. Hyperpolarized water as an authentic magnetic resonance imaging contrast agent. *Proceedings of the National Academy of Sciences* **104**, 1754–1759 (2007). 39

[119] Dorn, H., Gu, J., Bethune, D., Johnson, R. & Yannoni, C. The nature of fullerene solution collisional dynamics. a ^{13}C DNP and NMR study of the C_{60}/C_6D_6/TEMPO system. *Chemical Physics Letters* **203**, 549 – 554 (1993). 39

[120] Loening, N. M., Rosay, M., Weis, V. & Griffin, R. G. Solution-state dynamic nuclear polarization at high magnetic field. *Journal of the American Chemical Society* **124**, 8808–8809 (2002). 39

[121] Hausser, K. H., Stehlik, D. & Waugh, J. S. *Dynamic Nuclear Polarization in Liquids* (Academic, New York, 1968). 41

[122] Cassidy, M. *Hyperpolarized silicon particles as in-vivo imaging agents.* Ph.D. thesis, Harvard University (2012). 52, 63, 121, 128, 131

[123] Rej, E., Gaebel, T., Boele, T., Waddington, D. E. J. & Reilly, D. J. Hyperpolarized nanodiamond with long spin-relaxation times. *Nature communications* **6**, 8459 (2015). 65, 136, 137

[124] Kittel, C. *Introduction to Solid State Physics* (John Wiley and Sons., 1968). 66

[125] Ma, F., Xu, K. & Fan, D. Strain energy anisotropy in germanium and other diamond-cubic polycrystalline films. *Thin solid films* **500**, 164–168 (2006). 66

[126] Momma, K. & Izumi, F. Vesta 3 for three-dimensional visualization of crystal, volumetric and morphology data. *Journal of Applied Crystallography* **44**, 1272–1276 (2011). 67, 68, 70

[127] Zaitsev, A. M. *Optical Properties of Diamond: A Data Handbook* (Springer-Verlag Berlin Heidelberg, 2001). 66, 69

[128] Jelezko, F. & Wrachtrup, J. Single defect centres in diamond: A review. *Physica status solidi (a)* **203**, 3207–3225 (2006). 66, 71

[129] Jelezko, F. & Wrachtrup, J. Read-out of single spins by optical spectroscopy. *Journal of Physics: Condensed Matter* **16**, R1089 (2004). 66, 71

[130] Hunt, D. *et al.* Identification of the neutral carbon <100>–split interstitial in diamond. *Physical Review B* **61**, 3863 (2000). 66

[131] Smith, H. E., Davies, G., Newton, M. E. & Kanda, H. Structure of the self-interstitial in diamond. *Phys. Rev. B* **69**, 045203 (2004). 66

[132] Hounsome, L. S. *et al.* Origin of brown coloration in diamond. *Phys. Rev. B* **73**, 125203 (2006). 66

[133] Iakoubovskii, K., Dannefaer, S. & Stesmans, A. Evidence for vacancy-interstitial pairs in Ib–type diamond. *Phys. Rev. B* **71**, 233201 (2005). 66

[134] Kiflawi, I., Collins, A. T., Iakoubovskii, K. & Fisher, D. Electron irradiation and the formation of vacancy–interstitial pairs in diamond. *Journal of Physics: Condensed Matter* **19**, 046216 (2007). 66

[135] Iakoubovskii, K. *et al.* Annealing of vacancies and interstitials in diamond. *Physica B: Condensed Matter* **340**, 67 – 75 (2003). 66, 69

[136] Dannefaer, S. & Iakoubovskii, K. Defects in electron irradiated boron-doped diamonds investigated by positron annihilation and optical absorption. *Journal of Physics: Condensed Matter* **20**, 235225 (2008). 66, 69

[137] Twitchen, D. J., Newton, M. E., Baker, J. M., Anthony, T. R. & Banholzer, W. F. Electron-paramagnetic-resonance measurements on the divacancy defect center R4/W6 in diamond. *Phys. Rev. B* **59**, 12900–12910 (1999). 66

[138] Iakoubovskii, K. & Stesmans, A. Dominant paramagnetic centers in ^{17}O-implanted diamond. *Phys. Rev. B* **66**, 045406 (2002). 66

[139] Kiflawi, I., Bruley, J., Luyten, W. & Van Tendeloo, G. Natural and man-made platelets in type–Ia diamonds. *Philosophical Magazine B* **78**, 299–314 (1998). 66

[140] Goss, J. P. *et al.* Extended defects in diamond: The interstitial platelet. *Phys. Rev. B* **67**, 165208 (2003). 66

[141] Iakoubovskii, K. & Adriaenssens, G. Characterization of platelet-related infrared luminescence in diamond. *Philosophical magazine letters* **80**, 441–444 (2000). 66

[142] Chen, J. H., Bernaerts, D., Seo, J. W., Van Tendeloo, G. & Kagi, H. Voidites in polycrystalline natural diamond. *Philosophical magazine letters* **77**, 135–140 (1998). 66

[143] Kiflawi, I. & Bruley, J. The nitrogen aggregation sequence and the formation of voidites in diamond. *Diamond and Related Materials* **9**, 87 – 93 (2000). 66

[144] Walker, J. Optical absorption and luminescence in diamond. *Reports on Progress in Physics* **42**, 1605 (1979). 69

[145] Collins, A. T. The detection of colour-enhanced and synthetic gem diamonds by optical spectroscopy. *Diamond and Related Materials* **12**, 1976 – 1983 (2003). 69

[146] Loubser, J. H. N. & van Wyk, J. A. Electron spin resonance in the study of diamond. *Reports on Progress in Physics* **41**, 1201 (1978). 69

[147] DiVincenzo, D. P. Quantum computation. *Science* **270**, 255 (1995). 71

[148] Wrachtrup, J. & Jelezko, F. Processing quantum information in diamond. *Journal of Physics: Condensed Matter* **18**, S807 (2006). 71

[149] Gaebel, T. *et al.* Room-temperature coherent coupling of single spins in diamond. *Nature Physics* **2**, 408–413 (2006). 71

[150] Jelezko, F., Gaebel, T., Popa, I., Gruber, A. & Wrachtrup, J. Observation of coherent oscillations in a single electron spin. *Phys. Rev. Lett.* **92**, 076401 (2004). 71

[151] Jelezko, F. *et al.* Observation of coherent oscillation of a single nuclear spin and realization of a two-qubit conditional quantum gate. *Phys. Rev. Lett.* **93**, 130501 (2004). 71

[152] Childress, L. *et al.* Coherent dynamics of coupled electron and nuclear spin qubits in diamond. *Science* **314**, 281–285 (2006). 71

[153] Hanson, R., Mendoza, F., Epstein, R. & Awschalom, D. Polarization and readout of coupled single spins in diamond. *Physical review letters* **97**, 087601 (2006). 71

[154] Neumann, P. *et al.* Quantum register based on coupled electron spins in a room-temperature solid. *Nature Physics* **6**, 249–253 (2010). 71

[155] Treussart, F. Photoluminescence of single colour defects in 50 nm diamond nanocrystals. *Physica B: Condensed Matter* **376**, 926–929 (2006). 71

[156] Barnard, A. S. Diamond standard in diagnostics: nanodiamond biolabels make their mark. *The Analyst* **134**, 1751–1764 (2009). 71

[157] Chao, J. L. Nanometer-sized diamond particle as a probe for biolabeling. *Biophysical Journal* **93**, 2199–2208 (2007). 71

[158] Chang, Y.-R. *et al.* Mass production and dynamic imaging of fluorescent nanodiamonds. *Nature nanotechnology* **3**, 284–288 (2008). 71

[159] D'Haenens-Johansson, U. F. *et al.* Near-colorless HPHT synthetic diamonds from AOTC group. *Gems & Gemology* **50** (2014). 71

[160] Bundy, F., Hall, H., Strong, H. & Wentorf, R. Man-made diamonds. *Nature* **176**, 51–55 (1955). 71

[161] Bundy, F. Pressure-temperature phase diagram of elemental carbon. *Physica A: Statistical Mechanics and its Applications* **156**, 169 – 178 (1989). 71

[162] Bovenkerk, H., Bundy, F. P., Hall, H., Strong, H. & Wentorf, R. Preparation of diamond. *Nature* **184**, 1094–1098 (1959). 71

[163] Burns, R. *et al.* Growth of high purity large synthetic diamond crystals. *Diamond and Related Materials* **8**, 1433–1437 (1999). 72

[164] Burns, R. *et al.* Growth-sector dependence of optical features in large synthetic diamonds. *Journal of crystal growth* **104**, 257–279 (1990). 72

[165] Strong, H. & Chrenko, R. M. Further studies on diamond growth rates and physical properties of laboratory-made diamond. *The Journal of Physical Chemistry* **75**, 1838–1843 (1971). 72

[166] Sumiya, H. & Satoh, S. High-pressure synthesis of high-purity diamond crystal. *Diamond and Related Materials* **5**, 1359–1365 (1996). 72

[167] Ekimov, E. *et al.* Superconductivity in diamond. *Nature* **428**, 542–545 (2004). 72

[168] Wort, C. J. & Balmer, R. S. Diamond as an electronic material. *Materials Today* **11**, 22 – 28 (2008). 72

[169] DeCarli, P. S. & Jamieson, J. C. Formation of diamond by explosive shock. *Science* **133**, 1821–1822 (1961). 72

[170] Fang, X., Mao, J., Levin, E. & Schmidt-Rohr, K. Nonaromatic core–shell structure of nanodiamond from solid-state NMR spectroscopy. *Journal of the American Chemical Society* **131**, 1426–1435 (2009). 72, 79

[171] Mita, Y. Change of absorption spectra in type-Ib diamond with heavy neutron irradiation. *Phys. Rev. B* **53**, 11360–11364 (1996). 73

[172] Krueger, A. New carbon materials: biological applications of functionalized nanodiamond materials. *Chemistry–A European Journal* **14**, 1382–1390 (2008). 73

[173] Komatsu, N., Kadota, N., Kimura, T. & Osawa, E. Solution–phase ^{13}C NMR spectroscopy of detonation nanodiamond. *Chemistry Letters* **36**, 398–399 (2007). 73

[174] Lin, C. R., Wei, D. H., Dao, M. K. B., Chung, R. J. & Chang, M. H. Nanocrystalline diamond particles prepared by high-energy ball milling method. *Applied Mechanics and Materials* **284**, 168–172 (2013). 73

[175] Gaebel, T. *et al.* Size-reduction of nanodiamonds via air oxidation. *Diamond and Related Materials* **21**, 28–32 (2012). 74, 110, 137

[176] Furman, G., Kunoff, E., Goren, S., Pasquier, V. & Tinet, D. Nuclear spin-lattice relaxation via paramagnetic impurities in solids with arbitrary space dimension. *Physical Review B* **52**, 10182 (1995). 77, 103, 137

[177] Furman, G., Kunoff, E., Goren, S., Pasquier, V. & Tinet, D. Fractional power time dependence of the nuclear magnetization in the presence of paramagnetic impurities. *Solid state nuclear magnetic resonance* **4**, 255–258 (1995). 77

[178] Furman, G., Panich, A., Yochelis, A., Kunoff, E. & Goren, S. Nuclear spin-lattice relaxation of dipolar order caused by paramagnetic impurities. *Physical Review B* **55**, 439 (1997). 77

[179] Blumberg, W. Nuclear spin-lattice relaxation caused by paramagnetic impurities. *Physical Review* **119**, 79 (1960). 77, 103

[180] Henrichs, P. M., Cofield, M. L., Young, R. H. & Hewitt, J. M. Nuclear spin-lattice relaxation via paramagnetic centers in solids. ^{13}C NMR of diamonds. *Journal of Magnetic Resonance (1969)* **58**, 85–94 (1984). 79

[181] Terblanche, C. J., Reynhardt, E. C., Rakitianski, S. A. & Van Wyk, J. A. ^{13}C spin–lattice relaxation in natural diamond: Zeeman relaxation in fields of 500 to 5000 G at 300 K due to fixed paramagnetic nitrogen defects. *Solid state nuclear magnetic resonance* **19**, 107–129 (2001). 79

[182] Zhou, J. *et al.* Study of natural diamonds by dynamic nuclear polarization enhanced ^{13}C nuclear magnetic resonance spectroscpy. *Solid State Nucl Magn Reson* **3**, 339–351 (1994). 79

[183] Reynhardt, E. & Terblanche, C. ^{13}C relaxation in natural diamond. *Chemical physics letters* **269**, 464–468 (1997). 79

[184] Pruski, M., Lang, D. P., Hwang, S.-J., Jia, H. & Shinar, J. Structure of thin diamond films: A ^{1}H and ^{13}C nuclear magnetic resonance study. *Phys. Rev. B* **49**, 10635 (1994). 79

[185] Alam, T. M. Solid state ^{13}C magic angle spinning NMR spectroscopy characterization of particle size structural variations in synthetic nanodiamonds. *Materials Chemistry and Physics* **85**, 310–315 (2004). 79

[186] Lefmann, K. *et al.* NMR spectra of pure ^{13}C diamond. *Phys. Rev. B* **50**, 15623 – 15627 (1994). 79

[187] Shabanova, E., Schaumburg, K. & Sellschop, J. ^{13}C NMR investigations of spin–lattice relaxation in 99% ^{13}C-enriched diamonds. *Journal of Magnetic Resonance* **130**, 8–17 (1998). 79

[188] Komatsu, N., Kadota, N., Kimura, T. & Osawa, E. Solution–phase ^{13}C NMR spectroscopy of detonation nanodiamond. *Chemistry Letters* **36**, 398–399 (2007). 79

[189] Shames, A. *et al.* Defects and impurities in nanodiamonds: EPR, NMR and TEM study. *Journal of Physics and Chemistry of Solids* **63**, 1993–2001 (2002). 79, 101

[190] Panich, A. *et al.* Nuclear magnetic resonance study of ultrananocrystalline diamonds. *The European Physical Journal B-Condensed Matter and Complex Systems* **52**, 397–402 (2006). 79, 101

[191] Andrew, E. R., Bradbury, A. & Eades, R. G. Nuclear magnetic resonance spectra from a crystal rotated at high speed. *Nature* **182**, 1659 (1958). 82

[192] Lowe, I. Free induction decays of rotating solids. *Physical Review Letters* **2**, 285 (1959). 82

[193] Zavoisky, E. *Paramagnetic absorption in the perpendicular and parallel fields for salts, solutions and metals.* Ph.D. thesis, Moscow Inst. of Phys. of Acad. of Sci of USSR (1994). 87

[194] Bleaney, B. & Penrose, R. Paramagnetic resonance at low temperatures in chromic alum. *Proceedings of the Physical Society* **60**, 395 (1948). 87

[195] Stoll, S. & Schweiger, A. Easyspin, a comprehensive software package for spectral simulation and analysis in EPR. *Journal of Magnetic Resonance* **178**, 42–55 (2006). 88, 102, 153

[196] Rovere, M. *et al.* Low temperature electron spin resonance investigation of ultrananocrystalline diamond films as a function of nitrogen content. *Diamond and Related Materials* **15**, 1913 – 1916 (2006). 93

[197] Raman, C. V. A new radiation. *Indian J. Phys.* **2**, 387–398 (1928). 94

[198] Ferrari, A. C. & Robertson, J. Raman spectroscopy of amorphous, nanostructured, diamond-like carbon, and nanodiamond. *Philosophical Transactions of the Royal Society of London A: Mathematical, Physical and Engineering Sciences* **362**, 2477–2512 (2004). 96

[199] Wada, N., Gaczi, P. J. & Solin, A. Diamond–like 3–fold coordinated amorphous carbon. *J. Non-cryst. Solids* **35-36**, 543–548 (1980). 96

[200] Salis, S., Gardiner, D. J., Bowden, M., Savage, J. & Rodway, D. Monitoring the quality of diamond films using raman spectra excited at 514.5 nm and 633 nm. *Diam Relat Mater.* **5**, 589 – 591 (1996). 96

[201] Mura, S. & Couvreur, P. Nanotheranostics for personalized medicine. *Advanced drug delivery reviews* **64**, 1394–1416 (2012). 100, 136

[202] Cassidy, M., Ramanathan, C., Cory, D., Ager, J. & Marcus, C. M. Radical-free dynamic nuclear polarization using electronic defects in silicon. *Physical Review B* **87**, 161306 (2013). 100, 136

[203] Zhang, X.-Q. *et al.* Polymer-functionalized nanodiamond platforms as vehicles for gene delivery. *ACS nano* **3**, 2609–2616 (2009). 100, 136

[204] See collection of articles in recent issue of. *Nat. Nanotechnol.* **10**, 101–184 (2015). 100

[205] Lurie, D. J., Davies, G. R., Foster, M. A. & Hutchison, J. M. Field–cycled PEDRI imaging of free radicals with detection at 450 mT. *Magnetic resonance imaging* **23**, 175–181 (2005). 109

[206] Baumann, P. & Nemanich, R. Surface cleaning, electronic states and electron affinity of diamond (100),(111) and (110) surfaces. *Surface science* **409**, 320–335 (1998). 110, 120

[207] Bornet, A., Melzi, R., Jannin, S. & Bodenhausen, G. Cross polarization for dissolution dynamic nuclear polarization experiments at readily accessible temperatures 1.2<T< 4.2 K. *Applied Magnetic Resonance* **43**, 107–117 (2012). 120

[208] Marco-Rius, I. *et al.* Quantitation of a spin polarization–induced nuclear overhauser effect (SPINOE) between a hyperpolarized ^{13}C–labeled cell metabolite and water protons. *Contrast Media & Molecular Imaging* **9**, 182–186 (2014). 120, 121

[209] Pichler, B., Judenhofer, M. & Wehrl, H. PET/MRI hybrid imaging: devices and initial results. *European Radiology* **18**, 1077–1086 (2008). 122

[210] Strange, J. H. & Halse, M. R. *Imaging Techniques for Solids and Quasi-Solids* (John Wiley & Sons, Ltd, 2007). 123, 126

[211] Hoult, D. & Lauterbur, P. C. The sensitivity of the zeugmatographic experiment involving human samples. *Journal of Magnetic Resonance* **34**, 425 – 433 (1979). 124

[212] Gadian, D. G. & Robinson, F. N. H. Radiofrequency losses in NMR experiments on electrically conducting samples. *Journal of Magnetic Resonance* **34**, 449–455 (1979). 124

[213] Parra-Robles, J., Cross, A. R. & Santyr, G. E. Theoretical signal-to-noise ratio and spatial resolution dependence on the magnetic field strength for hyperpolarized noble gas magnetic resonance imaging of human lungs. *Medical Physics* **32**, 221–229 (2005). 124

[214] Doty, F. D., Entzminger, G., Kulkarni, J., Pamarthy, K. & Staab, J. P. Radio frequency coil technology for small–animal MRI. *NMR in Biomedicine* **20**, 304–325 (2007). 124

[215] Mispelter, J., Lupa, M. & Briguet, A. *NMR probeheads for biophysical and biomedical experiments* (Imperial College Press, London, 2006). 124, 125

[216] Rainey, J. K., DeVries, J. S. & Sykes, B. D. Estimation and measurement of flat or solenoidal coil inductance for radiofrequency NMR coil design. *Journal of Magnetic Resonance* **187**, 27 – 37 (2007). 125

[217] Tsai, L., Mair, R., Rosen, M., Patz, S. & Walsworth, R. An open-access, very-low-field MRI system for posture-dependent ^{3}He human lung imaging. *Journal of Magnetic Resonance* **193**, 274 – 285 (2008). 125

[218] Callaghan, P. T. *Principles of nuclear magnetic resonance microscopy* (Oxford University Press, Oxford, 1993). 125

[219] Milani, J. *et al.* A magnetic tunnel to shelter hyperpolarized fluids. *Review of Scientific Instruments* **86**, 024101 (2015). 128

[220] Hovav, Y., Feintuch, A., Vega, S. & Goldfarb, D. Dynamic nuclear polarization using frequency modulation at 3.34 T. *Journal of Magnetic Resonance* **238**, 94 – 105 (2014). 128

[221] Bornet, A. *et al.* Microwave frequency modulation to enhance dissolution dynamic nuclear polarization. *Chemical Physics Letters* **602**, 63 – 67 (2014). 128

[222] Li, D. *et al.* Intrinsic origin of spin echoes in dipolar solids generated by strong π pulses. *Phys. Rev. B* **77**, 214306 (2008). 131

[223] Li, D., Dementyev, A. E., Dong, Y., Ramos, R. G. & Barrett, S. E. Generating unexpected spin echoes in dipolar solids with π pulses. *Phys. Rev. Lett.* **98**, 190401 (2007). 131

[224] Franzoni, M. B., Acosta, R. H., Pastawski, H. M. & Levstein, P. R. Storage of quantum coherences as phase-labelled local polarization in solid-state nuclear magnetic resonance. *Philosophical Transactions of the Royal Society of London A: Mathematical, Physical and Engineering Sciences* **370**, 4713–4733 (2012). 134

[225] Franzoni, M. B. & Levstein, P. R. Manifestations of the absence of spin diffusion in multipulse NMR experiments on diluted dipolar solids. *Physical Review B* **72**, 235410 (2005). 134

[226] Ma, W.-L. *et al.* Uncovering many-body correlations in nanoscale nuclear spin baths by central spin decoherence. *Nature communications* **5**, 4822 (2014). 134

[227] Zhang, L. *et al.* Nanoparticles in medicine: therapeutic applications and developments. *Clinical pharmacology and therapeutics* **83**, 761–769 (2008). 136

[228] Hens, Z. & Martins, J. C. A solution NMR toolbox for characterizing the surface chemistry of colloidal nanocrystals. *Chemistry of Materials* **25**, 1211–1221 (2013). 136

[229] Protesescu, L. *et al.* Unraveling the core–shell structure of ligand-capped Sn/SnOx nanoparticles by surface-enhanced nuclear magnetic resonance, mossbauer, and X-ray absorption spectroscopies. *ACS nano* **8**, 2639–2648 (2014). 136

[230] Rossini, A. J. *et al.* Dynamic nuclear polarization surface enhanced NMR spectroscopy. *Accounts of chemical research* **46**, 1942–1951 (2013). 136

[231] Grüning, W. R. *et al.* Molecular–level characterization of the structure and the surface chemistry of periodic mesoporous organosilicates using DNP–surface enhanced NMR spectroscopy. *Physical Chemistry Chemical Physics* **15**, 13270–13274 (2013). 136

[232] Rossini, A. J. *et al.* One hundred fold overall sensitivity enhancements for silicon-29 NMR spectroscopy of surfaces by dynamic nuclear polarization with CPMG acquisition. *Chemical Science* **3**, 108–115 (2012). 136

[233] Lelli, M. *et al.* Fast characterization of functionalized silica materials by silicon-29 surface-enhanced NMR spectroscopy using dynamic nuclear polarization. *Journal of the American Chemical Society* **133**, 2104–2107 (2011). 136

[234] Lesage, A. *et al.* Surface enhanced NMR spectroscopy by dynamic nuclear polarization. *Journal of the American Chemical Society* **132**, 15459–15461 (2010). 136

[235] Gajan, D. *et al.* Hybrid polarizing solids for pure hyperpolarized liquids through dissolution dynamic nuclear polarization. *Proceedings of the National Academy of Sciences* **111**, 14693–14697 (2014). 136

[236] Lingwood, M. D. *et al.* Hyperpolarized water as an MR imaging contrast agent: feasibility of in vivo imaging in a rat model. *Radiology* **265**, 418–425 (2012). 136

[237] Mochalin, V. N. *et al.* Adsorption of drugs on nanodiamond: toward development of a drug delivery platform. *Molecular pharmaceutics* **10**, 3728–3735 (2013). 136

[238] Manus, L. M. *et al.* Gd (III)–nanodiamond conjugates for MRI contrast enhancement. *Nano letters* **10**, 484–489 (2009). 142

[239] Krebs, J. J. Proton spin polarization of water adsorbed on sucrose chars. *The Journal of Chemical Physics* **34**, 326–329 (1961). 142

[240] Krebs, J. & Thompson, J. Dynamic nuclear polarization studies of charred carbohydrates. *The Journal of Chemical Physics* **36**, 2509–2514 (1962). 142

[241] Uebersfeld, J., Motchane, J. & Erb, E. Augmentation de la polarisation nucléaire dans les liquides et gaz adsorbés sur un charbon. extension aux solides contenant des impuretés paramagnétiques. *J. phys. radium* **19**, 843–844 (1958). 142

[242] Dementyev, A. E., Cory, D. G. & Ramanathan, C. Dynamic nuclear polarization in silicon microparticles. *Phys. Rev. Lett* **100**, 127601 (2008). 161

[243] Whiting, N. *et al.* Real-time MRI-guided catheter tracking using hyperpolarized silicon particles. *Scientific reports* **5**, 12842 (2015). 161